Technische Universität München
TUM School of Natural Sciences

Development and Operation of Next-Generation Low-Temperature Detectors for the COSINUS Dark Matter Search

Moritz Kellermann

Vollständiger Abdruck der von der TUM School of Natural Sciences der Technischen Universität München zur Erlangung eines

Doktors der Naturwissenschaften (Dr. rer. nat.)

genehmigten Dissertation.

Vorsitz: apl. Prof. Dr. Norbert Kaiser

Prüfende der Dissertation:

1. Prof. Dr. Stefan Schönert
2. Hon.-Prof. Dr. Allen C. Caldwell

Die Dissertation wurde am 14.04.2025 bei der Technischen Universität München eingereicht und durch die TUM School of Natural Sciences am 14.05.2025 angenommen.

Abstract

In the past decades, the search for dark matter has developed into a rich field of experimental (astro-)particle physics with the ambition to uncover the nature of our universe. Many experiments and techniques were developed to look for minuscule energy depositions from direct interactions of hypothetical dark matter particles with our known Standard Model matter.

For more than 25 years, the DAMA/LIBRA experiment measures an annually modulating signal in the (1-6) keV_{ee}-range, a signature expected for dark matter. While many other experiments exclude the DAMA/LIBRA parameter space, a fully model-independent cross-check can only be done by employing the same detector material: sodium iodide.

COSINUS is a new experiment that will carry out a model-independent cross-check of the DAMA/LIBRA result by operating sodium iodide as a low-temperature detector at $\sim$15 mK. By equipping absorbers with transition edge sensors, it is possible to read out the heat created in particle recoils in addition to the emitted scintillation light. This allows for low energy thresholds for nuclear recoils and enables particle discrimination of interacting particles on an event-by-event basis. With this technique, it is possible to have a background-free measurement of nuclear recoils and thus exclude a nuclear origin of the DAMA/LIBRA signal with only 100 kg days of data.

A modern low-background facility equipped with a dry dilution refrigerator was built recently underground at Laboratori Nazionali del Gran Sasso. By utilizing a water tank with 7 m diameter, instrumented as active muon veto, a background rate of (0.11 ± 0.02) counts/(kg year) is expected. In this work, the design, installation, and commissioning of the refrigerator were prepared, and a SQUID-based low-noise, low-background cryogenic cabling solution for the simultaneous readout of 48 detectors was developed. It is based on superconducting Nb-Ti cables, printed circuit boards made from copper and polyimide, as well as miniaturized spring connectors.

Since the deposition of a transition edge sensor directly on sodium iodide is not possible with the currently available technology, an alternative layout, the remoTES, was developed in this work. In the remoTES, the sensor is deposited on a separate wafer and connected to the absorber via a gold link. This thesis describes the first remoTES measurements on Si and TeO_2, the adaption to sodium iodide, and dedicated optimization studies and simulations. It is shown that the remoTES can fulfill the target criteria of COSINUS, and an energy resolution of 410 eV was reached using a 3.7 g NaI-absorber. Finally, a detector design and manufacturing procedure for a COSINUS dark matter detector for the first run is proposed.

One of the largest noise sources in low-temperature detectors are vibrations in the acoustic frequency range that are produced by the refrigerator itself or in its local environment. In a dry dilution refrigerator, which uses a pulse tube cooler working at 1.4 Hz to reach low temperatures, it is crucial to decouple the detectors from noise sources to ensure operation stability. In this work, the vibrational backgrounds within the laboratory and the refrigerator are characterized, and a dedicated spring-based passive decoupling system operating inside the refrigerator at the detector level was developed. The system is designed to decouple vibrations larger than 1 Hz in vertical as well as horizontal directions. It was tested on a mechanical mockup system and in a dilution refrigerator and validated successfully with COSINUS detectors with masses up to 30 g.

Zusammenfassung

In den vergangenen Jahrzehnten entwickelte sich die Suche nach dunkler Materie in ein reichhaltiges Teilgebiet der (Astro-)Teilchenphysik mit dem Ziel die Natur unseres Universums zu ergründen. Zahlreiche Experimente und Techniken wurden entwickelt um kleinste Energieübertragungen aus Wechselwirkungen unserer Standardmodellmaterie mit hypothetischen Teilchen dunkler Materie zu messen. Seit mehr als 25 Jahren misst das DAMA/LIBRA Experiment ein jährlich modulierendes Signal im (1-6) keV$_{ee}$-Bereich; eine Signatur die von dunkler Materie erwartet wird. Auch wenn viele andere Experimente den DAMA/LIBRA Parameterbereich für dunkle Materie ausschließen, kann eine komplett modellunabhängige Überprüfung nur mit dem gleichen Detektormaterial stattfinden: Natriumiodid.

COSINUS ist ein neues Experiment, welches das DAMA/LIBRA-Ergebnis modellunabhängig überprüfen wird, indem es Natriumiodid als Tieftemperaturdetektor um 15 mK betreiben wird. Dadurch, dass die Absorber mit Phasenübergangsthermometern ausgestattet werden, wird es ermöglicht, die deponierte Wärme zusätzlich zum Szintillationslicht zu messen. Dies begünstigt niedrige Energieschwellen für Kernrückstöße und erlaubt eine Unterscheidung von wechselwirkenden Teilchen bei jedem einzelnen Ereignis. Mit dieser Technik wird eine untergrundfreie Messung von Kernrückstößen ermöglicht und ein Ursprung des DAMA/LIBRA-Signals durch Streuung an Atomkernen kann mit nur etwa 100 (kg Tagen) ausgeschlossen werden.

Kürzlich wurde ein moderner untergrundarmer experimenteller Versuchsaufbau, ausgestattet mit einem trockenen Entmischungskryostaten, im Untergrundlabor Laboratori Nazionali del Gran Sasso fertiggestellt. Dank eines Wassertanks mit 7 m Durchmesser und Höhe, betrieben als aktives Myonenveto, wird eine Ereignisrate von Myon-induzierten Neutronenereignissen von (0.11 ± 0.02) Ereignissen/(kg Jahr) erwartet.

In dieser Arbeit wurde die Auslegung, Installation und Inbetriebnahme des Kryostaten vorbereitet und eine SQUID-basierte, rauscharme und radioreine Verkabelungslösung für 48 Kanäle entwickelt. Sie basiert auf supraleitenden Nb-Ti Kabeln, Leiterplatten aus Kupfer und Polymid, und miniaturisierten Federkontakten.

Die Fertigung eines Phasenübergangsthermometers auf Natriumiodid ist mit den aktuell verfügbaren Technologien nicht möglich. Im Rahmen dieser Arbeit wurde eine alternative Kopplung zwischen Kristall und Sensor, das remoTES, entwickelt. Bei einem remoTES wird der Sensor auf einem separaten Kristall gefertigt und mit dem Absorber über einen Goldlink verbunden. Diese Arbeit beschreibt die ersten remoTES-Messungen mit Si und TeO$_2$, die Adaptierung auf Natriumiodid, und zugehörige Optimierungsstudien und Simulationen. Es wird gezeigt, dass das remoTES die Zielkriterien von COSINUS erfüllen kann; eine Energieauflösung von 410 eV wurde mit einem 3.7 g Absorber erreicht. Abschließend wird ein Plan und eine Fertigungsprozedur für einen COSINUS-

Detektor zur Überprüfung der Kernrückstoßhypothese des DAMA-Signals im Rahmen des ersten Runs vorgestellt.

Vibrationen im akustischen Frequenzbereich sind eine der größten Störquellen von Tieftemperaturdetektoren. Sie werden vom Kryostaten selbst, oder in seiner Umgebung erzeugt. Trockene Entmischungskryostaten verwenden einen Pulsrohrkühler mit einer Arbeitsfrequenz von 1.4 Hz. In diesen Kryostaten ist es besonders wichtig, Sensoren von Störquellen zu entkoppeln, um einen stabilen Betrieb zu gewährleisten. Diese Arbeit beinhaltet eine Charakterisierung der Vibrationen im Labor und im Kryostaten, und die Entwicklung eines federbasierten passiven Vibrationsentkopplungssystems auf Detektorebene im Kryostaten. Das System wurde ausgelegt um Vibrationen größer als 1 Hz, sowohl in vertikaler als auch in horizontaler Richtung zu entkoppeln. Es wurde an einem mechanisch-equivalenten Aufbau getestet und mit COSINUS-Detektoren mit Massen bis 30 g validiert.

Contents

Chapter 1

Introduction

The nature of Dark Matter (DM) remains one of the biggest mysteries in modern physics. Observations on all length scales require an additional, non-luminous "dark" matter, which is more than five times more abundant than the known baryonic matter [1]. While its existence and abundance are known from observations of its gravitational effects, it became clear that it can not be explained by the Standard Model (SM) of particle physics. In the last decades, many experiments have been conducted to search for DM, but no confirmed case for its detection has been made so far.

Cryogenic Observatory for SIgnatures seen in Next-generation Underground Searches (COSINUS) is a new experiment that is embarking on the quest to hunt for DM. It is located in the underground laboratory "Laboratori Nazionali del Gran Sasso (LNGS)", Italy, and utilizes cryogenic detectors made from sodium iodide (NaI). Its first goal will be the cross-check of the DAMA/LIBRA results, an experiment with a standing claim for the detection of DM in our galactic halo [2]. What makes COSINUS unique in this context is the operation of the same target material with a new technology in a modern low background facility [3]. Operating NaI as cryogenic calorimeters will offer three main advantages [4]:

1. A low energy threshold for nuclear recoils.
2. Particle discrimination on an event-by-event basis, and thus a complete background rejection for nuclear recoils.
3. The intrinsic measurement of the NaI-Quenching Factors (QFs).

This PhD project was carried out within the COSINUS group of the Max-Planck-Institut für Physik (MPP). It started in 2021 as the very first PhD project of the group and progressed parallel to the construction of the COSINUS facility. The topics studied involve all facets of COSINUS, in particular, the development of the COSINUS cryogenic facility and cryogenic NaI-based detectors. The following thesis is divided into six chapters:

- **Chapter 1:** This introduction.
- **Chapter 2:** A general introduction to DM, from its many observations to the experiments trying to find DM-induced particle recoils.

- **Chapter 3:** Details about the COSINUS strategy and newly built facility at LNGS. Furthermore, technical details of the dry dilution refrigerators and newly developed cabling are shown.
- **Chapter 4:** Details of the past and current COSINUS detector designs, as well as the results of optimization studies carried out in this work.
- **Chapter 5:** Vibrational backgrounds in COSINUS, how they affect detectors, and technical details on the vibration mitigation strategy developed in this work.
- **Chapter 6:** A conclusion and outlook on the next steps of COSINUS.

Each chapter deals with vastly different topics that lie between particle physics, condensed matter physics, and mechanical engineering. Therefore, each chapter will have its own introduction of important concepts and outlook for future developments.

Chapter 2

Dark Matter

2.1 Cosmological Standard Model

The Λ-Cold Dark Matter (ΛCDM) model was developed in the early 20^{th} century based on simple assumptions within the framework of general relativity. It is considered to be today's standard model of cosmology due to its great success in describing large-scale effects. Such effects include the Cosmic Microwave Background (CMB) (see also section 2.2.5), the large-scale distribution of galaxies, or the abundance of light elements in our universe. A brief summary of the basic concepts is described below.

The cosmological principle states that the universe is homogeneous and isotropic on large scales, meaning that any observer at any location within the universe is subject to the same physical laws. In 1929, Edwin Hubble published a measurement indicating a linear relation between the radial velocity of faraway galaxies (with respect to the observer on Earth) and their distance [5]. The relation describing the velocity v and proper distance d of a galaxy is called Hubble's law

$$v = H_0 \cdot d, \tag{2.1}$$

where H_0 is the Hubble constant at the present time.

One possible explanation, first published by Georges Lemaître [6], is the expansion of space itself by a time-dependent scale factor, $a(t)$, which is related to the Hubble parameter by $H(t) = \frac{\dot{a}(t)}{a(t)}$ and $H_0 = H(t_0)$ with the age of the universe t_0. A common description of this expanding universe is given by the Friedmann-Lemaître-Robertson-Walker metric with a curvature parameter $k \in (0, +1, -1)$

$$ds^2 = -dt^2 + a^2(t)[\frac{dr^2}{1-kr^2} + r^2(d\Theta^2 + sin^2\Theta d\Phi^2)]. \tag{2.2}$$

It is an exact solution of the Einstein field equations and can be used, with the aforementioned Einstein field equations, to derive the first Friedmann equation

$$H^2(t) - \frac{8\pi G}{3}\rho(t) = -\frac{kc^2}{a(t)^2} + \frac{\Lambda c^2}{3}. \tag{2.3}$$

G is the gravitational and Λ the cosmological constant, an addition commonly interpreted as vacuum energy and necessary to explain an accelerating expansion. The equation describes the matter-energy content in our universe and its evolution in time. One can define a critical matter-energy density for which the universe would be flat ($k = 0$) at present, assuming a vanishing cosmological constant

$$\rho_{crit,0} = \frac{3H_0^2}{8\pi G}. \tag{2.4}$$

Then the density parameter $\Omega(t)$ can be defined and separated in contributions by matter ($\Omega_m(t)$), radiation ($\Omega_\gamma(t)$), and vacuum ($\Omega_\Lambda, \rho_\Lambda = \frac{\Lambda c^2}{8\pi G}$)

$$\Omega(t) = \frac{\tilde{\rho}(t)}{\rho_{crit}(t)} = \frac{\rho_m(t) + \rho_\gamma(t) + \rho_\Lambda}{\rho_{crit}(t)} = \Omega_m(t) + \Omega_\gamma(t) + \Omega_\Lambda. \tag{2.5}$$

The matter component can be further separated into a baryonic component Ω_b and a cold DM component Ω_c. Inserting the density parameter into equation 2.3 gives for today's universe (at $t = t_0$) and $\rho(t) = \rho_m(t) + \rho_\gamma(t)$

$$\frac{kc^2}{a_0^2 H_0^2} = \Omega(t_0) - 1. \tag{2.6}$$

By measuring the present matter-energy density, it is possible to determine the curvature of space-time and subsequently derive the evolution of the universe. The currently known numbers are summarized in table 2.1.

Parameter	Symbol	Number
Hubble parameter[1]	H_0	67.4 ± 0.5 (km/s)/Mpc
matter density:	$\Omega_{m,0}$	0.315 ± 0.007
baryonic	$\Omega_{b,0}$	0.0493 ± 0.0006
DM	$\Omega_{c,0}$	0.265 ± 0.007
radiation density	$\Omega_{\gamma,0}$	$(5.38 \pm 0.15) \cdot 10^{-5}$
vacuum density	$\Omega_{\Lambda,0}$	0.685 ± 0.007

Table 2.1: Cosmological parameters summarized by the Particle Data Group [7]. The numbers reported here are derived from strongly model-dependent fits and assume a flat ($k = 0$) universe described by the ΛCDM-model.

Today, it is assumed that matter makes up around 32 % of the mass-energy of the universe, with baryonic matter accounting for about 16 % of that. This means that 84 % of the mass in the universe is dark to the typical measurement methods and henceforth called "Dark Matter". Experimental evidence for the existence of DM exists on different length scales of the universe, from observations of single galaxies to structures spanning the whole observable universe. A selection of the phenomena is discussed in section 2.2.

---

[1] There is currently a significant tension between measurements of the Hubble parameter depending on the method [8]. The number reported here corresponds to measurements via CMB anisotropies.

2.2 Evidences for Dark Matter

2.2.1 Galaxy Rotation Curves

The most intuitive evidence for DM can be observed in the rotation velocities of single spiral galaxies. The velocity v of a body with mass m at radius r can be calculated by applying Newton's law of gravitation for the radial force:

$$|F_r| = \frac{mv^2}{r} = G\frac{mM(r)}{r^2} = |F_G| \tag{2.7}$$

$$v = \sqrt{\frac{GM(r)}{r}} \quad \text{with} \quad M(r) = \int \rho(r)dV$$

G is the gravitational constant, and $\rho(r)$ the mass-density of the galaxy at radius r. With a constant density, a linear increase of the rotation velocity $v(r) \propto r$ would be expected. For large radii and constant mass (as most of the mass is contained within the galactic core), the rotation velocity is expected to fall with the square root of the distance $v(r) \propto \frac{1}{\sqrt{r}}$.

With the increased sensitivity of modern spectrometers, it was possible to precisely measure the rotation velocity of galaxies at large distances. In 1970, Vera Rubin and Kent Ford published a measurement on the movement of stars in the Andromeda Galaxy, which showed a higher galaxy rotation velocity than expected [9], indicating a higher mass than previously measured. Following this study, the large share of undetected non-luminous matter was confirmed for several other galaxies [10]. Figure 2.1 shows a comparison of the expected and measured rotation curve of the galaxy M33.

The discrepancy can be resolved by introducing an additional mass consisting of DM around the galaxy. From the actual rotation curve, the actual mass distribution can be extracted, and the mass profile for the DM component can be derived. Generally, DM is expected to be distributed as a spherical halo around the much smaller visible galaxy.

2.2.2 Cluster Kinematics

Historically, one of the most important works was published by Fritz Zwicky in 1933. He was the first to apply the virial theorem to calculate the mass of the coma cluster, with the result that there has to be an additional "Dark Matter" with much higher density than luminous matter [12]. In a bound (isotropic) system, such as a galaxy cluster, the virial theorem states

$$< E_{kin} >= -\frac{1}{2} < E_{pot} > \tag{2.8}$$

The mean kinetic energy $< E_{kin} >$ is given by

$$< E_{kin} >= \frac{M}{2} \cdot < v^2 > \text{ with } < v^2 >= \frac{1}{M} \cdot \sum_i m_i v_i^2 \tag{2.9}$$

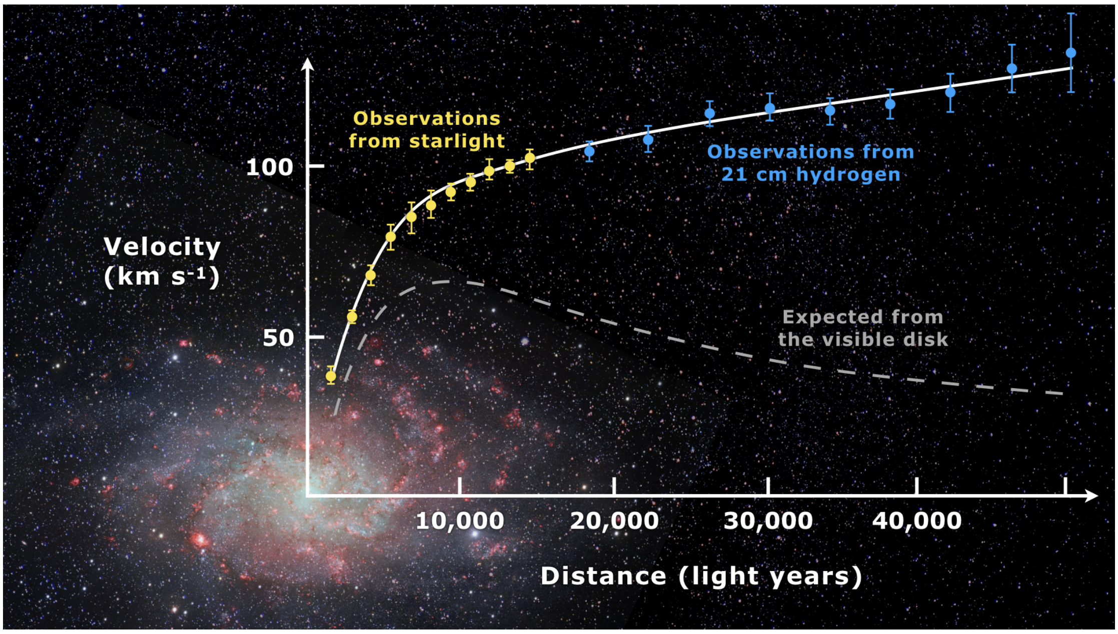

Figure 2.1: Rotation curve for the galaxy M33 [11]. The dashed line shows the expected velocity derived from the visible disk without DM. The yellow and blue data points are from optical observations from starlight and the 21-cm line, respectively. The solid line is a fitted function assuming a DM contribution to the total mass.

M and $< v^2 >$ are the total mass of the galaxy cluster and the average squared velocity of the single galaxies. m_i and v_i are the mass and velocity of every single galaxy bound in the cluster.

The potential energy E_{pot} can, again, be calculated with Newton's law of gravitation

$$E_{pot} = -\frac{G}{2} \sum_{i,j,i \neq j} \frac{m_i m_j}{r_{ij}} = -G \frac{M^2}{r_G} \text{ with } r_G = \frac{2M^2}{\sum_{i,j,i \neq j} \frac{m_i m_j}{r_{ij}}}, \tag{2.10}$$

where G is the gravitational constant and r_{ij} the distance between two galaxies. The mass of the galaxy cluster can then be estimated from the virial theorem

$$M = \frac{r_G < v^2 >}{G}. \tag{2.11}$$

For the coma cluster, Zwicky calculated that the mass has to be at least 400 times larger than expected from luminous matter only [12].

2.2.3 Gravitational Lensing

Another way to look for non-luminous matter in the universe is the gravitational lensing effect. The principle is shown in figure 2.2.

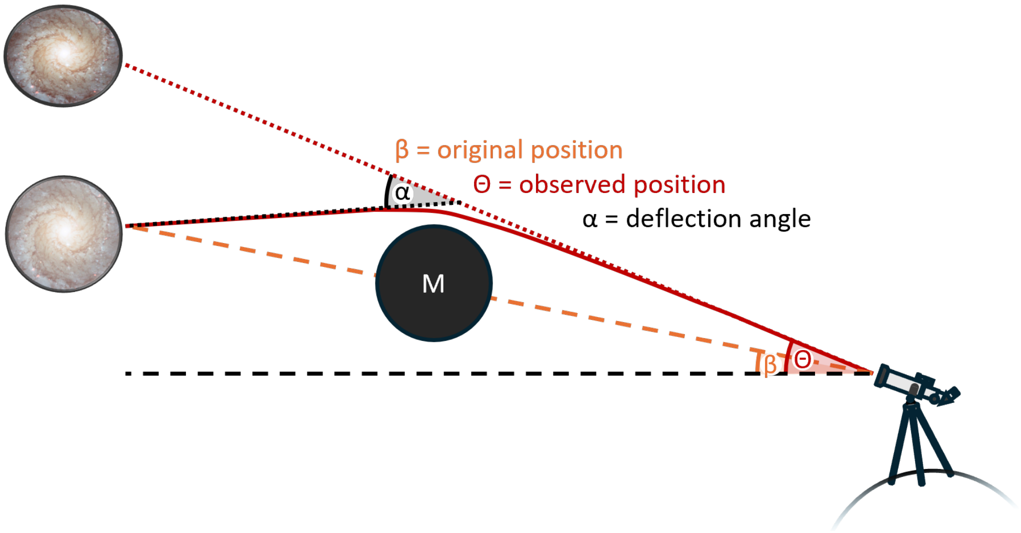

Figure 2.2: Gravitational lensing principle. Around a mass M, the light path is bent by a deflection angle α. Instead of being observed at the original position β, a distorted object will be observed at position Θ.

Due to the curvature of space-time in the presence of mass, the path of an electromagnetic wave is deflected by an angle α, similar to an optical lens. Depending on the configuration of the light source, mass, and observer, gravitational lensing can be classified into three categories [13].

In strong lensing, visible distortions, such as rings, arcs, or multiple images, appear near a light source due to a heavy foreground mass. From the radius of the arc, the foreground mass can be calculated.

In microlensing, multiple images are generated but not resolved by the telescope. Its signature is a change in intensity of the received light when a massive body passes the line of sight to a distant light source.

In weak lensing, the apparent shapes of galaxies are distorted by a foreground mass distribution. They are stretched tangentially to mass overdensities or radial to mass underdensities. The average deformation, or cosmic shear, can be measured by averaging the shape of many galaxies in a small window. Generally, one can measure E-modes produced by gravitational lensing and B-modes that, if measured with a high share, would indicate a non-gravitational origin of the shear (e.g. distortions within the measuring instrument). Figure 2.3 shows the principle of the different modes.

For DM analysis, the cosmic shear can be converted into a convergence field κ. This quantity describes the lens that leads to the measured shear and is directly proportional to the mass density along the line of sight [14]. Figure 2.4 shows a DM map from the COSMOS survey of the Hubble Space Telescope, calculated from the cosmic shear.

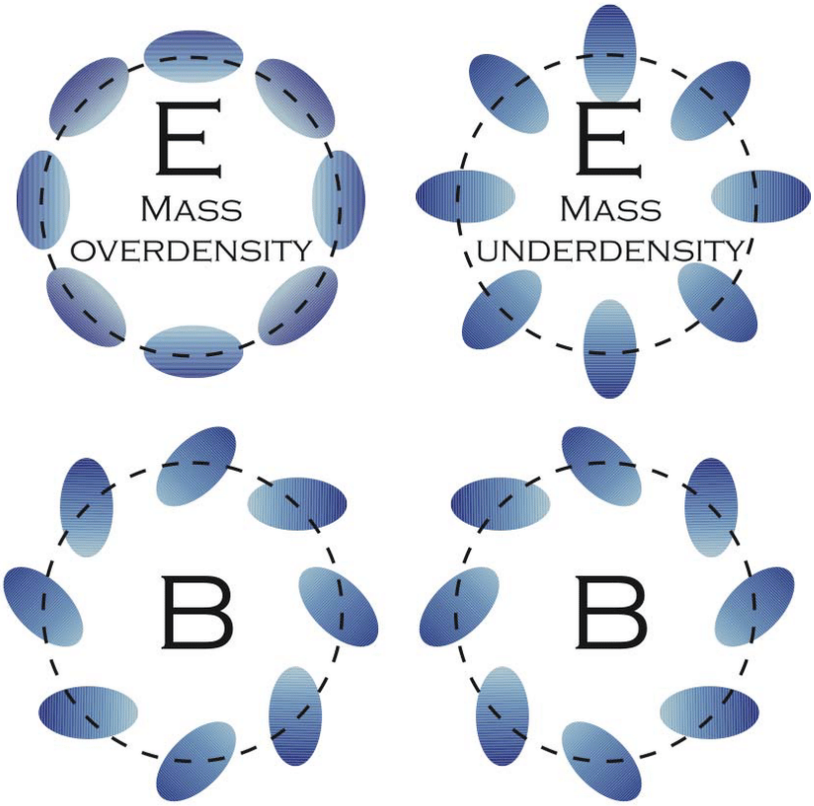

Figure 2.3: Signatures found in shear maps. The shape of galaxies is distorted by the foreground mass distribution. The galaxy is stretched tangential to overdensities and radial to underdensities (E-modes). Curl-like deformations (B-modes) are not inherently produced in high shares by gravitational lensing and hint at systematic effects. In cosmic shear studies, the shape of galaxies is evaluated statistically and checked for E-modes and B-modes. Taken from [13].

In July 2023, the Euclid satellite was launched with the goal of exploring the composition and evolution of the dark universe. In 6 years, it will map more than a third of the sky and allow for dedicated weak lensing studies. Euclid has been taking data since February 2024; the mission is planned to proceed until 2030 [16].

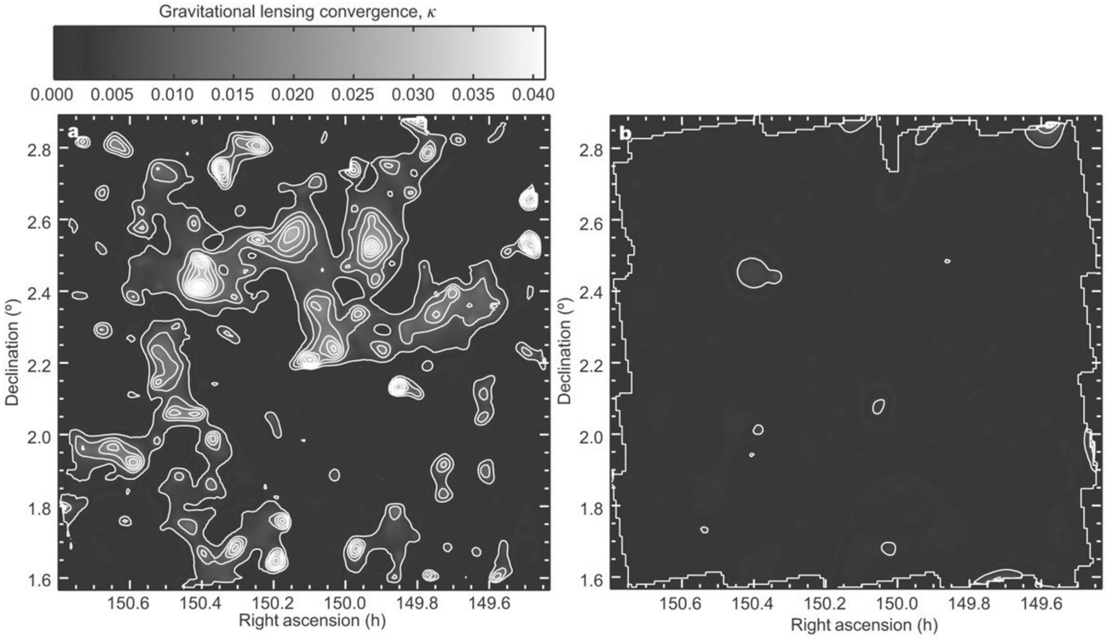

Figure 2.4: DM distribution measured with the COSMOS survey [15]. On the left, the gravitational lensing convergence field is shown. It is a quantity derived from measured E-modes and is proportional to the foreground mass density. On the right, the convergence field for B-modes is shown. It can be used as a cross-check for systematics. In this example, most of the measured window is free of B-modes, indicating low systematic uncertainties.

2.2.4 Bullet Cluster

An almost direct observation of DM can be seen in the bullet cluster. The bullet cluster is a galaxy cluster that collided with another galaxy cluster about 10^8 years ago [17]. By combining different data sets, it is possible to decrypt the physics of the collision [18]. Figure 2.5 shows a composition of optical data from the Magellan and Hubble Space Telescopes, X-ray measurements recorded by the Chandra Telescope, and mass data derived from gravitational lensing.

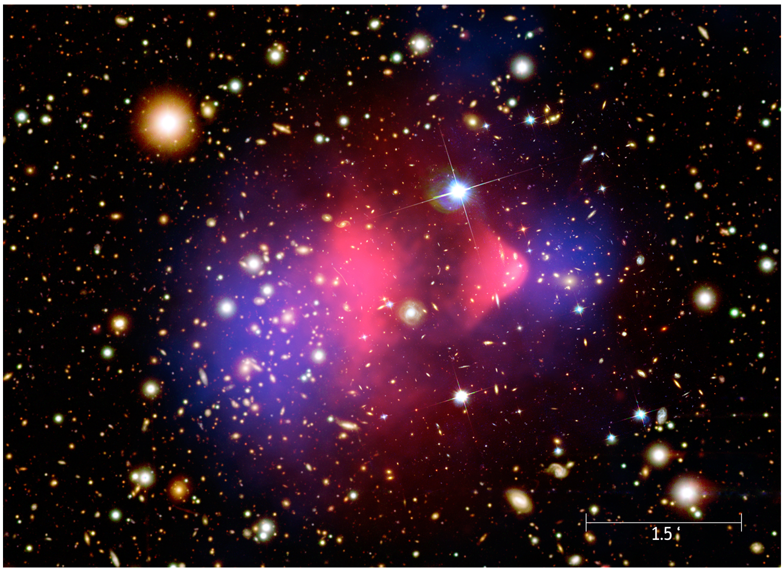

Figure 2.5: Composite image of the bullet cluster [19]. In the background, optical data from the Magellan and Hubble Space Telescopes are shown. The pink region shows X-ray data from the Chandra Telescope, and the blue region marks mass overdensities calculated from weak lensing. The scale in the bottom right corner marks an angle of $1.5\,'$.

The mass distribution (blue) shows two well-separated centers of mass for the two galaxy clusters, while the space in between is actively emitting X-ray radiation (pink). This indicates that the bulk masses of the galaxy clusters, dominated by DM, could pass through each other without interacting. Meanwhile, the space between both galaxy clusters is populated by hot interstellar gas that heated up during the collision between the clusters due to electromagnetic interactions. As a consequence, the interstellar gas slowed down and lagged behind the centers of mass.

2.2.5 Cosmic Microwave Background Radiation

The most precise measurement of the DM abundance happened on a cosmological scale using information from the CMB radiation. It is present in the whole universe and follows a mostly isotropic blackbody spectrum with a temperature of $2.725\,\mathrm{K}$ with anisotropies on the order of $100\,\mu\mathrm{K}$ (excluding the dipole anisotropy) [7].

In the early universe, the following reactions were in thermal equilibrium:

$$\begin{array}{rcll} \gamma & \longleftrightarrow & e^+e^- & \text{pair production/annihilation} \\ e^- + \gamma & \longleftrightarrow & e^- + \gamma & \text{Compton/Thomson scattering} \\ H + \gamma & \longleftrightarrow & p + e^- & \text{ionization/recombination of hydrogen} \end{array}$$

When the universe cooled below the ionization energy of hydrogen, 13.6 eV, most of the electrons and protons recombined into neutral hydrogen. Hence, the number density of free electrons available for scattering reduced, and the mean free path for scattering increased. The CMB decoupled around 380,000 years after the Big Bang when the expansion rate of the universe became greater than the interaction rate of scatterings. The leftover photons from the equilibrium, at the time around 3000 K, redshifted, due to the expanding universe, to today's temperature. Any fluctuation in the spectrum measured can be traced back to fluctuations in the gravitational potential in the early universe.

The CMB was mapped by the satellites COBE [20], WMAP [21], and Planck [22] with increasing resolution. Figure 2.6 shows a sky map of the CMB anisotropies measured by the Planck satellite.

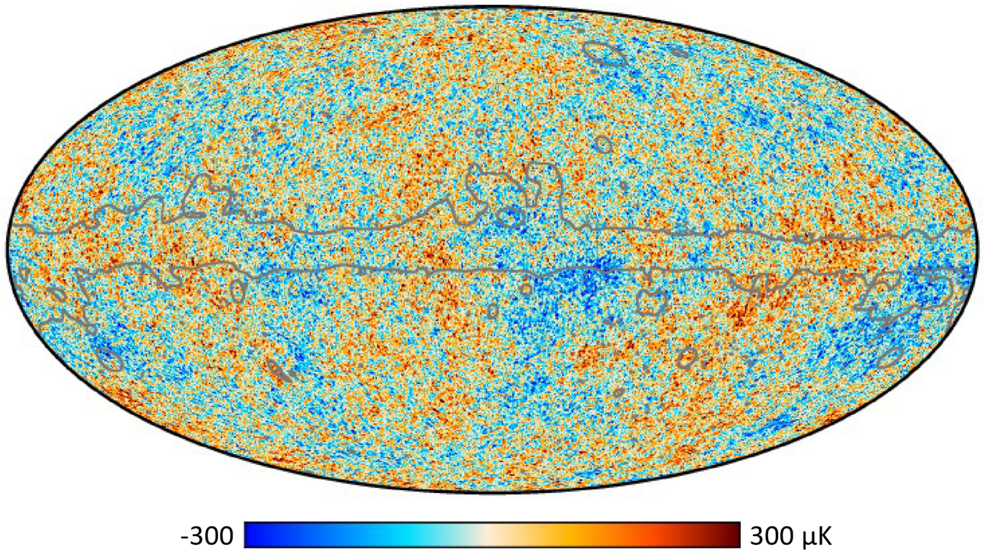

Figure 2.6: CMB anisotropies measured by the Planck satellite [22]. Colder regions are marked in blue, and warmer regions in red. The gray solid lines show the edge of the Milky Way that was subtracted from the data.

In the further analysis, the temperature anisotropies can be expanded in angular multipole moments by applying a spherical Fourier transform. The spectral power D_ℓ^{TT} is then acquired by averaging over all orientations of each angular momentum ℓ. Figure 2.7 shows the measured power spectrum for the Planck 2018 dataset.

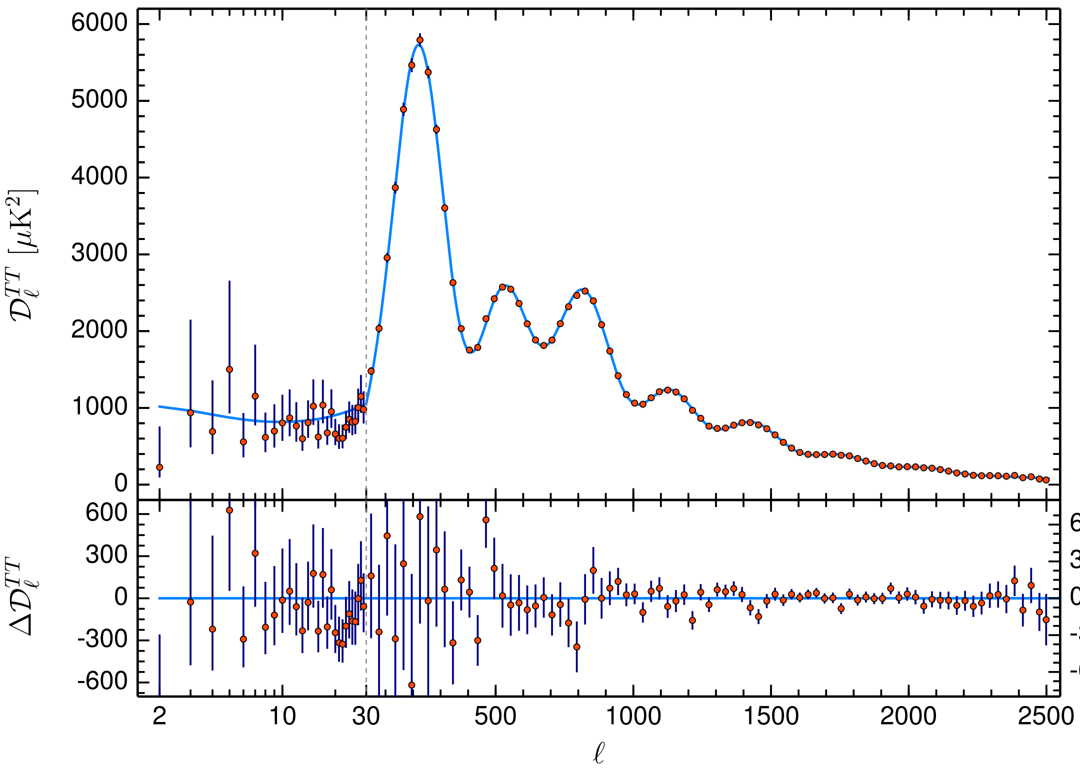

Figure 2.7: Temperature power spectrum for each angular multipole moment of the Planck 2018 dataset [1]. The error bars show the measured data, and the blue line shows the fitted cosmological model. On the bottom, the residuals are shown.

The resulting curve shows a plateau for angular moments $l \lesssim 30$, followed by three dominant and then multiple increasingly suppressed peaks. The three main peaks are mainly produced by baryonic acoustic oscillations:

small over-densities in the early universe lead to a gravitational attraction and movement of the surrounding matter and photons towards the centers of the over-densities. At some point, the outward radiation pressure dominates against the gravitational pull and moves baryonic matter and photons away from the over-density again, leading to an oscillation. The first and second peaks of the CMB-power spectrum correspond to the first maximal and minimal compression, respectively, and allow determining the baryon density in our universe. The third peak corresponds to a second compression and allows extracting the DM content.

Each absolute as well as relative peak position and height depend on the exact mass-energy density of the components in our universe. A complete fit of the ΛCDM-model to the data allows extracting all cosmological parameters with high precision, including the existing DM mass-energy density.

2.2.6 Large Scale Structure Formation

Another evidence for DM are the structures (i.e. galaxies and galaxy clusters) spanning the complete universe. They are not distributed homogeneously over the sky but instead tend to group together, leaving voids in other spaces.

During the evolution of the universe, the small density fluctuations, which are known from CMB at the time of photon decoupling, had to grow to the structure we see today. It is assumed that this could happen due to clustering driven by cold (non-relativistic) DM. The best tool to study the formation of large-scale structures are N-body simulations, e.g. the Millennium Simulation [23].

2.3 Candidates for Dark Matter

2.3.1 Required Properties

All of the currently known evidences for DM are exclusively observations of gravitational interactions, and besides the average mass-energy density, nothing else is exactly known about it. The most model-independent limits on the allowed mass range of DM objects can be set by the properties of dwarf galaxies. They belong to the smallest objects, where effects of DM can currently be observed. While the lowest possible mass, $\mathcal{O}(10^{-21})$ eV, was derived from the stellar kinematics of the dwarf galaxy Leo II [24], the upper limit for DM masses can be estimated to be close to the lightest dwarf galaxies of $\mathcal{O}(10^{5})$ solar masses, for which a DM-halo is observed.

This opens up a parameter space of 87 orders of magnitude where DM could hide. With additional assumptions (e.g. on interaction types) and motivations (e.g. for a production mechanism), the parameter space can be reduced drastically.
Common DM candidates can be roughly divided into 3 categories: wave-like DM for very light candidates $m_{DM} \lesssim 1\,\mathrm{eV}$, macroscopic DM for very heavy candidates $m_{DM} \gtrsim m_p \approx 10^{28}\,\mathrm{eV}$, and particle-like DM for particles in between $1\,\mathrm{eV} \lesssim m_{DM} \lesssim m_p$. Although wave-like and particle-like could be considered the same, their detection methods would differ greatly. To explain DM, a particle candidate should satisfy the following known bounds and properties:

1. The abundance of DM particles cannot exceed the DM density inferred from measurements (CMB gives a value of $1.26\,\mathrm{MeV/cm^3}$), and on small scales, their distribution should ideally fit to the shape of the galactic DM halos[2].

2. DM particles only interact very weakly, if at all, with the known SM particles. Besides gravitational interaction, no other DM-SM interaction has been observed yet. Therefore, it is assumed that DM is electrically neutral[3] and non-baryonic.

---

[2] The exact shape of DM halo profiles towards the galaxy core is currently disputed, as simulations and measurements disagree. This is known as the Core-Cusp problem [25]. However, this plays only a minor role in direct detection experiments as our solar system is sufficiently far away from the galactic center.

[3] Some models allow a small charge much smaller than the elementary charge e. They are known as millicharged DM.

3. In cosmology and astrophysics, DM is assumed to behave like a collisionless fluid. This is well demonstrated in the bullet cluster. Therefore, self-interaction between DM particles has to be very limited.

4. The DM particle had to be cold at the time of photon decoupling, meaning it was (and still is) non-relativistic with velocities far below light speed. This is one of the main assumptions of the ΛCDM-model and is necessary to explain the large-scale structures in our universe. In a hot DM scenario, the structures would appear more washed out than they were measured [26].

5. DM was available during the development of the universe to dominate the large-scale structure formation. As we still see the effects of DM in the recent universe, DM has to be stable, at least on timescales of the age of the universe $\mathcal{O}(10^{17}\,\mathrm{s})$.

Figure 2.8 shows different groups and examples for DM theories. Currently, the most popular candidates for DM are Weakly Interacting Massive Particles (WIMPs) and Axion-Like Particles (ALPs), which are described in the following sections. It should be noted that it is not necessary that a single candidate has to explain all of DM, but DM could also be a combination of multiple independent candidates. For example, technically, neutrinos with the known flavors (ν_e,ν_μ,ν_τ) can be seen as a part of DM, as they fulfill most of the criteria. They are massive particles that are only weakly interacting and that have a known production mechanism in the early universe. However, as they would be mostly relativistic, they can not be cold DM. With the known number density of thermal neutrinos, about 100 per cm^3 per flavor, the current limits on their rest mass ($m_\nu < 0.45\,\mathrm{eV}$ [28]) exclude a significant contribution by neutrinos.

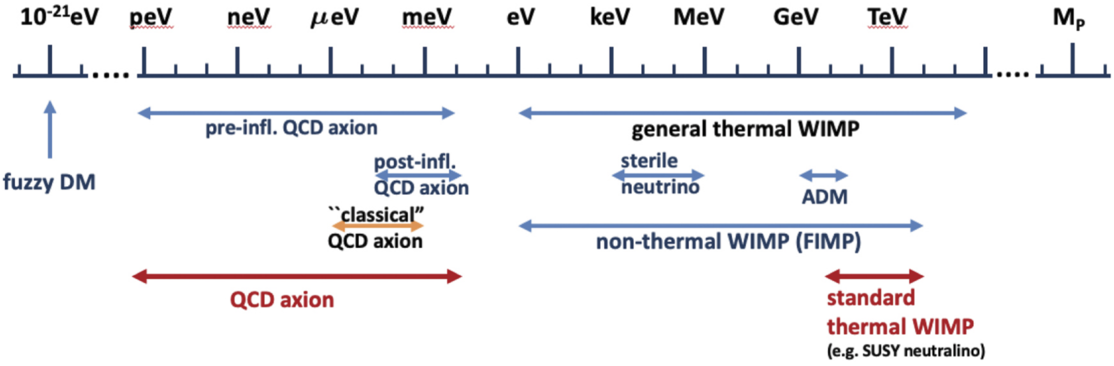

Figure 2.8: Popular DM candidates and their corresponding mass ranges [27].

2.3.2 WIMPs

WIMP theories assume that there exists an interaction between SM particles SM and DM particles χ. This naturally leads to a mechanism for the creation of DM with only few parameters. In the early universe, there was a thermal equilibrium between creation and annihilation of DM

$$SM + \overline{SM} \leftrightarrow \chi + \overline{\chi}. \tag{2.12}$$

At some point, due to the expanding universe, the number density and temperature of DM-particles are too low to annihilate, and the temperature of SM-particles is too low for new DM to be produced. This leads to a freeze-out similar to the creation of the CMB. In this simple model, today's DM abundance would depend directly on the thermally averaged pair annihilation cross-section of DM. Figure 2.9 shows the DM abundance for different temperature-dependent pair annihilation cross-sections.

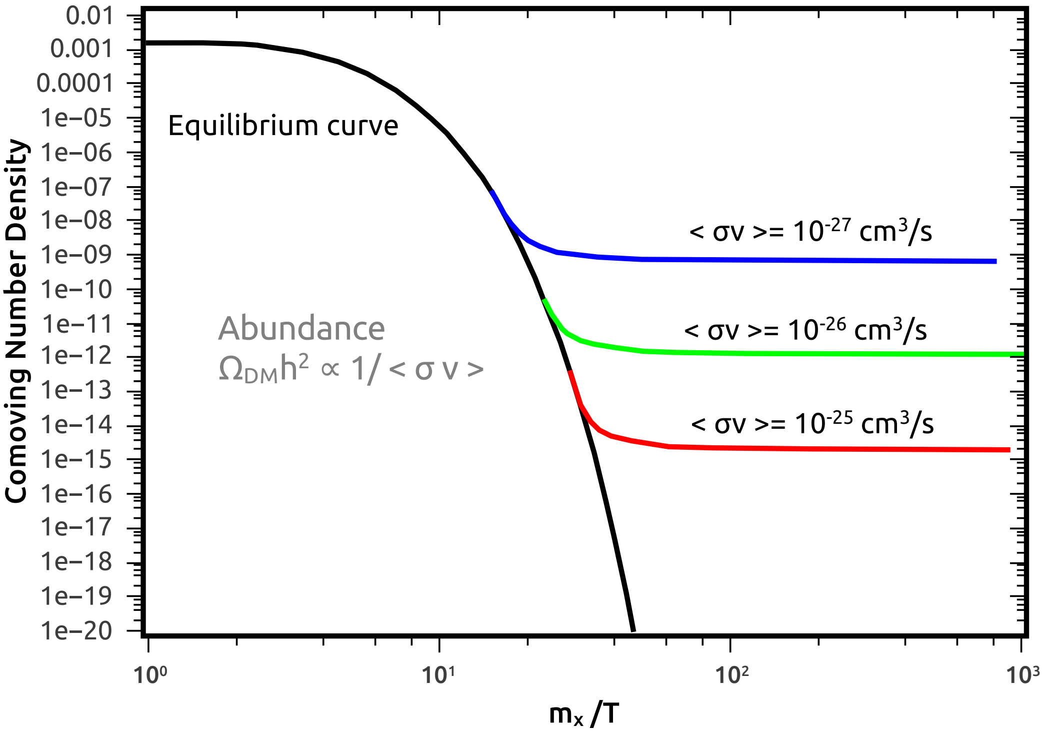

Figure 2.9: Freeze-out mechanism of WIMP-DM [29]. The plot shows how the number density of a WIMP evolves. It starts constant during thermal equilibrium and then falls when annihilation dominates. Depending on the annihilation cross-section, the WIMP decouples, and its number density stays constant. The colored curves show different scenarios with different annihilation cross-sections.

It turned out that particles in the mass range (10 GeV - 10 TeV) with interaction cross-sections on the weak-interaction scale could lead exactly to the DM abundance as observed today. Additionally, prominent theories beyond the SM, such as Super Symmetry, predicted stable particles in the same parameter space. This coincidence of very well-fitting numbers got famously dubbed "WIMP miracle" [30].

So far, no collider experiment has found a particle beyond the SM, and direct detection experiments are pushing detection thresholds lower and lower. The classical WIMP, as in "a particle on weak interaction scale", lost a lot of its grace. However, generally, a relic particle from cosmogenic freeze-out remains the most popular DM candidate. Current and next-generation DM-searches are starting to explore the "hidden sector", an assortment of theories for DM particles with masses below 10 GeV that are only very weakly coupled to the SM [31]. Section 2.4 will give an overview of the current experiments searching for WIMP-DM.

2.3.3 QCD Axion and ALPs

The Quantum Chromo Dynamics (QCD)-Lagrangian in the SM allows for a Charge conjugation Parity (CP)-symmetry violating term with a defining angle θ. One consequence of this CP violation would be a neutron electric dipole moment. However, current measurements give very strong limits on the neutron dipole moment, indicating $\theta < 10^{-10}$. This very small (or non-existing) CP-violating term would require an uncharacteristic, very precise fine-tuning of the SM and is therefore called "strong CP problem".

The QCD-Axion is a new massive boson that solves the strong CP problem, based on an idea of Peccei and Quinn [32]. It is introduced with a new field, the axion field, which allows treating the angle θ effectively as a dynamic quantity. At the global minimum of the field, the CP-violating term is canceled, and thus, the CP problem is solved. Axions are massive bosons that could be produced thermally (as hot DM) or non-thermally (as cold DM) in the early universe. Their possible masses span many orders of magnitude below $1\,\mathrm{eV/c^2}$ [33].

A more general class of particles that follow the Axion framework but do not necessarily solve the strong CP problem are called ALPs. The main method to check directly for them is by utilizing the (inverse) Primakoff effect. In a strong magnetic field, ALPs should convert to photons and vice versa. Searches for ALPs can be roughly categorized into three groups [33]:

- Experiments that try to produce ALPs in the laboratory and subsequently detect them. The most well-known method involves "light shining through wall"-experiments. Photons emitted by a strong source should convert to axions (within a strong magnetic field), pass an optical barrier, and subsequently convert back to photons (within a strong magnetic field). One example of an experiment of this category is the ALPSII experiment [34].

- Experiments that try to detect ALPs produced in the sun. Experiments of this group are called helioscopes. They utilize a strong magnet to try converting solar ALPs into photons and subsequently use optics to focus and measure them. The largest experiment in this category will be the IAXO experiment [35].

- Experiments that try to detect ALPs from the DM-halo of the Milky Way. Experiments of this group are called haloscopes and typically use strongly resonating cavities in a magnetic field to achieve high sensitivity for ALPs in a small mass range. One example is the RADES experiment [36].

2.3.4 Sterile Neutrinos

Sterile neutrinos are chargeless massive leptons that do not belong to one of the known neutrino flavors (ν_e, ν_μ, ν_τ). Besides being part of DM, their existence could solve various open questions of neutrino physics, such as the lightness of the known neutrino flavors [37].

One possible way to detect sterile neutrinos is by precisely measuring β-decay spectra, e.g. in the KATRIN experiment [28]. The existence of a sterile neutrino that mixes with the known flavors would introduce a kink-like signature in the energy spectrum, which allows recovering the mass and mixing of the sterile neutrino eigenstate. The TRISTAN project is a planned extension to the KATRIN setup to measure such a signature in tritium (^{3}H) [38]. Other detection methods would include neutrino capture in inverse β-decay or scattering of sterile neutrinos on large-scale detectors [37].

2.3.5 Other Candidates

Besides WIMPs and ALPs, many other candidates have been proposed to explain DM. Historically, one of the most popular candidates were Massive Astrophysical Compact Halo Objects (MACHOs). MACHOs are macroscopic, typically baryonic, objects that, due to their dimness, can not easily be detected by earth-based telescopes. Some examples are exoplanets, black holes, or brown dwarfs. Gravitational lensing studies showed that, while MACHOs do exist, their number is far too low to explain DM [39].

One exception are Primordial Black Holes (PBHs), a subcategory of MACHOs. They are small black holes created in the early universe that survived until today. PBHs in a small parameter space of masses could still explain all of the DM and will be researched by the next-generation gravitational wave telescopes [40, 41].

There also exist theories that do not postulate DM but try to describe the evidences with alternative ideas. One example is Modified Newtonian Dynamics (MOND), which modifies Newton's second law for low accelerations to describe galaxy rotation curves correctly [42]. While these theories can be very successful in describing specific evidences, they usually require a lot of fine-tuning and fail to explain other evidences.

2.4 Direct Detection of Particle Dark Matter

The field of experimental DM physics deals with the question of how we could detect DM. It generally splits into three categories: direct detection, indirect detection, and production of DM. Figure 2.10 shows the different detection channels possible.

Direct detection experiments expect scattering between DM particles and SM particles and look for small energy depositions in the detectors. In indirect detection, astrophysical observations are used to probe for possible annihilation products of DM,

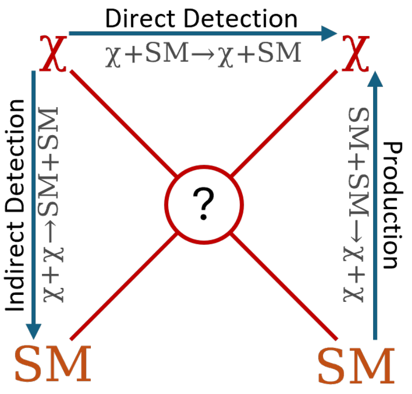

Figure 2.10: Possible detection channels for particle DM. In each channel, SM matter and DM interact with each other in a different way.

while in collider-based experiments, a loss in the total energy due to DM production is expected. In all methods, some interaction besides gravitational interaction is utilized for the measurement.[4] From hereon, the focus will lie on direct detection of WIMP DM.

When a non-relativistic DM particle interacts with a target, we assume it scatters on single atoms within it, i.e. on a nucleus or an electron. The differential recoil rate $\frac{dR}{dE_R}$ for nuclear recoils would be described by [44]:

$$\frac{dR}{dE_R} = N_T \frac{\rho_\chi}{m_\chi} \int_{v_{min}(E_R)}^{v_{esc}} dv f(v) v \frac{d\sigma}{dE_R}(v, E_R) \tag{2.13}$$

The parameters ρ_χ and m_χ are the local DM density and DM mass, respectively, and depend solely on the DM halo properties of the Milky Way. Material-specific effects are encoded in the number of target nuclei N_T and WIMP-nucleus interaction cross-section $\frac{d\sigma}{dE_R}(v)$. By integrating from the minimal relative velocity required for a nuclear recoil v_{min} to the escape velocity of the galaxy v_{esc}, the DM particle velocity distribution $f(v)$ in the galactic rest frame is taken into account.

2.4.1 Dark Matter in Our Solar System

For a good estimation of the expected DM interaction rate, it is crucial to have precise information about the local properties of the DM halo in our galaxy. To measure the local DM density, two methods are employed [45]:

1. The local DM abundance can be derived from the kinematics of a few tracer stars near our sun. This method requires very few assumptions but a precise knowledge of all objects in our vicinity. Therefore, the results are usually subject to large systematic uncertainties.

---

[4] A first experiment to test DM interacting only gravitationally has been proposed recently [43].

2. As described in section 2.2.1, the shape of the DM halo can be computed from the rotation curve of the Milky Way. This method can be very precise but needs strong initial assumptions, such as the profile shape of the halo. A common assumption is a spherical halo that follows a Navarro-Frenk-White (NFW) profile with the halo-specific constants ρ_0 and R_s [46]:

$$\rho(r) = \frac{\rho_0}{\frac{r}{R_s}(1 + \frac{r}{R_s})^2}. \tag{2.14}$$

Although more recent studies with slightly different numbers exist (see [47] for a recent review), most collaborations use the standard halo model to compute their DM results. This allows for a direct comparison between recent and older experiments as long as they report a null result.

The important numbers in use are 544 km/s for the galactic escape velocity, 220 km/s for the velocity of the solar system, and $0.3\,\mathrm{GeV/cm^3}$ for the local DM density [48, 49]. Furthermore, particles of the halo are approximated to follow a Maxwell-Boltzmann distribution with a cutoff at the galactic escape velocity [49].

2.4.2 Dark Matter Signatures

To resolve small energies with high resolution, most experiments build detectors that utilize one or more of three typical signal channels. They either measure the ionization of semiconductor targets or liquid noble gases, light emitted by scintillators, or heat deposited in crystalline absorbers in the form of phonons. Figure 2.11 shows a Venn diagram of the channels and lists recent experiments utilizing them.

The energy split of an event depends on the target material and interaction type. Typical numbers are $\sim 90\,\%$ in phonons, and $\sim 10\,\%$ in scintillation light or $\sim 10\,\%$ in ionization.

DM searches are rare event searches, meaning that single events from unknown sources could be interpreted as a discovery. Therefore, it is essential to first reduce and reject any known backgrounds in the experiments and then screen and simulate every part in the experimental setup to understand the induced background. Most experiments are located underground to shield the setups from cosmic radiation and employ active vetoes for particles that would still reach the targets. Another layer of passive shielding minimizes the event rate induced by ambient radioactivity. Different search strategies are used within the community to minimize the effect of backgrounds:

- **Modulation searches** look for a periodic variation of the interaction rate in a detector. The solar system moves with a velocity of 220 km/s along the galaxy through the static DM halo [48]. In the rest frame of the solar system, this would be seen as a unidirectional wind of DM particles. Since the Earth revolves around the sun, the relative velocity between Earth and the DM halo will change throughout the year, which will have a direct effect on the interaction rate. This modulation of relative velocities, and thus of the interaction rate, would have a maximum in

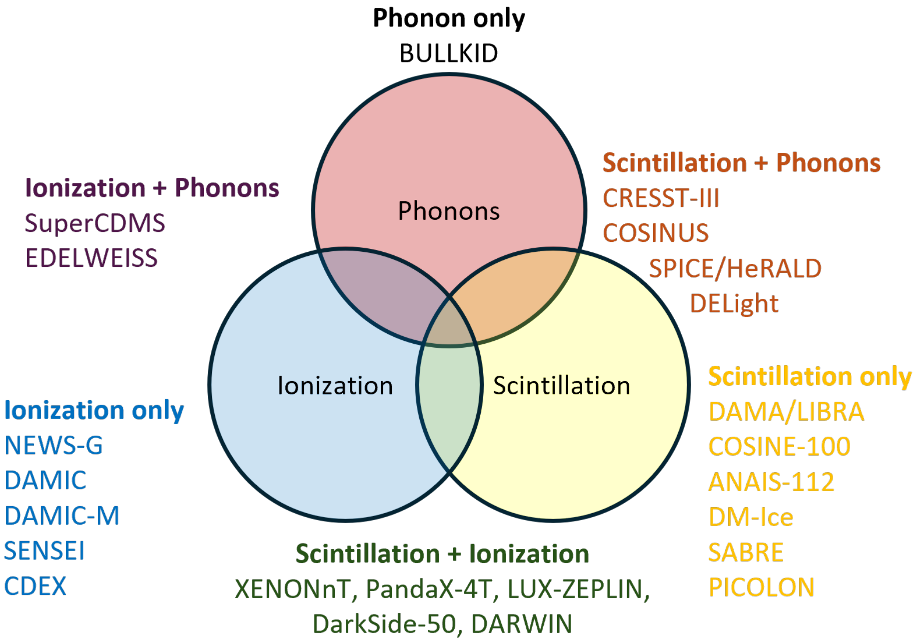

Figure 2.11: Common detection channels used in direct DM searches and an incomplete list of DM experiments utilizing them.

June and a minimum in December [50]. A sketch of the principle is shown in figure 2.12.

This signature is exclusive to DM, i.e. no other background that can produce a modulation with the same phase is known.[5] In addition to annual modulation, there should also be a daily modulation due to the rotation of the Earth. However, the amplitude would be much lower. A clear annual modulation with the correct phase is measured by the DAMA/Large sodium Iodide Bulk for RAre processes (LIBRA) experiment for more than 25 years. Details on that experiment can be found in section 2.4.4.

- **Directional searches** capitalize on the fact that the DM "wind" is expected from one fixed direction. Considering the movement of our solar system in the galactic frame, the DM flux is expected to come from the direction of the Cygnus constellation [52]. As no other cosmic background from this direction is expected, a directional flux of recoil events would be an excellent signature of DM. Furthermore, directional resolution would be a possible way to discriminate neutrinos from DM in future experiments.

- **Signal events over a known background** would be the classical way to measure

---

[5] Other seasonal effects, for example, an annual modulation of the muon flux and possibly muon-induced neutrons [51], are known but can not reproduce the same phase.

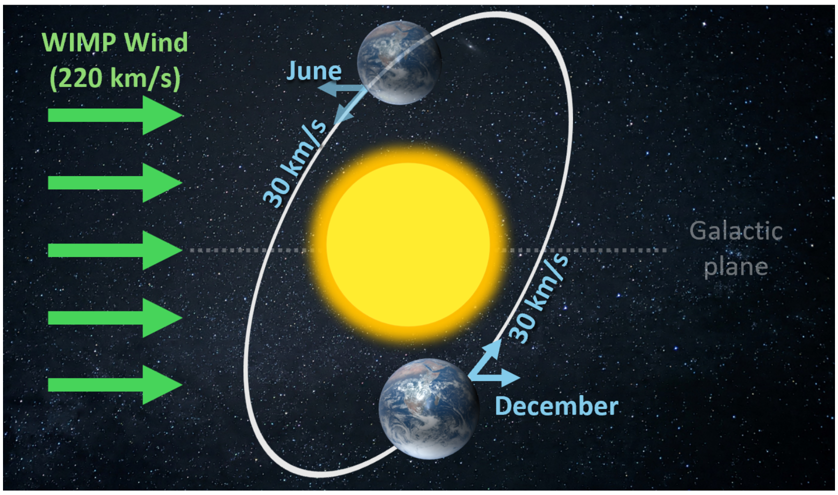

Figure 2.12: Principle of annual modulation. The solar system is moving through the DM halo of the Milky Way, leading to a relative WIMP wind from a fixed direction. The Earth, revolving around the sun, would move against the wind in June and with the wind in December, leading to an annual modulation of relative velocities, which results in an observable modulation of the interaction rate.

rare events. Experiments following this strategy require perfect knowledge of their background. An excess of measured events not predicted by the background model could indicate a DM signal.

Generally, reducing the background is more effective than trying to separate the signal and background after data taking. Most DM models predict nuclear recoils, so electron recoils would be one major background. By utilizing multiple readout channels, many experiments try to identify the recoil type on an event-by-event basis and reject non-nuclear recoils.

If an experiment does not measure events that can be exclusively traced back to a DM origin, an exclusion limit is calculated. The exclusion limit gives constraints about which combinations of DM mass and interaction cross-section are incompatible with the data at hand. It is heavily dependent on target mass, charge, and form factor, as well as halo assumptions. Generally, the community differentiates between spin-dependent and spin-independent elastic scattering limits depending on the coupling of DM to SM particles [53]. Figure 2.13 shows a recent compilation of spin-independent limits for WIMP masses between (0.1 - 1000) $\mathrm{GeV/c^2}$.

A DM exclusion limit has a typical banana-like shape. It marks the lower border of

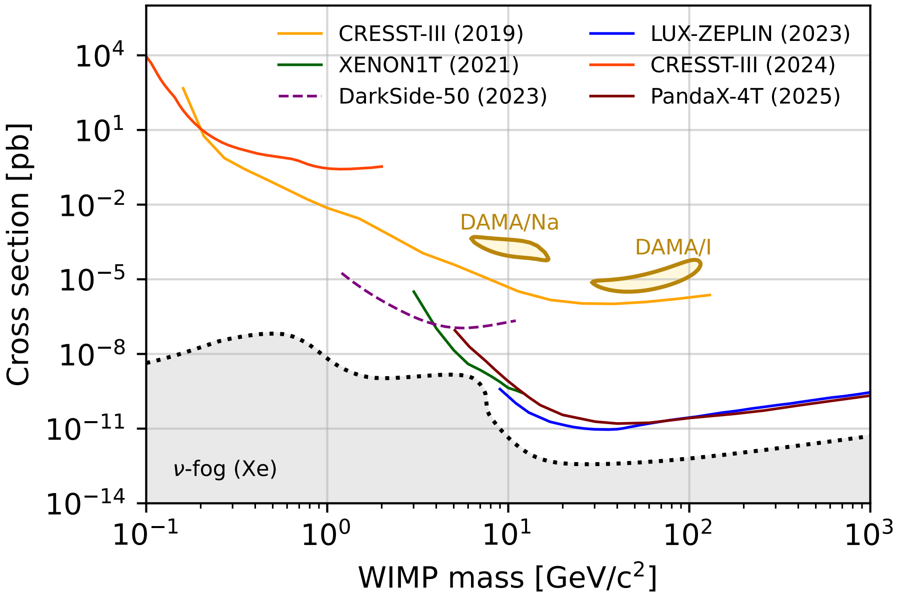

Figure 2.13: Leading exclusion limits on the spin-independent DM-nucleon scattering cross-section for WIMP masses between (0.1 - 1000) GeV/c^2. The curves shown were taken from CRESST-III [54, 55], XENON1T [56], DarkSide-50 [57], LUX-ZEPLIN [58] and PandaX-4T [59]. The parameter space above the curves is excluded, as the experiment could not detect a new particle with these properties. One exception is the DAMA/LIBRA experiment that measured a signal, which, for spin-independent interactions, would correspond to the yellow-shaded regions [60]. The gray shaded area marks the neutrino fog for Xe [61], the parameter space, where solar neutrinos would be measured via coherent elastic scattering on the Xe-nucleus.

the excluded parameter space.[6] For very low and very high DM masses, the sensitivity of experiments decreases due to their energy detection threshold and the reduced DM particle density, respectively. The exact slope is defined by the scattering kinematics. If a target material consists of multiple elements, the resulting limit is a superposition of the limits of each element, introducing kinks in the limit. Similarly, in ionization detectors, the resulting limit is a superposition of different limits for different numbers of ionized electrons.

For low cross-sections, most limit plots show the “neutrino fog” (in the past known as “neutrino floor”), a natural limitation to direct detection of DM via nuclear recoils [61]. Below a target-dependent limit, Coherent Elastic Neutrino-Nucleus Scattering (CEνNS) with atmospheric and solar neutrinos is expected. This interaction would be

---

[6] Technically, there is also an upper border for the excluded parameter space. Particles above this line would not reach the shielded detector due to their large interaction cross-sections.

indistinguishable from a DM particle scattering on a nucleus on an event-by-event basis.[7]

As soon as an experiment measures a DM-like signature, e.g. the annual modulation of DAMA/LIBRA (see section 2.4.4), an island can be drawn into the parameter space which would be compatible with the data under the standard assumptions mentioned before. In this case, the next step would be to meticulously scan the experimental setup for possible backgrounds and try to find a non-DM explanation. One example would be the XENON1T excess. In 2020, the collaboration published the detection of an excess of ∼50 events in the (1-7) keV_{ee} region. The data would have been compatible with a solar axion model; however, a ^{3}H-contamination as a SM-only explanation could not be excluded [62]. In the successor, XENONnT, special measures were taken to reduce any possible ^{3}H-contamination, and with enhanced sensitivity, the excess could not be confirmed [63]. If no possible non-DM explanation is found that can account for the signal, an independent cross-check with an unrelated experimental setup is needed to exclude as many sources of bias as possible.

2.4.3 Direct Detection Landscape for Particle Dark Matter

Currently, there is a rich landscape of DM direct detection experiments that try to measure particle DM. While every experiment is unique in its technical details, the field can be roughly divided into the four subcategories listed below.

1. **Liquid noble gas detectors** are leading the direct detection landscape for $m_\chi \gtrsim 1\,\mathrm{GeV/c^2}$. Their advantage is the high exposure (due to their scalability) and low backgrounds (due to the radiopurity) they can reach.[8] Currently, the main actors are the XENONnT [64], PandaX-4T [65], and LUX-ZEPLIN (LZ) [58] experiments with liquid Xe, and DarkSide [57] with liquid argon (Ar). Although no DM has been found[9], a milestone for the community has been reached in July 2024, when the XENONnT collaboration announced the first detection of solar boron-8 (^{8}B) neutrinos via CEνNS [66]. The next generation of liquid noble gas experiments plans to probe the parameter space down to the neutrino fog [67, 68].

2. **Cryogenic detectors** are dominating the search for low mass sub-GeV DM. Because the number density of DM increases for lower mass candidates, small-scale experiments are still able to set competitive limits. Currently, the main actors are the SuperCDMS experiment that reads out heat and ionization signals from silicon (Si) [69] and CRESST-III that operates calcium tungstate ($\mathrm{CaWO_4}$) as cryogenic scintillating calorimeter [70]. COSINUS, by operating NaI as cryogenic scintillating calorimeters, will also be part of this category, although targeting higher masses than its peers.

---

[7] If the neutrino flux and interaction cross-section are well known, a statistical detection of DM would still be possible.

[8] The XENONnT reports a background rate as low as (15.8 ± 1.3) events/ (t year keV) in the (1, 30) keV energy region [63].

[9] yet

Cryogenic experiments currently suffer from a not yet understood background source, the so-called Low Energy Excess (LEE). Below recoil energies of $\sim 100\,\mathrm{eV}$ they measure an unexpected rise in event rate, limiting the prospects to improve their exclusion limits to lower energies [71]. The research on this is still ongoing. However, a DM origin was excluded, and a detector-specific effect is likely.

For even lower masses, new ideas for cryogenic detectors were proposed and are being researched. For example, in the HeRALD [72] and DELight [73] projects, the possibility of using superfluid helium-4 (^{4}He) as target material is investigated.

3. **Charged Coupled Devices (CCDs)** feature an excellent spatial and energy resolution and hence were commonly used as imagers for astronomy. They utilize semiconductors as targets and measure the charge accumulated by ionization in each pixel after some readout time. With skipper-CCDs, a new readout system was developed to repeatedly read the accumulated charge in a non-destructive way, minimizing the readout noise [74]. An additional advantage of CCD-based detectors is the possibility to image particle tracks and therefore discriminate background.[10]

   Currently, the DAMIC [75], DAMIC-M [76], and SENSEI [77] collaborations are using skipper-CCDs with detector masses on the order of grams. They achieve single-electron sensitivity for ionization signals with thresholds at the target material band gap (1.1 eV for Si [78]), allowing them to set leading limits for DM-electron scattering in the sub-GeV range.[11]

   Recently, the DAMIC experiment measured an excess of $11^{+4.4}_{-3.8}$ events at $89^{+36}_{-24}\,\mathrm{eV}_{ee}$ from an unidentified source [79]. However, a WIMP interpretation would be in tension with other experiments, and further investigations of its origin are ongoing. In the future, the target mass of the existing experiments will be scaled up, and new experiments are planned to operate underground [80], as well as in space [81].

4. **Other** unique ideas exist and, while under "standard assumptions" not being competitive with the leading experiments, they are either very good at testing specific models or paving the way for new technologies. Examples would be bubble chambers such as PICO [82], gaseous proportional counters like NEWS-G [83], or directional searches like CYGNUS [84].

Not yet mentioned here were inorganic scintillator experiments, mostly operated at Room Temperature (RT). The most famous experiment in this category is the DAMA/NaI experiment and its follow-up, the DAMA/LIBRA experiment.

2.4.4 DAMA

DAMA is a rare event search project with facilities located underground at LNGS. It is widely known for its DM search programs (DAMA/NaI, DAMA/LIBRA) using

---

[10] For DM, ionization of multiple pixels is unlikely.

[11] Due to ionization quenching their sensitivity to nuclear recoils is lower.

scintillating NaI detectors. The measurement setup is shown in figure 2.14.

Figure 2.14: Schematic (left) and photos of the DAMA/NaI (middle) and DAMA/LIBRA (right) setups [85–87].

DAMA/NaI was proposed in 1990 and started taking data in 1995. The measurement setup is described in [88]. It used 13 thallium (Tl)-doped NaI crystals with a combined mass of ∼100 kg as target material for DM scattering. The crystals were shielded by a composite passive radiation shield produced from copper (Cu), lead (Pb), cadmium (Cd) and polyethylene (PE). The scintillation light was measured using Photomultiplier Tubes (PMTs). Data-taking ended in 2002, and the installation of its successor started. In the seven years of data taking (107731 kg·d), DAMA/NaI found an annually modulated rate in the (2-6) keV$_{ee}$[12] energy range, with a significance of 6.3 σ [89].

DAMA/LIBRA increased the target size to 25 crystals with a combined mass of about ∼250 kg. The data taking of DAMA/LIBRA phase 1 went from 2003 until 2010 when another upgrade was implemented. All PMTs were replaced with a new model with better quantum efficiency and lower background. [2]

DAMA/LIBRA is expected to finish data-taking end of 2024 and is decommissioned in 2025 [90]. For about 22 annual cycles, DAMA consistently measured an annual modulation that fits the DM hypothesis. Figure 2.15 shows the annually modulated rate (with a flat background subtracted) measured by DAMA/LIBRA.

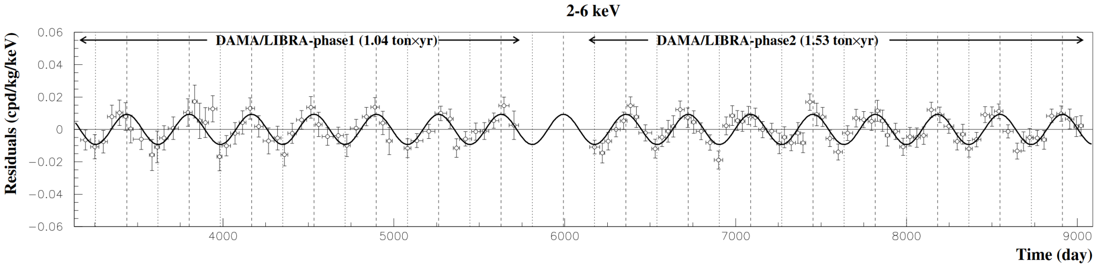

Figure 2.15: Annually modulated rate measured by the DAMA/LIBRA experiment in the (2-6) keV$_{ee}$ range. Taken from [91].

---

[12] keV$_{ee}$ means keV electron equivalent. More details can be found in section 2.4.5.

The measured modulation has an amplitude of 0.01 counts/(keV kg day), a period of 1 year, and a phase leading to a maximum on June 2nd, just as expected from a DM induced modulation. Overall, a significance of 13.7σ was reached [91].

However, to date, no other experiment could confirm this signal. This includes many experiments with better resolution and exposure, as shown before in figure 2.13. Over time, many hypotheses for possible backgrounds were proposed, but none could explain a non-DM origin of the modulated rate. To confirm or exclude a DM origin, one must take a closer look at the target material, NaI. Since the differential recoil rate is heavily dependent on the interaction cross-section, which is strongly dependent on the nuclear physics of the target material, a comparison between different targets might be subject to strong systematic uncertainties. Therefore, for a truly model-independent cross-check, it is necessary to probe the parameter space of DAMA/LIBRA with the same target material [92].

2.4.5 Comparing DAMA-like Experiments

Several experiments try to cross-check the annual modulation with their own NaI-based measurement setups. Figure 2.16 shows a map with all past and current NaI-based DM searches.

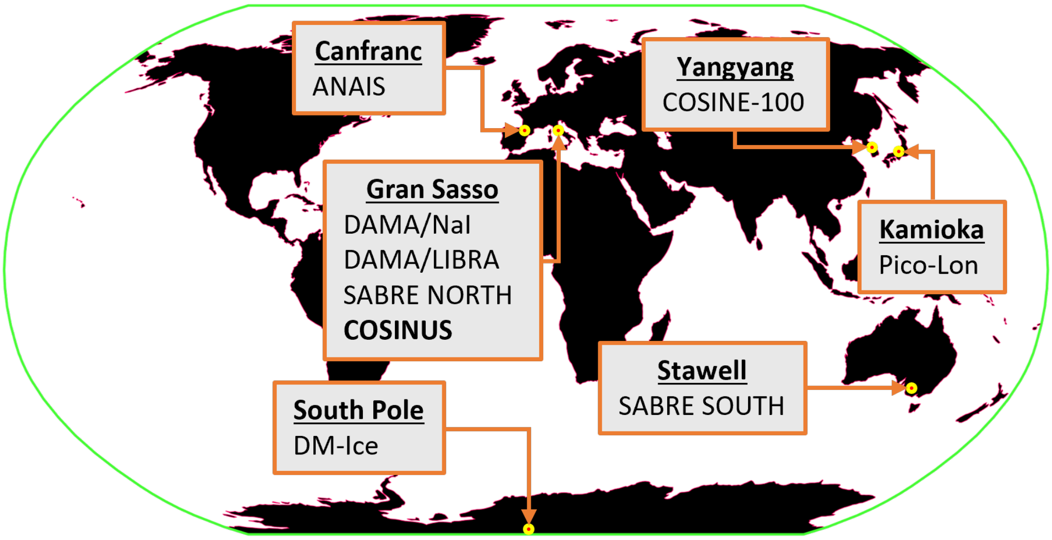

Figure 2.16: World map of the past and current NaI-based DM experiments.

All experiments are briefly summarized below in ascending order based on their data-taking starting date. Additionally, the COSINUS experiment will be discussed in detail in the next chapter.

- **DM-Ice** is an experiment located at the South Pole and further described in [93]. It was deployed in December 2010 as part of the IceCube experiment and measured the scintillation light of 17 kg NaI(Tl). By comparing the phase of the annual modulation with DAMA/LIBRA, it was supposed to probe the possibility of a seasonal effect. However, it could not reach the sensitivity necessary to exclude or confirm an annual modulation.

- **COSINE-100** is a joint effort of the DM-Ice collaboration and the KIMS collaboration, a South Korean experiment that utilized Tl-doped caesium iodide (CsI) detectors to search for DM [94]. 106 kg of NaI(Tl) are deployed at the Yangyang underground laboratory in South Korea, and data was taken between 2016 and 2023. In the published three-year analysis, 61.3 kg of the target mass were used for an inconclusive result about the existence of the modulation [95].[13] Currently, preparations for the COSINE upgrade, COSINE-200, are ongoing.
- **ANAIS-112** operates 112.5 kg NaI(Tl) in the Canfranc underground laboratory. It is taking data since August 2017, and with three years of data it claimed a 3σ-exclusion of the DAMA/LIBRA signal, the most restricting result so far [97].[14] Additionally, the collaboration runs a Research and Development (R&D) campaign, ANAIS+, to equip the crystals with Si-photomultipliers operated at 100 K [99].
- **COSINUS** follows a different approach to probe the DAMA/LIBRA signal. Instead of looking purely at the scintillation light, the crystals are operated as low-temperature scintillating calorimeters. This allows the heat signal to be read out in addition to the scintillation light, which enables particle discrimination on an event-by-event basis. Data taking will start in 2025 at LNGS with ~ 300 g detector mass. COSINUS will be discussed in detail in the next chapter.
- **SABRE** is a collaboration of two separate sub-experiments with the same crystal production procedure, detector concept, and Data Acquisition system (DAQ). One of its biggest advantages is the radiopurity of the crystals they achieved [100], which is close to the purity of the DAMA/LIBRA crystals [101].

  SABRE North will be located at LNGS and opted for a fully passive shielding made from PE and Cu. A demonstrator run in 2020 reached a count rate of (1.20 ± 0.05) counts/(keV kg day) [102]. SABRE South is located at the Stawell Underground Physics Laboratory in Australia and uses a liquid scintillator active muon veto [103]. Comparing both experiments will allow the collaboration to identify season-dependent and site-dependent contributions to the background.
- **PICOLON** (Pure Inorganic Crystal Observatory for LOw-energy Neutr(al)ino) is a Japanese project with the goal of being subjected to less background than DAMA/LIBRA. To reach this goal, they developed a method to grow ultrapure NaI(Tl) crystals. The project is planning to build a detector with 250 kg of NaI(Tl)

---

[13] Results from the modulation analysis of the full dataset claiming a 3σ-tension in the $(1-3)$ keV$_{ee}$-range with DAMA/LIBRA were available as preprint at the time of submission of this thesis [96].

[14] Results from the six-year data analysis claiming a 4σ-exclusion were available as preprint at the time of submission of this thesis [98].

in 42 modules and do a model-dependent cross-check of the DAMA/LIBRA result with 1 year of data [104].

- **ASTAROTH** (All Sensitive crysTal ARray with lOw THreshold) is a R&D-project that tries to read out the crystals with Si-photomultipliers [105]. These would benefit from a higher Light Yield (LY) and, if cooled, from lower non-scintillating noise than the currently used PMTs.

From all the listed experiments, only COSINE and ANAIS have a sufficiently large dataset to try to make a statement on the DAMA signal. However, even when using the same target material, a comparison between these experiments is not trivial. For a truly model-independent cross-check, it is necessary to exclude the existence of any annual modulating signal in the $(1-6)\,\mathrm{keV}_{ee}$ range. The most important systematic aspects, background control and QF, are further discussed below.

Background

By only looking at scintillation light, it is impossible to differentiate between sodium (Na)-, iodine (I)- or electronic recoils on an event-by-event basis. This makes an impeccable background model a strict requirement to exclude any annual modulation of DM. Relevant background sources are potassium-40 (^{40}K), lead-210 (^{210}Pb), uranium-238 (^{238}U), thorium-232 (^{232}Th) as contaminants in the crystals or experimental setup. Furthermore, ^{3}H or radon-222 (^{222}Rn) could be introduced during various production steps of an experiment. Passive shielding and active vetoes try to minimize any background contribution from outside of the experiment, such as events induced by cosmic radiation. Figure 2.17 compares the background rates in NaI-based experiments.

One of the main reasons why DAMA/LIBRA could not yet be cross-checked properly is their crystals' extraordinary purity and low background rate. Only recently have other experiments been getting close to the required background rate for a model-independent cross-check.

Quenching Factor

In scintillation processes, the generated light depends on the type of interaction and interacting particle. Usually, for elastic nuclear recoils, the light is quenched, i.e. less scintillation light is emitted than for electron recoils of the same energy. The conversion factor between recoil energy E_R and measured energy from scintillation light E_γ is called QF

$$QF = \frac{E_\gamma}{E_R}. \tag{2.15}$$

To differentiate between measured scintillation light and nuclear recoil energy, the units are commonly given in keV_{ee} (electron-equivalent) and keV_{nr} (nuclear recoil). For example, if DAMA/LIBRA measures a particle event at $1\,\mathrm{keV}_{ee}$ (since they look at the

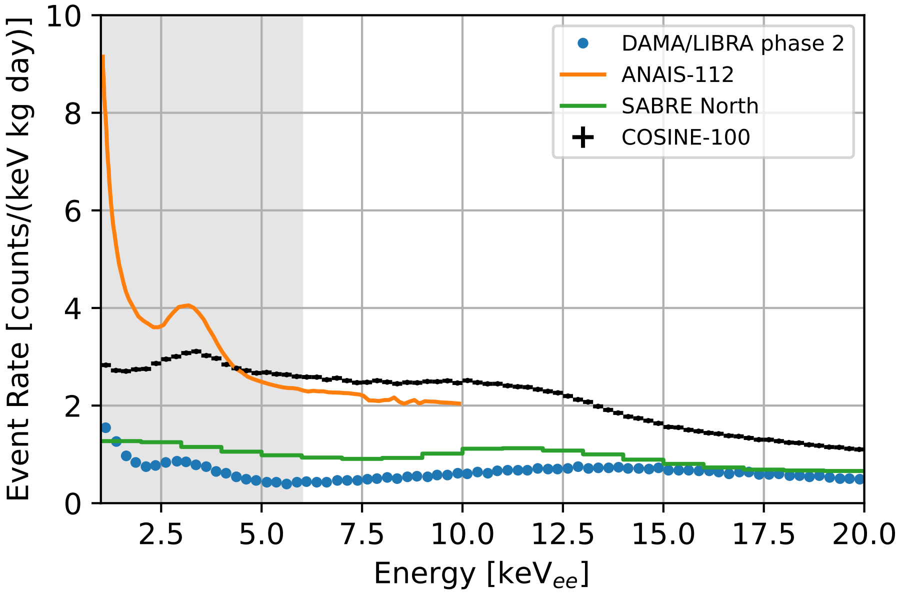

Figure 2.17: Comparison of the measured event rate in current NaI-based DM experiments. The data shown is from DAMA/LIBRA phase 2 [2], ANAIS-112 3-years data [106], SABRE North proof-of-principle [107] and COSINE-100 1.7-years data [108]. The gray shaded area corresponds to (1-6) keV$_{ee}$. Although DAMA/LIBRA is the oldest experiment, it achieves the lowest background event rate.

scintillation light), it would correspond to 3.3 keV$_{nr}$ if it was a nuclear recoil with a QF of 0.3.

For NaI at RT, small dopants of Tl on the order of ppm are typically introduced to the crystals to improve the scintillation efficiency at RT and to shift the emitted scintillation light to higher wavelengths. Generally, QFs depend on the energy as well as crystal properties, such as the Tl-content or purity. A comparison of recent NaI(Tl) QF-studies, including results from a yet unpublished study from COSINUS, is shown in figure 2.18.

Although NaI(Tl) is widely used for scintillating detectors in particle physics, the energy-dependent QF is not well researched. One reason is the advanced experimental setup and analysis procedure required to precisely extract the QF at low energies. Typically, a mono-energetic neutron beam (e.g. in an accelerator facility) is irradiating the target equipped with a Light Detector (LD). The neutrons scatter on the crystal nuclei, deposit energy, and are deflected by an angle Θ. By measuring this angle, the deposited energy can be recovered. However, to calibrate and interpret the energy spectrum at low energies, a detailed simulation of the setup is required.

Depending on the QF, the interpretation of the DAMA/LIBRA signal, as well as any cross-check with scintillation-only experiments, will change drastically. This effect is

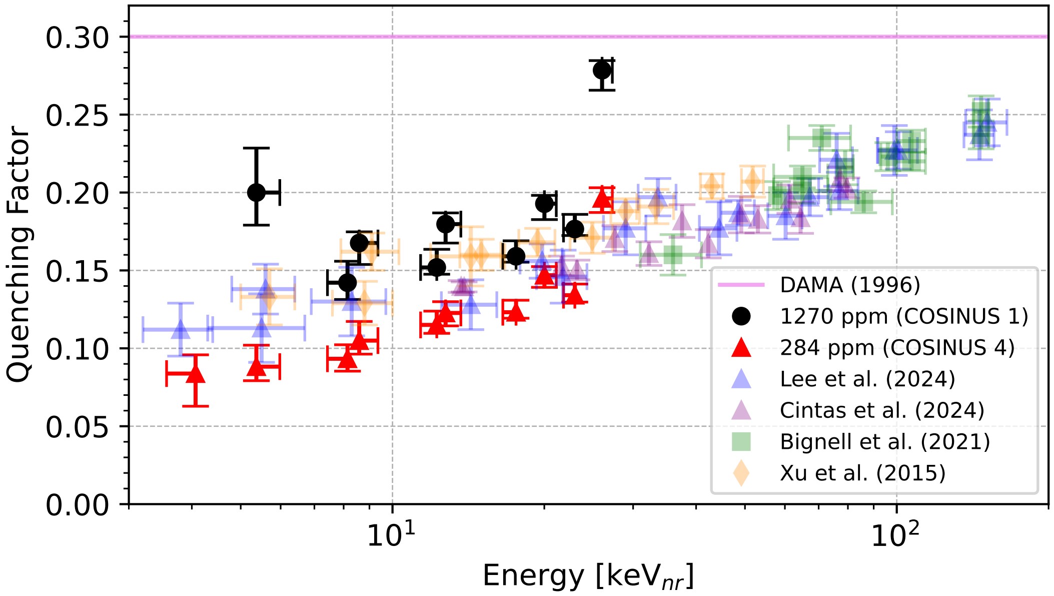

Figure 2.18: QF measurements of Na-recoils in NaI for different studies. "COSINUS 1" and "COSINUS 4" are from a not yet published study carried out at the Tandem accelerator of the Triangle Universities Nuclear Laboratory [109]. 1270 ppm and 284 ppm (10^4 ppm = 1 %) correspond to the Tl-concentration within the crystals. For DAMA/NaI, a flat QF of 0.3 for Na-recoils was reported [88]. Other results were taken from [110–113]. The reported QFs deviate strongly from each other, implying strong systematic deviations between the studies. The COSINUS data shows a clear energy and Tl-dependence of the QF.

illustrated in figure 2.19.

Two crystals made from the same material could have different QFs and, therefore, access completely different parts of the nuclear recoil spectrum. Although both crystals probe the $(1 - 6)\,\mathrm{keV}_{ee}$ energy range, one could then measure the bulk of a WIMP distribution, while another would only measure the tail. In both cases, the absolute event rate might not be different due to the strong electron recoil background. However, one crystal would measure an annual modulation, while the other does not. To arrive at the correct conclusion, it is of utmost importance to have a precise knowledge of the QFs and to compare the experiments Region Of Interest (ROI).

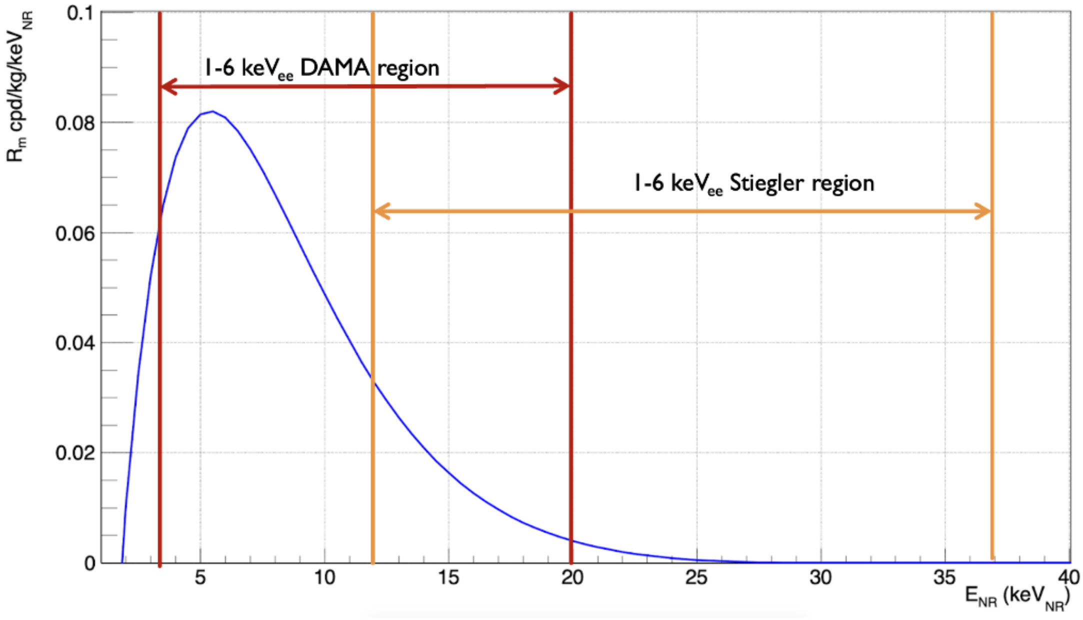

Figure 2.19: Effect of the QF on the accessible energy range of nuclear recoils. The plot shows the nuclear recoil rate for an illustrative DM-model. Depending on the target crystal's actual QF, a different part of the distribution is accessible. In the shown example, $(1-6)\,\mathrm{keV}_{ee}$ measured from a crystal with the DAMA QF [88] will include the bulk of the distribution, while a crystal with the QF reported by Stiegler et al. [114] will measure only the tail of the distribution. Only a small part is probed by both crystals. In addition to the different expected signal rates, the expected background changes with different QF as well. Taken from [115].

Chapter 3

COSINUS

COSINUS is a new experiment with the goal of cross-checking the DAMA/LIBRA results. It started as a R&D project between 2016-2019 [116]. In 2020, the COSINUS collaboration was founded and consists of participants from five institutions in four countries. The LNGS-management assigned a space for the experiment at the end of 2020 [117]. Since March 2021, COSINUS is an experiment recognized by the European Organization for Nuclear Research (CERN) [118].

From 2021 to 2023, a new low-background cryogenic facility was built in hall B of LNGS. It was officially inaugurated in 2024, and data-taking will start in 2025, with the first results expected later in the year.

3.1 Strategy

COSINUS plans to operate pure NaI crystals as cryogenic scintillating calorimeters, simultaneously reading out the heat and light signals. The addition of the heat channel has multiple advantages over a scintillation-light-only measurement:

- Most of the recoil energy is converted into heat. The readout of this channel allows for very low thresholds for nuclear recoil events.
- The combination of heat and light signal allows for particle discrimination on an event-by-event basis, hence the rejection of any events outside the signal region (e.g. electron recoils).
- Although it is not required for a DM result, it is possible to measure the energy-dependent QF of each crystal in situ without any special preparation.

The sensors of choice for COSINUS are Transition Edge Sensors (TES), which can achieve excellent energy resolution at low thresholds. Chapter 4 will report on the detector working principle and optimization efforts within COSINUS. The following sections will go into detail about the advantages and explain how COSINUS will be able to give competitive results with much less exposure in comparison to other NaI-based DM searches.

3.1.1 Dual Channel Readout

If a particle deposits energy in a scintillator crystal such as NaI, a small fraction of the deposited energy is converted to scintillation light. This conversion happens in multiple stages: following the primary interaction, electron-hole pairs are created that quickly cascade into secondary excitations. These excitations then thermalize to electron-hole pairs with energies around the band gap energy of the scintillator (5.9 eV for NaI(Tl) [119]). Energy is transported to the luminescence centers when relaxing further, which finally leads to the emission of scintillation light. [120]

Due to light quenching, the amount of light emitted by a scintillator from an energy deposition of a particle is dependent on the interaction type (i.e. the target and interatomic potential between particle and target). Typically, electron recoils have the highest light output, while elastic recoils on heavy nuclei produce less light. Figure 3.1 shows the signals of LD and Phonon Detector (PD) for an electron recoil and a nuclear recoil of the same energy in NaI.

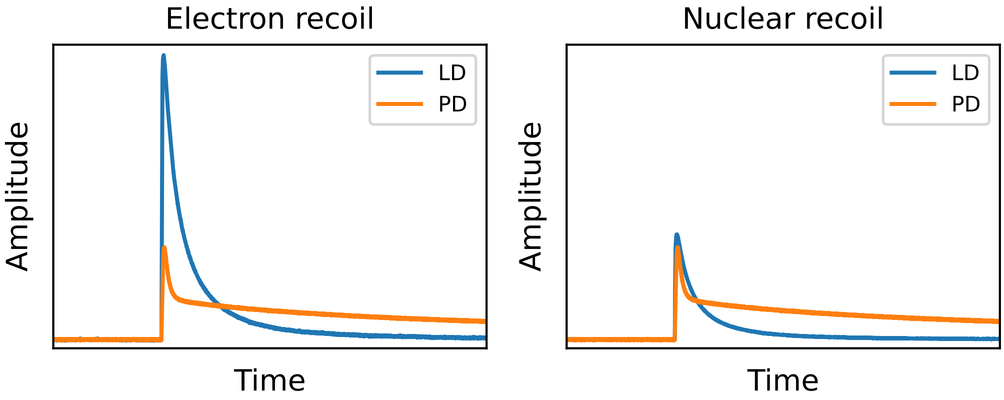

Figure 3.1: LD and PD signal for an electron recoil (left) and a nuclear recoil (right). It should be noted that while the amplitude of the LD changes due to quenching, the absolute amount of light measured depends on more parameters (e.g. LD sensitivity and light collection efficiency). However, this is true for both nuclear and electron recoils and, therefore, irrelevant for their ratio (or QF).

It is now possible to compare the energy in the LD and the energy in the PD for each single event. This is shown in figure 3.2 on the example of the DAMA/LIBRA signal interpreted as WIMP scattering on a nucleus.

The events are arranged in multiple bands, one for each interaction type. Their width is given by the LD performance and Poissonian fluctuations of emitted photons. By definition, the band at $E_L = E_p$ corresponds to electron recoils and photon interactions (e^-/γ-band).[1] Other bands are attributed to nuclear recoils, with their slope being the QF.

It is expected that WIMPs at the energy scale of the DAMA/LIBRA signal interact by nuclear recoils. Therefore, WIMP-nuclei scattering would occupy the nuclear recoil

---

[1] Most calibration sources used for energy calibration are X-ray emitters. The split between e^- and $\gamma-$events is often not resolved.

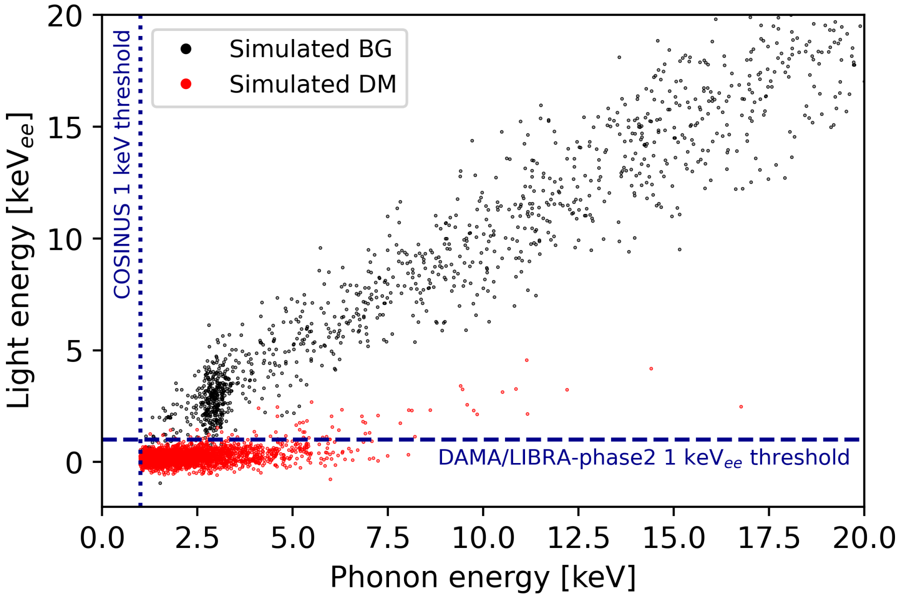

Figure 3.2: Light and phonon energy for simulated events in 100 kg day of exposure. The black data points show background events from a flat e^-/γ-background of 1 count/(keV kg day) and 20 ppb of ^{40}K. Events from hypothetical 10 GeV DM particles scattering on Na- and I-nuclei are shown in red. For the DM-particles, a spin-independent interaction cross-section of $2 \cdot 10^{-4}$ pb was assumed, and the QFs were fixed to 0.3 for Na and 0.09 for I. The dashed and dotted lines show the DAMA/LIBRA-phase2 (measuring light) and COSINUS (measuring phonons) energy thresholds, respectively.

band. DAMA-like experiments (measuring only scintillation light) and COSINUS (measuring scintillation light and heat) would be then sensitive to different parts of the DM distribution due to their different energy thresholds for nuclear recoils. A more common visualization of the particle discrimination are LY plots. LY is defined by the ratio of energy measured in the light channel and energy measured in the phonon channel ($LY = \frac{E_L}{E_{ph}}$), normalized to 1 for electronic recoils. Figure 3.3 shows the data, shown before in figure 3.2, as a LY plot in COSINUS.

The plot is populated by the different bands measured, most prominently the e^-/γ-band around $LY = 1$. Situated at lower LY are the nuclear recoil bands for Na- and I-recoils.[2] The widths of the bands shown in the plot describe the 90% intervals of all events attributed to each band. The gray shaded area marks the energy range of (1-6) keV$_{ee}$ measured in the LD only (i.e. LY $\in [1/E_{ph}, 6/E_{ph}]$). Again, WIMPs are expected to occupy the nuclear recoil bands.

From figures 3.2 and 3.3, it becomes evident that the introduction of the heat channel allows for much lower energy thresholds for nuclear recoils and thus higher sensitivity for

---

[2] The bands within the plots were drawn based on the QF published in [122]

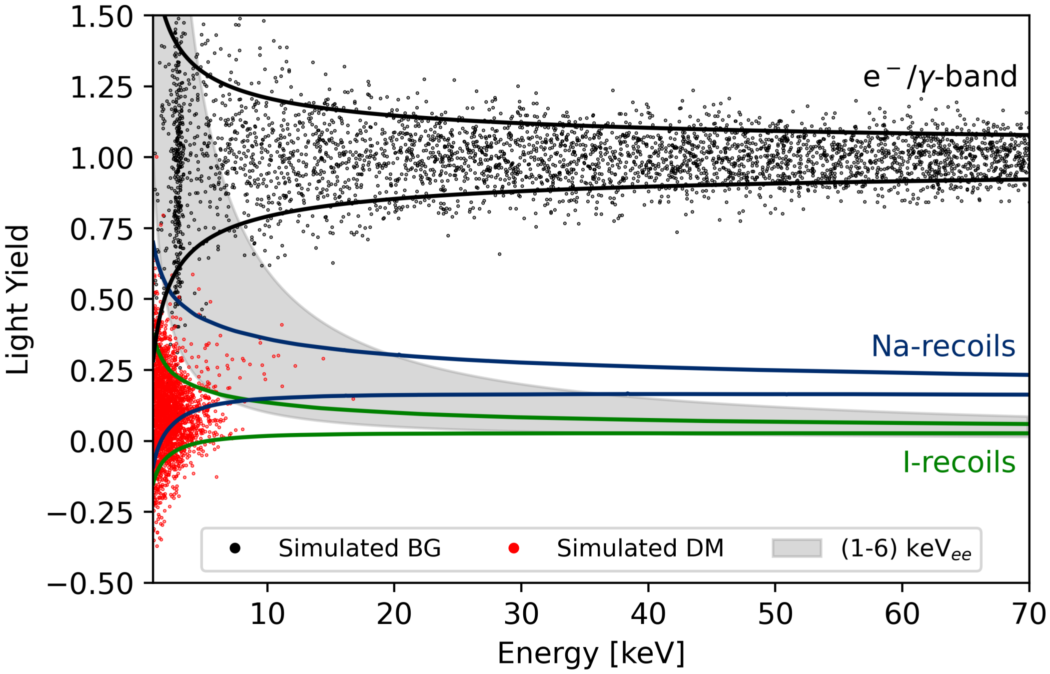

Figure 3.3: LY of simulated data for an exposure of 100 kg-day with a flat electronic background of 1 count/(keV kg day) and a ^{40}K contamination of 20 ppb (black). The red events correspond to a hypothetical WIMP scattering off Na and I nuclei. The gray shaded region marks the (1-6) keV$_{ee}$ energy region containing the events that would be measured by DAMA/LIBRA. Reproduced from [121].

their detection. Furthermore, the complete e^-/γ-band can be rejected as background, enabling a signal-only measurement. Another benefit of this technique is the in-situ determination of the QF of the absorber crystal. A phenomenological fit of the bands yields the energy-dependent QF for the crystal measured [123].

3.1.2 Signal-Only Measurement

Due to the lack of particle discrimination, all NaI-based DM experiments, except COSINUS, only measure an interaction rate that combines signal and background. The signal can only be disentangled via complex simulations or by unique signatures. COSINUS instead, can specifically look for nuclear recoils and thus avoid the largest part of the background. By using a specialized experimental setup and carefully selecting its materials, it can be background-free in the expected signal region.

With a signal-only experiment, it is not necessary to collect a lot of data. An exposure of the order of 100 kg days can already lead to a model-independent exclusion of a nuclear origin of the DAMA/LIBRA signal without the need to check for annual modulation. In comparison, a DAMA/LIBRA-like experiment requires a much higher exposure of order 10^4 kg day, collected over the years, to check for annual modulation. In [92], the principle of the COSINUS strategy is explained in detail and will be summarized in the following:

Let S be the modulation amplitude of DAMA/LIBRA and $\bar{R}$ the average measured rate, with R_{max} being the rate measured on 1^{st} of June and R_{min} the rate on 1^{st} of December

$$S = \frac{1}{2}(R_{max} - R_{min}) \tag{3.1}$$

$$\bar{R} = \frac{1}{2}(R_{max} + R_{min})$$

Then, in general, the average rate must be equal to or larger than the modulation amplitude

$$S \leq \bar{R} \tag{3.2}$$

Therefore, if COSINUS can give a bound on the rate of nuclear recoils $\bar{R}$ that is smaller than the modulation amplitude S (by not measuring any event), it disproves a nuclear origin of the signal.

In other words, if COSINUS does not measure any event in the region of interest, there is no signal that could modulate to create the DAMA/LIBRA result. Since both experiments use the same target material, this comparison does not require any input of the target material or DM model. Figure 3.4 shows the required rate that needs to be excluded by COSINUS for the completely model-independent exclusion, as well as some model-dependent cases with loosened conditions for a hypothetical WIMP with a mass of 10 GeV.[3]

From this prediction, the COSINUS design goal was set. Within one year of data, 100 kg day should be collected with a nuclear recoil energy threshold of 1 keV. This will be reached by eight detectors with an absorber mass of 34 g. Afterwards, the mass will be increased for a combined exposure of 1000 kg day. With that, any falling recoil spectrum can be checked after one year, while any arbitrary recoil spectrum will be excluded with the full dataset.

A follow-up study is soon to be published to confirm the physics reach of COSINUS. In this study, the nuclear recoil spectrum is recovered from the complete reported modulation spectrum using the QF and energy resolution of DAMA/LIBRA and then compared to a limit set by a background-free COSINUS detector. The results turn out to be very robust against variations of the DAMA/LIBRA detector parameters but sensitive to the achieved threshold of the COSINUS detector.

3.1.3 Demonstration of the COSINUS Principle

In June 2022, COSINUS measured a prototype detector in a CRESST test facility deep underground in LNGS, previously reported in [4]. It consisted of a 3.6 g NaI PD with an energy resolution of (441 ± 11) eV and a LD with an energy resolution of (988 ± 52) eV_{ee}.

---

[3] The WIMP mass is only needed for the model-dependent exclusion limits shown in the plot. The exclusion of any arbitrary recoil spectrum does not require any DM mass input.

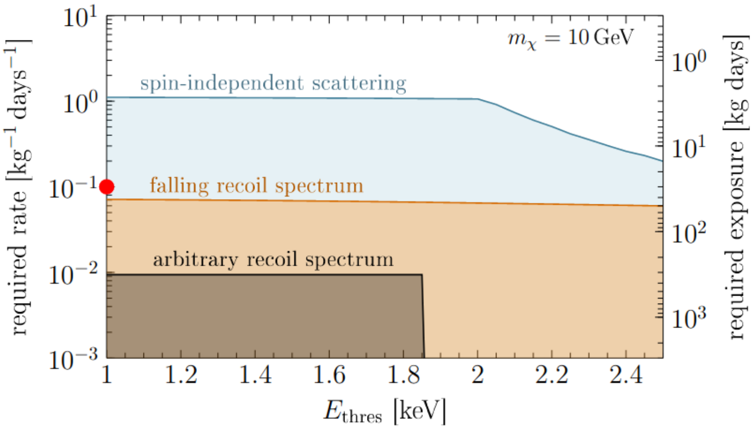

Figure 3.4: Exclusion conditions of a 10 GeV WIMP for a COSINUS-like experiment. The x- and y-axis show the energy threshold and the required excluded rate (left) or the required background-free exposure (right). The different shaded regions mark which assumptions can be excluded if a detector reaches the corresponding performance. The red dot marks a realistic target sensitivity for COSINUS. It should be highlighted that “arbitrary recoil spectrum” exclusion does not depend on the DM mass. Taken from [92].

Further technical details of the detectors are described in chapter 4.

The measurement included a neutron calibration campaign with an americium (Am)-beryllium (Be)-neutron source (2000 Bq) with an exposure of 4.0 g day. It was used to define the acceptance region for DM events and to measure the QF. Furthermore, 11.6 g day of data were taken without an external calibration source. Figure 3.5 shows the LY plot for the background dataset.

In the background dataset, the neutron band is almost empty, except for leakage of an internal iron-55 (^{55}Fe)-calibration source around 6 keV. When calculating a DM exclusion limit for the nucleon-DM spin-independent elastic scattering cross-section (shown in figure 3.6), the exclusion power of the COSINUS strategy becomes clear.

By defining the acceptance region in the nuclear recoil band, it is possible to set an up to two orders of magnitude stricter limit in the parameter space. Furthermore, it is shown that with 11.6 g day of exposure and without the need for a dedicated background model, a limit can be set that is only three orders of magnitude less strict than the limits from COSINE-100 with five orders of magnitude higher exposure. Additionally, the accessible energy region for COSINUS is much lower, despite being limited by leakage from the ^{55}Fe-source.[4]

---

[4] In the final COSINUS detectors, no internal calibration source is planned to be used.

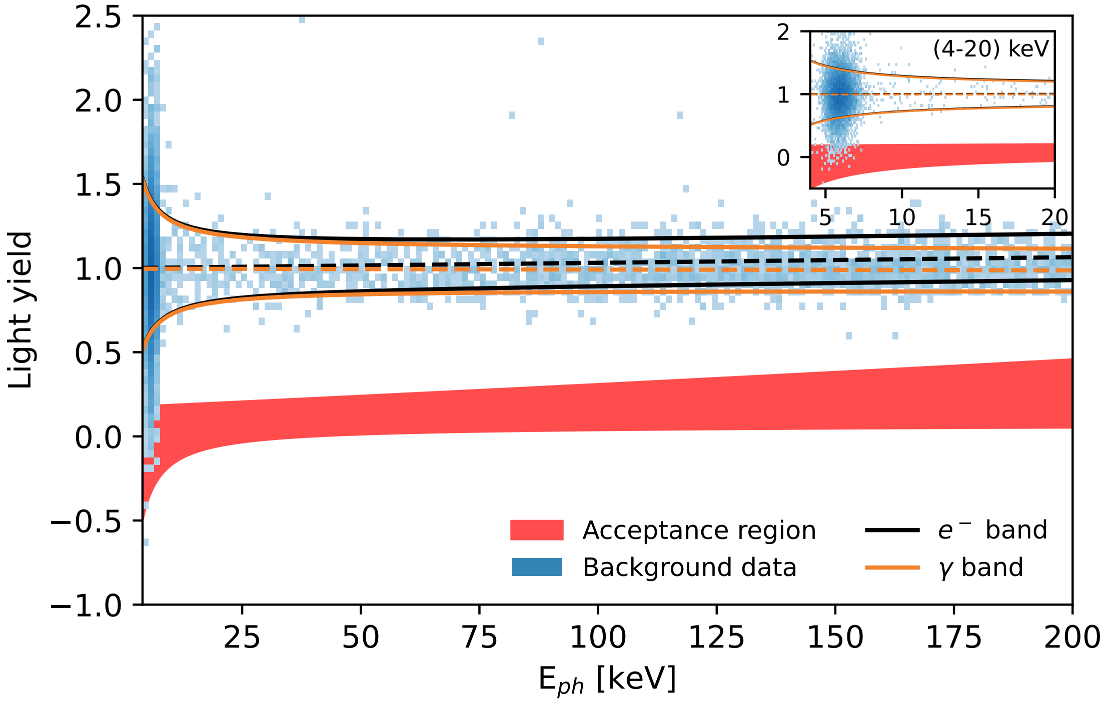

Figure 3.5: LY for the measured events. The red-shaded area marks the acceptance region of nuclear recoils as defined by the neutron calibration. The acceptance region is well separated from the e^-- and γ-bands (black and orange) and almost event-free, except for leakage from the internal calibration source around 6 keV. Adapted from [4].

3.1.4 Electron Recoils

The strategy works well under the assumption of nuclear recoils. However, while most theories expect nuclear recoils from WIMPs around this mass range, electron recoils can not be excluded. If COSINUS shows that the DAMA/LIBRA modulation does not originate from nuclear recoils, there are a few options to investigate the electron recoil band:

- One option would be to also do an annual modulation search. However, similar to other light-only experiments, the electron recoil band in COSINUS will not be background-free, and high exposure and measuring time are required. In a cryogenic detector, such as the ones used in COSINUS, the achieved energy resolution scales with the heat capacity of the target crystal. Therefore, comparatively small detectors with absorber masses up to 100 g are the natural limit for this method. Since collecting a large exposure is much easier for light-only experiments with bigger crystals, they are better suited for an annual modulation search than COSINUS.

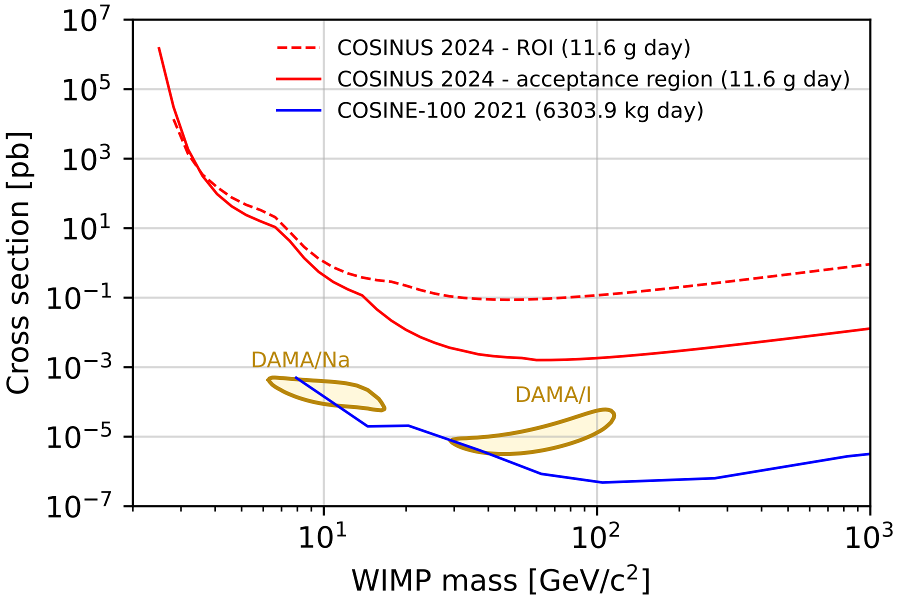

Figure 3.6: Spin-independent DM exclusion limits for the COSINUS underground measurement in 2022. The DAMA/LIBRA signal is depicted as two islands, showing the compatible parameter space to the measured annual modulation. An exclusion limit, published by the COSINE-100 collaboration in 2021 with an exposure of 6303.9 kg days, is shown as a blue line. The exclusion limits from the COSINUS prototype module (red) demonstrate the effectivity of the COSINUS strategy when defining an acceptance region (solid line) and without defining an acceptance region (dashed line). With 11.6 g day of data, it is possible to achieve an exclusion limit of only a factor 10^3 worse than COSINE-100 with a factor $5.4 \cdot 10^5$ less exposure. For low energies, the exclusion limit is limited by leakage from an internal calibration source. Adapted from [4].

Additionally, the systematic uncertainties introduced from the QF are strongly reduced for electron recoils. Since the energy scale for electron recoils is calibrated easily with X-ray emitters, comparing DAMA/LIBRA and other light-only experiments becomes much more straightforward.

- Another option was suggested in [124]. A DM particle recoiling off an electron would, depending on its momentum transfer and mass, also transfer energy to the electron. This energy then excites the intrinsic scintillation mechanism, leading to a set number of photons. By counting the number of photons measured, it would be possible to constrain mass and momentum transfer of DM to a specific range.

  For this option, a single-photon sensitivity of the LD is required. While it was shown recently that this can be achieved with a CRESST-like detector [55], this energy range is yet suffering from the LEE, leading to a high rate of background events. If COSINUS decides to pursue this strategy, it will be necessary to study the scintillation properties of pure NaI in finer detail and to join the global efforts to identify the origin of the LEE.

3.1.5 Detection Scenario

If COSINUS detects nuclear recoils, a paradigm change is needed. A unique benefit is the ability to specify the nuclear recoil energy of every single event without the use of a QF. While its competitors can, at best, confirm the existence of annual modulation in a specific energy range, COSINUS will be the only NaI-based experiment that is able to give further information on a potential signal, such as its spectral shape.

Any event that appears in the acceptance region (i.e. in the nuclear recoil bands) could be of the same origin as the DAMA/LIBRA modulation. Therefore, it would be important to learn as much as possible about these excess events and exclude any possible background source that could mimic the signal. The parameters that can help to identify the source are the energy spectrum, rate, time dependencies of the rate, and the nucleus the particle is recoiling from (i.e. Na- or I-recoil). Overall, a DM origin of the DAMA/LIBRA signal can only be confirmed if an annually modulating signal is detected without any background source being able to account for that.

3.2 Setup

To avoid any background in the detectors in the first place, a specialized low background facility was built in hall B underground at LNGS. It is a direct neighbor of the XENONnT-experiment [64] and the LUNA accelerator facility [125]. Figure 3.7 shows a Computer-Aided Design (CAD) rendering and picture of the COSINUS experimental facility.

The facility was approved by the LNGS management and scientific committee in 2020, and construction started at the end of 2021. In the following years, the facility buildings were finished (2022), the electrical infrastructure was included (2023), and the scientific instrumentation was set up (2023). Cryogenic refrigerator, muon veto, and IT infrastructure have been operational since 2024.

3.2.1 Experimental Facility

A complete drawing of the facility is shown in figure 3.8. It is separated into three parts: the water tank to provide low-background conditions, the clean room for detector assembly and mounting, and a control building to control and operate the detectors.

The water tank is instrumented as an active muon veto. Inside a drywell in the middle of the water tank and behind passive Cu-shielding, a custom-made dry dilution refrigerator with a base temperature of $<10\,\mathrm{mK}$ is located. Muon veto and dilution refrigerator will be described in detail in sections 3.2.3 and 3.3, respectively. The refrigerator can be moved out of the drywell with a custom-made lifting system and accessed from the clean room, as depicted in figure 3.9.

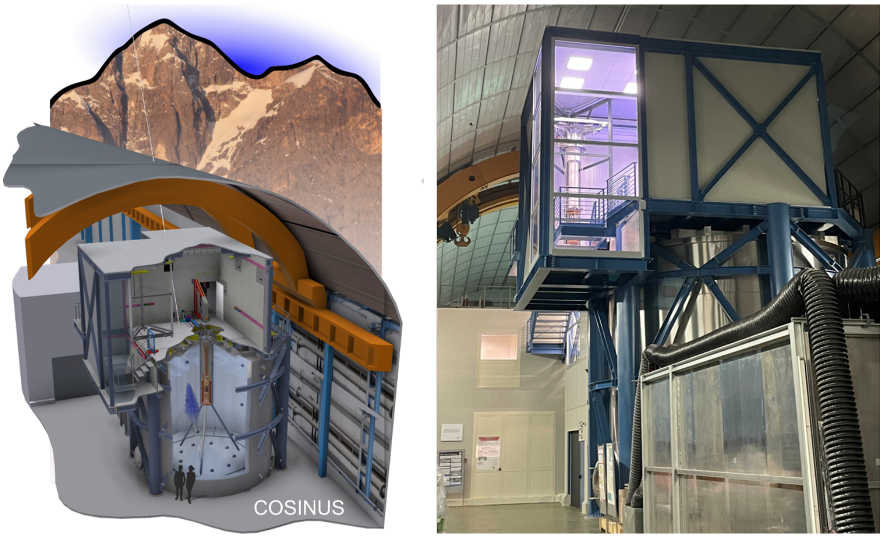

Figure 3.7: On the left: CAD rendering of the COSINUS facility. On the right: photo of the facility in hall B at LNGS. The COSINUS dry dilution refrigerator is visible through the window.

The control building consists of three floors, from bottom to top: the service level, the control room, and the utility area. On the service level, the water loop control system of the water tank, a compressor necessary for the operation of the dilution refrigerator, servers for data storage, and a small workshop are installed. Fully equipped working desks, as well as a monitoring system for the clean room and refrigerator, are located in the control room on the first floor, while the utility area contains everything needed to run the experimental setup, e.g. the gas handling system of the refrigerator.

One of the dominant noise sources limiting the sensitivity and operation stability of cryogenic detectors are vibrations. They can induce current noise in cables or be converted to heat directly at the detector modules. Therefore, the whole setup was designed with vibration decoupling in mind. A breakdown of the vibration mitigation strategy was previously published in [126]. To prevent the transfer of any vibrational noise, the control building was carefully separated from the water tank plus clean room structure. Furthermore, the clean room was built on two nested but separate frames. This is shown in figure 3.10. The refrigerator is connected purely to the inner frame during operation. It is a designated low-noise zone placed on four pillars filled with sand for further granular damping. Any connection to the outer frame is bridged with a loose sailing cloth. This allows for sealing the clean room while still keeping both frames separated. Chapter 5 gives a more detailed description of the vibration decoupling strategy and show measurement results to demonstrate and prove its performance.

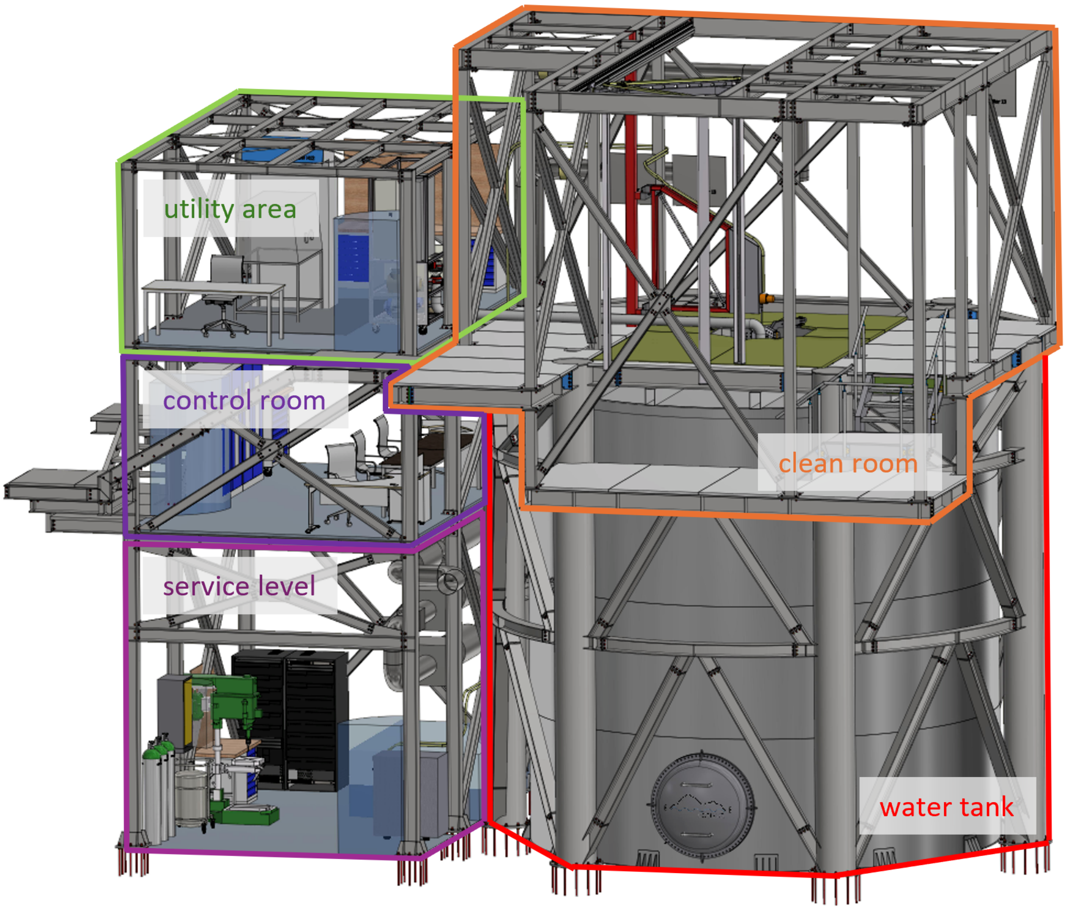

Figure 3.8: The COSINUS experimental facility. The facility is roughly divided into five different sections with different functions: the utility area (green), the control room (purple), the service level (pink), the clean room (orange), and the water tank (red).

3.2.2 Passive Shielding

For a rare event search, it is of utmost importance to minimize known backgrounds by carefully avoiding any internal contamination via thorough screening as well as by excessive shielding from outside sources. These outside sources include, most prominently, muon-induced neutron events and events from ambient radioactivity.

Cosmic muons are produced indirectly from cosmic rays scattering on the Earth's atmosphere. The most effective measure against them is to build the setup underground at LNGS. There, the experiment is shielded by a rock overburden of roughly 3600 m w.e.

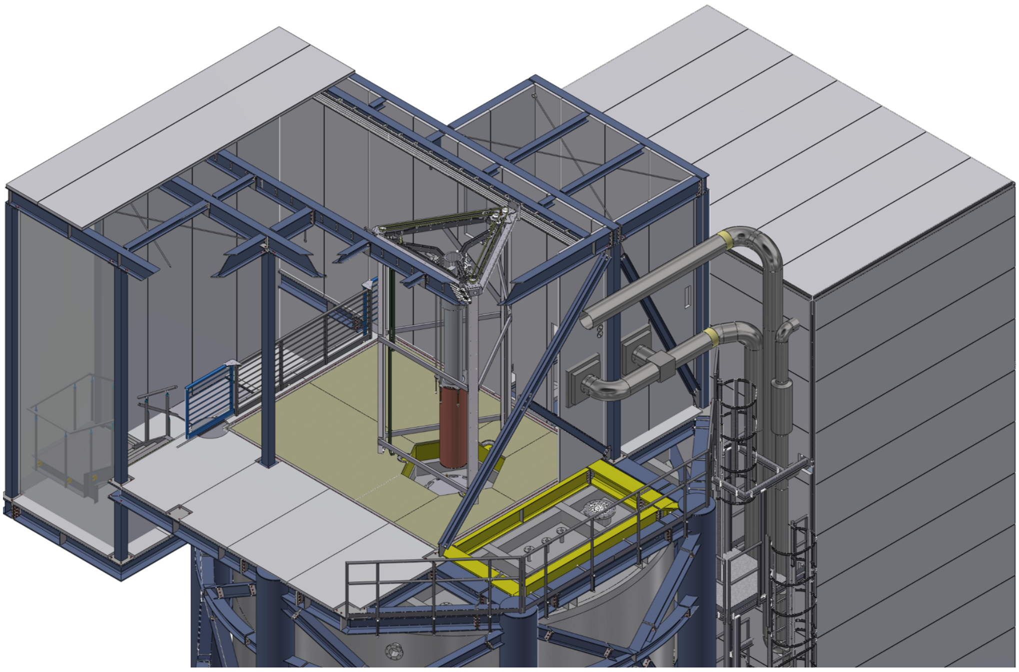

Figure 3.9: Clean room of the COSINUS facility. In the current view, the refrigerator (long cylindrical structure in the middle of the room) is mounted to a lifting system (triangular structure in the middle of the room). It can be moved along rails to a detector mounting area, which is accessible via a staircase.

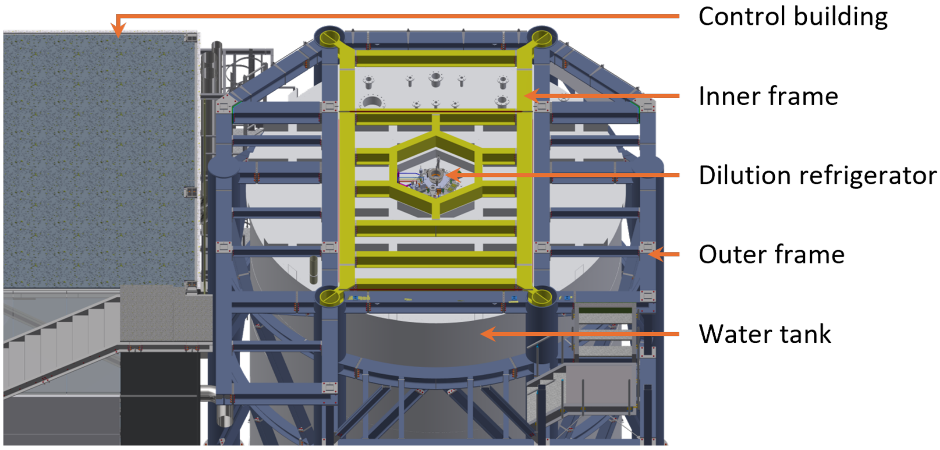

Figure 3.10: Two frame system of the COSINUS facility. The yellow frame hosts the dilution refrigerator and detectors, which require low vibrational noise conditions. Adapted from [126].

[127].[5] This leads to a reduction of the muon flux by a factor of $\sim 10^6$ to a muon flux of $\sim 10^{-8}$ muons/(cm^2 s) after a substantial part of the muons attenuated in the rock [128]. Any leftover muons reaching the experiment are tagged by an active muon veto, which will be discussed in section 3.2.3.

Ambient radioactivity comprises particles from the radioactive decay of isotopes within the direct environment of the experiment. Typically, materials with high atomic mass are used to shield from γ-radiation, while neutrons are moderated when scattering on materials with low atomic mass.[6] When designing passive shielding, it is important to consider the shielding material's intrinsic contamination to not introduce a new source of background events (e.g. ^{210}Pb).

Before constructing the COSINUS setup, a simulation-based conceptual design study for the passive shielding strategy in COSINUS was carried out [129]. The chosen design is a multi-layered shielding around the detector volume. A cross-sectional view is shown in figure 3.11. From outside to inside, it consists of:

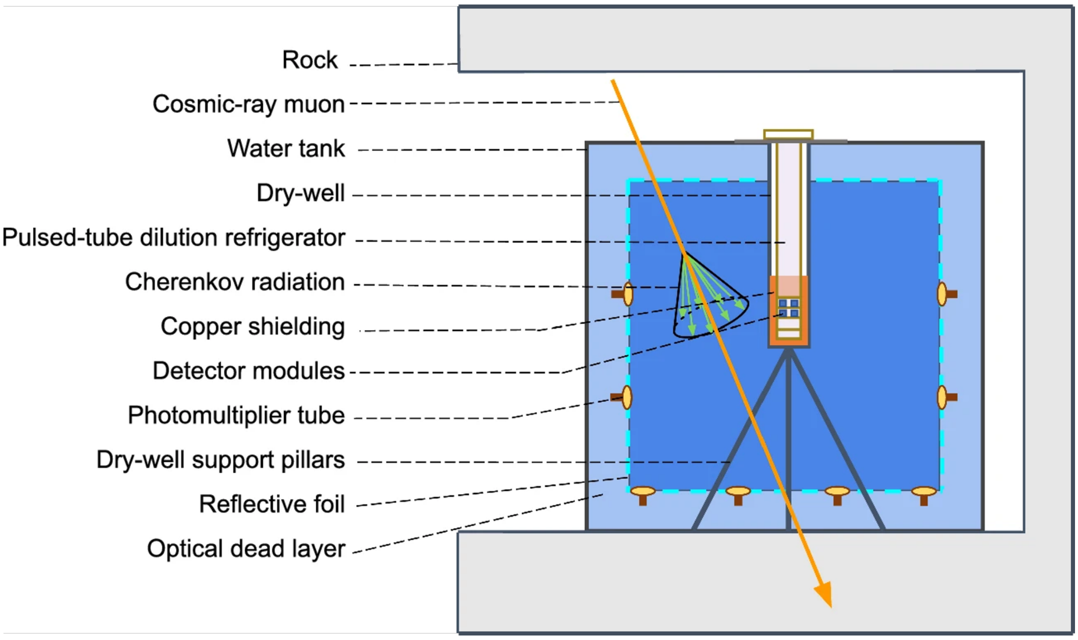

Figure 3.11: Cross-sectional view of the COSINUS facility as simulated in [3]. The sizes are not up to scale. The detector modules are shielded by layers of copper, water, and rock. The water tank is instrumented with PMTs and acts as muon veto. A non-instrumented layer of water (“optical dead layer”) reduces the trigger rate of the muon veto from non-muon-related photons. Adapted from [3].

---

[5] Compared to a flat overburden, a mountain overburden, such as the Gran Sasso mountains, is strongly dependent on the position and direction.

[6] α-particles and electrons do not have a high penetration depth and thus don't need a dedicated shielding.

- The water tank made from stainless steel (AISI 304). It is composed of three rings from top to bottom with thicknesses of 6 mm, 7 mm, and 8 mm.
- A pure water layer with a diameter of 7 m. It has three functions: First, it moderates neutrons such that the expected neutron flux from ambient radiation is negligible ($< 10^{-13}\,\mathrm{cm}^{-2}\mathrm{s}^{-1}$ [129]). Second, it shields the refrigerator from ambient γ-radiation. Third, it acts as an active medium to generate Cherenkov radiation to actively veto muon-induced neutron events. The number of surviving particles for different water thicknesses was demonstrated with simulations and is visualized in figure 3.12.
- The drywell in which the refrigerator is located. It was produced from 4 mm steel plates (AISI316L) chosen from the purest of three batches. The ground plate has a thickness of 15 mm.
- An external Cu-shielding made from 8 cm Cu (Cu-OF01). It accumulates to approximately 2 t of Cu distributed on 48 bricks plus a ground plate. The function of this layer is to reduce the γ-radiation flux reaching the detectors, originating from contaminants within the steel of the drywell.
- The refrigerator thermal shields. They are five layers with a combined thickness of 12 mm, made from Cu (NOSV [130]).

Additionally, an internal particle shield is mounted directly above the experimental volume to shield the detectors from γ-radiation originating from contaminants within the refrigerator. The shield consists of ten thoroughly cleaned plates made from pure Cu (NOSV). Each plate has a diameter of 300 mm and thickness of 30 mm, reaching an accumulated mass of 190 kg. Figure 3.13 shows photos of the Cu-parts of the inner shielding and the internal particle shield.

The conceptual design study gave a first estimate of (3.5 ± 0.7) counts/(kg year) for the nuclear recoil event rate, assuming a single 2.4 kg NaI-detector with a detection threshold of 1 keV. Almost all of these events are muon-induced neutron background. A complete detailed background model considering the exact final detector geometry and material contaminants is currently being developed. To this end, a screening campaign of all materials in use for COSINUS is ongoing.

3.2.3 Active Muon Veto System

With the passive shielding, the expected event rate from ambient neutrons is negligible. However, cosmic muons produce neutrons over a variety of channels within and outside the shielded region. Most prominently, these include muon-induced spallation reactions and neutron production in muon-induced hadronic cascades as well as electromagnetic cascades [131]. The resulting neutrons can be created close to the physical volume and might not be sufficiently moderated by the water layer. Their energy spectrum extends up to GeV-energies [129].

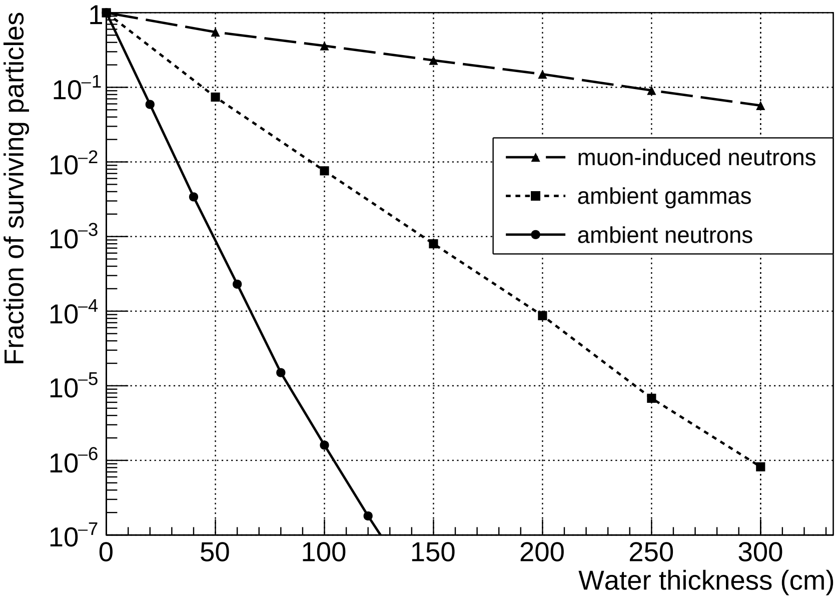

Figure 3.12: Surviving fraction of particles in pure water. The COSINUS water tank (about 300 cm of water) reduces the ambient neutron and gamma rates by many orders of magnitudes. Nevertheless, the muon-induced neutron rate is only minorly affected. Taken from [129].

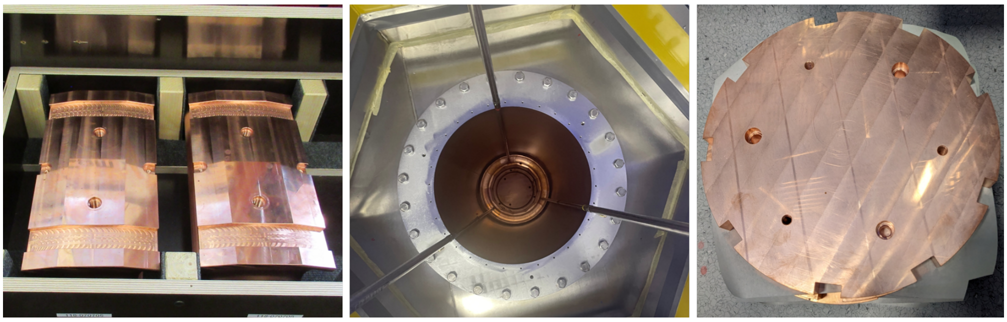

Figure 3.13: Cu-shieldings of COSINUS. Single bricks of the inner shielding are shown on the left. The middle image shows one of four assembled rings being lowered into the drywell. In the last image, one of the ten plates of the internal particle shield is shown.

To deal with this unavoidable background, the water tank of COSINUS will be instrumented as active muon veto. In total, 30 PMTs are mounted in the tank to tag muons by measuring either photons from Cherenkov radiation emitted by the muons in the water or photons produced in muon-induced cascades. A nuclear recoil event in the detector, which is measured in coincidence with a muon in the tank, could then be discarded from the dataset as a possible muon-induced neutron background.

High-reflectivity multi-layered foils cover the sides and floor to improve the light collection capabilities of the PMTs. They consist of two layers of Tyvek of type 1082D and one layer of PE in between and were procured from Shijiazhuang Dajia New materials Technology Co., Ltd [132]. The drywell and tripod it sits on are covered with specular reflector foil of type DF2000MA from 3M [133]. Between the tank wall and reflector foil, a non-instrumented gap called "dead layer" is left. Its function is to shield the instrumented part from ambient non-muon-related photons using the water as an absorber. Most of these photons are produced in the natural decay chains of ^{238}U-, ^{232}Th-, and ^{40}K-contaminants within the stainless steel of the water tank. Photographs of the muon veto are shown in figure 3.14.

Figure 3.14: Muon veto within the water tank. The walls and floor are covered in a reflecting Tyvek foil. The drywell, and the tripod it connects to, are covered in specular reflecting foils. In total, 30 PMTs are distributed over the tank mantle and bottom.

The muon tagging efficiency was optimized following a dedicated simulation study [3]. Generally, two types of event classes were separated. In "muon events" the muon is measured directly from the emitted Cherenkov photons in water. They mostly illuminate the bottom of the tank, with an increasing rate towards the center. For "shower events" instead, secondary particles from muon interactions are absorbed closer to the tank walls, leading to a higher illumination at the walls. A split of around 95% muon events and 5% shower events is expected.

Based on the simulation, the precise PMT arrangement, the size of the dead layer, and the PMT trigger conditions were set. The predicted veto efficiency is $(99.63 \pm 0.16)\%$ for muon events and $(44.4 \pm 5.6)\%$ for shower events, leading to a total veto efficiency of $(97.0 \pm 0.3)\%$. This would reduce the expected background from (3.5 ± 0.7) counts/(kg year) to (0.11 ± 0.02) counts/(kg year), assuming a detection threshold of 1 keV.

3.2.4 Magnetic Field Compensation

Magnetic fields within the experimental volume can have detrimental effects on the sensitivity and stability of detectors. A TES, as used by COSINUS for both LD and PD, is a superconducting thin film that is operated within its transition between superconducting and normal conducting state (see chapter 4).

In this region, a small temperature change of the order of μK leads to a measurable change of electric resistance of the order of mΩ. Magnetic fields perpendicular to the film plane strongly influence the operating conditions. Changes of 20 μT can lead to a shift of the critical temperature by 1 mK and an additional widening of the transition[7] [134, 135].

In 2022, during the construction of the facility, the magnetic field was measured inside the drywell with a Barlington Mag-13 three-axis fluxgate magnetometer [136]. The result for the vertical field component is shown in figure 3.15.

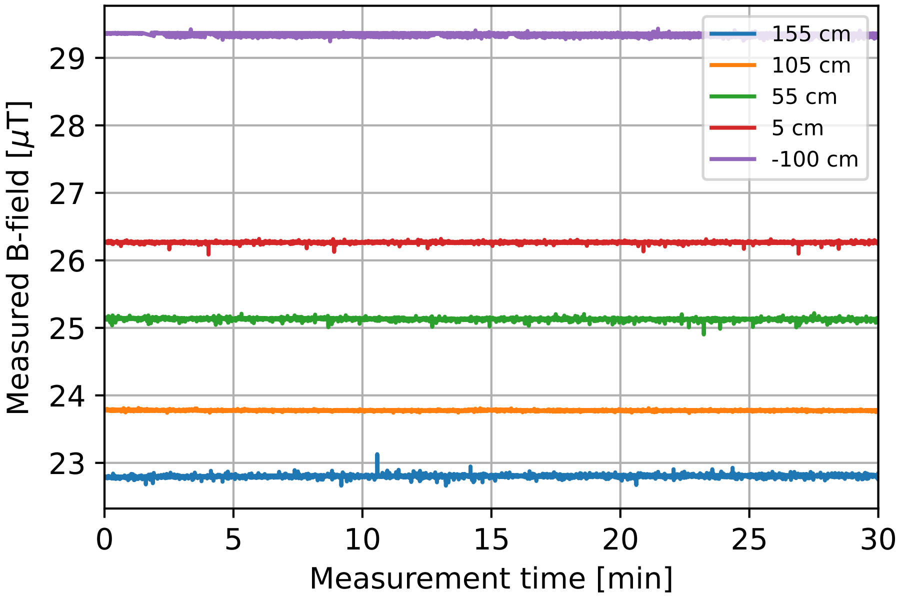

Figure 3.15: Vertical magnetic field measured in the drywell. The distances given correspond to the height above the bottom of the drywell. Negative numbers correspond to a measurement position below the bottom of the drywell. The measurements fluctuate up to 0.5 μT.

Vertical field strengths within the drywell between 22 μT and 27 μT were measured, with the highest fields being closest to the laboratory floor. During idle laboratory operation, fluctuations of up to 0.5 μT were measured.

To compensate for the vertical magnetic field in the physical volume, a triple coil system was mounted around the drywell within the water tank. It has 10 windings

---

[7] The magnitude is strongly dependent on the thermometer film quality.

with a wire thickness of 20 AWG on each coil. The coil was designed to apply vertical magnetic fields up to 150 μT with a maximum current of 5 A. Figure 3.16 shows an image of the coil system as installed.

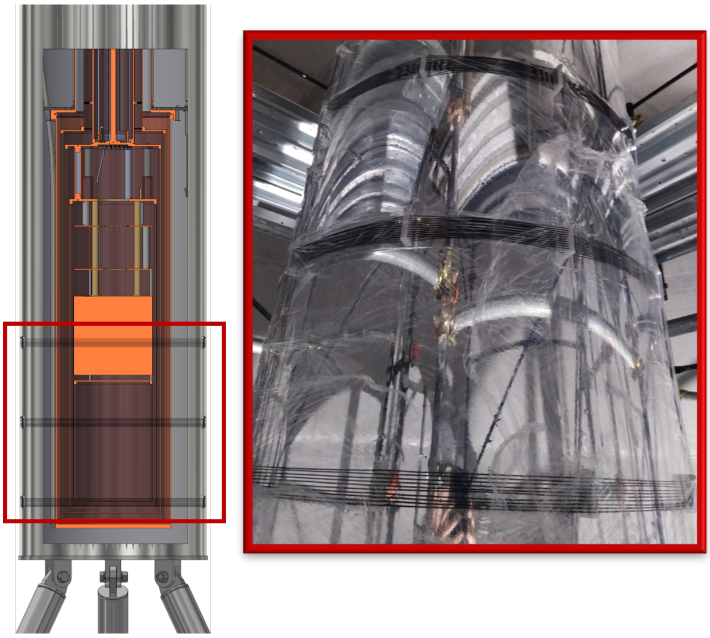

Figure 3.16: Coil system for the magnetic field compensation. On the left, a CAD rendering of the drywell and the refrigerator within it are shown. The horizontal black lines mark the position of the coils. A photo of the coils is shown on the right. The drywell was wrapped in foil after mounting to keep it clean during the installation of the muon veto system.

Aside from the active magnetic compensation, passive shielding utilizing superconducting aluminum (Al) is under investigation. Due to Faraday's law, the magnetic field would be frozen within a superconducting can and, therefore, be resistant to fluctuations. The planned procedure for the minimization of magnetic field effects would be to measure the external magnetic field before or during the cool-down of the refrigerator and then set up the active compensation to minimize it. As soon as the passive magnetic shield becomes superconducting, this minimized field is frozen and, from thereon, resistant to changes in external conditions. The principle of this system will be proven within the first COSINUS measurements and could be a big step towards operating big arrays of TES-based detectors with similar conditions.

3.3 Cryogenic Refrigerator

3.3.1 Refrigeration Techniques

A dilution refrigerator is an apparatus that allows to cool detectors down to temperatures below 10 mK. The cooling happens thereby in multiple stages, the details of which strongly depend on the refrigerator model. It usually requires some form of pre-cooling to reach 4 K, the temperature around which ^{4}He condenses, and uses an advanced circuit that mixes and separates helium-3 (^{3}He) and ^{4}He in their liquid phase, to reach 10 mK.

For pre-cooling, the historically most widespread method is cooling by coupling the refrigerator to a liquid ^{4}He-bath ("wet refrigerator"). As long as the bath is periodically refilled, it provides a practically inexhaustible cooling power at 4.2 K due to its latent heat of vaporization. ~1 K is then reached by pumping on a small liquid ^{4}He-volume, conventionally called "1 K-pot", and therefore reducing the vapor-pressure inside.[8] Compared to refrigerators with mechanical coolers, the benefit of this pre-cooling method is its superior cooling power, as well as relatively low vibrational noise.[9] However, a wet refrigerator requires trained personnel and specialized infrastructure to handle cryogenic liquids. Furthermore, the cost of ^{4}He is rapidly increasing [138], disfavoring this method.

In dry dilution refrigerators, the ^{4}He-bath is replaced with a Pulse Tube (PT) cooler. It cools to temperatures around 4 K by running through a cycle of adiabatic (i.e. no heat exchange) and isochoric (i.e. constant volume) processes. The technical details depend on the PT-model in use. A simplified schematic of the working principle and technical drawings of the parts are shown in figure 3.17.

The system consists of four main parts: a compressor with a high pressure gradient, a rotary valve to switch between the high-pressure and low-pressure lines, a regenerator for short-term heat storage, the PT head which provides the cooling to the refrigerator in two stages (60 K and 4 K), and a buffer volume with an impedance Z to the PT head. In a simplified view the volume within the system can be divided into three sub-volumes V_1, V_2 and V_3 with different functions. V_1 is thereby the volume that will provide the cooling in the end. By periodically switching the valve between both positions, it runs through all five steps of the pre-cooling cycle:

1. The rotary valve switches from the low-pressure line to the high-pressure line, which leads to an adiabatic compression of V_1, forcing it to move through the regenerator. A heat exchanger can dissipate some of the generated heat; the rest is stored in the regenerator.

2. The compressed gas leads to a compression of V_2 and subsequently V_3, forcing V_3 to flow into the buffer volume. Meanwhile, V_1 experiences an isochoric relaxation.

3. The rotary valve switches from the high-pressure to the low-pressure line. Due to the impedance between PT head and buffer, the gas of V_3 is still within the buffer. Therefore, V_1 experiences an adiabatic expansion, leading to further cooling.

---

[8] The 1 K-pot is usually connected to and continuously replenished from the liquid ^{4}He-bath, leading to unlimited cooling as long as the bath is kept full.

[9] Nevertheless, the 1K-pot is known to be a common source for vibrations [137].

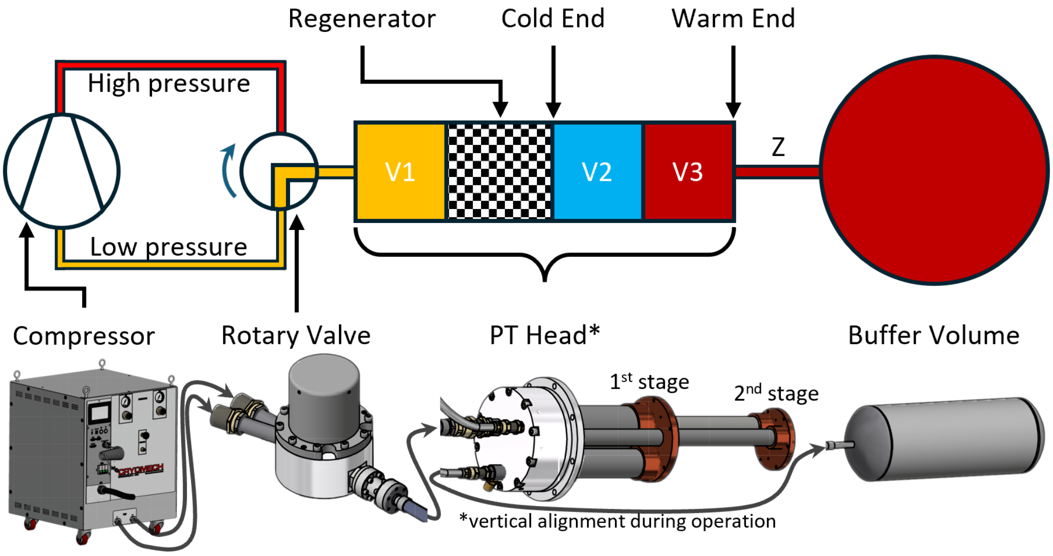

Figure 3.17: PT cooler working principle. The rotary valve turns with a specific working frequency to apply alternating high and low pressure to the PT head. Z marks a defined impedance to the gas flow. The parts are not drawn with the same scale. Technical drawings taken from [139].

4. The compressed gas of V_3 flows back into the PT head leading to a compression of V_2 and subsequently V_1, forcing V_1 to flow back through the regenerator.
5. Initial conditions for V_1 are restored. However, the PT now has a cold and warm end that can be utilized for further use.

A two-stage system, like the PT in use for COSINUS, works similarly to two chained one-stage systems.

The advantages of dry refrigerators are the lower operation costs[10] and the long intervention-free run times they can achieve. However, due to the introduction of the new moving volumes at high pressures, the vibration noise in dry refrigerators is significantly higher [140].

To reach 10 mK, both dry and wet dilution refrigerators use a mixing circuit that circulates a mixture of ^{3}He and ^{4}He through all temperature stages. The working principle is based on the minimum solubility of ^{3}He in liquid ^{4}He, independent of the temperature. The cooling is then provided by the enthalpy difference between the concentrated and diluted ^{4}He-volumes. A schematic of a mixing circuit is shown in figure 3.18.

The heart of the mixing circuit is the DU within the refrigerator, which consists of the Mixing Chamber (MC), the Still, and a flow impedance. During regular operation the

---

[10] Mostly energy consumption, which is dominated by the PT and its water cooling (about 20 kW for COSINUS).

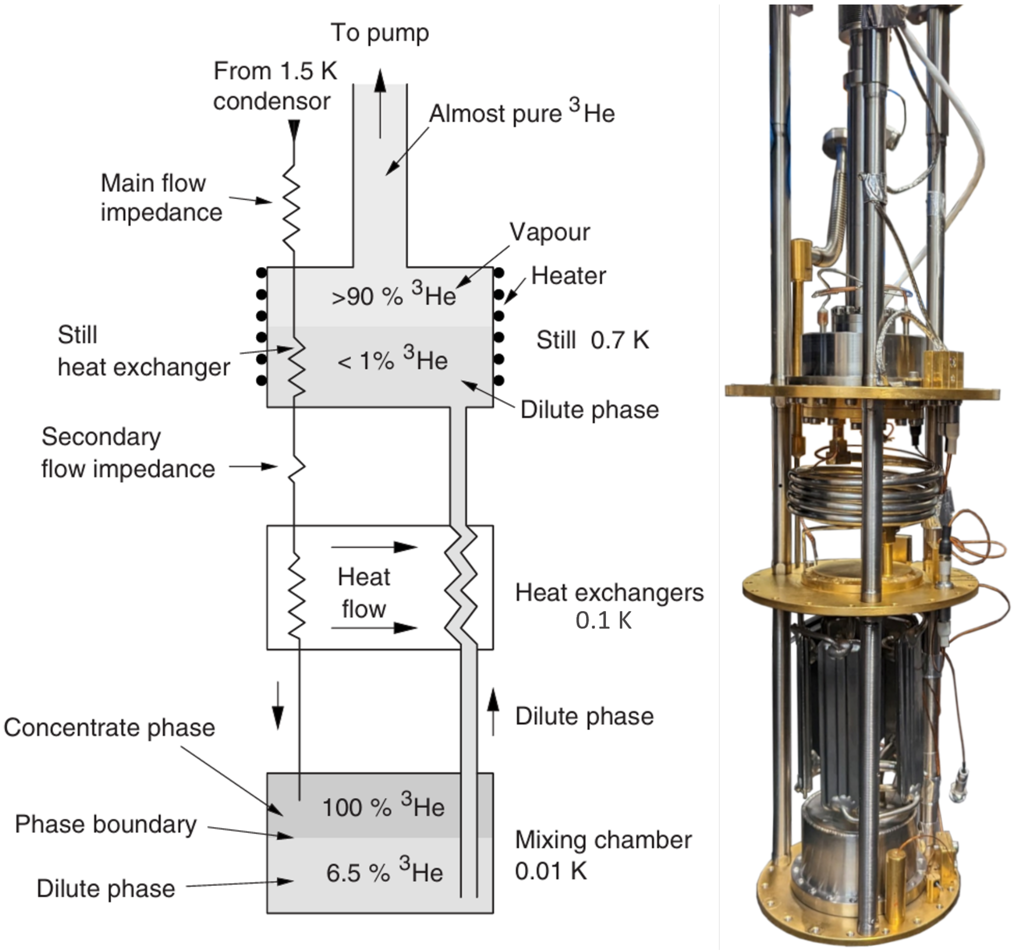

Figure 3.18: On the left: schematic depiction of a mixing circuit. Adapted from [141]. On the right: DU from a COSINUS dry dilution refrigerator.

MC is filled with the ^{3}He/^{4}He-mixture and ^{3}He circulates through the complete circuit in following steps:

1. The ^{3}He is pushed into the refrigerator and pre-cooled on the first (60 K) and second stage (4 K) of the PT.
2. The incoming gaseous ^{3}He is cooled further via heat exchangers with the outgoing ^{3}He and pushed through a flow impedance with high condensing pressure. This leads to cooling (and subsequent condensing) via the Joule-Thomson effect.[11]
3. The liquefied ^{3}He is cooled further via heat exchangers to temperatures around 100 mK

---

[11] In wet dilution refrigerators, this cooling stage is realized in a more powerful way by pumping on a ^{4}He-volume (“1K-pot”).

4. In the MC, the ^{3}He is diluted in ^{4}He, leading to cooling. The cooling power is directly proportional to the flow rate of the mixing circuit. The minimum achievable temperature is limited by the temperature of the pre-cooled ^{3}He.

5. The mixture is moved up to the Still by osmotic pressure and then heated to separate the ^{3}He from ^{4}He. This is possible due to their different evaporation temperatures and provides additional cooling power.

6. The ^{3}He gas is pumped out of the refrigerator via a turbo-molecular pump. On the way out, the heat is exchanged with the incoming ^{3}He for pre-cooling.

Overall, the parameter controlling the cooling power of the refrigerator at low temperatures is the flow rate of the circuit, while the base temperature mainly depends on the temperature reached in the pre-cooling stages.[12]

3.3.2 COSINUS Dry Dilution Refrigerators

Two dry dilution refrigerators manufactured by CryoConcept [142] are in use by COSINUS. They are using a Cryomech PT420RM [139] for pre-cooling to 4 K and a turbo-molecular pump of type HiPace400 by Pfeiffer Vacuum GmbH [143] for the mixing circuit. One unit, used for research and development (R&D), is a standard model and located at MPP in Garching. It has a cooling power of 10.35 μW at 20 mK and reached a base temperature of 6.3 mK (without payload). The other unit is a custom-made model fitted to the facility at LNGS. Its main difference is the 170 cm long extension at the 4 K stage. It has a cooling power of 8.25 μW at 20 mK and reached a base temperature of 9.57 mK without payload.

Figure 3.19 shows photos of both refrigerators during operation. Both units were produced to have interchangeable parts. The physical volume has similar dimensions, and the thermal shields are produced from the same batch of ultrapure low background Cu (NOSV). Because of this, it is possible to test every detector or cabling part in the R&D refrigerator in Garching before sending it to LNGS.

A feature specific to refrigerators produced by CryoConcept is the patented Ultra-Quiet Technology (UQT). It allows for a vibrational decoupling of the PT from the experimental volume. Chapter 5 includes a more detailed description of the system. Figure 3.20 shows a CAD of the insides of the R&D refrigerator located in Garching. A CAD of the COSINUS refrigerator is shown in the appendix.

The structure is given by a vertical DU on which horizontal plates are mounted for each temperature stage. In COSINUS these include the first PT stage ((60) K), the second PT stage (4 K), the Still stage (800 mK), the “cold plate” (100 mK) and the MC stage ($<$ 10 mK). All stages from 1 K, and higher have a thermal radiation shield to prevent thermal shortcuts by means of thermal radiation. The particle shield made from Cu is located below the MC plate but thermalized to the Still plate because of the higher cooling power available at that stage (of the order of 10 mW).

---

[12] This is limited by the performance of the heat exchangers.

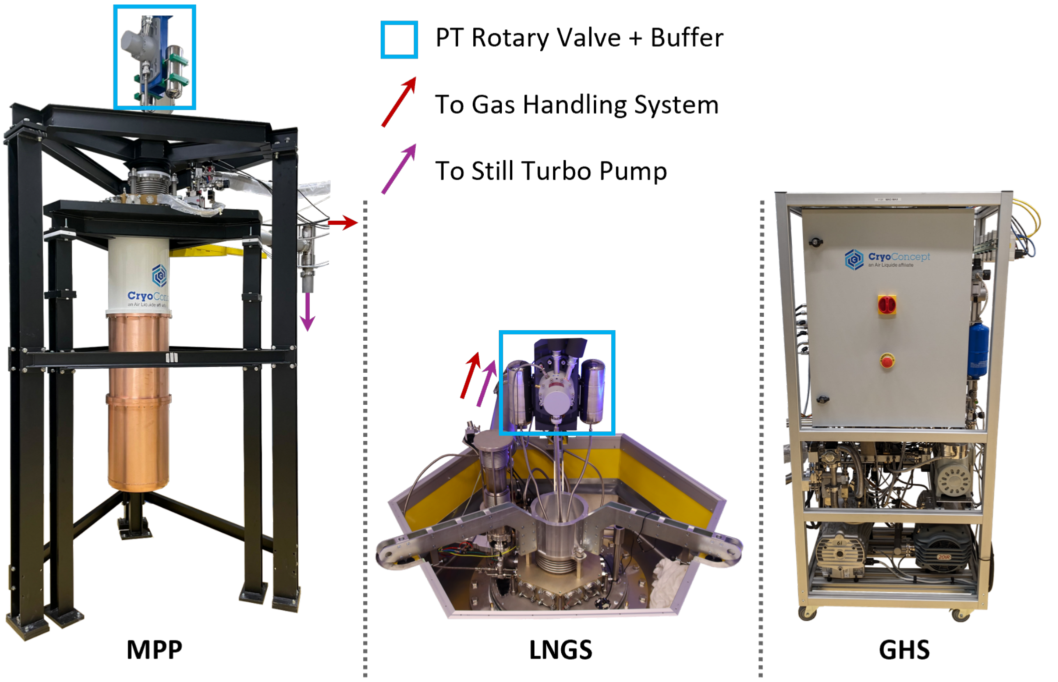

Figure 3.19: Photographs of the refrigerators located at MPP in Garching (left) and in the COSINUS facility at LNGS (middle). The right image shows the GHS, which is similar for both refrigerators. All images are shown with different scales.

Only recently, dry dilution refrigerators have been used for DM research. A major difference with respect to the well-established wet refrigerators is the absence of an Inner Vacuum Chamber (IVC). In wet refrigerators, it is common to have two vacuum chambers: the Outer Vacuum Chamber (OVC), which is (during regular operation) filled with liquid ^{4}He, and the IVC between the ^{4}He-bath and the inner refrigerator parts. During pre-cooling, the IVC is filled with gaseous ^{4}He as exchange gas, which allows for quick isotropic cooling of all parts until the condensation temperature.[13]

In a dry refrigerator, typically, no IVC is used, as there is no liquid ^{4}He-bath. While its absence comes with the advantage of having only feedthroughs at RT to the OVC (under vacuum), it also means that no exchange gas can be used for pre-cooling.[14]

This leads to longer cool-down times (from $\sim 20\,\mathrm{h}$ to ~ 3 days), and, generally, special attention has to be given when mounting parts to the refrigerator:[15]

- All parts must be properly thermalized to avoid hot spots within the refrigerator. Big contact areas and cross-sections of thermal links are recommended.

---

[13] Before condensation, the exchange gas has to be pumped away.

[14] Using exchange gas in a dry refrigerator would create a shortcut to RT.

[15] The following advice is valid for any refrigerator. However, parts in a dry refrigerator can only cool down via thermal conduction (or radiation), while in wet refrigerators, everything is cooled isotropically to $\sim 4\,\mathrm{K}$ via the exchange gas. Therefore, dry refrigerators tolerate fewer faults.

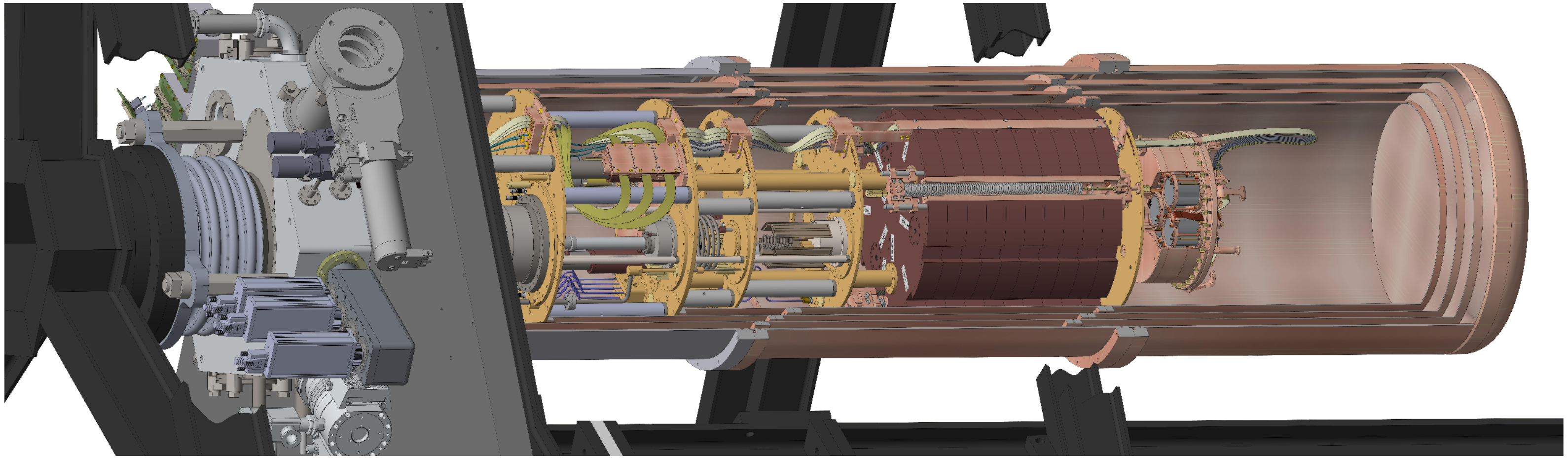

Figure 3.20: Complete drawing of the COSINUS refrigerator located in Garching, including detectors and cabling. The refrigerator consists of five temperature stages (visible as golden horizontal plates) from top to bottom: first PT stage (60 K), second PT stage (4 K), Still (800 mK), Cold plate (100 mK) and MC (<10 mK). The internal particle radiation shield made from Cu is thermally connected to the Still. The detectors (at the bottom) are connected to a detector plate, which is thermally connected to the MC.

- Non-metallic materials should be avoided as much as possible due to their low heat conductivity. They tend not to thermalize well and radiate thermal radiation with comparatively high temperatures.
- Openings between temperature stages (i.e. open screw holes or small slits) should be covered completely to avoid leakage of thermal radiation.
- Temperature-sensitive parts should be completely covered with an additional thermal radiation shield to avoid any line of sight to a warm part.

The COSINUS refrigerator at MPP takes 10 days to cool from RT to base temperature when the particle shield with a mass of approximately 190 kg is mounted. When dismounting the shield, the time is reduced to 3 days.

3.3.3 Cabling and Readout Scheme

The sensors of choice for COSINUS are tungsten (W)-TES: superconducting thin films made from W that are operated within the phase transition between superconducting and normal conducting state. By utilizing the strong dependence of the electrical resistance on the temperature, precise calorimetric measurements are possible. The cabling of COSINUS is optimized to measure resistances of less than 100 mΩ with high precision. Hereinafter, the technical considerations of such a cabling scheme within a dry dilution refrigerator are explained. Chapter 4 will describe the detector and readout principles in more detail.

Within the refrigerator, different parts need to be mounted at different temperature stages:

- The operating point of a W-TES is typically between (10-30) mK. Therefore, the **detectors** need to be on the lowest temperature stage of the refrigerator at 10 mK. Other benefits at lower temperatures are reduced thermal noise levels and less heat capacity.[16]
- In the readout scheme foreseen for the detectors, **shunt resistors** are required to read out a TES. They are on the order of 10 mΩ and custom fitted to every sensor.[17] In CRESST, the shunts were mounted in separate boxes on the MC plate at a temperature of 10 mK. In COSINUS, this will be modified by making the shunts part of the detector modules.
- The input bias and heater currents will be filtered with **low pass filters** to avoid aliasing effects. All filters should be mounted on the 1 K-plate or below to minimize thermal Johnson noise from the resistors.

---

[16] According to the Debye model the specific heat capacity of a crystal C scales with the temperature T via $C \propto T^3$.

[17] Ideally, the TES and shunt resistances are equal.

- DC **Superconducting Quantum Interference Devices (SQUIDs)** are extremely precise magnetometers based on Superconductors (SCs) that can measure small changes in the magnetic flux. In combination with an input coil, they are typically used in TES-based experiments as low-noise analog amplifiers. They are mounted in superconducting magnetic shields, in most cases made from niobium (Nb), to shield them from external magnetic fields. Due to the required superconductivity in various parts, the SQUIDs need to be mounted on a temperature stage below 9 K, the critical temperature of Nb.
- A Field Programmable Gate Array (FPGA)-based **DAQ** will be used to send the required input bias and heater currents, as well as to measure the SQUID output signals. It is located next to the refrigerator at RT.

COSINUS foresees a modular cabling solution for 16 detector channels (“cabling segment”), which is interchangeable between both refrigerators. Figure 3.21 shows a block diagram of the necessary parts for COSINUS. The cabling should be robust enough to survive many cool-downs, and defective parts should be easy to replace. Furthermore, as every resistor introduces Johnson noise, superconducting Nb-titanium (Ti) cables should be used where applicable. To avoid inductive effects or noise induced by microphonic, piezoelectric, or triboelectric effects, cables should be mounted rigidly connected to the refrigerator. A concept drawing is shown in figure 3.22

A cabling segment can be pre-assembled on a working table and mounted to the refrigerator without the need for any soldering. It is interrupted at three stages (RT, 800 mK, and detector box) using special connectors. In the refrigerator at LNGS, three cabling segments supplying 3×16 detector channels will be installed, while the R&D refrigerator will only operate one cabling segment (16 channels). The details of all parts are described in the following subsections.

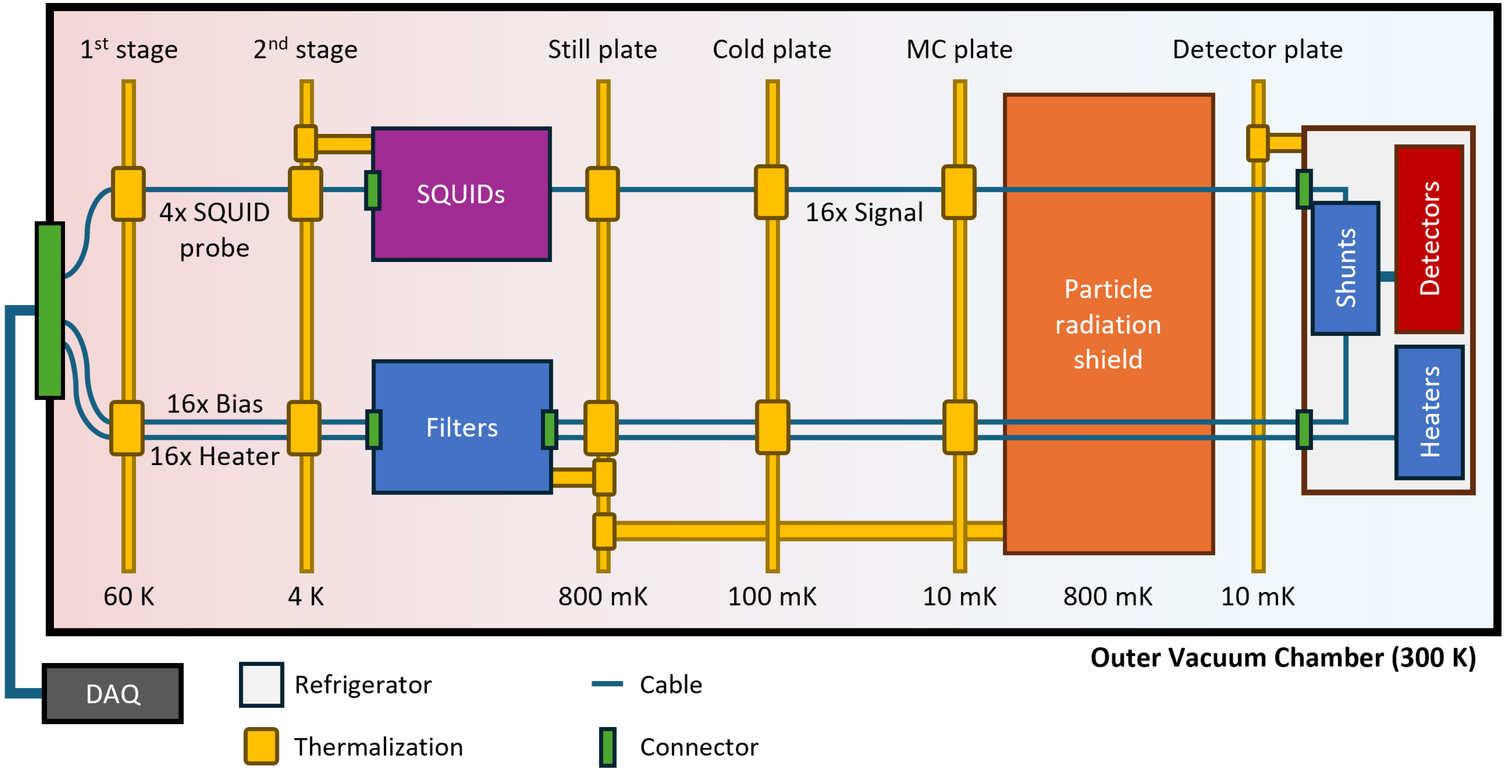

Figure 3.21: 16-channel cabling block diagram: the brown box marks the detector box, which contains the detector modules with a shunt resistor and a heater per detector channel. The upper line includes four probe cables to the 16(4×4) SQUIDs and 16 superconducting wire pairs between SQUIDs and shunts. The lower line consists of 16 wire pairs to supply the detectors with bias current and 16 wire pairs for the heaters.

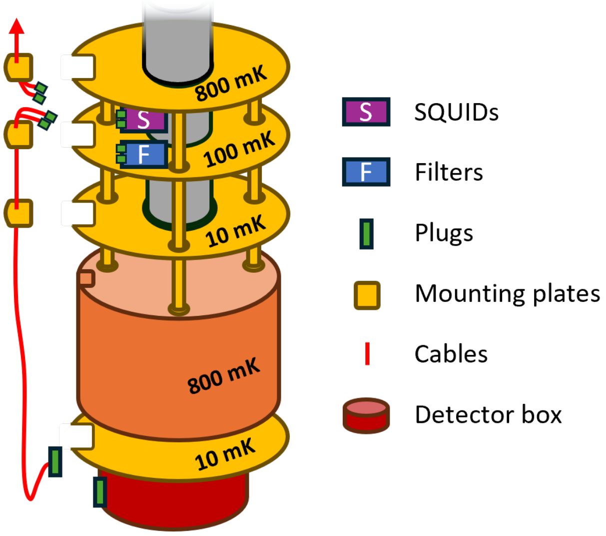

Figure 3.22: Cabling concept of COSINUS. The cables are routed as one tree and fixed to mounting plates, which can easily be thermalized on the refrigerator. One segment provides 16 detector channels and serves one detector box.

Cables

Generally, four different types of cables are used in a COSINUS cabling segment:

1. SQUID probe cables are part of a commercial Direct Current (DC) SQUID system and routed from the SQUIDs up to feedthrough plugs at RT. They are responsible for the transmission of control and response signals between the SQUIDs, pre-amplifier, and DAQ.

2. Signal cables connect the SQUID input coil with the shunt resistors located at the detector modules. They transmit the signals to be amplified to the SQUIDs. Twisted pairs of superconducting Nb-Ti wire in a Cu-nickel (Ni) matrix were chosen to avoid any undefined resistances that could introduce noise to the system. All signal cables were procured from GVL Cryoengineering [144] and are insulated by formvar and Teflon and shielded by a woven Cu-Ni mantle on the outside.

3. Woven cables consist of 16 twisted pairs interlaced with single ground wires and woven together into a single flat band cable. The cables are made of Nb-Ti wire in a Cu-Ni matrix and were procured from Tekdata Interconnections Limited [145]. Their purpose is to supply the detectors with bias and heating currents. Hence, they connect the detectors at base temperature with feedthrough plugs at RT. All lines are filtered with low pass filters.

4. Copper-Kapton-Copper (CuKaCu) are circuit board-like pieces made from three layers: A Cu layer as a structural basis and for thermal contact to the refrig-

erator heat bath, a Kapton layer for electrical isolation, and Cu-traces for the actual connections. Due to the very low radioactive background, they take care of the connections close to the detectors. However, since the connections are made from normal conducting Cu, they should only cover short distances with a high conducting cross-section, such that the line resistance is negligible.

One cabling segment will use 4 SQUID readout cables, 16 signal cables, 3 woven cables, and 16 CuKaCu-flatbands. Pictures of each cable type in use are shown in figure 3.23

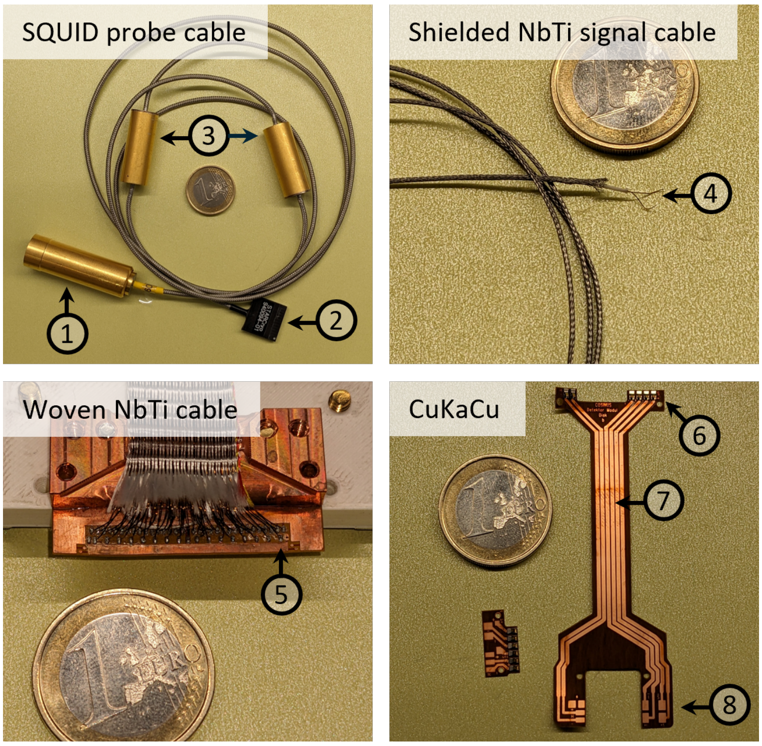
SQUID probe cable

Shielded NbTi signal cable

Woven NbTi cable

CuKaCu

Figure 3.23: Cable types in use within the COSINUS refrigerator. The numbers correspond to: (1) connector at 4 K (to the SQUID), (2) connector at RT to a feedthrough box and (3) thermalization of the cable for the first (60 K) and second (4 K) temperature stages, (4) twisted NbTi-cable pair, (5) woven cable breakout piece, (6) spring finger connector, (7) Cu-trace and (8) bonding pad for wire bonds.

SQUIDs

COSINUS will use SQUIDs of type SQ300 by STAR Cryoelectronics [146] for a total of 48 (16) channels in the refrigerator located at LNGS (MPP in Garching). For this type, four SQUIDs share one housing made from Nb. Figure 3.24 shows a photo of the SQUIDs and their housing.

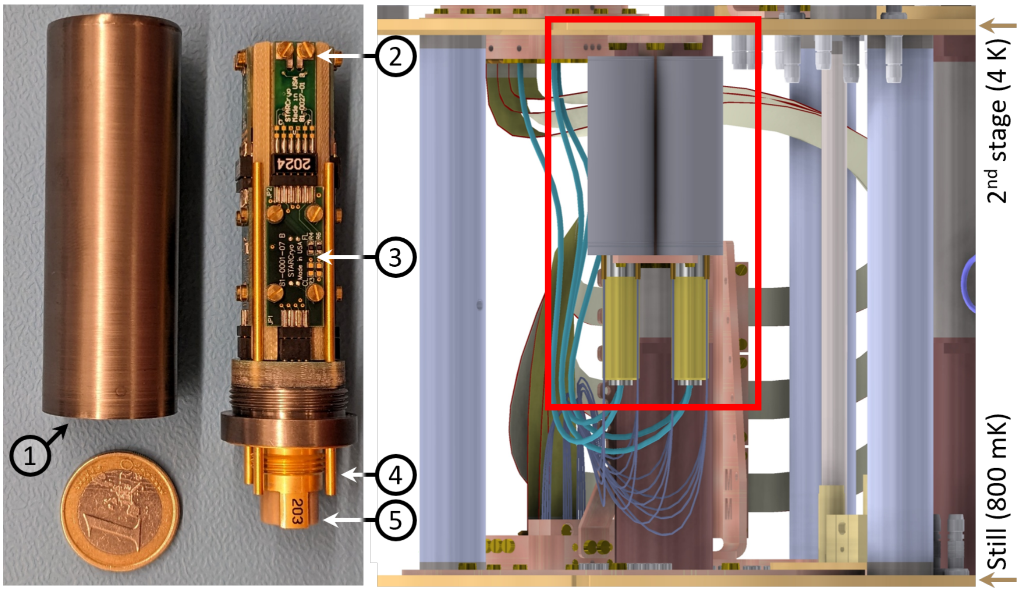

Figure 3.24: On the left: photo of a SQUID module (contains four SQUIDs). The numbers correspond to: (1) Nb-housing for magnetic shielding, (2) input coil contacts, (3) internal SQUID PCB, (4) signal cable feedthrough and (5) connector for SQUID probe cable. On the right: mounting scheme within the refrigerator. The SQUID probe cables are shown in turquoise, while the signal cables are shown in blue.

One cabling segment will include 16 SQUIDs in four Nb-housings, all mounted in a Cu-harness on the Still plate (800 mK). Towards higher temperature stages, one SQUID probe cable connects to a plug on the Nb-housing. The breakout into the single channels is done internally. To lower temperatures, the signal cables, twisted pairs of superconducting Nb-Ti wire for each SQUID, are routed out of the housing.

Thermalizations

All cables need to be thermalized at every temperature stage to divert the heat introduced through the cables to the appropriate cooling stages and to avoid heat leaks. For this, they are pressed between two Cu-plates, which are collected into a bigger Cu-block containing all cables for the complete segment. The block can then be screwed into cutouts on the refrigerator plates. Figure 3.25 shows a drawing and photos of the thermalizations as foreseen.

A special treatment is given to the SQUID probe cables. From their vendor, a thermalization concept was already foreseen with the cables being glued into gold (Au)-covered Cu-blocks. They are integrated into the COSINUS solution without any need for modification.

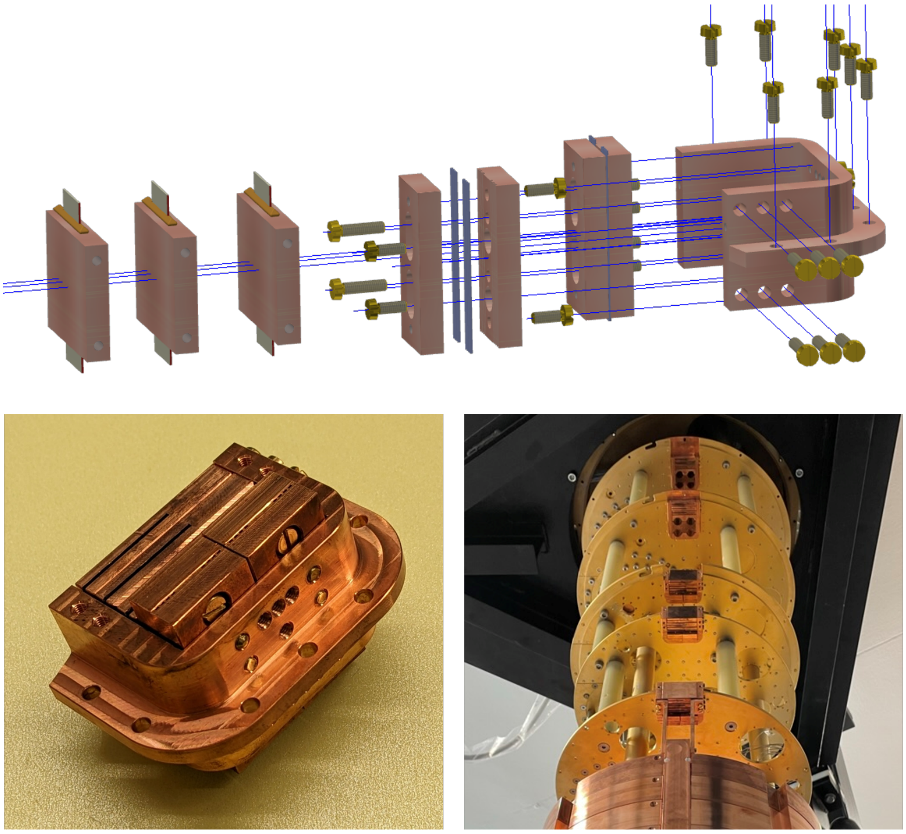

Figure 3.25: Cable thermalization principle. All cables are thermalized via two pressed Cu-pieces and collected in larger Cu-modules. The modules are then screwed on the plates within the refrigerator.

Connectors

Connectors are indispensable for the cabling concept. Three different types are foreseen:

1. The SQUID probe cables are connected to the SQUIDs via a LEMO plug as predefined by the manufacturer.
2. SQUID probe cables and woven cables need to be fed through the cryostat shell at RT to be read out by the DAQ. For this purpose, the refrigerator is equipped with multiple general-purpose ports between its outside and inside. The design that will be used for the feedthrough connectors utilizes commercial D-Sub connectors. It is shown in figure 3.26.

   The cables are routed through ISO-KF parts into custom-made boxes and connected to PCBs, which can be screwed on top of the box to close it. An O-ring ensures vacuum tightness.
3. Commercial plugs are not optimized for radiopurity and can take up much valuable

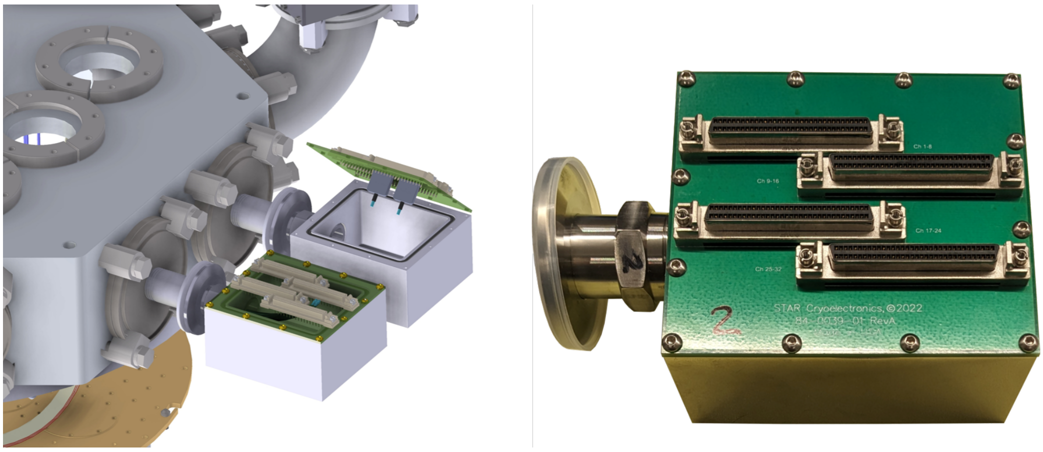

Figure 3.26: Feedthrough plugs at RT. Cables can be connected from inside and outside to the corresponding sockets within a PCB. The PCB is closing a metal box connected to the inside of the refrigerator. An O-ring ensures high vacuum tightness.

space within the refrigerator. Therefore, for the connections at the filters and at the detector box, a new type of plug based on Spring Finger Contacts (SFCs) was developed. SFCs are pressed contacts commonly used on small PCBs and exist in many shapes and sizes. They consist of a contact point (e.g. a pin) attached to a spring, which is soldered to the PCB. The contact is then made by pressing a counterpiece against the pin. Figure 3.27 shows images of the implementation of SFCs in COSINUS.

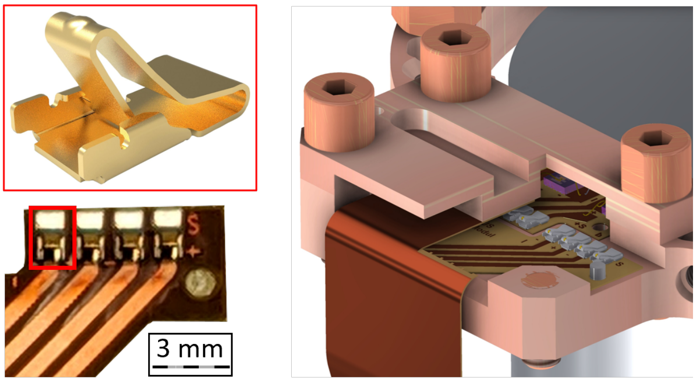

Figure 3.27: Implementation of SFCs (top left [147]) in COSINUS. On the bottom left, an image of a CuKaCu with 4 SFCs soldered on it is shown. The right image shows how connections between different pieces are made by pressing them together.

The feasibility of SFC for COSINUS was tested in two independent ways in a cryogenic facility provided by the CRESST group at MPP. The model tested was of type TE 2306334-3 from TE Connectivity [148].

Three SFCs were soldered on a PCB, which was then pressed against a counter piece such that they were connected in series. Two stacked washers with a thickness of 0.3 mm each acted as distance pieces for the SFC for a defined contact force per SFC. All traces on the PCB were tinned with soldering tin. Figure 3.28 shows a photograph of test samples.

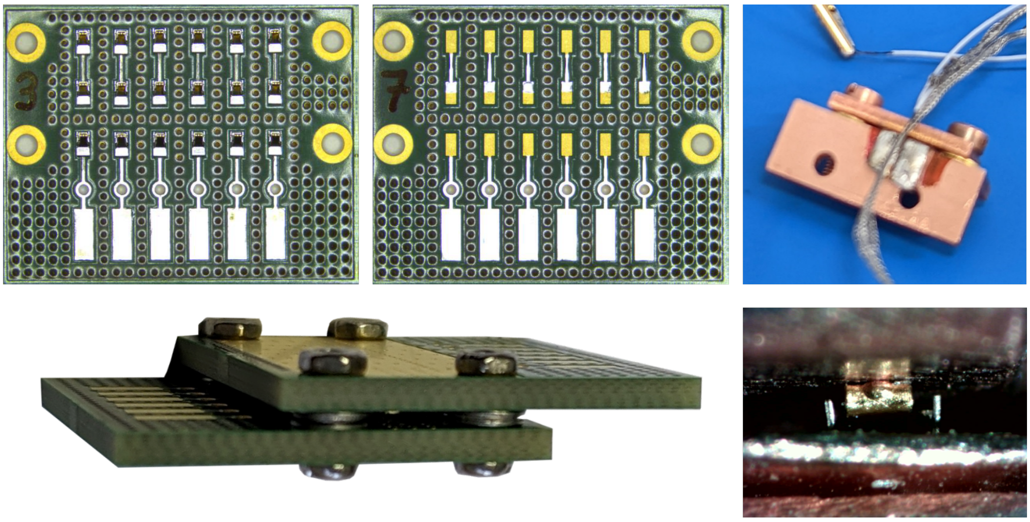

Figure 3.28: On the left and in the middle: SFC test samples for testing in a ^{4}He-dewar. One sample consisted of six lines on two PCBs, interrupted by three SFCs each. The traces were tinned to minimize parasitic resistance when measuring the contact resistance at cold. On the right: sample for testing on a detector in a dilution refrigerator. A single SFC is connected in series with a TES to check for parasitic resistance introduced by the SFC. In both tests, the distance of the connecting parts and, therefore, the SFC-pressure was defined using M3-washers as distance pieces.

The resistance of the sample was first measured in a ^{4}He-filled dewar at 4.2 K with a 4-point measurement system with a resolution of 10 mΩ. A resistance of 50 mΩ was measured at RT and 10 mΩ at 4.2 K. By pumping on the dewar, the temperature could be reduced further, and a superconducting transition attributed to tin ($T_c = 3.7\,K$) was observed. Below the transition temperature, the resistance was not measurable, thus below 10 mΩ.

The second measurement was done in a dilution refrigerator. A SFC was soldered on CuKaCu traces, which were connected in series with the TES. Two stacked M3-washers with a thickness of 0.3 mm each acted as distance pieces for the SFC. The residual resistance after the TES became superconducting gave an upper limit of 1.3 mΩ on the resistance of the connector.

Filter Boxes

The filter boxes are mounted on the Still plate and have two functions: First, they allow the application of low-pass filtering on all heater and bias lines of the woven cables. Second, they act as interruptions on the Still plate to allow taking out only the lower part of a cabling segment.

The basis of a filter box is a CuKaCu PCB equipped with a mask for surface-mounted devices that define the low-pass frequency. At the same time, it is possible to transpose the connections in case one of the wires in the woven cables breaks. Photographs of the filter concept are shown in figure 3.29.

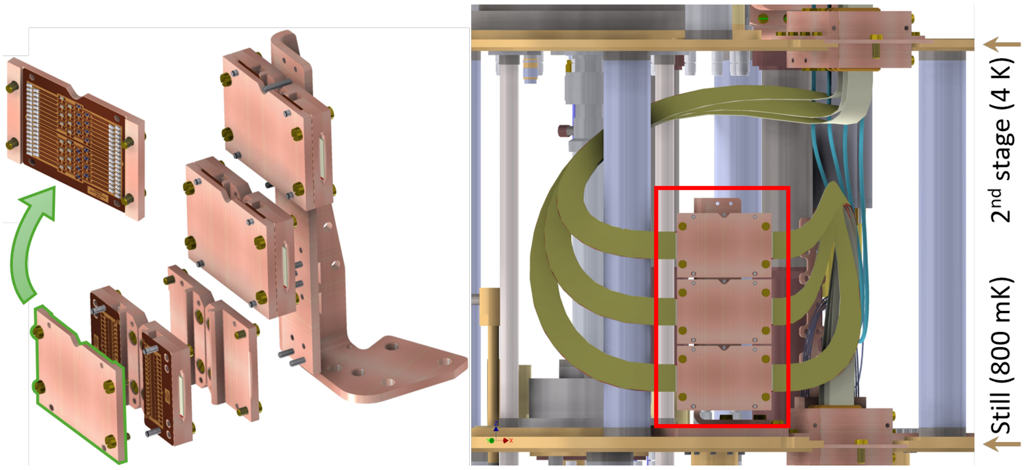

Figure 3.29: Filter boxes of COSINUS. The boxes serve as an interruption point for the cabling by using SFCs in their design. A removable CuKaCu PCB allows one to choose the filter frequency freely by mounting resistors and capacitors. Furthermore, changing the pinout of the flatband cables is possible in case of a defective line.

The woven cables are connected to the filter box with SFC on both sides. The exact cutoff frequencies for the filters are yet to be defined.

Distribution plate

All connections have to be distributed to the detectors in the detector box. To this end, a special CuKaCu PCB is currently being drafted. Figure 3.30 shows the current design. Every connection between the distribution plate and cables, as well as between the distribution plate and the CuKaCu-pieces in the detector modules, is done with SFCs.

Particle Shield Bypass

All cables will be thermalized on the MC plate and then routed to the detector box below the particle shield. However, any contact with the warmer particle shield must be

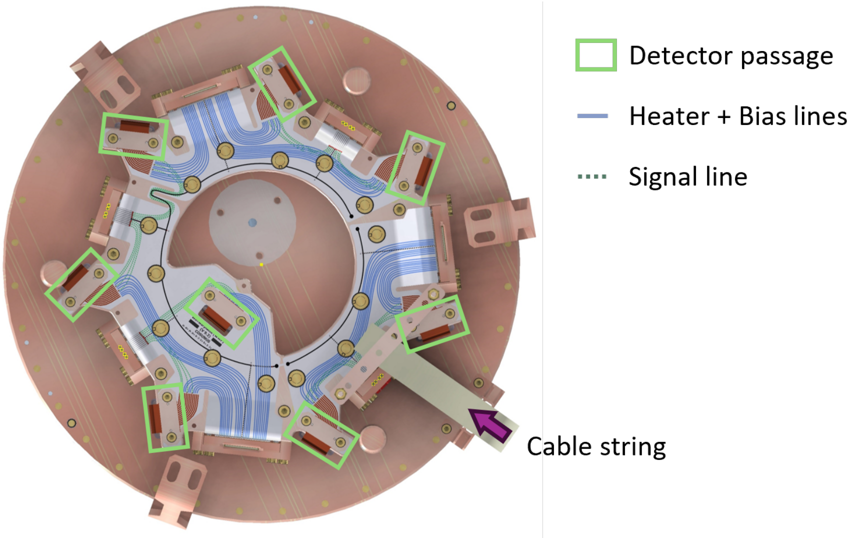

Figure 3.30: Distribution plate to the detectors. One cabling segment is guided to one detector box, where the cables are split and distributed to the detector modules on the inside. SFCs are used for the connections between single parts.

avoided. To ensure this, a Cu-cable duct thermalized to the MC is foreseen. The cables are routed through the duct so that contact with the particle shield is impossible. Up to six plastic screws with low thermal conductance can ensure a bad heat conductance between the particle shield and bypass in case of a touch.

Shunt resistor

For the resistance measurement, a shunt resistor to compare the TES-resistance to is required. Its resistance should be constant on the order of $10\,\mathrm{m\Omega}$ (ideally equal to the resistance to be measured). It can be adjusted to each detector for optimal sensor running conditions. In COSINUS, this is realized with Au thin films on sapphire (Al_2O_3) or Si wafers produced by magnetron sputtering. The wafers are then glued directly to the module. Figure 3.31 shows a drawing of the planned implementation and a shunt prototype.

The shunt has a zebra-like design with a resistive Au thin film and perpendicular stripes made from Al on top. By choosing a combination of Al-stripes for bonded connections, the shunt resistance can be selected differently for each detector on the module itself.

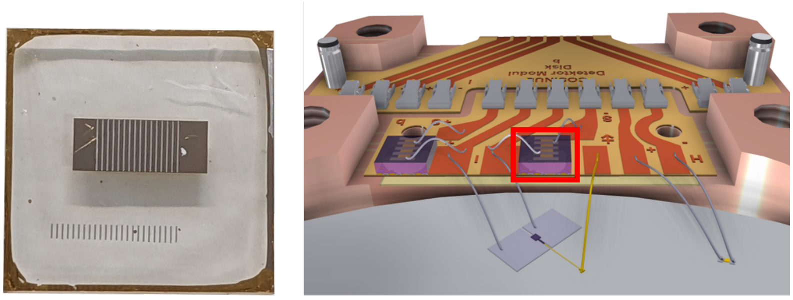

Figure 3.31: Shunt implementation for COSINUS. On the left, a prototype is shown. A thin film of Au provides the resistance, while stripes of Al serve as bonding interface. By choosing two stripes, the shunt resistance can be chosen flexibly. On the right, a CAD of the detector module equipped with shunt resistors is shown.

Detector box

The detector box is not directly part of the cabling but is nevertheless a vital component of the complete concept. The 48 detector channels will be distributed on 24 detector modules with one LD and one PD each. The design of the modules will be described in more detail in chapter 4.

One detector box will fit eight detector modules. For coincidence studies, seven are arranged in a circle, and one is in the middle. Therefore, for the COSINUS design goal, three detector boxes are needed, and one cabling segment will supply one detector box. A drawing of the detector box is shown in figure 3.32.

A single filled detector box is limited to a mass of 10 kg for a total mass of 30 kg, which will be relevant for the passive vibration decoupling system described in chapter 5. Other constraints for the detector box are air-tightness and a valve that opens inside the refrigerator such that the box can be pumped.[18] The reason for that is to avoid degradation of the crystals due to their extreme hygroscopicity.

---

[18] A temperature-dependent valve that opens below 100 K, but above 77 K was developed within the COSINUS project before.

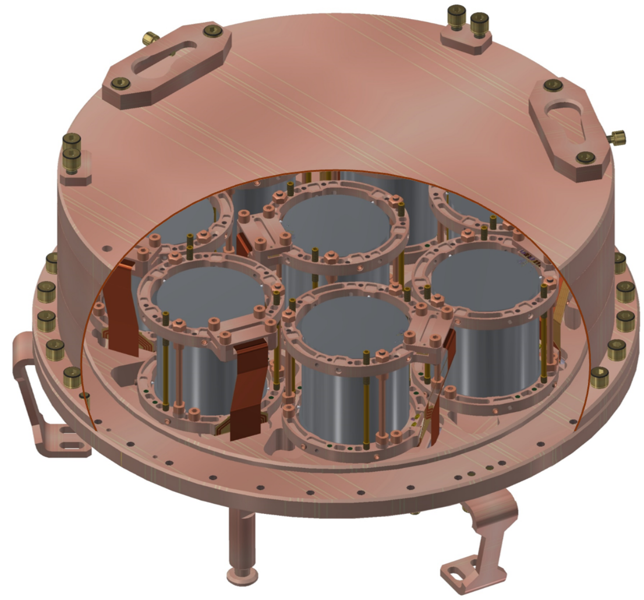

Figure 3.32: COSINUS detector box. One box can contain up to 8 detector modules. For the operation of NaI, the box is vacuum-tight and equipped with a temperature-dependent valve.

Chapter 4

Transition Edge Sensors

COSINUS opted for TES to operate NaI crystals as cryogenic scintillating calorimeters. The expertise and technology for using these thermometers for cryogenic calorimeters have been nurtured by the CRESST experiment and the MPP over many decades. Today, they see widespread use in X-ray astronomy and rare event searches due to their excellent energy resolution up to $\sigma_E = 1\,\mathrm{eV}$ [55]. In DM searches, the most commonly used TES is a thin film made from α-W ($T_c = 15\,\mathrm{mK}$).[1] Typical absorber materials include $CaWO_4$, Al_2O_3, Si or germanium (Ge). In astronomy, large arrays of bilayer-TES (e.g. iridium (Ir)-Au, Ti-Au or Al-Ti) with critical temperatures on the order of 100 mK, coupled to metallic absorbers (e.g. Au), are frequently employed [149].

TES-based detectors are heavily related to the condensed matter properties of the materials in use at cryogenic temperatures. Therefore, the next sections will provide a brief summary of the basic concepts of phonons and superconductivity.

4.1 Phonons

Crystals are solid objects whose constituents are arranged in an ordered lattice. Each atom is subject to intermolecular forces with its neighbors, creating a periodic potential. Within a solid, the momentum and energy of the atoms can be propagated as sound waves. They are described by lattice-dependent dispersion relations, which relate wave vector $\vec{k}$ with frequency ω. A quantum-mechanical treatment introduces a new type of (quasi-)particle, the phonon, a boson, which carries part of the energy and momentum of the sound wave.

The possible phonon modes are given by the aforementioned dispersion relation and strongly depend on position and orientation in the lattice. With more atom species, additional possible modes are added. Figure 4.1 shows the dispersion relation and density of states for phonons in NaI.

The phonon states are occupied in accordance with the Maxwell-Boltzmann distribution. At the Debye temperature Θ_D, all states are occupied. In this framework, the (phononic) heat capacity C is directly related to the density of states as described by the Debye model. This leads to a temperature dependence of $C \propto T^3$.[2]. Therefore, understanding the energy flow within a crystal requires investigating the creation and propagation of phonons.

---

[1] W thin films are known to exist in two phases, the stable α-W and a metastable β-W.

[2] For metals, a linear term for the contribution of free electrons is added.

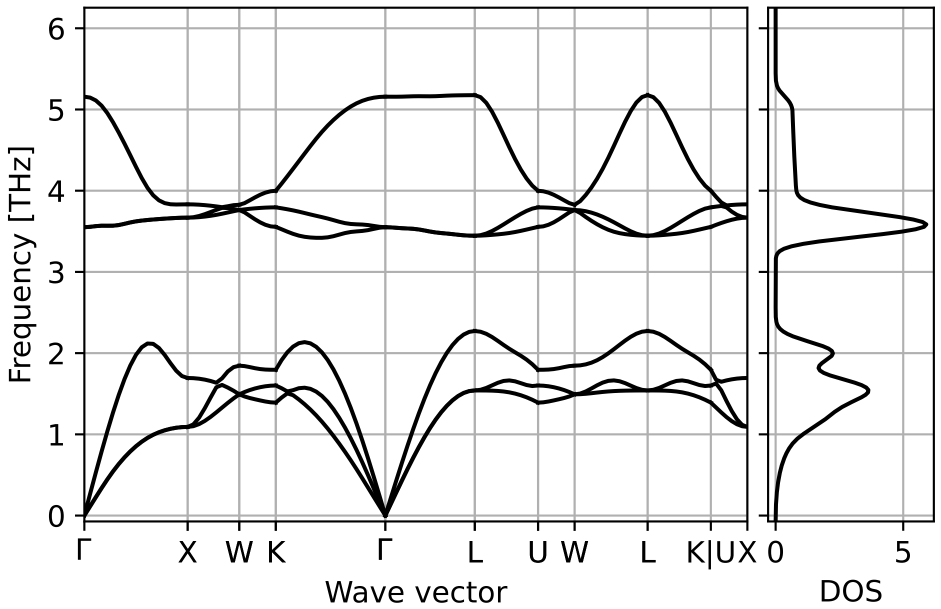

Figure 4.1: Phonon dispersion relation (left) and density of states (DOS, right) for NaI [150, 151]. The phonon dispersion relation shows six possible modes in two bands. The band with lower frequencies corresponds to acoustic phonons and describes a common movement of adjacent atoms. The higher frequencies are populated by optical phonons, where neighboring atoms, here Na and I, move against each other. In the band gap, no states are available.

In a cryogenic detector, we consider three main sources for the creation of phonons:

1. **Particle recoils** off the crystal lattice can create very high-energy optical phonons that quickly decay into acoustic phonons, which subsequently downconvert to phonons with lower frequencies [152].
2. **Applied heating** via a resistive thin film on the substrate heats and stabilizes it at specific temperatures. Microscopically, phonons with a thermal distribution are created via electron-phonon coupling.
3. **Mechanical stress and microfractures** can produce short outbursts of phonons that could be easily mistaken for particle-induced events. Their energy distribution usually follows a power law [153].

The created phonon population will propagate through the crystal and scatter off impurities in the bulk and on surfaces. With each scattering, a phonon can downconvert into multiple phonons with smaller energies. For a strong signal that is well separable from the thermal background, it is crucial to maximize the lifetime and minimize the collection time of high-energy phonons. The more high-energy phonons a thermometer can collect, the sharper its measured signals are, thus achieving better energy resolution. Therefore, using single crystals with a low number of lattice defects in the bulk, as well as on the surface, is a strict requirement. This can be achieved by polishing the crystal surface, minimizing impurities during production, and carefully handling the crystal to avoid new cracks. Generally, crystals with high Debye temperature are better suited for cryogenic detectors, as they typically feature higher sound speeds and lower heat capacities, leading to faster collection and higher amplitude.

Besides the preparation of the absorber, the choice of the thermometer and its geometry can play a significant role in its performance. By covering more area with the thermometer, phonons can be collected more quickly and with higher efficiency before they down-convert. A simple simulation of the process will be presented in section 4.8.1

4.2 Superconductivity

In 1911, Heike Kamerlingh Onnes discovered superconductivity in Leiden, Netherlands. His research group investigated the electrical resistance of mercury (Hg) at low temperatures and observed an abrupt drop to zero at a temperature of 4.2 K. In general, two major properties differentiate a SC from a normal conductor. It has zero electrical resistance, and it exhibits the Meißner effect, i.e. it behaves like an ideal diamagnet that expels any external magnetic field. In the last century, numerous SCs besides Hg have been discovered, and condensed matter scientists compete to engineer materials with increasingly higher critical temperatures.

SCs are divided into two categories, “type I” and “type II”. Their difference is illustrated in figure 4.2.

A type I SC is characterized by a critical temperature T_C, a critical magnetic field strength H_C, and critical current density j_C. If these parameters are below their critical values, the material is in its superconducting phase, i.e. it exhibits a vanishing resistance and completely expels the magnetic field. Typically, mono-atomic conductors (e.g. Al, Pb, Hg, Ir, W) are type I SCs with transition temperatures below 10 K.

A Type II SC has two critical field strengths, the lower H_{C1} and the higher H_{C2}. Below H_{C1}, the material behaves like a type I SC, and above H_{C2} superconductivity within the material breaks. However, between lower and upper critical field strength, a mixed state, the “Shubnikov phase” exists. In this state, the magnetic field is not completely expelled by the SC, but part of the magnetic flux can penetrate it through flux tubes. According to the Ginzburg-Landau theory, this can be described by vortices of supercurrent around the flux tubes. These vortices generally move through the SC but can be trapped on crystal defects, a phenomenon known as the flux pinning effect. One of the most commonly used type II SC at very low temperatures is Nb-Ti (T_c ∼10 K).

Superconductivity has been successfully described by the London, Ginzburg-Landau, and Bardeen-Cooper-Schrieffer (BCS) theories. The BCS theory is a statistical microscopic theory that introduced cooper pairs to explain both types of SC. It assumes an attractive force between two electrons due to electron-phonon interaction such that they

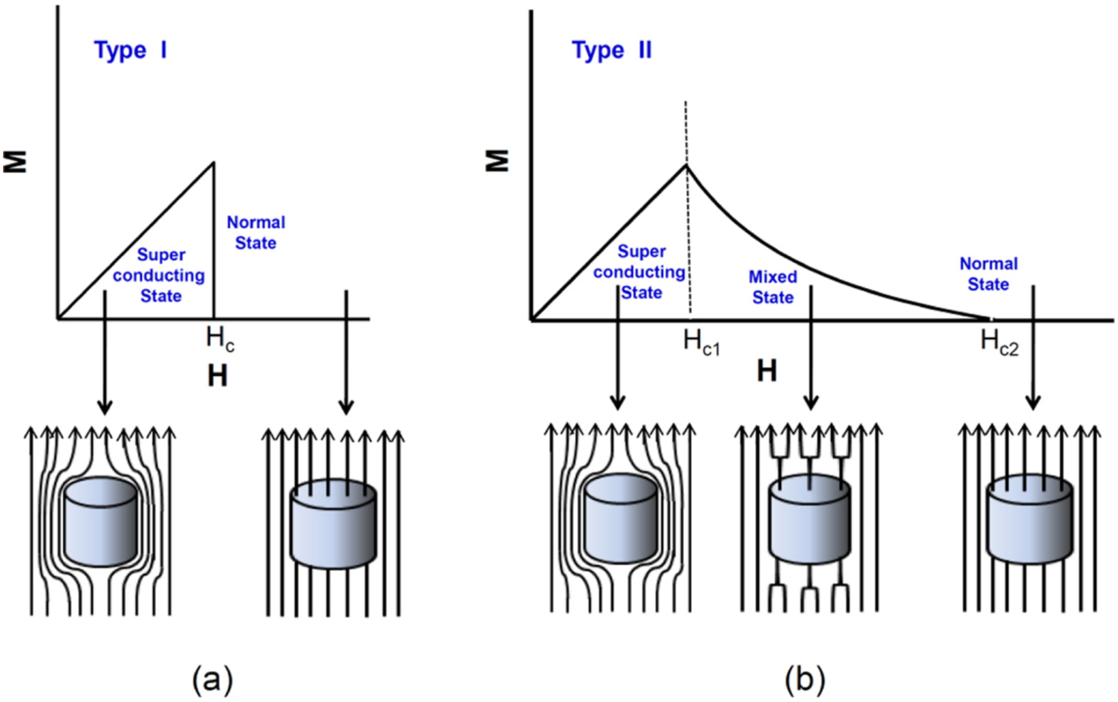

Figure 4.2: Magnetic field response of type I and type II SCs. A type II SC (b) can have a mixed state with partial penetration of the magnetic field, while a type I SC (a) always expels the complete field. Taken from [154].

couple together. Cooper pairs behave like bosons and thus are able to occupy the same ground state below the Fermi energy. Between the ground state and exited states exists an energy gap, which can be interpreted as binding energy per partner. This gap is directly related to the critical temperature T_C. If a Cooper pair is excited due to an energy deposit, it breaks into two quasiparticles that behave like electron-hole pairs. These quasiparticles can diffuse through the SC and eventually recombine again.

In a real SC film, the transition between normal and superconducting state is gradual and has a specific width depending on various film properties. These include geometry, purity, grain size, and mechanical stress within the film, as well as applied current density and magnetic field strength [155].

4.3 TES Working Principle

A TES is a SC thin film operated within its superconducting transition. In this regime, a temperature change on the order of μK leads to a resistance change on the order of mΩ. Thus, if the TES is attached to an absorber, energy depositions can be detected by measuring the change in resistance. The principle is shown in figure 4.3.

In the simplest approximation, the deposited energy ΔE can be related to the tem-

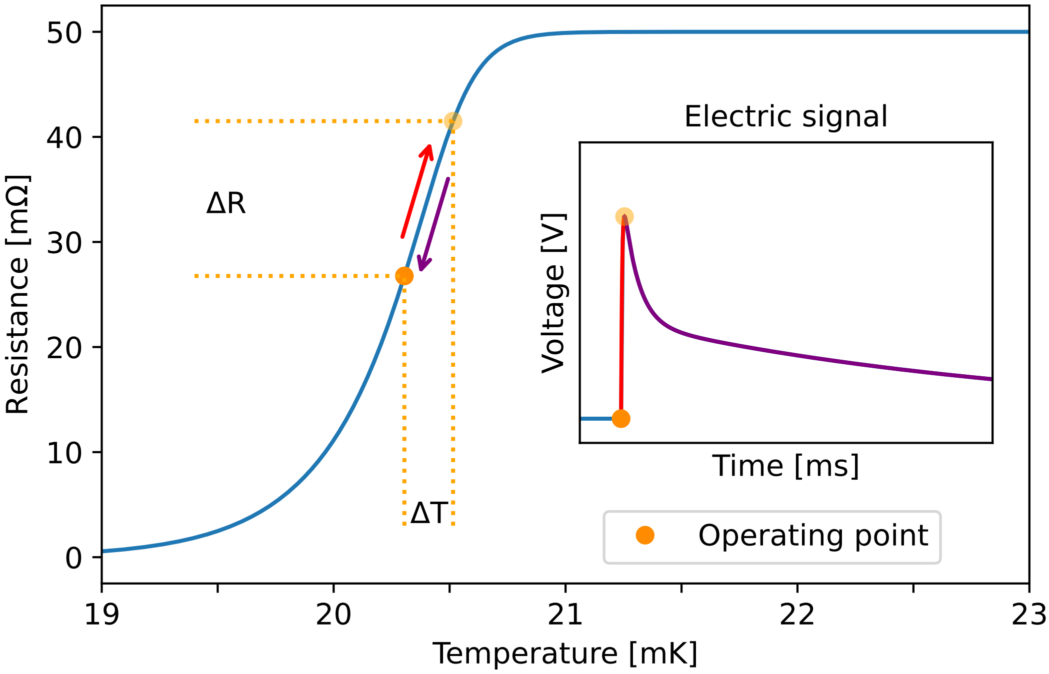

Figure 4.3: TES working principle. The operating point (orange) is typically set in the upper half of the linear range of a superconducting transition. An energy deposition will warm up the TES and change its resistance. The warm-up and subsequent cool-down lead to a characteristic pulse shape, as shown in the insert. The shown temperatures and resistances correspond to typical measured values but do not describe a real measured transition.

perature change ΔT by

$$\Delta E = C\Delta T \tag{4.1}$$

where C is the absorber (plus TES) heat capacity. A more detailed model is described in section 4.5.2. COSINUS uses a TES design that was developed and optimized in the CRESST experiment. Figure 4.4 shows a schematic and a photo of this design.

W is used as TES-film due to its low transition temperature at $T_c = 15\,\text{mK}$. It is flanked by two Al-films that serve as connection points to bias the film with a bias current. At the same time, they serve as phonon collector films that increase the effective area of the thermometer without increasing heat capacity (see also section 4.9). A Au-link connects the film to the heat bath, allowing the detector to return to its operating point. Most of the detectors have a “heater” thin film made of Au on their surface, which allows for the adjustment of the TES-temperature to the optimal operation point within the transition through ohmic heating. Externally injected voltage pulses to the heater allow for measuring and monitoring the detector response.

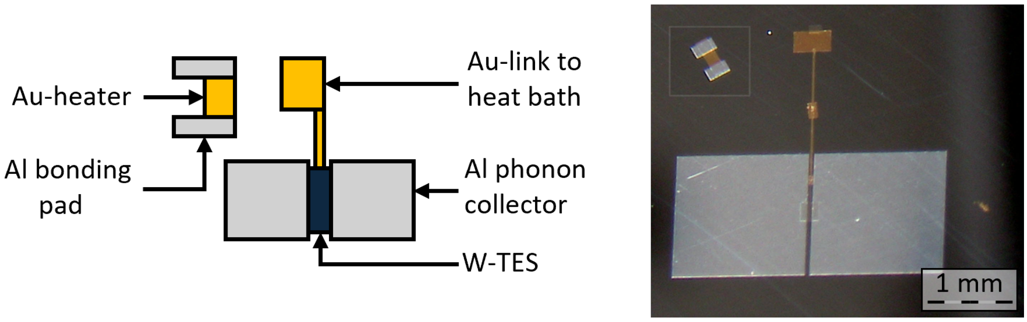

Figure 4.4: Schematic depiction of a TES (left) and a microscope image of a real sensor (right). The TES consists of a W-film flanked by two Al-pads, which are used to apply a constant bias current to the sensor and to collect non-thermal phonons (see also section 4.9). It is connected to the heat bath via a Au-link. A heater film made from Au and flanked by Al-bonding pads is deposited close to the sensor.

4.4 Readout Circuit

To measure small resistance changes, a cryogenic low-noise readout system, based on SQUIDs, is used. There exist two variants of SQUIDs: Radio Frequency (RF) SQUIDs and DC SQUIDs. At low temperatures ($\sim 4\,\mathrm{K}$), the latter are commonly used for their superior sensitivity. A DC SQUID is a superconducting circuit interrupted with two thin isolating spots (“Josephson Junctions”). It can be used as a very precise magnetometer with extremely low noise. In low-temperature calorimetry, such as in COSINUS, they are often used as amplifiers. The readout scheme of the COSINUS detectors is shown in figure 4.5.

The TES is connected in a parallel circuit with a shunt resistor with constant resistance R_s and the SQUID input coil with inductance L. If a constant bias current I_B is applied to the circuit, it is split according to the resistances of both branches:

$$I_L = I_B \frac{R_{TES}}{R_s + R_{TES}}. \tag{4.2}$$

The current flowing through the input coil in the shunt branch creates a magnetic field, which is subsequently measured by the SQUID and monitored by the DAQ. Any change in temperature $\Delta\mathrm{T}$ and subsequent TES-resistance change can then be related to a change in measured current ΔI_L in the shunt branch:

$$\Delta I_L = \frac{\partial I_L}{\partial R_{TES}} \frac{\partial R_{TES}}{\partial T} \Delta T = I_B \frac{R_s R_{TES}}{(R_s + R_{TES})^2} \alpha \Delta T. \tag{4.3}$$

Thereby, the parameter $\alpha = \frac{1}{R_{TES}} \frac{\partial R_{TES}}{\partial T}$ describes the slope of the transition curve. When considering the Johnson noise of the resistors and SQUID amplifier noise, the best signal-to-noise ratio is expected when the resistance of the TES and the resistance of the shunt R_s are approximately the same [156].

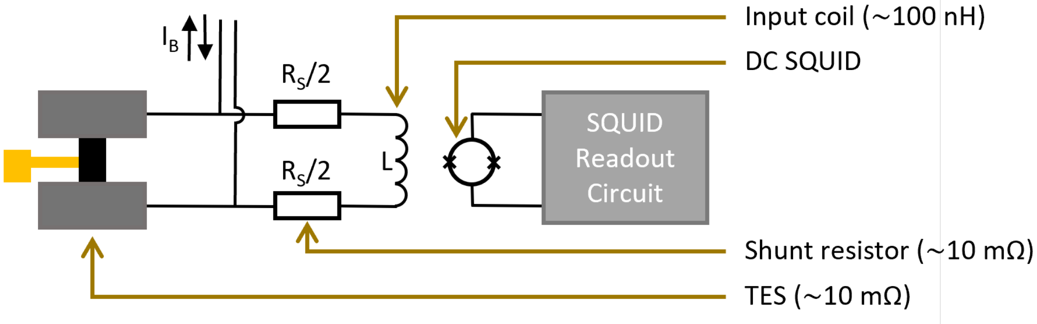

Figure 4.5: Readout circuit of a TES. The TES is connected in parallel to the DC SQUID input coil and symmetric shunt resistors with a constant defined resistance. A bias current is applied to the circuit and splits according to the resistance ratio of both branches. Any current flowing through the input coil leads to a magnetic field change, which is picked up by the SQUID.

Typically, the conversion factor between the current going through the input coil and the voltage measured by the DAQ is on the order of $10\,\mathrm{V}/\mu\mathrm{A}$. It depends on the input coil inductance as well as the SQUID-internal feedback loop details.

4.4.1 Probing the Superconducting Transition

When the resistance, and thus the temperature, of the TES changes, the current splitting in the branches changes accordingly. For low TES resistances, e.g. if it is colder and closer to its superconducting state, more current will go through the TES branch and less through the SQUID branch. As a result, a smaller response is measured.

The transition curve can be probed by sending current steps to the circuit and comparing high and low voltage states.[3] The difference between both states corresponds to a fixed point of the transition curve. A superconducting TES corresponds to a step height of close to zero[4], where almost all of the current flows to the TES and almost no signal is picked up by the SQUID. Figure 4.6 shows examples of two types of transition measurements commonly done in COSINUS: heater sweeps and MC sweeps.

In heater sweeps, the ohmic heater, located directly on the absorber (or wafer) near the TES, is utilized. Steps with different bias currents are sent and plotted against the voltage input into the heater. This allows one to find the optimal operating point, meaning bias current and heater input, for a detector with a given transition shape.[5]

In MC sweeps, small current steps (conventionally 100 nA) are sent. The MC is continuously ramped up (or down) slowly, and the step sizes can be plotted against the

---

[3] For systematics control, the step is sent symmetrically around zero.

[4] Not exactly zero due to possible residual resistances (e.g. contact resistances).

[5] A TES-transition can have features such as kinks leading to different sensitivities in different possible operating points.

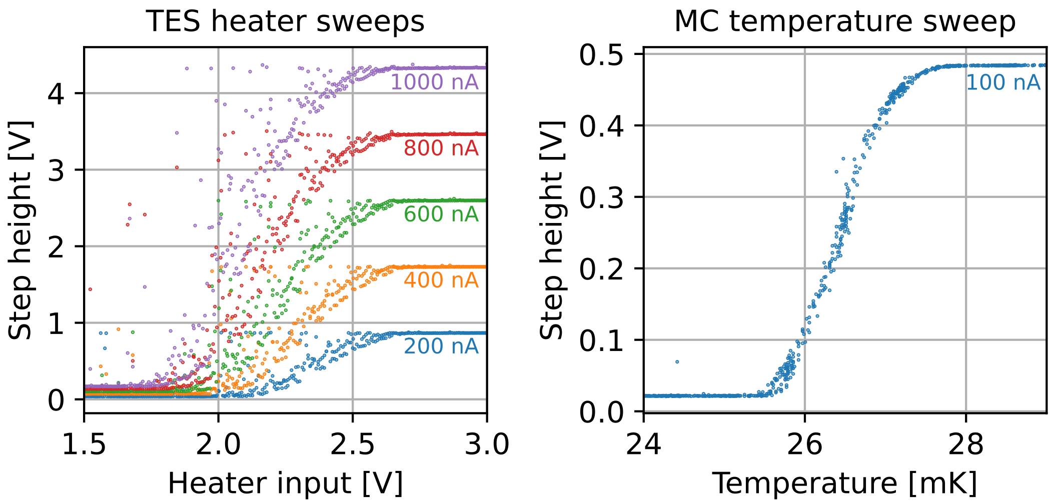

Figure 4.6: Transition measurements in COSINUS. On the left, a transition is probed with respect to the TES heater current for different bias currents (200 nA, 400 nA, 600 nA, 800 nA and 1 μA). On the right, a transition with respect to the bath temperature is shown (the bias used is 100 nA). The main source of deviating readings are particle interactions during the measurement. The step height can be converted linearly to TES resistance.

temperature. These sweeps are done to probe the transition temperature and shape of the transition curve. Ideally, it lies at low temperatures (<30 mK) and has a steep slope (<1 mK width) to achieve high sensitivity. For an accurate measurement, a well-calibrated thermometer close to the sensor is required. In the examples shown in figure 4.6, a ruthenium dioxide (RuO_2)-thermometer by Bluefors [157], calibrated with a noise thermometer, was used.

Most transition measurements exhibit a hysteresis, depending on whether the transition is probed from warm to cold or cold to warm. This occurs due to the self-heating of the TES from the bias flowing through it. When the TES is cold and superconducting, it is not heated by resistive heating, thus staying superconducting for longer. However, when the TES is "warm", thus resistive, the TES is heated by its own bias current and requires more cooling to reach the transition temperature [158]. Another known source for hysteresis is the different couplings of the TES and RuO_2-thermometer to the heat bath. If the TES is coupled less strongly, it takes longer to cool down and lag behind the thermometer readings and vice versa. Thus, a systematically lower or higher transition temperature would be measured. However, this effect can be reduced by slowing the temperature sweeping speed.

4.5 COSINUS Detector Design

To provide a model-independent cross-check of DAMA/LIBRA, COSINUS needs to use NaI as absorber material. NaI is a salt widely used in particle detectors for its scintillating properties. Its important physical properties are listed in table 4.1.

Density	3.67 g/cm^3
Melting point	661°C
Specific heat capacity	52.1 J (mol K)$^{-1}$
Electronic band gap	5.89 eV[6]
Emission peak wavelength	415 nm (Tl-doped) 310 nm (pure)

Table 4.1: Properties of NaI [159, 119, 160].

Compared to “conventionally” used materials for low-temperature detectors (e.g. Al_2O_3, Si), NaI is extraordinarily soft with a hardness of 2 on the Mohs scale [161]. This makes it very delicate to handle, and the simplest handling steps can introduce scratches and cracks. Furthermore, due to its extreme hygroscopicity, a ten-minute exposure of a crystal to humid air (>100 ppm) can lead to a complete degradation of the surface. This degradation can significantly reduce phonon lifetimes as well as scintillation yield. To conserve the quality of the crystals, they always need to be handled in a dry atmosphere using specialized equipment, such as a nitrogen (N_2)-flooded glove box. Figure 4.7 shows photos of NaI crystals used by COSINUS.

In a classical “CRESST-like” TES-based detector, the sensor would be deposited directly on the absorber by evaporation of multiple thin films (silicon dioxide (SiO_2), W, Al, Au). However, the temperatures reached during this deposition process are much higher than the melting point of NaI, which excludes this option. A new method to read out phonon signals from NaI was developed and optimized by COSINUS. Many R&D-detectors were built with different materials, and models were constructed and tested to describe their pulse shapes.

4.5.1 Thermal Model for TES-based Detectors

For the optimization of a detector, it is crucial to understand its signal formation. A thermal model describing the pulse shape of TES-based detectors was published in [162] in 1995 and has been successfully used to describe signals in the CRESST experiment ever since. In the following, this basic thermal model will be summarized. Figure 4.8 shows a scheme with the relevant components.

The system consists of a heat bath (delivered by the refrigerator), the phononic system of the absorber, and the phononic, as well as the electronic system of the thermometer. Absorber and electronic system of the thermometer are coupled to the heat bath via the

---

[6] The reported literature values for the electronic band gap energy vary. The one in this table is the most commonly cited number.

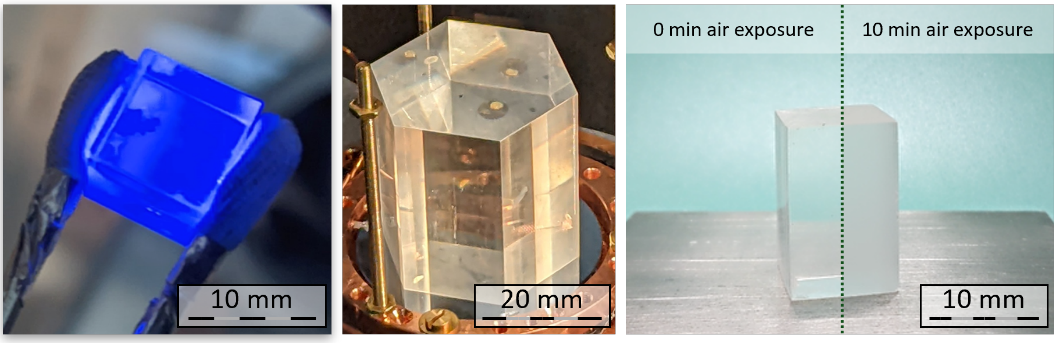

Figure 4.7: NaI crystals used in COSINUS. The left photo demonstrates the scintillation properties (blue light emission) of NaI(Tl) with a (10x10x10) mm^3 crystal. In the middle, the largest crystal size in consideration for COSINUS is shown (hexagonal with a side length of 18 mm and height of 38 mm for a mass of ~90 g). The right photo shows a comparison of a (20x10x10) mm^3 crystal before (left) and after (right) a 10 min exposure to humid air. The crystal's surface degraded from a polished transparent surface and became opaque.

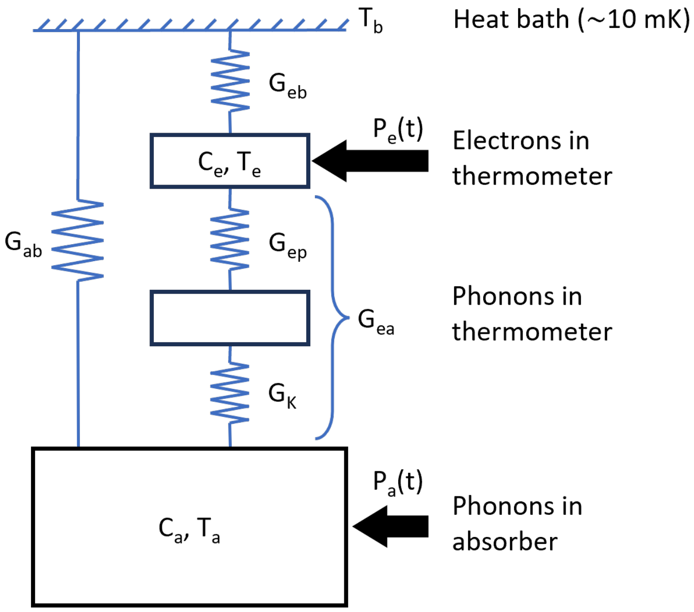

Figure 4.8: Thermal components for a system consisting of a TES and an absorber. Redrawn from [162].

thermal conductances G_{ab} and G_{eb}, respectively (due to the absorber holding structure and thermal link of the TES). Phonons of the absorber can cross the boundary to the thermometer film (described by the Kapitza coupling G_K) and couple to phonons in the thermometer. Within the thermometer, electron-phonon coupling G_{ep} leads to the

C_a	absorber heat capacity
C_e	electronic heat capacity
T_a	absorber temperature
T_e	thermometer temperature
G_{eb}	thermal coupling (TES-bath)
G_{ab}	thermal coupling (absorber-bath)
G_K	Kapitza conductance
G_{ep}	electron-phonon coupling in thermometer
P_e	power input in thermometer
P_a	power input in absorber

Table 4.2: Parameters for the thermal system as shown in figure 4.8.

heating of the electronic system. Each system is characterized by its temperature T_j and heat capacity C_j, where $j \in \{a, e\}$. G_{ea} effectively describes an indirect thermal coupling of absorber phonons and thermometer electrons. The power inputs into either system are denoted as P_e and P_a. Equations 4.4 and 4.5 describe the relations in the complete system; the parameters are listed in table 4.2.

$$C_e \frac{dT_e}{dt} + (T_e - T_a)G_{ea} + (T_e - T_b)G_{eb} = P_e(t) \tag{4.4}$$

$$C_a \frac{dT_a}{dt} + (T_a - T_e)G_{ea} + (T_a - T_b)G_{ab} = P_a(t) \tag{4.5}$$

To solve the equations, it is assumed that, on the scale of the signal, the change of physical parameters with temperature (ΔT$\sim \mathcal{O}(\mu$K)) are negligible. Thus, all heat capacities and conductivities are treated as constants.

For the power input, the following procedure is assumed: A particle recoil induces high-energy/high-frequency phonons, which fill up the entire absorber after a short randomization time (on the order of ns). From the initial phonon population, a fraction $(1-\epsilon)$ thermalizes in the absorber due to crystal defects in the bulk and on the surface, while the rest enter the thermometer and thermalizes there. This process is governed by three time constants: the thermalization time in the crystal $\tau_{crystal}$, the thermalization time in the thermometer film τ_{film} and the combined thermalization time τ_n, which is defined as $(\frac{1}{\tau_{film}} + \frac{1}{\tau_{crystal}})^{-1}$. The fraction ϵ can then be expressed as $\epsilon = \frac{\tau_{crystal}}{\tau_{crystal}+\tau_{film}}$.

Based on this, the power inputs can be defined as[7]

$$P_e(t) = \Theta(t) P_0 e^{-t/\tau_n} \tag{4.6}$$

and

---

[7] This assumes that the only heating is done by the particle recoil. In reality, there is another heat contribution by an artificial heater source to keep the TES in its operation point, independent of the heat bath.

$$P_a(t) = \frac{1-\epsilon}{\epsilon} P_e(t), \tag{4.7}$$

where the power P_0 is given by $\frac{\epsilon \Delta E}{\tau_n}$, with ΔE being the energy deposited during the particle recoil into the absorber phonon system.

One solution to this system is a combination of exponential functions:

$$\Delta T_e(t) = \Theta(t)[A_n(e^{-t/\tau_n} - e^{-t/\tau_{in}}) + A_t(e^{-t/\tau_t} - e^{-t/\tau_n})]. \tag{4.8}$$

τ_n is the aforementioned time constant for non-thermal phonons thermalizing in the thermometer film, while τ_{in} and τ_t are time constants that can be interpreted as the relaxation time of the thermometer and relaxation time of the absorber, respectively. They are dependent on the heat capacities and thermal couplings in the system.

The term with A_n is henceforth called "non-thermal component" and describes the high-energy phonons reaching the thermometer and thermalizing there. A_t is the amplitude of the "thermal component", which describes the phonons thermalizing in the absorber and subsequently reaching the thermometer as a large, lower energetic population. Both amplitudes are strongly dependent on the thermal parameters and time constants (with $s_i = \frac{1}{\tau_i}$), which depend on the thermal parameters as well.

$$A_n = -\frac{P_0(s_{in} - (G_{ab}/C_a))}{\epsilon(s_{in} - s_t)(s_{in} - s_n)}\left(\frac{s_t - (G_{ab}/C_a)}{G_{eb} - (C_e/C_a)G_{ab}} - \frac{\epsilon}{C_e}\right) \tag{4.9}$$

$$A_t = -\frac{P_0(s_t - (G_{ab}/C_a))}{\epsilon(s_t - s_{in})(s_t - s_n)}\left(\frac{s_{in} - (G_{ab}/C_a)}{G_{eb} - (C_e/C_a)G_{ab}} - \frac{\epsilon}{C_e}\right) \tag{4.10}$$

One example of a pulse that can be described with this model is shown in figure 4.9. For many detector materials, the heat capacity and conductivities at mK temperatures have not been measured and can only be estimated theoretically or from pulse fits using this model. Furthermore, the time constants $\tau_{crystal}$ and τ_{film} can vary depending on the production quality of the detector, e.g. in a non-polished crystal, the phonon down-conversion on lattice defects at the surface occurs more rapidly[8], leading to a lower $\tau_{crystal}$.

The energy resolution of a detector does not solely depend on the signal amplitude and shape but also on the intrinsic and extrinsic noise of the system. To describe noise contributions from thermal fluctuations or electrical noise in the readout circuit, the thermal model can be expanded to account for a readout circuit similar to figure 4.5 by applying Kirchhoff's circuit laws. A third term, which is dependent on the input coil inductivity L, TES-current I_{TES}, shunt resistance R_s, bias current I_B and TES-resistance R_{TES}, is then added to the system of differential equations:

$$-L\frac{dI_L}{dt} + R_s I_B - (R_{TES}(T_e) + R_s)I_f = \Delta U_{noise} \tag{4.11}$$

---

[8] In a simplified view, the phonon is caught at a rough surface and scatters many times in a short time window.

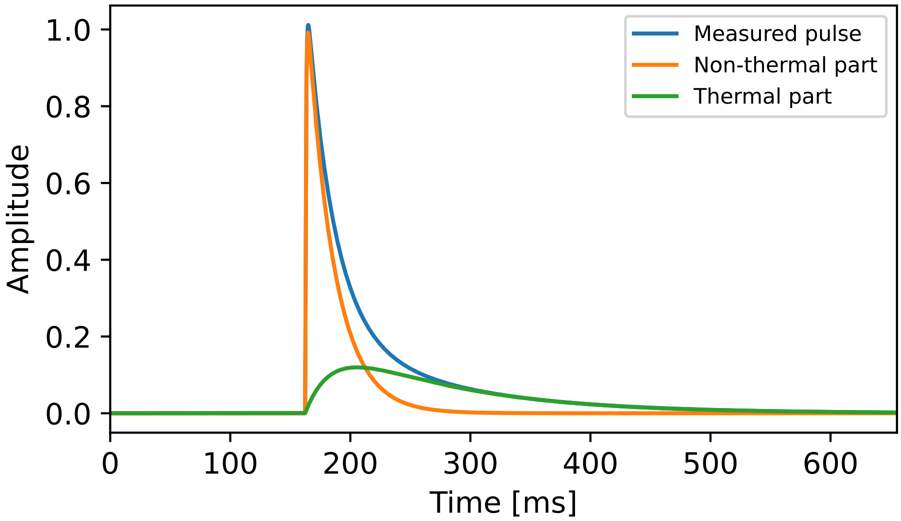

Figure 4.9: Signal for a particle pulse in a cryogenic detector described by the model in [162]. The measured pulse (blue) can be described with a "non-thermal" part (orange), which is related to the phonons thermalizing in the thermometer film, and a "thermal part" (green), which is related to phonons thermalizing in the absorber.

This addition allows the modeling of noise in the system as an additional power input (e.g. Joule heating), input power fluctuations, or current fluctuations. In [163], the system was solved for a simplification, where the absorber is decoupled from the thermometer and major noise contributions were identified:

- **Thermal noise from the absorber** stems from the coupling of the absorber to the heat bath. It generally increases with the operation temperature as well as the heat bath temperature.
- **Electrical Johnson noise** is caused by thermal fluctuations of electrons in a resistor. It increases with temperature as well as resistance.
- **Excess Johnson noise** contains white (flat spectrum) noise that behaves like Johnson noise from unknown or unspecified sources (e.g. from contact resistances).
- **SQUID amplifier noise** is noise added later after amplification of the signals. It depends purely on the specifications of the commercial SQUID-system.
- **1/f noise** is a noise contribution that increases almost linearly for low frequencies and is typically dependent on the readout system and DAQ.
- **Electromagnetic interferences** usually contribute to the noise at very specific frequencies and can be coupled in at various stages.

In the detector design optimization, the signal amplitude should be maximized while minimizing any noise contribution.

4.5.2 Baseline Design

The first COSINUS detector design, initially referred to as "baseline design", consists of the NaI absorber-crystal and a carrier crystal, onto which the TES is deposited. Both crystals would be connected by an interface layer of glue or oil. The successful propagation of phonons through an interface layer connecting the same crystal material has been demonstrated previously by the CRESST experiment [164, 165]. Figure 4.10 shows a schematic representation and photo of the COSINUS baseline design.

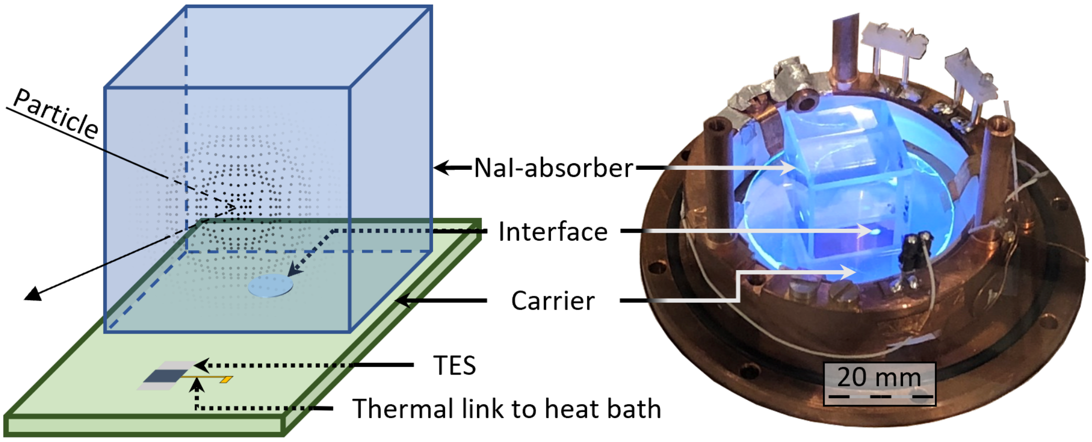

Figure 4.10: Deprecated baseline design for the readout of NaI. The left image shows a schematic of the design. On the right, a photo of an assembled detector is shown. In this design, the absorber is connected to an instrumented carrier via an interface made from glue, grease, or oil.

In this design, a particle recoil in the absorber would create high-energy phonons, which, upon reaching the interface, can either be transmitted to the carrier or reflected back to the absorber while thermalizing. The transmitted phonons would then scatter to the TES and thermalize there, just as described by the model in section 4.5.1.

Multiple underground measurements with CsI- and NaI-absorbers have been published in [166], [167] and [168]. Additional, yet unpublished, measurements have been conducted at a neutron beam facility. The chosen carrier crystal material was cadmium tungstate ($CdWO_4$) due to its good phonon propagation properties (i.e. high Debye temperature). Furthermore, all modules were equipped with LDs to read out the scintillation light emitted by the absorber crystals.

In all detector modules, signals from calibration sources radiating on the absorber were successfully measured, and a pulse shape discrimination between "absorber events" and "carrier events" was possible. Nevertheless, all measurements with this design showed inconsistencies with the prevalent hypotheses:

- Events attributed to the absorber could not be accurately fitted with the two-component model described in section 4.5.1. Instead, a model incorporating a third component with additional amplitude and time constant provided a better fit to the data.
- None of the detectors equipped with a LD showed the population of a nuclear recoil band when exposed to a neutron source. As a result, event-by-event particle discrimination could not be demonstrated for this design.
- Neutron Transmutation Doped (NTD) thermistors are cryogenic thermometers with slower response time than TES. Instead of measuring a non-thermal and thermal component, they measure an integrated signal and thus are more sensitive to the long-lived thermal component. A detector module equipped with a NTD sensor instead of a TES was able to measure a separate nuclear recoil band in NaI.

A possible explanation is that the light emitted by the NaI-absorber in reaction to the recoil is reabsorbed in the carrier crystal, leading to a light-enhanced phonon signal. In this case, the signal of both LD and PD is dominated by absorbed scintillation light. Particle discrimination on an event-by-event basis, where the phonon signal is compared to the scintillation light signal, is hampered, as the detector module would effectively consist of two LDs.

In [169], the pulse shape model was extended to account for the effects of the carrier crystal. The new scheme is shown in figure 4.11. The system of differential equations then extends to:

$$C_e \frac{dT_e}{dt} + (T_e - T_c)G_{ce} + (T_e - T_b)G_{eb} = P_e(t) \tag{4.12}$$

$$C_c \frac{dT_c}{dt} + (T_c - T_e)G_{ce} + (T_c - T_a)G_{ac} + (T_c - T_b)G_{cb} = P_c(t) \tag{4.13}$$

$$C_a \frac{dT_a}{dt} + (T_a - T_c)G_{ac} + (T_a - T_b)G_{ab} = P_a(t). \tag{4.14}$$

The newly introduced parameters are the heat capacity C_c and temperature T_c of the carrier crystal, the corresponding couplings of the components G_{lm} with $l, m \in \{a, c, e, b\}$, and the Kapitza conductances of the interface to carrier $G_{K,ic}$ and absorber $G_{K,ia}$. The power inputs for this system are defined to describe the following procedure:

1. The initial particle recoil creates a non-thermal high-frequency phonon population and excites the crystal to emit scintillation light. A fraction $(1-\eta)$ of the phonons thermalizes in the absorber, while the remaining fraction is transmitted to the carrier.[9] The resulting power input into the absorber is

$$P_a(t) = \frac{1-\eta}{\epsilon\eta} P_0 e^{-t/\tau_n} \tag{4.15}$$

---

[9] This step is similar to the previous model in section 4.5.1.

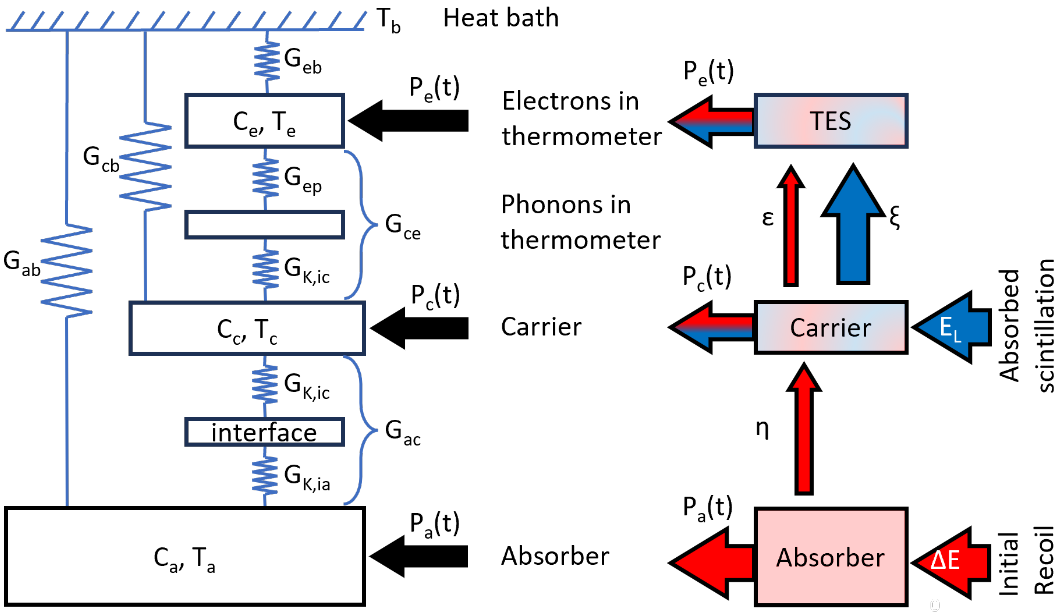

Figure 4.11: On the left: Thermal components for a system with TES, carrier and absorber. Redrawn from [169]. On the right: split of the power components from the different sources into the system.

with $P_0 = \epsilon\eta\frac{\Delta E}{\tau_n}$. Here, τ_n is the time constant for non-thermal phonons that are thermalizing in the thermometer. It consists of the time constants for phonons thermalizing in the absorber τ_a, in the carrier τ_c, and in the thermometer film τ_{film}: $\tau_n = (\frac{1}{\tau_{film}} + \frac{1}{\tau_c} + \frac{1}{\tau_{crystal}})^{-1}$.

2. In the carrier, a fraction $(1-\epsilon)$ of the inherited high-frequency phonons thermalizes as well. Additionally, scintillation photons absorbed in the carrier create an additional non-thermal high-frequency phonon population, of which a fraction $(1-\xi)$ thermalizes in the carrier, leading to the power input

$$P_c(t) = \frac{1-\epsilon}{\epsilon}P_0 e^{-t/\tau_n} + \frac{1-\xi}{\xi}P_L e^{-t/\tau_l}. \tag{4.16}$$

$P_L = \xi\frac{E_\gamma}{\tau_l}$ describes the second phonon population generated by absorbing light (E_γ being the energy absorbed through the scintillation light). The characteristic time constant for these phonons thermalizing in the thermometer film is $\tau_l = (\frac{1}{\tau_{film}} + \frac{1}{\tau_c})^{-1}$.

3. Any non-thermal phonon, which “survives” until reaching the thermometer, can couple to the electronic system of the thermometer film, leading to the power input

$$P_e(t) = P_0 e^{-t/\tau_n} + P_L e^{-t/\tau_l} \tag{4.17}$$

It contains contributions of both the initial phonon signal (P_0) and the absorbed light signal (P_L).

One solution of this system is a combination of six exponential functions, three of which correspond to phonons from the initial recoil signal ("A-terms") and the remaining three to phonons from absorbed light ("B-terms") [169]:

$$\begin{aligned}\Delta T_e(t) = [&A_n(e^{-t/\tau_n} - e^{-t/\tau_{in}}) + A_{t1}(e^{-t/\tau_{t1}} - e^{-t/\tau_n}) + A_{t2}(e^{-t/\tau_{t2}} - e^{-t/\tau_n}) \\ &+ B_l(e^{-t/\tau_l} - e^{-t/\tau_{in}}) + B_{t1}(e^{-t/\tau_{t1}} - e^{-t/\tau_l}) + B_{t2}(e^{-t/\tau_{t2}} - e^{-t/\tau_l})].\end{aligned} \tag{4.18}$$

Both parts consist of three terms, of which two (A_{t1}/B_{t1} and A_{t2}/B_{t2}) describe the thermal components and one (A_n/B_l) represents the non-thermal component. Similar to the model described in section 4.5.1, the time constants τ_{in}, τ_{t1} and τ_{t2} describe the relaxation time of the thermometer and the relaxation times of the absorber and carrier, respectively. With this extension, it is possible to explain why a model with a second thermal component improves the description of the observed events compared to a single thermal component. Figure 4.12 shows a pulse of a detector with the COSINUS-baseline design that can be described with this model.

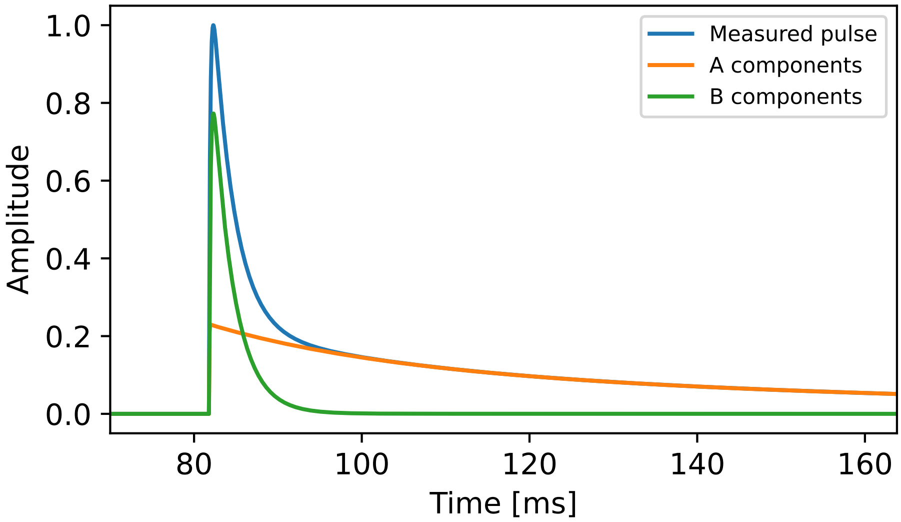

Figure 4.12: Signal for a particle pulse in a detector with the composite baseline design [170]. The measured pulse (blue) can be split into a pulse made of "A-components" (orange), which is related to the phonons in the absorber, and a pulse made of "B-components" (green), which is related to light absorbed in the carrier.

Since for COSINUS particle discrimination and a good energy resolution for nuclear recoils are essential, the composite baseline design was deemed unsuitable for this project. A new method to read out the heat signal of NaI had to be found.

4.5.3 remoTES

The current COSINUS detector module design utilizes the remoTES, a novel method to couple the TES to the absorber. This design was initially proposed in the preprint [171]. Figure 4.13 shows a schematic of the design as implemented by COSINUS.

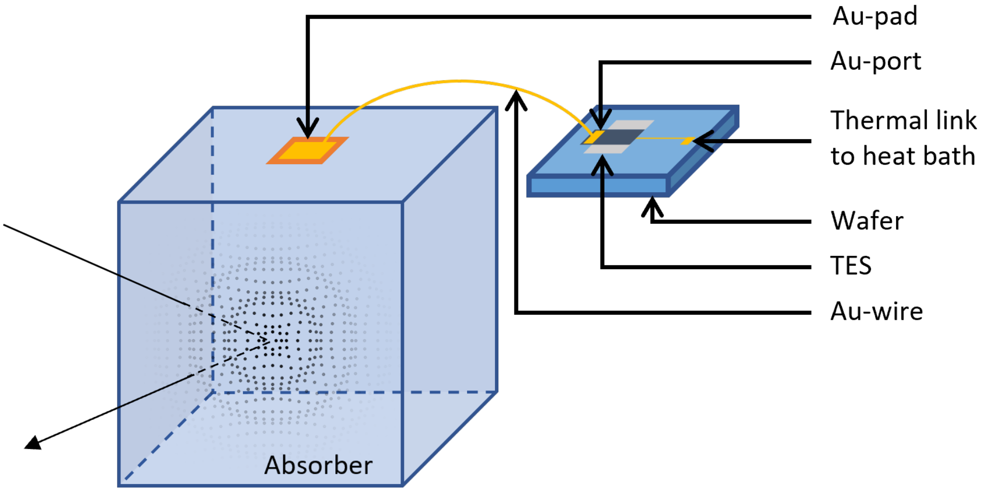

Figure 4.13: Schematic of the remoTES-design. The TES is deposited separately from the absorber on a wafer. The signal is transmitted via a Au-link consisting of Au-pad on the absorber, Au-bond wire, and Au-port on the TES.

Unlike the prior baseline design, this setup does not include a carrier crystal. Instead, the TES is deposited on a completely separate wafer and connected to the absorber via a Au-link. The link consists of a Au-pad on the absorber, a Au-bond wire, and a Au-port on the TES. In contrast to the carrier in the baseline design, the wafer ideally does not contribute to the signal generation in the sensor. The principle for signal propagation is shown in figure 4.14.

The initial particle recoil creates a high-energy phonon population, which scatters through the crystal and eventually reaches the Au-pad. In the Au-pad, the phonons interact with electrons via electron-phonon coupling. The electronic heat conductance of the Au leads then to a subsequent heating of the electronic system of the TES and thus a measurable signal. A similar design is currently being explored by the AMoRE-II [172] and RICOCHET [173] experiments.

The remoTES design offers several promising advantages, not only for COSINUS, but possibly for cryogenic calorimeters in general:

- Since the absorber crystal itself is spared from most fabrication steps, its quality and purity can be preserved more easily.
- The production of TES is currently not very reproducible, and both the transition shape and the transition temperature can vary significantly between batches. The

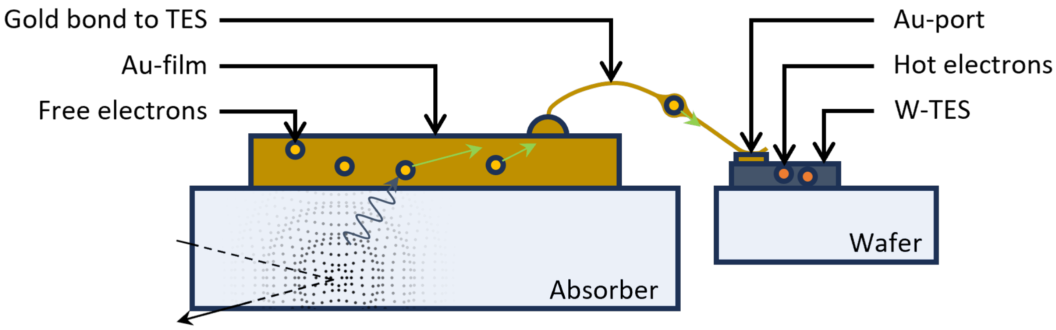

Figure 4.14: Signal creation in the remoTES design. A high-energy phonon population is created following a particle recoil. The phonons can enter the Au-film and transmit energy to the electrons via electron-phonon coupling. Hot electrons can diffuse through the Au-wire and Au-port and interact with the electronic system of the TES.

remoTES allows for the production of larger batches of TES with similar conditions because of its possibility for "chip"-like fabrication. As the remoTES-wafer is not designed to be an instrumented part, the material can be freely chosen, and the fabrication details can be optimized for one material and one geometry.

- Since the TES can be reused for different absorbers, it is possible to exclude TES-related systematic uncertainties in detector studies.
- The TES is mounted separately from the absorber, which provides easier access to the absorber faces. This can be particularly beneficial for light collection or for implementing an α-particle veto.

4.6 remoTES Research

Since the first test of a remoTES in 2021, the design has been tested with different materials and production methods. Most of the measurements reported here were taken in an above-ground wet ^{3}He/^{4}He-dilution refrigerator provided by the CRESST group of the MPP.[10] The refrigerator reached base temperatures below 10 mK and was equipped with four SQUIDs manufactured by Applied Physics Systems (APS) [174]. Figure 4.15 shows a photograph of the refrigerator.

For data taking and detector stabilization, two independent DAQs were available: a VME-based hardware-triggered DAQ with four simultaneous channel readouts, and a continuous DAQ with two simultaneous channel readouts.

The detector properties to be optimized in COSINUS are the energy threshold and energy resolution for events close to the threshold, also called "baseline resolution".

---

[10] At the time of the measurement still located in Munich.

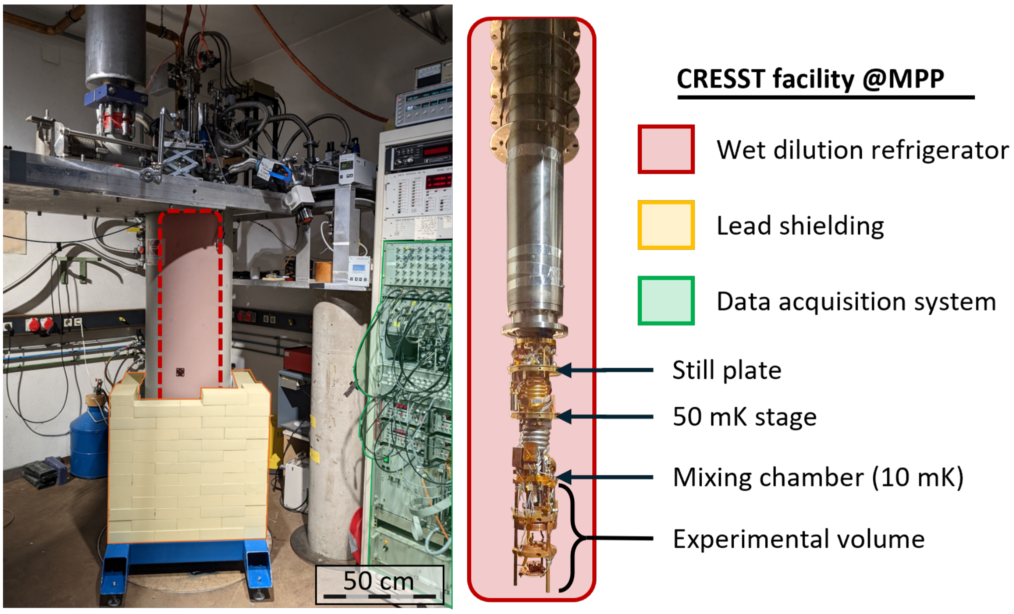

Figure 4.15: Photograph of the "Cryo2" test facility of the CRESST group at MPP.

Classically, a good resolution is directly related to a good Signal-to-Noise Ratio (SNR). In the detector analysis, the method that optimizes SNR and achieves the best performance for amplitude reconstruction involves an "Optimal Filter (OF)".[11] The OF is constructed by comparing the spectral shape of the signals of interest and the Noise Power Spectrum (NPS). A filtered data stream features similar pulse heights but lower noise than the raw data.

To extract the required information, for each signal shape that is found in the data, a "Standard EVent (SEV)" is created. A SEV is an average of multiple real events with similar pulse shapes scaled to an amplitude of 1. It represents an artifact- and noise-free signal, which can ideally be described by one of the pulse shape models. Similarly, NPS are generated from the data over the entire data-taking time. The principle of SEV, NPS, and the resulting filter is shown in figure 4.16.

This method is reliable for measurements where the noise conditions and the operating point are stable and where the pulse height of a signal is well below the truncation limit of the sensor, i.e. where the transition shape of the TES is still linear. If the signals pile up due to a high background rate (or the measurement conditions change), triggered events are not described well by one (SEV-like) pulse on top of noise (described by the NPS) anymore. Instead, the pulses sit on the decaying tail of previous pulses. In this case, a template fit can be applied for a more robust estimate by fitting the SEV superimposed on a polynomial baseline description of the data. The standard analysis chain from raw data to an energy resolution estimation for a detector module is described in appendix B.

---

[11] Another prominent name for the same principle is "matched filter".

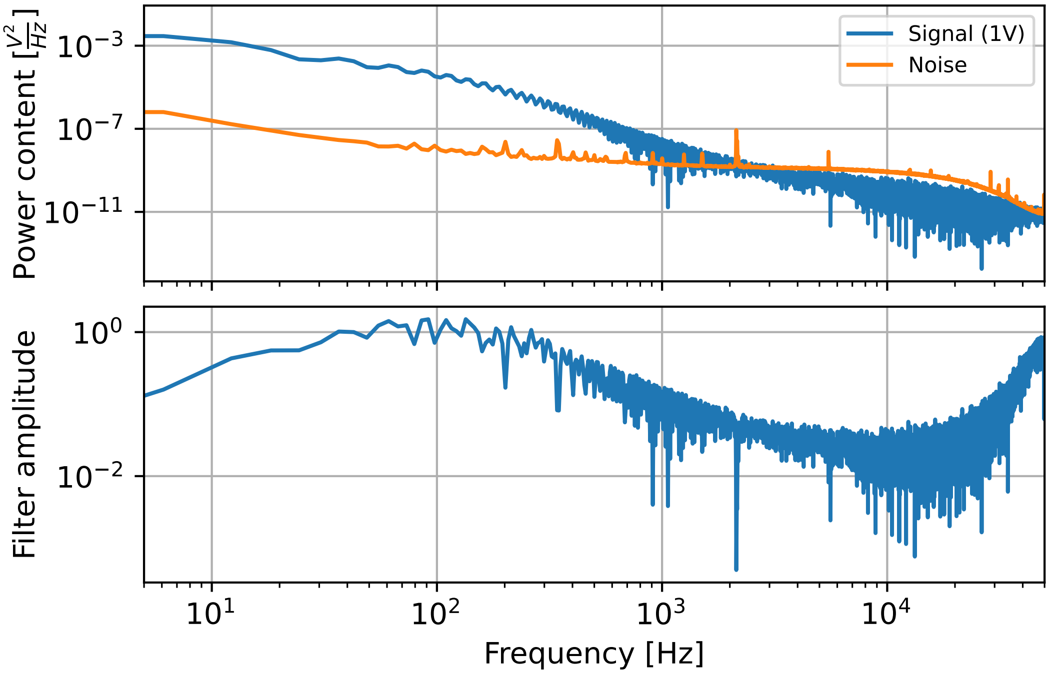

Figure 4.16: Creation of an OF. The OF is built to optimize SNR depending on the spectral shape of signal and noise power. In this example, the best SNR is reached around 100 Hz, and other frequencies are suppressed.

The typical shape of a NPS shows a strong $1/f$ component, which decreases for higher frequencies until it is dominated by white noise (constant power per frequency). Single frequencies can be amplified by electromagnetic interferences, leading to peaks on the NPS-baseline. For high frequencies, the NPS is suppressed by a built-in anti-aliasing filter. Its power content depends on the readout details (e.g. SQUID-model and shunt resistance), the detector details (TES-film resistance and transition shape), as well as the operation temperature.

The signals, as described by the model in section 4.5.1, consist of a short-lived non-thermal component and a long-lived thermal component. Their signal power is concentrated in the low-frequency region, typically well below 100 Hz. However, as seen in the OF, the frequencies contributing most to the resolution are not necessarily those with the highest signal power.

Typically, signals with a strong non-thermal component perform better than those with a stronger thermal component due to their higher bandwidth. Another benefit is the shorter decay time, which reduces the pile-up of events. In above-ground measurements, pile-up is a major challenge, as it impedes the creation of clean SEV and NPS.

The milestones of the remoTES design are listed in the following subsections. Most of the measurements were previously published in [175, 176, 4, 177]. Table 4.3 gives a short overview of the remoTES-detectors described in this work.

Published in	Target material	Energy resolution [eV]	Section
[175]	Si	87.8 ± 5.6	4.6.1
[175]	TeO_2	193.5 ± 3.1 / 154 ± 3[12]	4.6.1 / 4.7.1
[176]	NaI	2070 ± 10	4.6.2
[4]	NaI	441 ± 11	4.6.2
-	TeO_2	1470 ± 50	4.7.1
-	TeO_2	310 ± 20	4.7.1
-	TeO_2	450 ± 20	4.7.1
[178]	Si	133 ± 3	4.7.2
[178, 177]	Si	167 ± 8	4.7.2
[178, 177]	Si	89 ± 2	4.7.3
[178, 177]	Si	1159 ± 134	4.7.3
[163]	NaI	410	4.7.4

Table 4.3: remoTES-detectors studied in this work.

4.6.1 Proof of Principle

The very first remoTES detectors utilized Si and α-tellurium dioxide (TeO_2) as absorber materials. Si was chosen because it is a well-studied standard material for particle detectors [179, 180], while α-TeO_2 was chosen as an easier-to-handle substitute for NaI with similar heat capacity and phonon band gap. The measurement results were previously published in [175]. Although both detectors employed the remoTES design, their fabrication details differ substantially.

The Si-detector used an absorber with dimensions of (20x10x5) mm^3 and was equipped with a 200 nm thick Au-pad deposited by magnetron sputtering. A single Au-bond wire with 17 μm diameter connected the Au-pad and Au-port at the TES. On the crystal side, the bond wire was glued using a silver-loaded conductive paint of type EM-Tec AG44 from Micro to Nano BV [181], while on TES side it was bonded via ultrasonic wedge bonding.

The α-TeO_2 detector used an absorber of size (20x10x2) mm^3. A Au-foil with a thickness of 400 nm was glued to the crystal with a two-component epoxy glue and contacted with two Au-bonds, each with a diameter of 17 μm and wedge-bonded on both sides.

Both detectors used the same remoTES-wafer (Al_2O_3, dimensions of (10x10x0.4) mm^3), which was equipped with a TES that had a W-film with a thickness of 100 nm and an area of (70x300) μm^2. In both cases, the wafer was pressed onto the Cu-holding structure. For calibration purposes, the absorbers were irradiated with an ^{55}Fe X-ray source ($K_\alpha = 5.89\,\mathrm{keV}$). The TeO_2-detector used an additional source pointed towards the Au-pad on the absorber. Figure 4.17 shows photographs of both detector modules.

With these measurements, it was demonstrated that the remoTES-design can work and energy resolutions of (87.8 ± 5.6) eV and (193.5 ± 3.1) eV were reached for Si and

---

[12] This run was reanalyzed for this thesis. The difference stems from a slightly different analysis procedure.

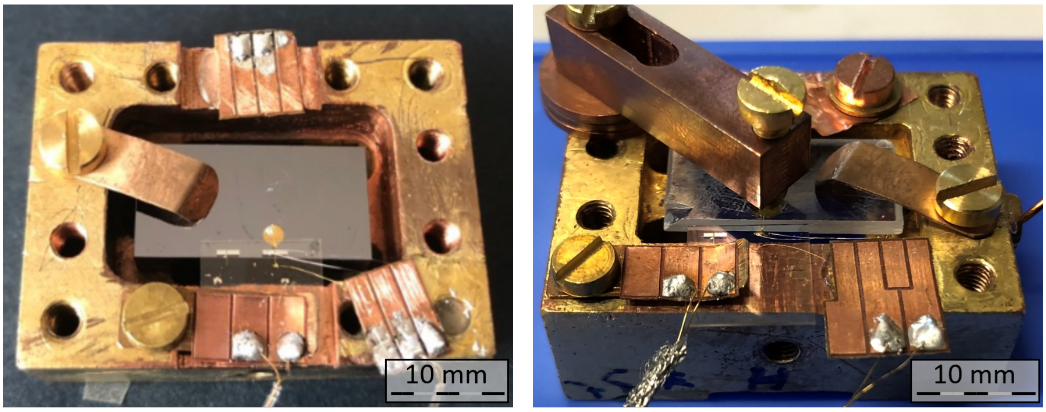

Figure 4.17: Photographs of two remoTES detector modules. On the left: a detector using a Si-absorber. On the right: a detector using a TeO_2-absorber. An additional ^{55}Fe-source at the tip of the central screw irradiates the Au-pad on the TeO_2-absorber.

TeO_2, respectively. Furthermore, the events could be categorized based on their pulse shape into "absorber recoils", "wafer recoils", and "direct gold hits". Their SEVs are shown in figure 4.18.

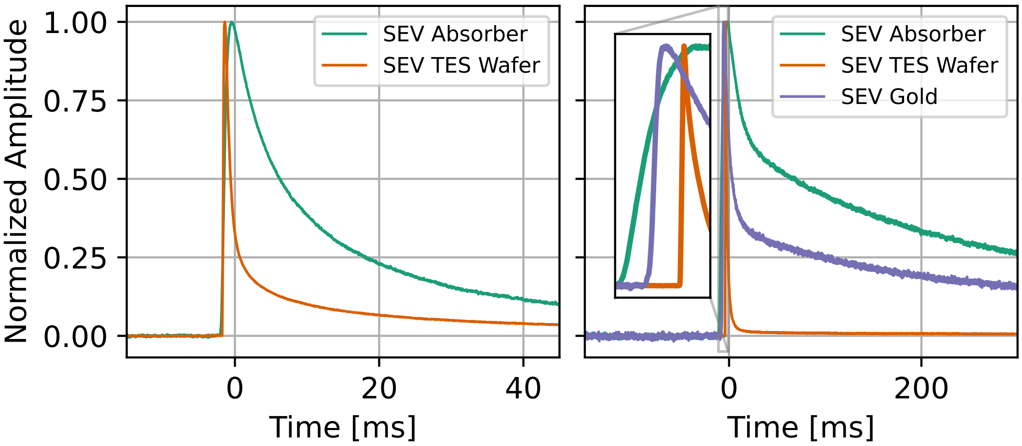

Figure 4.18: SEV for the remoTES detectors. On the left, the SEVs corresponding to events in the absorber and wafer of the Si-remoTES are shown. The right plot shows the SEVs for TeO_2, including a new class corresponding to events in the Au-link. Reprinted from [175].

The allocation of the names to the event classes was done by using the event rate as the main criterion, with pulse shape information serving as the validation criterion. The absorber is the most massive component of the detector, and thus, the class with the most events is expected to be absorber events. The second most frequent event class corresponds to wafer events. Due to the wafer's strong coupling to TES and heat bath and its small size, very fast events are expected and observed. Au-events fall in between, and, due to the overall low volume, they are only visible when the calibration source directly irradiates the Au-pad.

Besides proving the principle, several more aspects relevant to understanding the detector physics can be obtained from these detectors:

- Wafer events are a background for the absorber events of interest. Although they can be separated easily, it is advisable to increase their energy threshold and reduce their rate. In later designs, this was achieved by a stronger coupling of the wafer to the heat bath, as well as by adding additional structures on the wafer to increase its heat capacity.
- Despite a thin layer of glue below the Au-pad, remoTES-events show a fast component, typically attributed to non-thermal phonons thermalizing in the thermometer film (Au-pad in this design). As with the CRESST results on glued crystals in [164, 165], it seems likely that a thin layer of glue does not prevent phonons from reaching the Au-pad and thermalizing there.
- The successful signal transmission via the silver-loaded glue within the Au-link confirms that the heat is conducted via electrons and not via phonons.

4.6.2 Application to NaI

First NaI-remoTES

After successfully demonstrating the remoTES principle, the next step was adapting the design to NaI. All production steps involving the NaI-absorber crystal were carried out in a N_2-flooded glove box. These steps included the deposition/gluing of the Au-pad on the crystal, connecting absorber and TES with a Au-bond wire, as well as mounting the detector in an airtight Cu-housing. The Cu-housing is equipped with a cryogenic valve that opens around 100 K, allowing to pump away the N_2-atmosphere inside the housing during the cooling process.

By the end of 2021, the first successful COSINUS NaI-remoTES was operational. An article reporting on this measurement was published in [176]. The NaI PD consisted of a (10x10x10) mm^3 NaI(Tl)-crystal, equipped with a 4 mm^2 Au-pad of 1 μm thickness. The Au-pad was a foil cut from a uni-crystalline Au-nugget and tempered to provide a good crystal lattice with good conductance. "Epo-Tek 301-2", a two-component epoxy [182], was used to glue the foil on the crystal. Given its long curing time (at least 24 h), the epoxy was only applied approximately 6 h after mixing to prevent any potential damage to the crystal from the glue catalyst.

An additional heater on a (1x3x3) mm^3 Si-wafer was glued to the absorber-crystal. The TES-wafer used in this module was a (20x10x1) mm^3 disk with a (100x407x0.156) $\mu\mathrm{m}^3$ W-film. It was connected to the Au-pad on NaI using two Au-bonds. Figure 4.19 shows a drawing of the PD.

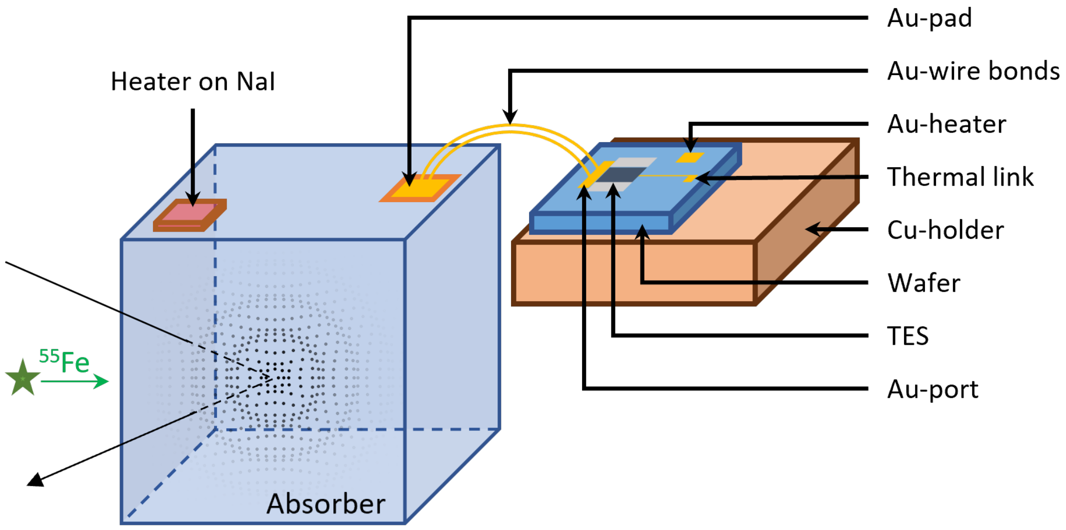

Figure 4.19: RemoTES-design as first applied on the NaI-remoTES. The detector had an additional heater glued to the absorber and was connected to the TES with two Au-bond wires.

The PD described above was operated alongside a LD consisting of a (20x20x0.4) mm^3 Al_2O_3-wafer. To enhance its light absorption properties, the wafer was coated with a thin layer of Si (silicon-on-sapphire (SOS)). Like the PD, the LD was equipped with a TES. All relevant fabrication details can be found in table 4.4.

The entire module, consisting of PD and LD, was calibrated with an external cobalt-57 (^{57}Co)-γ-source and an Am-Be neutron source.[13] The energy baseline resolution was determined to be (2.07 ± 0.01) keV for the PD and (2.02 ± 0.05) keV$_{ee}$[14] for scintillation light measured in the LD. The SEV for absorber events and NPS are shown in figure 4.20.

In comparison to events in the Si- and TeO_2-prototype detectors, a NaI-event features a very large thermal component with lifetimes on the order of seconds. Furthermore, the NaI-remoTES energy resolution is an order of magnitude worse than previous remoTES-detectors. This systematic difference can be related to a multitude of reasons. NaI is a soft material with a small Debye temperature and slow speed of sound, leading to intrinsically longer collection times. Additionally, compared to the previous Si-absorber, the heat capacity of the NaI-absorber is considerably higher.

On the fabrication side, poor detector quality leads to performance losses as well. Due to its softness, the NaI-crystal is prone to surface damages, which can lead to an inefficiency in the collection of non-thermal phonons in the Au-pad before they thermalize due to scattering on lattice defects. This detector module also featured an additional

---

[13] An internal ^{55}Fe-source was mounted but could not be used for calibration since the detector energy threshold was higher than the expected Xray-energy of 5.9 keV.

[14] keV$_{ee}$ means keV electron equivalent (see also chapter 2.4.5)

	Component	Properties
PD	NaI-absorber	$(10\times10\times10)$ mm^3 Mass: 3.7 g
	Au-pad on NaI	Area: 4 mm^2 Thickness: 1 μm
	Two Au-wires	Lengths: (6.7, 10.3) mm Diameter: 17 μm
	W-TES on wafer	Area: (100×407) μm^2 Thickness: 156 nm
	Al_2O_3 wafer	$(10\times20\times1)$ mm^3
	Au-heater	Area: (200×150) μm^2 Thickness: 100 nm
	Au-heater on Si	Area: (3×3) mm^2 Thickness: 1 mm Glued to NaI-absorber
	Thermal link	Resistance (300 K): 82.3 Ω
	Achieved resolution	(2.07 ± 0.01) keV
LD	Al_2O_3 SOS-wafer	$(20\times20\times0.4)$ mm^3
	W-TES on SOS-wafer	Area: (284×423) μm^2 Thickness: 200 nm
	Phonon collectors	Al/W bilayers Area: (526×1027) μm^2 Thickness: 1 μm
	Achieved resolution	(2.02 ± 0.05) keV$_{ee}$

Table 4.4: Summary of PD and LD component properties. Adapted from [176].

Si-based heater, adding parasitic heat capacity to the NaI-absorber.

Besides the first successful operation of a NaI-remoTES, another milestone achieved with this detector was the first indication of particle discrimination on an event-by-event basis in a NaI-detector. When irradiating the detector module with an Am-Be neutron source, an additional event class with low LY was observed. The LY plots are shown in figure 4.21.

The event class, attributed to nuclear recoils, appears quenched over the complete energy range, with the LY decreasing below 150 keV. Its observation demonstrates that particle discrimination on an event-by-event basis with cryogenic NaI-detectors is possible. For energies higher than 150 keV constant QFs of (0.489 ± 0.072) and (0.115 ± 0.013)

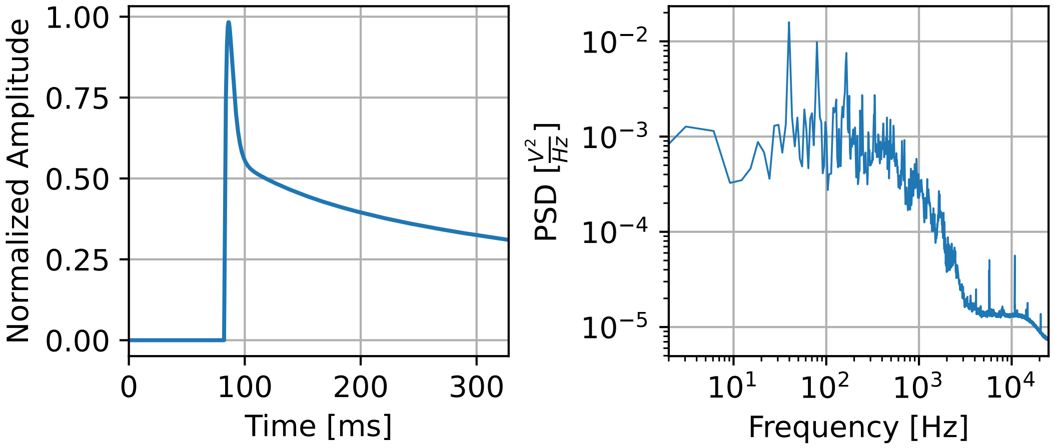

Figure 4.20: SEV and NPS for the PD. Compared to the previous remoTES-detectors, NaI-events feature an extremely long decay time for the thermal component of the signal.

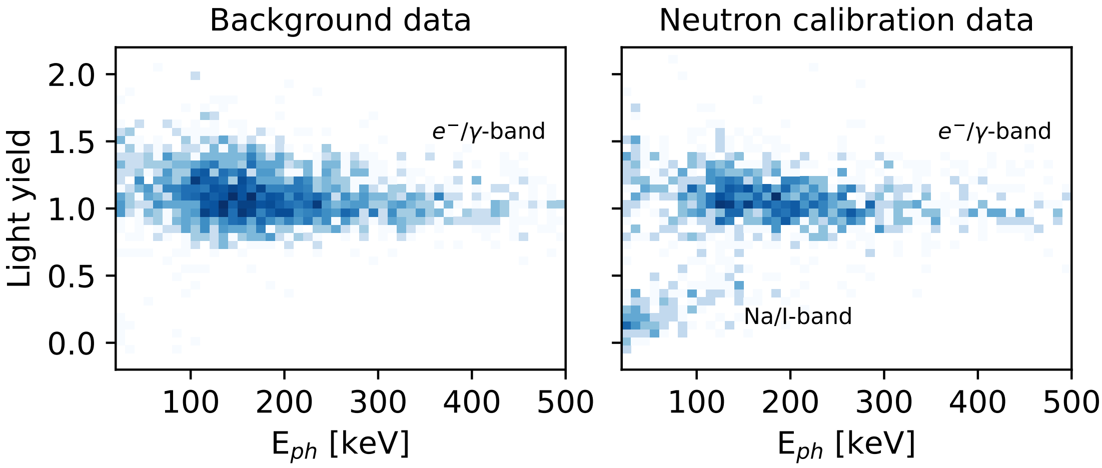

Figure 4.21: Particle discrimination in the first successful NaI-remoTES. On the left, the LY plot without an external calibration source is shown. The right plot shows the LY for a neutron calibration dataset. While in the background dataset, only one event population is visible, for the neutron calibration, a second band attributed to nuclear recoils appears. Both histograms are density plots with logarithmic color scale. Reproduced from [176].

were extracted for Na- and I-recoils, respectively using an empirical band fit. The uncertainties are dominated by the energy resolution of both detectors.

The achieved energy resolutions of both PD and LD were not yet close to the design goal (1 keV) of COSINUS and did not allow for a better characterization of the detector, such as the scintillation efficiency of the crystal. A significant limitation in this measurement was the pile-up of events. While the decay time of PD-events is on the order of seconds, the absolute trigger rate for a 3.7 g NaI-detector is on the order of Hz, leading to a general operation instability and low cut efficiencies.

Proof of the COSINUS-principle

To demonstrate the COSINUS strategy with better energy resolution and less background, in summer 2022, the measurement was repeated in the CRESST test facility deep-underground at LNGS. A detailed report of the measurement is given in [4]. The facility is located in a side tunnel between hall A and hall B with an overburden of 3600 m w.e. It contains a wet dilution refrigerator of type MINIKELVIN 400-TOF from Leiden Cryogenics B.V. surrounded by an external Pb-shield with a thickness of 100 mm. Three SQUIDs by Applied Physics Systems and a VME-based hardware-triggered DAQ allow the operation of up to three TES-based detectors at the same time. For this measurement, an additional continuous DAQ equipped with electronics to operate and read out two detectors was used. It is a prototype version of the DAQ developed by the Institut für Hochenergiephysik der Österreichischen Akademie der Wissenschaften in Vienna, Austria, and is equipped with heater and bias electronics to control the operating point of each sensor.

The detector module consists of a NaI-remoTES PD with a (10x10x10) mm^3 absorber and a beaker-shaped Si-LD. Figure 4.22 shows a drawing of the module; the important detector properties are listed in table 4.5.

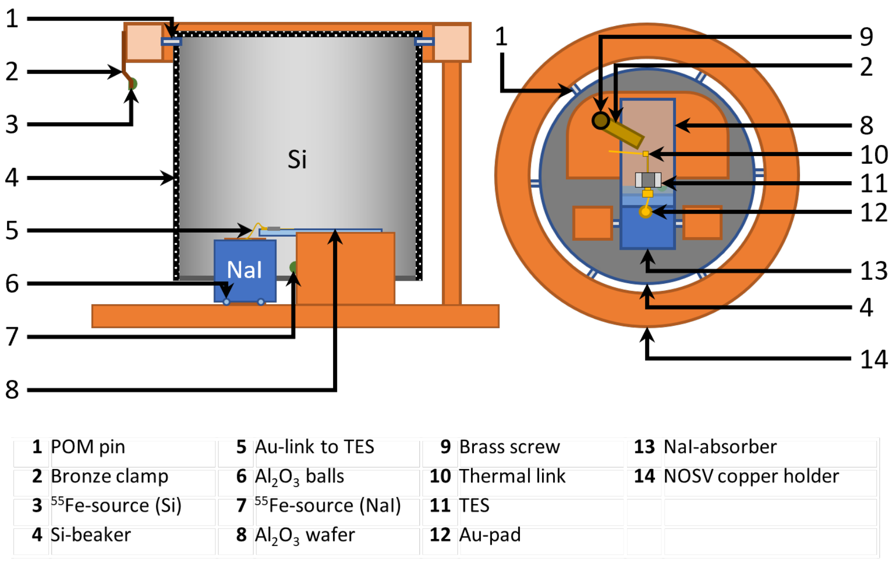

Figure 4.22: Detector design used for the underground measurement in summer 2022. On the left, a cross-sectional view is shown. The right drawing depicts the module from the top (through the beaker). Also published in [4].

	Component	Properties
PD	NaI-absorber	$(10\times10\times10)$ mm^3 Mass: 3.7 g
	Au-pad on NaI	Area: 1.77 mm^2 Thickness: 1 μm
	Au-wire	Length: ~10 mm Diameter: 17 μm
	W-TES on wafer	Area: (100×400) μm^2 Thickness: 156 nm
	Al_2O_3 wafer	$(10\times20\times1)$ mm^3
	Au-heater	Area: (200×150) μm^2 Thickness: 100 nm
	Achieved resolution	(0.441 ± 0.011) keV
LD	Beaker	Height: 40 mm Outer diameter: 40 mm Thickness: 1 mm
	W-TES on Si beaker	Area: (100×400) μm^2 Thickness: 80 nm
	Au-heater on Si-beaker	Area: (200×150) μm^2 Thickness: 100 nm
	Achieved resolution	$(0.988 \pm 0.052)\,\mathrm{keV}_{ee}$

Table 4.5: Summary of PD and LD component properties. Adapted from [4].

The mounting scheme is shown in figure 4.23. It featured a bronze (CuSn)-spring with a mechanical resonance at a few Hz for vibrational decoupling. An internal particle shield made from low-background Pb with a diameter of 90 mm and a thickness of 100 mm was mounted above the module.

The module was calibrated using an internal ^{55}Fe-source source and external ^{57}Co and Am-Be neutron sources. In this measurement, it reached a baseline resolution of (0.441 ± 0.011) keV in the PD and $(0.988 \pm 0.052)\,\mathrm{keV}_{ee}$ in the LD. Figure 4.24 shows the SEV and NPS for this measurement.

The improved PD energy resolution can be mainly attributed to improved noise conditions and a significantly enhanced production quality, i.e. the crystal and Au-pad suffered from less damage during the manufacturing process. Furthermore, the parasitic heat capacity was reduced by only bonding a single Au-wire and omitting the Si-heater. These changes are also reflected in the shorter decay time of the SEV in this measurement. Additionally, by switching to a Si-beaker with better energy resolution, the light collection efficiency and overall performance could also be improved.

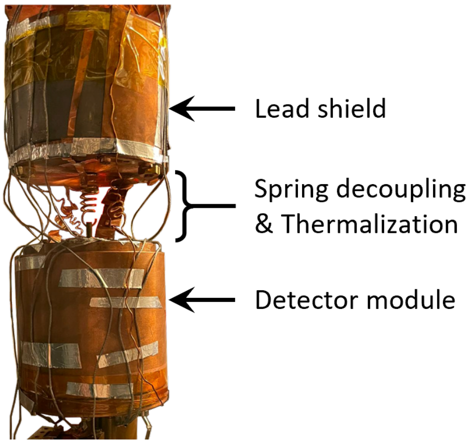

Figure 4.23: Mounting scheme of the NaI-remoTES detector. The detector is mounted on a spring with a resonance frequency of a few Hz. Above the detector, below the MC, a particle radiation shield made from Pb is mounted.

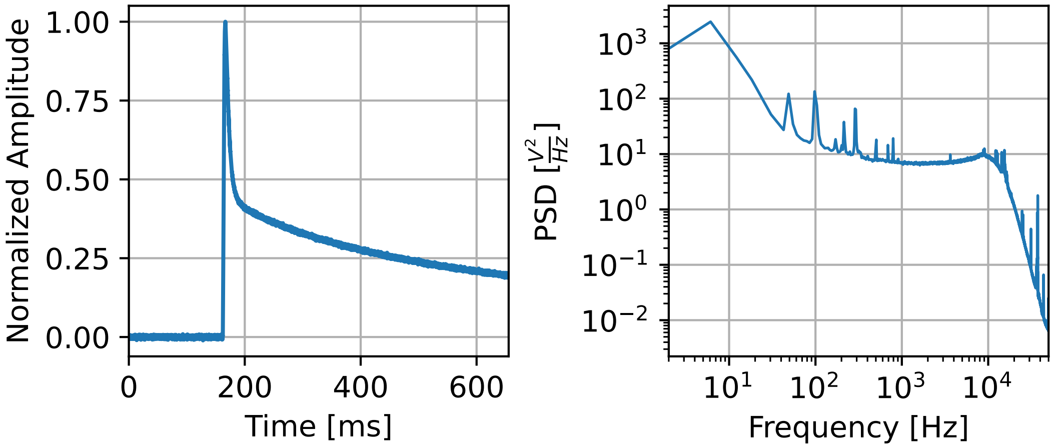

Figure 4.24: SEV (left) and NPS (right) for the NaI-remoTES used in the COSINUS proof-of-principle measurement. Compared to the previous NaI-remoTES measurement, the SEV is faster and the NPS contains less features.

As in the previous measurement, when irradiating the refrigerator with the neutron source, an additional class of events with lower LY is observed. This event class corresponds to nuclear recoils and consists of neutrons scattering elastically on Na-nuclei, I-nuclei, and inelastically on I-nuclei. A band fit, based on a maximum-likelihood framework [183], is applied to recover a description of the LY for nuclear recoils, and thus the energy-dependent QF. As DM is expected to elastically scatter on Na- or I-nuclei, the acceptance region for events is defined by the 90%-region of the bands. The LY plot is shown in figure 4.25, the resulting DM limit was presented in chapter 3. For low energies, the energy spectrum is dominated by events from the internal ^{55}Fe-source

($K_\alpha = 5.9\,\text{keV}$) that are leaking into the nuclear recoil bands. In the final COSINUS measurements, no internal source will be used for calibration.

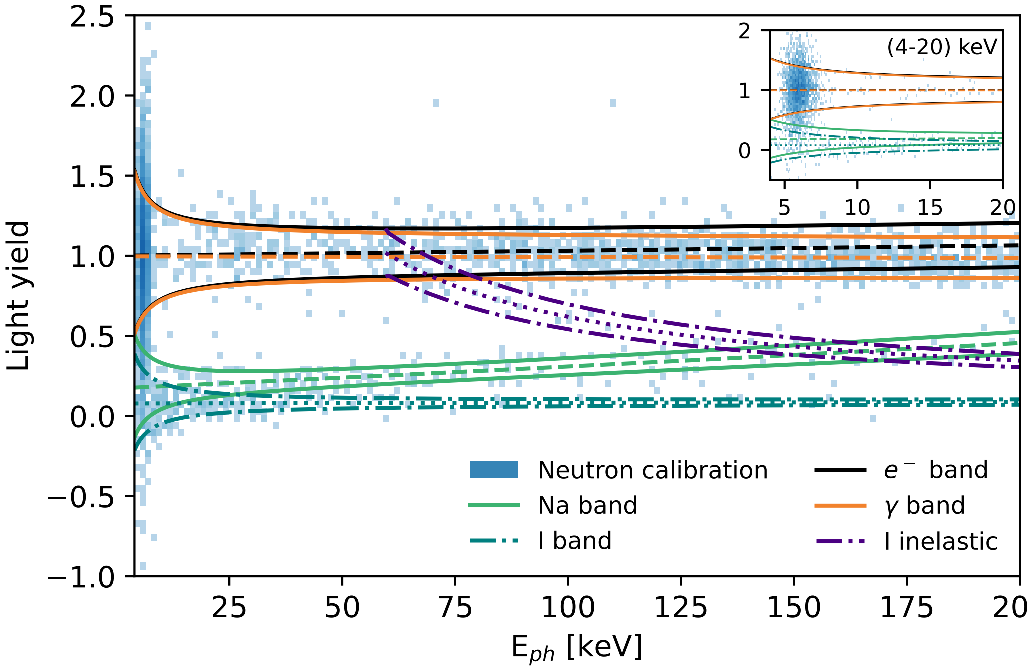

Figure 4.25: LY for the neutron calibration data sets. The drawn bands show the 90% ranges for the different event categories and were calculated by fitting an empirical model to the data. The inset shows the (4-20) keV region, which is dominated by events from the internal ^{55}Fe-source ($K_\alpha = 5.9\,\text{keV}$). Adapted from [4].

In comparison to the previous result from the above-ground measurement, the better detector resolution and light collection efficiency allowed for a precise fit of the QFs. They are described by the following functions using l_0, l_1, $k_{QF,n}$, a_n and d_n as free parameters.[15]

$$E_{l,e^-}(E) = l_0 E + l_1 E^2 \tag{4.19}$$

$$E_{l,n}(E) = (l_0 E + l_1 E^2) \times k_{QF,n}(1 - a_n e^{-E/d_n}) \tag{4.20}$$

The linear term $l_0 E$ was chosen to describe an increasing light output with energy, while the quadratic term $l_1 E^2$ can account for detector-specific effects and minor non-linearities. For nuclear recoils, an exponential term is added to describe the observed energy dependence of the QF. The fit values are listed in table 4.6.

---

[15] The parametrization was defined by the CRESST collaboration for $CaWO_4$ based on empirical observations using Birks' law. For NaI, the parametrization worked reasonably well.

Parameter	Fit value
l_0	0.8131 ± 0.0026
l_1	$(8.98 \pm 0.028) \times 10^{-4}\ \mathrm{keV}^{-1}$
$k_{QF,\mathrm{Na}}$	2.864 ± 0.079
a_{Na}	0.9197 ± 0.0032
d_{Na}	$(1.91 \pm 0.12) \times 10^3\,\mathrm{keV}$
$k_{QF,\mathrm{I}}$	0.1005 ± 0.0041
a_{I}	680 ± 450
d_{I}	$0.071 \pm 0.031\,\mathrm{keV}$

Table 4.6: Fit parameters for the energy-dependent description of the recoil bands. The values were acquired by a maximum likelihood fit. Adapted from [4]

At a total deposited energy of 10 keV QFs of 0.197 ± 0.019 and 0.0892 ± 0.0037 were calculated for Na- and I-recoils, respectively. For 150 keV, a QF of 0.43 ± 0.02 for Na and 0.101 ± 0.004 for I can be calculated. The crystals in both NaI-runs, above-ground and underground, were produced in the same batch from the same Tl-doped NaI-powder. Similarly, the QFs measured from both crystals agree within one standard deviation.

In summary, this measurement validated the COSINUS strategy and demonstrated that a reasonable energy resolution could be reached with a NaI-remoTES. Based on this finding, the COSINUS collaboration decided not to follow up on the previous baseline design in favor of the remoTES design. The next steps for research and development focus on scaling up the (10x10x10) mm^3 absorbers while optimizing the design to achieve lower energy resolutions.

4.7 remoTES Optimization

The remoTES innovates the traditional coupling by introducing a Au-link connecting absorber and TES. To optimize the detector design, it is necessary to investigate the properties of the Au-link and their effects on pulse shape and energy resolution, as well as the overall reproducibility of the detector performance parameters among different measurements. The following sections describe different R&D measurements with the goal of investigating each single component of the Au-link, i.e. Au-pad on the absorber, Au-bond wires and Au-port on the TES.

4.7.1 Number of Bond Wires

In section 4.6.1, a measurement on α-$\mathrm{TeO_2}$ was introduced as a proof-of-principle for the remoTES-design. This measurement was part of a previously unpublished series of measurements designed to investigate the Au-bonds of the Au-link. If the energy resolution was limited by a low heat conductance along the bond wire of the Au-link, the resolution should be improved by adding more bond wires in parallel.

To test this hypothesis, a series of measurements was performed, where the same detector was reused, and only the number of bonds was changed between one, two, four, and six. Its properties are listed in table 4.7. In all measurements, an ^{55}Fe-source was used to calibrate absorber events. Figure 4.26 shows the SEV and NPS for each run.

Component	Properties
α-TeO_2-absorber	$(20x10x2)\,mm^3$ Mass: 2.42 g
Au-pad (foil) on Si	Area: $4.9\,mm^2$ Thickness: 400 nm glued
Au-wires	Diameter: $17\,\mu m$ Length: 2 mm wedge-bonded
TES	W-TES on Al_2O_3 wafer wafer pressed on Cu

Table 4.7: Detector properties of the TeO_2-based remoTES. Between the different measurements, the number of Au-wires changed between one, two, four, and six.

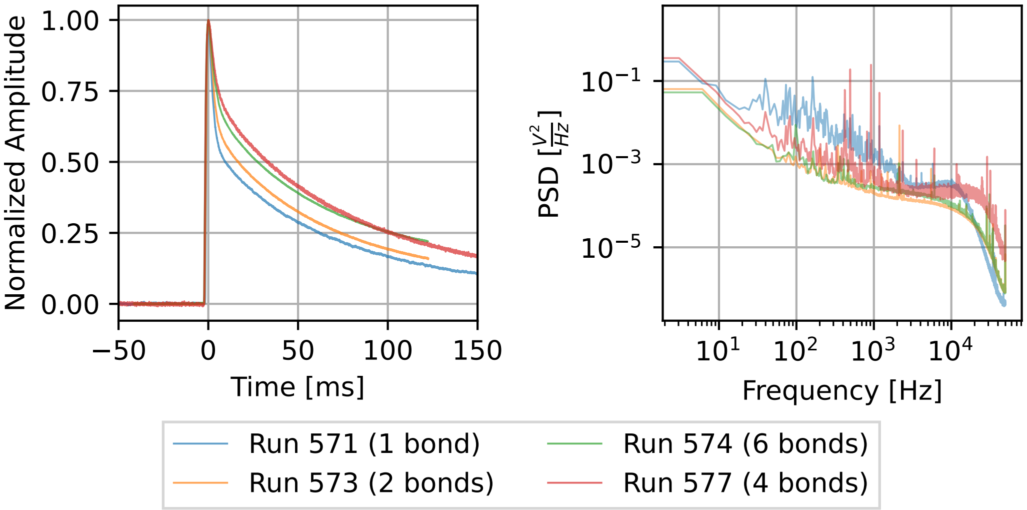

Figure 4.26: SEV and NPS of the TeO_2-remoTES for the four different measurements. With an increasing number of bond wires, the slow thermal part of the SEV is increasing as well.

The results reveal that for more bond wires, the long-lived thermal part increases relative to the fast non-thermal part. This can be explained by the additional heat capacity introduced by additional Au-wires. In table 4.8, the different detectors and their achieved energy resolutions are listed. An additional method was used to calculate the energy resolution for these measurements. In the SEV fit method, the SEV is scaled to the real event to recover the event parameters as fit parameters. Compared to the OF method, it performs slightly worse but is more resistant to changing noise conditions during and in between the measurements. The precise procedure is described in appendix B

Run number	Number of bonds	Energy resolution [eV]
571	1	1470 ± 50
573	2	154 ± 3
574	6	310 ± 20
577	4	450 ± 20

Table 4.8: Results of the measurements carried out with TeO_2. The only parameter changed in between the runs was the number of Au-bonds. The resolution generally worsened with more Au due to the added parasitic heat capacity. The bad resolution in run 571 can be traced back to its unstable noise conditions, as can be seen in their NPS.

In this measurement campaign, the detector with the smallest Au heat capacity and fastest pulse did not feature the best energy resolution. Instead, the detector with two bond wires had the best resolution. Due to not reproducible and reliable run conditions during the measurements, the detectors, particularly in the first measurement, also reveal different noise levels, and thus, the achieved energy resolution is not well suited as the only performance criterion. Nevertheless, the general trend of worsening resolution for more Au bond wires suggests that the current design is not limited by the heat conductivity along the Au-link.

These detectors are very convenient for pulse shape studies due to their controlled systematics. Almost all active detector parts, in particular the Au-pad and the TES, are the same for all four detectors, and only the heat capacity of the Au due to additional Au-bond wires changes in between.

Currently, a follow-up study is conducted to validate the models from sections 4.5.1 and 4.5.2 for the remoTES. The successful selection of a physical model can then guide the detector development strategy further.

4.7.2 Bond Type

In the field of ultrasonic wire bonding, two types of bonds are commonly used: wedge bonds and ball bonds. Their difference lies in the interface between wire and film. A wedge bond welds the wire to the film at a single flat spot on each end, while a ball bond is connected via a ball-shaped Au-spot melted to one end of the wire. The other end is welded in the same way as a wedge bond. Both types are illustrated in figure 4.27.

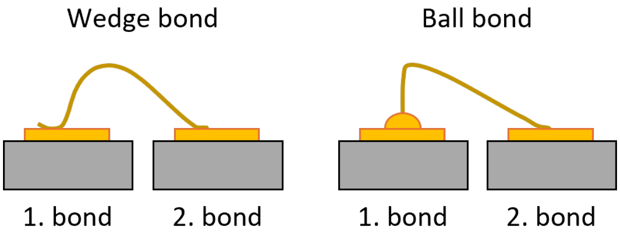

Figure 4.27: Types of wire-bonding. In a wedge bond, the wire is welded to the film on both ends. In a ball bond, one side is connected with a Au-ball instead.

From a fabrication point of view, the wedge bond seems more invasive than the ball bond: although it was possible to attach a bond, the film tore around the bond foot due to the shear forces involved. This tearing depends strongly on the thickness of the Au-pad and the quality of the material below. Fabrication tests indicated that thicker Au-films and harder materials beneath the film are beneficial to prevent damage.

Nevertheless, tests also showed that the ball bond does not stick on glued thin Au-films. Instead of tearing the Au-film apart, it could be observed that the high temperatures involved in ball bonding melted part of the glue and prevented adhesion. Figure 4.28 shows images from the production and typical issues encountered during the bonding process.

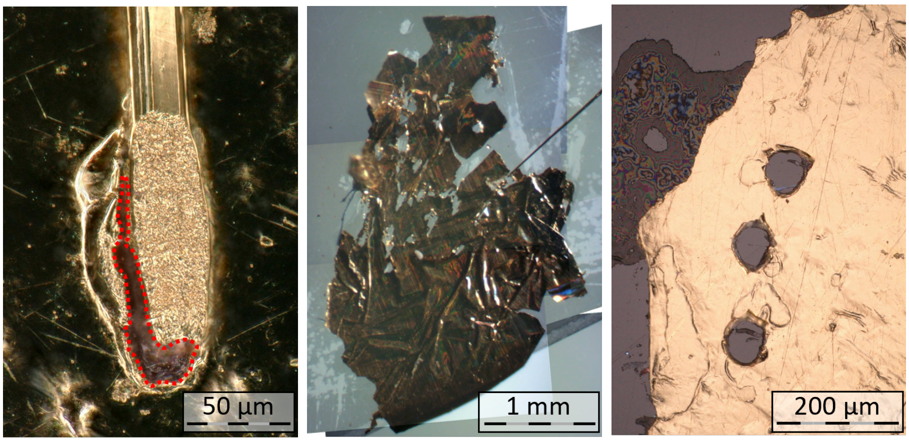

Figure 4.28: Common production damages. On the left, the Au-pad was torn by a wedge bond, leaving a hole in the Au-pad and the crystal below (marked in red). In the middle, multiple failed bonding attempts punched holes into the Au-pad. On the right, a ball bond melted the glue beneath the Au-pad.

Table 4.9 summarizes the results of bonding tests done on Si and NaI with different Au-pads. It should be noted that it is generally possible to attach bonds to any Au-pads on different absorbers; however, user experience is required, and multiple destructive attempts might be necessary before achieving a successful bond.

Absorber	Au-pad	Thickness	Bond method	Result[16]
Si	glued (GP-11 [184])	$1\,\mu$m	wedge	frequent failure
Si	glued (EpoTek 301-2)	$1\,\mu$m	ball	frequent failure
Si	sputtered	200 nm	ball	occasional failure
Si	glued (EpoTek 301-2)	$8\,\mu$m	ball	success
NaI	glued (EpoTek 301-2)	$1\,\mu$m	wedge	occasional failure
NaI	glued (EpoTek 301-2)	$8\,\mu$m	wedge	success
NaI	evaporated	<500 nm[17]	ball	frequent failure
NaI	evaporated	>$1\,\mu$m	ball	success

Table 4.9: Bond adhesion for different materials, Au-deposition/glueing methods, Au-thicknesses and bonding methods. Successful bonds were also achieved for other combinations; however, the bond adhesion was not studied in depth for those detectors.

One Si-remoTES prototype, from hereon denoted "Electra", was developed to investigate whether the bond foot, in general, limits the performance of the detector. The detector consisted of a (20x10x5) mm^3 Si-absorber with a circular sputtered Au-pad. Its area and thickness were 3 mm^2 and 200 nm, respectively. A single Au ball bond, with a diameter of $25\,\mu$m, connected Au-pad and TES, with the ball on the Au-pad side. In a subsequent iteration of the same detector, "Electra'", a second ball was deposited on the wedge side on top of the previous wedge bond foot. The results were previously published in [177, 178]. Figure 4.29 shows a photo and scheme of the detector design.

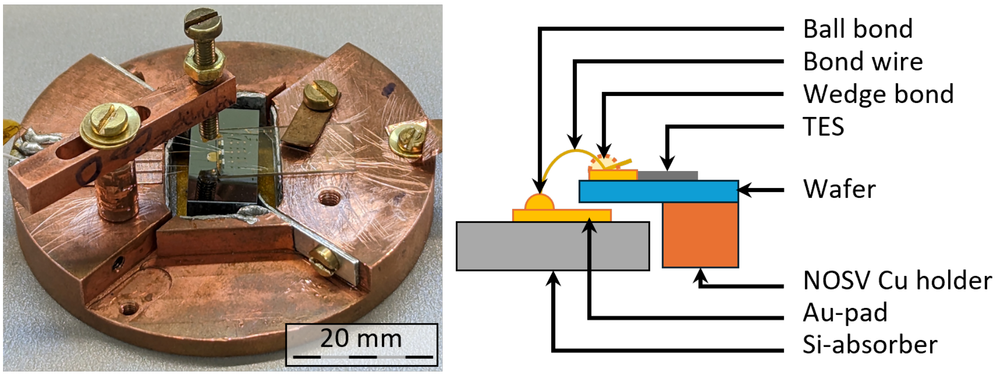

Figure 4.29: The Electra detector-design. A ball bond connects the absorber and wafer with the ball on the absorber side. In a further iteration, a second ball was added to the wafer side on top of the already existing wedge bond.

---

[16] The exact failure rate strongly depends on the user and used machines. Industrial standards and high statistics for a precise estimate were not possible.

[17] For most of the investigated NaI-samples, a precise, non-destructive determination of the film thickness was not possible.

Electra and Electra' were calibrated with ^{55}Fe-sources irradiating the absorber and reached baseline energy resolutions of $(133 \pm 3)\,\text{eV}$ and $(167 \pm 8)\,\text{eV}$, respectively. The SEVs of the events attributed to absorber events and the NPS for the measurements are shown in figure 4.30.

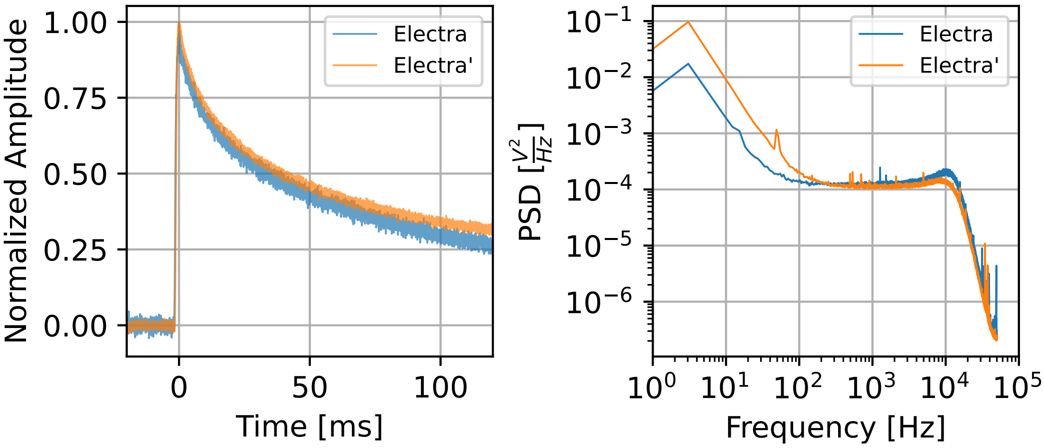

Figure 4.30: SEV and NPS for Electra and Electra'. The SEVs were moved to the same peak position. Both SEV show a similar shape.

An additional ^{55}Fe-source irradiated the Au-pad on the absorber to test the effect of the second ball on the conductivity along the Au-link. The SEV for events within the Au-pad are shown in figure 4.31.

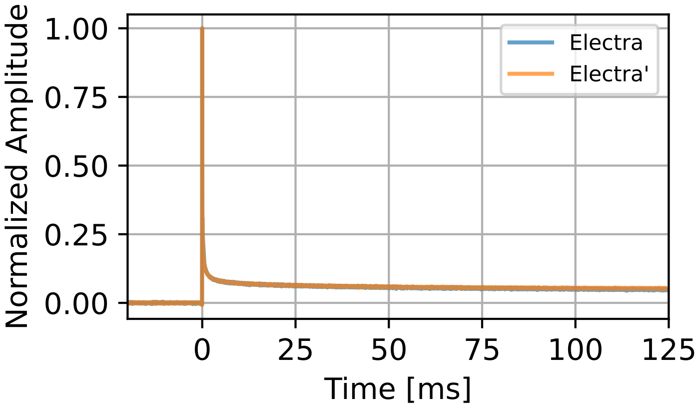

Figure 4.31: SEV of the Au-events of Electra and Electra'. The SEVs were moved to the same peak position, leading to a perfect overlap.

Both iterations have an almost equal pulse shape, showing that adding the second ball to the bond did not significantly change any detector properties relevant to its performance. Instead, it leads to the conclusion that a single ball bond, with the ball on the absorber side, transmits the signal effectively as long as the bond passes standard quality checks. These include a non-destructive pull test and an optical inspection of the ball-pad interface using a microscope.

4.7.3 TES-port

Two designs for the TES-port were tested, the "Au-bridge" and the "Au-island". The Au-bridge was a simple modification of the existing CRESST-like TES design, featuring an additional Au-film on the wafer that connects to the W-film. This connection enabled the signal transfer towards the W-film.[18] However, at the same time, the direct interface between Au-film and wafer introduced an additional loss channel into the wafer. Therefore, in the next iteration, the Au-island was introduced. In this design, the Au-film is deposited on top of the W-film such that there is no contact between Au-film and wafer. Figure 4.32 highlights the difference between both designs.

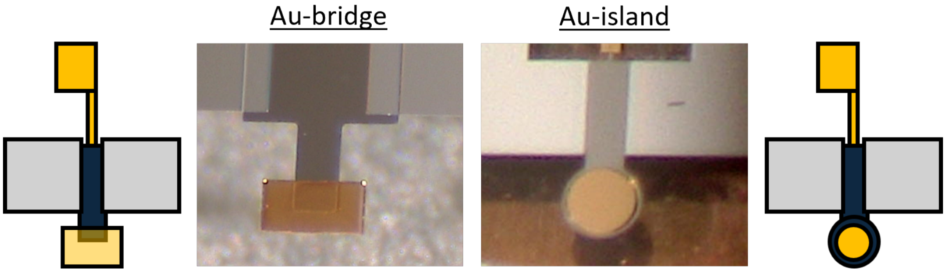

Figure 4.32: Differences between the bridge- and island-designs of the remoTES port. In the bridge design, the Au-film is in direct contact with the wafer below, while the Au-film in the island design is only connected to the W-film of the TES.

A Si-remoTES prototype, from hereon denoted "Olympia", was used to test the difference between both designs. It consisted of a (20x10x5) mm^3 Si-absorber with a glued Au-pad of 8 μm thickness and of 3 mm^2 area. TES and absorber were connected via a 25 μm ball bond with the ball on the absorber side. In its second iteration, "Olympia' ", the TES was exchanged from a model with Au-bridge to a newer model with Au-island. Figure 4.33 shows a scheme and photo of the detector design.

The SEV attributed to events in the absorber and the NPS for this measurement are shown in figure 4.34.

Olympia and Olympia' achieved energy resolutions of (89 ± 2) eV and (1159 ± 134) eV, respectively [178]. The poorer resolution of Olympia' was attributed to a production fault in its TES, which led to a bad sensitivity and increased noise levels, as is clearly visible in the NPS in figure 4.34.

The decay time of the SEV for Olympia', the detector utilizing the Au-island, is much faster than the one for Olympia, which uses the Au-bridge. This indicates that the signal

---

[18] In principle it would suffice to connect the Au-bond directly to the W-film. However, to directly connect a Au bond-wire to W-films is very challenging.

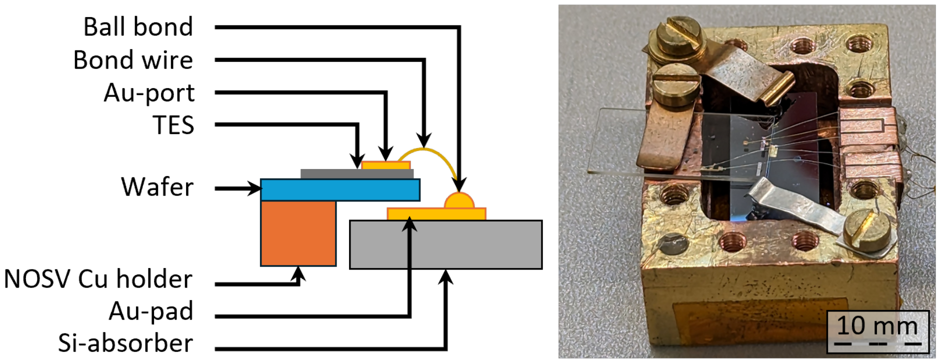

Figure 4.33: The Olympia detector design in its second iteration, Olympia', with aAu-island. In the first iteration, the Au-port was a Au-film that was in contact with both the TES and the wafer.

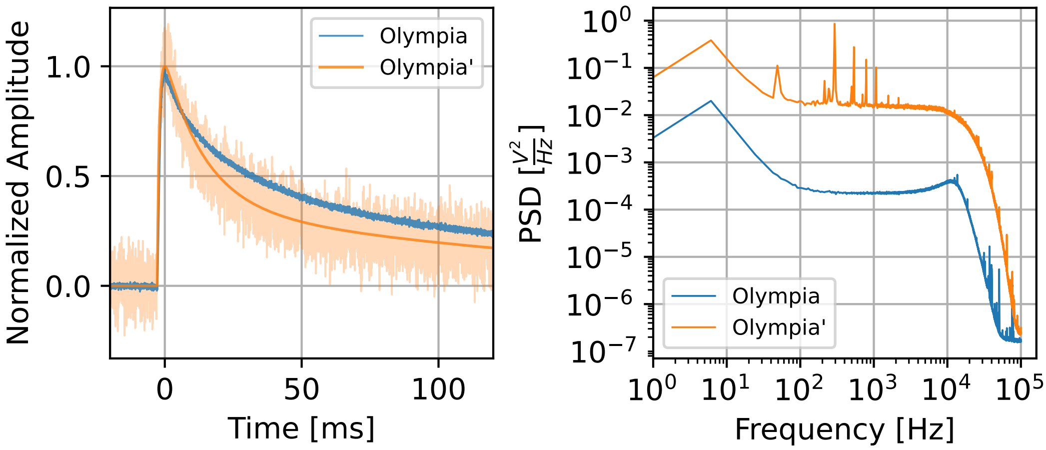

Figure 4.34: SEV and NPS for Olympia and Olympia'. For a better comparison, the noisy SEV of Olympia' was fitted with the function in equation 4.8. The SEVs were moved to the same peak position.

transmission between Au and W in the bridge design was limited and could be improved in the island design.

The same observation was confirmed when examining events from events within the Au-pad. Figure 4.35 shows the SEV for events within the Au-pad for both detectors. In the bridge design, the pulses have a significant long-lived component, which indicates that the heat flow to the TES is inhibited and can only happen over a long time frame. After switching to the Au-island design, this bottleneck is resolved, and the long-lived component is strongly reduced.

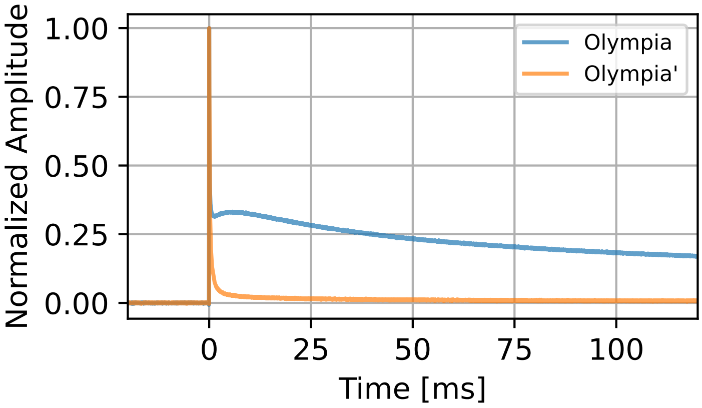

Figure 4.35: SEV for Au-events of Olympia and Olympia'. The SEVs were moved to the same peak position. In the Au-island iteration, Olympia', the slow component is strongly reduced.

4.7.4 Au-pad

In the remoTES-design, the Au-pad on the absorber should have the biggest impact on the achievable performance of the detector. It is responsible for collecting phonons and converting their energy into the electronic system. Ideally, it should cover as much area as possible to maximize phonon collection while not adding parasitic heat capacity. Similarly, the Au-layer can not be arbitrarily thin as this could impede the heat conductance along the Au-pad and pose practical challenges, such as attaching the bonding.

Another complexity stems from the deposition/gluing technique of the Au-pad. The physical properties (e.g. grain size, residual resistivity ratio, or purity) of films can vary strongly depending on the applied technique and its technical intricacies (e.g. adhesion layers below the film or thickness and choice of glue). In particular, the acoustic matching between the absorber and Au is known to play a big role in its collection efficiency.[19] For this reason, the Au-pad needs to be optimized separately for every absorber material, and comparisons can only be made by taking into account the heat capacities of the complete detector modules.

Silicon

For Si, this comparison was done with the modules Electra and Olympia that were described in the previous sections. A comparison of technical details and the achieved resolutions can be found in table 4.10.

Electra and Olympia have Au-pads with the same area but vastly different heat capacities due to their different thicknesses. Therefore, it was hypothesized that the detector

---

[19] Currently a study, where Cu instead of Au is utilized for the link between the absorber and TES, is ongoing. Due to the availability of phonon modes with higher energy in Cu compared to Au, a better transmission of high-energy phonons is expected.

Component	Electra/Electra'	Olympia/Olympia'
Si-absorber	(20x10x5) mm^3 Mass: 2.34 g	(20x10x5) mm^3 Mass: 2.34 g
Au-pad on Si	Area: 3 mm^2 Thickness: 200 nm Sputtered	Area: 3 mm^2 Thickness: 8 μm Glued
Au-wire	Diameter: 25 μm Ball-bonded on Au-pad/ Ball-bonded on Au-pad and Au-port	Diameter: 25 μm Ball-bonded on Au-pad
TES	W-TES on Al_2O_3 Thickness: 450 nm Au-bridge pressed on Cu	W-TES on Al_2O_3 Thickness: 156 nm Au-bridge/ Au-island pressed on Cu
Resolution	(133 ± 3) eV/ (167 ± 8) eV	(89 ± 2) eV/ (1159 ± 134) eV

Table 4.10: Detector properties of the Si-based remoTES. Properties only valid for one detector version are written in colored font. Adapted from [178].

with the thinner Au-pad would achieve much better energy resolutions (assuming similar noise conditions during operation). However, the measurements showed that the detector with the glued thick Au-pad performed better. In addition, neither detector could reach a baseline resolution close to the currently leading Si-detectors with a TES directly deposited onto the surface of the crystals, which are below 10 eV [179, 180].

One explanation could be the poor acoustic matching of Au and Si, which would lead to a reflection instead of a collection of most high-energy phonons at the Au-Si interface. The collection efficiency of the Au-pad is competing against the signal loss through the detector holding structure, which might then dominate for a badly collecting Au-pad. In Olympia, instead, there is a layer of glue between Au and Si. Since the glue is an amorphous material, phonons that propagate into it should quickly thermalize, which could have a net positive effect on signal collection. A comparison of the pulse shape to the physical models in sections 4.5.1 and 4.5.2 could give further insights into the role of the glue layer.

To understand the role of acoustic matching between materials, future remoTES studies should be done by varying either the crystal or exchanging the Au-pad to another material. The heat conductivity and transmission of phonons through boundary layers of two materials is an active field of research. One successful model to estimate the transmission probability of phonons through a boundary is the diffuse mismatch model, which compares the density of phonon states [185, 186]. When comparing Si with possible phonon-collecting materials, it turns out that Al, as used in CRESST, would be preferred over Au, since higher phonon frequencies are allowed within the collector and therefore transmitted ($f_{Si} \lesssim 15\,\mathrm{THz}$, $f_{Al} \lesssim 10\,\mathrm{THz}$, $f_{Au} \lesssim 5\,\mathrm{THz}$). However, as Al becomes superconducting around 1.2 K, a direct comparison of a Au-pad and an Al-pad is not possible. Currently, a Cu-pad is investigated as a Au-alternative ($f_{Cu} \lesssim 7\,\mathrm{THz}$).

In CRESST, the idea of equipping one absorber with two TES was successfully investigated to study the origin of LEE-events. It was shown that the energy of all events is split roughly equally in between both TES, provided that they have similar thermal properties [187]. Based on this idea, by equipping one absorber with two remoTES sensors (or with one classic TES and one remoTES), it could be possible to study the matching between materials experimentally.

According to the detector models, the time constant for the thermalization of non-thermal phonons τ_n should purely depend on the crystal, the detector geometry, and the thermalization probability in the film. Since in a double-remoTES, the geometry for both films can be the same, a direct comparison of τ_n would yield the ratio of thermalization probabilities as a measure of the acoustic matching.

Sodium Iodide

For NaI, there exists data from three runs with detectors of similar size. Two of them, the measurement taken at the end of 2021 (“Christmas run”) and the measurement taken in summer 2022 (“Summer run”), were described in section 4.6.2. The third measurement was taken above-ground in spring 2023 (“Spring run”) and previously reported in [163]. Its detector design was similar to the summer run (see figure 4.22) with a much thicker Au-pad and glue layer. A comparison of technical details and the achieved resolutions can be found in table 4.11. The Christmas run was the first successful measurement of NaI-remoTES and, due to a lack of experience, it had a worse production quality than later NaI-detectors. Therefore, it is excluded from the comparison.

Figure 4.36 shows a comparison of SEV and NPS. Similar to previous remoTES-detectors, in the summer run, the non-thermal component of the pulses dominated the pulse shape. With this strategy, the best baseline resolution for a NaI-detector so far has been achieved. However, a similar performance was achieved in the spring run using a different strategy. By utilizing a very thick Au-pad and by using a thick layer of glue beneath, the collection of the thermal part was optimized, leading to very long but distinct pulses.

In [163], both runs were studied in detail, and predictions based on simulations and modeling were made. It was shown that, while either strategy has the potential to meet the COSINUS design goal, the non-thermal design can potentially reach better energy resolutions at high masses.

Component	Summer Run	Spring Run
NaI-absorber	(10x10x10) mm^3 Mass: 3.7 g	(10x10x10) mm^3 Mass: 3.7 g
Au-pad on NaI	Area: 1.77 mm^2 Thickness: 1 μm Glued (thin layer)	Area: 1.1 mm^2 Thickness: 8 μm Glued (thick layer)
Au-wire	Number: 1 Diameter: 17 μm Length: 2.3 mm Wedge-bonded	Number: 2 Diameter: 17 μm Length: $\sim$ 10 mm Wedge-bonded
TES	W-TES on Al_2O_3 Thickness: 100 nm Au-bridge Pressed on Cu	W-TES on Al_2O_3 Thickness: 240 nm Au-bridge Pressed on Al_2O_3-balls
Resolution	(441 ± 0.011) eV [4]	410 eV [163]

Table 4.11: Detector properties of the NaI-based remoTES.

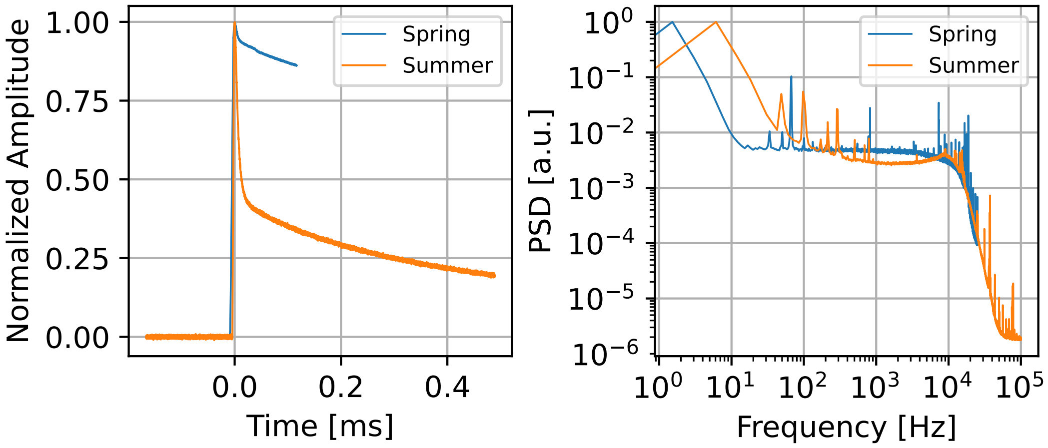

Figure 4.36: SEV and NPS for the NaI runs. The detectors were operated with different sampling rates and record lengths. Both measurements were taken in different facilities within different environments. For a better noise shape comparison, the NPS were normalized to 1 at their peak. The SEVs feature a drastically different share of the slow signal component.

Currently, the development of evaporated Au-films on NaI is ongoing. This is made possible by cooperation with Prof. A. Bandarenka, chair of Physics of Energy Conversion and Storage at Technische Universität München (TUM) and Ph. D. student R. Götz. With an evaporation machine within a glove box, thin films up to a thickness of 3 μm were successfully deposited on NaI. Figure 4.37 shows the evaporation machine and a NaI-crystal equipped with an evaporated Au-film.

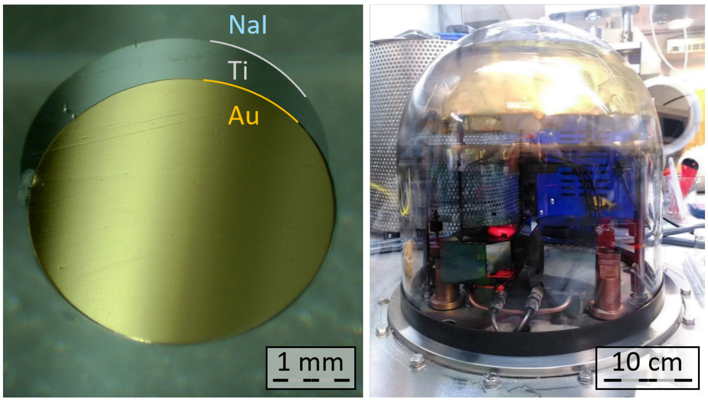

Figure 4.37: On the left: evaporated Au-film on NaI. The dark gray area is a Ti layer, which was misaligned to the gold. On the right: evaporation system used for the deposition.

From evaporated films on NaI, a better reproducibility and improved collection of non-thermal phonons due to the better interface between Au and NaI is expected.[20]Current fabrication tests indicate that a minimum thickness of 1 μm is recommended to successfully place a bond on the Au-film.

4.7.5 Scaling to Higher Masses

Most tests with NaI were done with a (10x10x10) mm^3 crystal. However, for the first COSINUS phase, it is planned to use crystals with the dimensions (21x21x21) mm^3. The main reason for testing smaller crystals is the high background rate above-ground, which makes it challenging to measure big crystals as they are limited by pile-up effects, resulting from a high rate of particle interactions. These pile-up effects harm the detector operation and thus do not allow for a solid detector performance estimation.

Following the successful underground run in 2022, a second run was performed in the CRESST underground test facility. It used a 90 g hexagonal crystal, with a side length of 18 mm and 38 mm height, as target volume[21] and was mounted in the same way in which the final detector modules are planned: to hold the crystal in place, it was glued to a Si-disk at eight spots and surrounded by a Si-beaker as a LD, which together act

---

[20] In current prototypes there is a thin ($\sim$ 10 nm) layer of Ti for adhesion beneath the Au-pad.

[21] This is the maximum size for a crystal to fit into a Si-beaker of COSINUS.

as 4π-shield for α-particles. The remoTES wafer was connected via a Au-link through a hole on the Si-disk to the absorber. Figure 4.38 shows photos of the measured module.

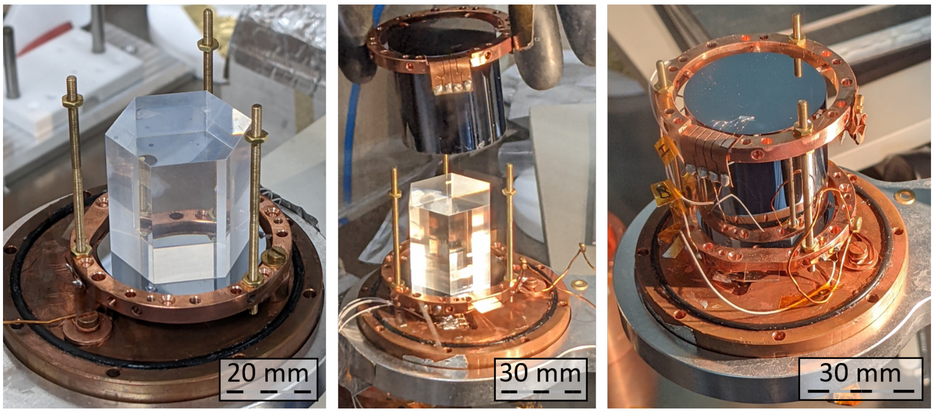

Figure 4.38: NaI remoTES-module with a hexagonal absorber crystal. The crystal is glued to a Si-disk and covered with a Si-beaker that is instrumented as a LD.

From cryogenic calorimeters, it is expected that the energy resolution is roughly related to the absorber mass with a scaling of $\Delta E \propto M^{2/3}$ [188]. Hence, by upscaling a 3.7 g NaI detector with 400 eV resolution, one would expect a resolution around 3 keV for a 90 g absorber. However, in this measurement, the achieved energy resolution was orders of magnitudes worse. There are two reasons for this poor performance: first, the bigger hexagonal crystal was produced from an older batch of powder with high impurity and worse production quality. This leads to worse phonon propagation properties and, thus, to a worse-than-expected resolution. Second, due to operational difficulties, the detector's operating point could not be properly optimized for the measurement.

Nevertheless, although the detector performed poorly, the run was a big success in terms of production technique. It was proven that a detector module with big crystals can be produced using current methods without damaging the crystal. Additionally, the crystals successfully withstood a transport from Munich to LNGS and back and could be read out with the remoTES-design.

4.8 Phonon Propagation and Collection

4.8.1 Scatter Simulations

The goal of the detector development is to optimize the collection of non-thermal phonons and, thus, their contribution to the measured signal. This contribution, and its time constant τ_n, depend strongly on the crystal quality and the geometry of the phonon collecting components (i.e. the TES, Au-pad or holding structures). Until now, τ_n was fitted from real pulses, and its dependencies were not studied in detail.

Simple assumptions can lead to a good intuition of non-thermal phonon propagation and collection in cryogenic detectors. In this work, a simulation for the propagation and collection of non-thermal ballistic phonons is described. The simulation was implemented in Python3 using the open-source package NumPy [189]. The following assumptions and simplifications were made:

- Longitudinal frequency-independent phonons that move with the longitudinal speed of sound are considered.[22]
- All phonons are assumed to originate from a single origin point with a random direction.
- No phonon interaction takes place within the bulk material. This implies an ideal absorber without lattice defects.
- When hitting a surface, the phonon is either diffusely reflected back into the crystal or thermalizes on the surface.
- When hitting a phonon collecting part, the phonon can be reflected, thermalized on the boundary, or transmitted to the phonon collector. An average transmission probability is used for all modes and angles. It is calculated using the diffusive mismatch formalism [185].

Figure 4.39 shows a flow chart of the algorithm for this simulation.

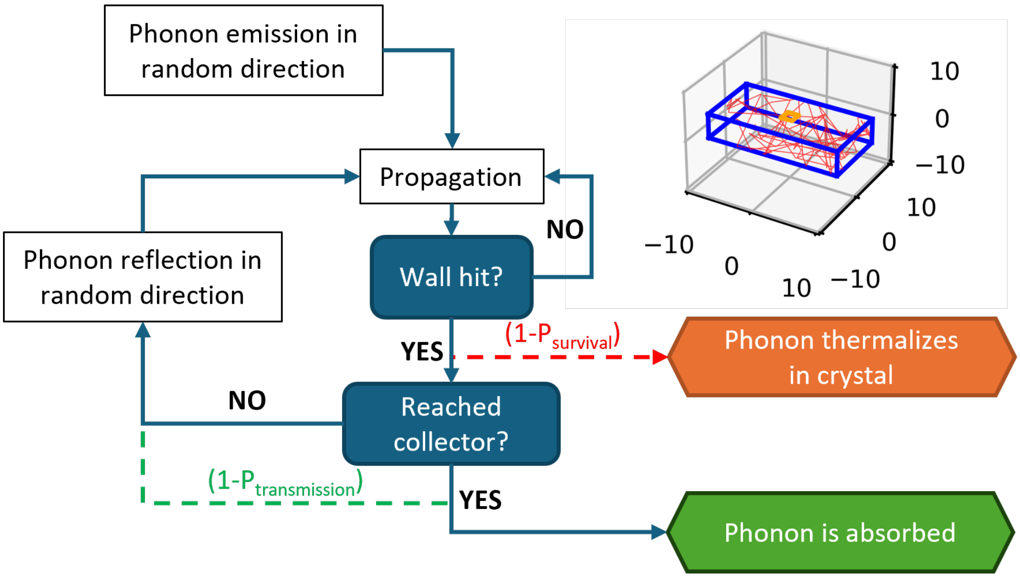

Figure 4.39: Algorithm for the phonon propagation simulation. The figure on the top right shows an example of a single phonon scattering through a crystal (blue) until it reaches the Au-pad (orange).

---

[22] The transversal speed of sound is usually in the same order of magnitude. A more proper treatment would consider different phonon modes with different speeds.

The input of the final simulation requires several parameters. These include the absorber sizes, area and position of phonon collecting parts, position of the initial interaction, and phonon thermalization, as well as reflection probabilities. For crystals with many impurities in the bulk, a mean free path for phonon-impurity scattering is considered. Furthermore, it is possible to define zones with different physical properties. The outputs are the number of scatters, the total distance traveled, and, if wanted, the exact path traveled for each phonon.

A large number of phonons are simulated, and their distance traveled until thermalizing in the collector or the crystal is collected in a histogram. The speed of sound can be used to change the scale from distance to phonon lifetime. Figure 4.40 shows the histogram for a detector with the same dimensions as the NaI-remoTES measured underground that was described in section 4.6.2. The input parameters for this specific simulation are given in table 4.12. From this simulation, by fitting an exponential function, it is possible to extract the detector-specific time constants $\tau_{crystal}$, τ_{film} and τ_n, as well as the efficiency ϵ. Table 4.13 shows a comparison of simulated and measured parameters for NaI.

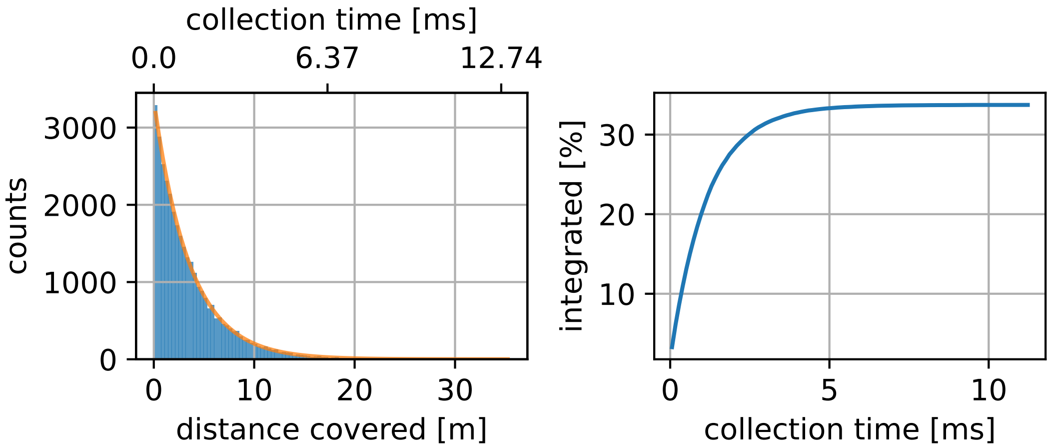

Figure 4.40: Simulation results for 10^5 phonons. In the left plot, a histogram with all simulated phonons and their traveled distance until being absorbed in the Au-pad is shown. The top axis shows the distance converted to time until collection. The right plot shows the integrated percentage of phonons that are absorbed in the collector before they thermalize.

With very simple and mainly geometric assumptions, it is already possible to reach a result close to measurements. One reason for the deviations is an overestimation of the absorption probability (as indicated by the high simulated ϵ). The glue of the interface is not included in the description of the acoustic mismatch and can inhibit phonon transmission. Furthermore, the crystal quality was assumed to be ideal in this simulation. The input parameters can be studied by fitting the physical pulse shape models to the SEV and comparing collection efficiencies ϵ between simulation and data.

Parameter	Input	additional information
Cuboid dimensions	$(10\text{x}10\text{x}10)\,\text{mm}^3$	same dimensions as NaI-remoTES
Start coordinates	centered	within crystal bulk
Au-position	centered	on crystal surface
Au-pad area	$1.77\,\text{mm}^2$	same area as NaI-remoTES
$P_{absorption}$	27%	calculated using diffuse mismatch formalism [185]
$P_{survival}$	99.9 %	rough estimate from typical measured $\tau_{crystal}$
speed of sound	$3140\,\frac{mm}{ms}$	calculated from elastic constant c_{11} [190]

Table 4.12: Input parameters for the simulation of a NaI-remoTES detector.

Parameter	Simulated	Measured
τ_{film}	(3.419 ± 0.011) ms	-
$\tau_{crystal}$	(1.720 ± 0.005) ms	-
τ_n	(1.135 ± 0.005) ms	2.042 ms (fitted SEV)
ϵ	0.34	-

Table 4.13: Simulated parameters for a NaI-remoTES. The uncertainties given correspond to the fit uncertainties from fitting an exponential function to the phonon population lifetime.

Figure 4.41 shows simulation results for a $(100\text{x}10\text{x}1)\,\text{mm}^3$ thin NaI-wafer with different positions of the initial interaction. The closer the initial interaction is to the collecting Au-pad, the shorter the collection time and the higher the collection efficiency. This simulation allows us to get an intuitive understanding of the position dependencies of the initial interaction depending on the detector geometry. In the future, it could help to characterize and improve new detector designs that utilize multiple sensors on the same absorber [191, 187] or study non-standard detector geometries such as the beaker-shape used in COSINUS.

However, (i) information about the crystal orientation and anisotropies, (ii) a proper treatment for the different phonon modes, and (iii) a more precise description of the transmission and reflection of phonons at crystal boundaries, taking into account the phonon dispersion relations of both materials should be considered as first steps.

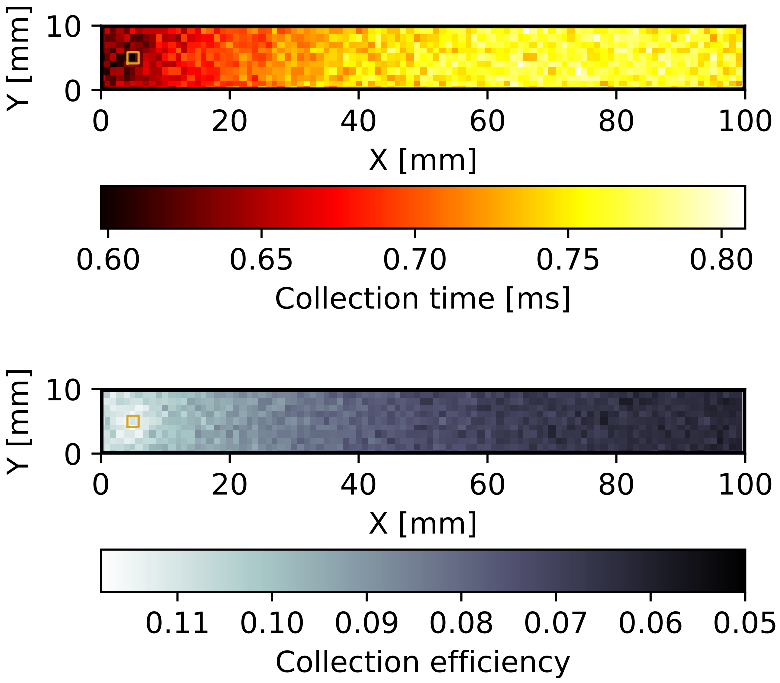

Figure 4.41: Position dependence of the collection of phonons in a thin wafer ((100x10x1) mm^3). The top plot shows the simulated collection time τ_n for different positions. The bottom plot shows the corresponding collection efficiencies ϵ. The orange square marks the area of the collecting Au-pad.

4.9 COSINUS Light Detectors

The particle discrimination capabilities of COSINUS depend on both the phonon and light signals. Therefore, it is vital to optimize the energy resolution and light collection efficiency of the LD as well. The LDs of COSINUS are beaker-shaped Si-absorbers equipped with TES in the classical CRESST-like design. They have a wall thickness of 1 mm and an outer diameter of 40 mm or 41 mm based on their production line. Photos of one of the beaker-shaped absorbers are shown in figure 4.42.

In the CRESST-like design, the Al bonding pads also function as phonon collectors. The working principle is depicted in figure 4.43. When a high energy phonon enters the superconducting Al-film, it excites the Cooper-pairs to “break” into quasi-particles. The quasi-particles then diffuse through the Al-film and can reach the W-film, where they interact with its electrons. In this way, the effective collecting area of the TES is increased while adding a negligible amount of heat capacity due to the superconductivity of the phonon collector.

This principle has a natural limit given by the mean free path of recombination of the quasi-particles. In a dedicated measurement campaign, the phonon collector size on a beaker-shaped LD was systematically reduced to find its optimum.

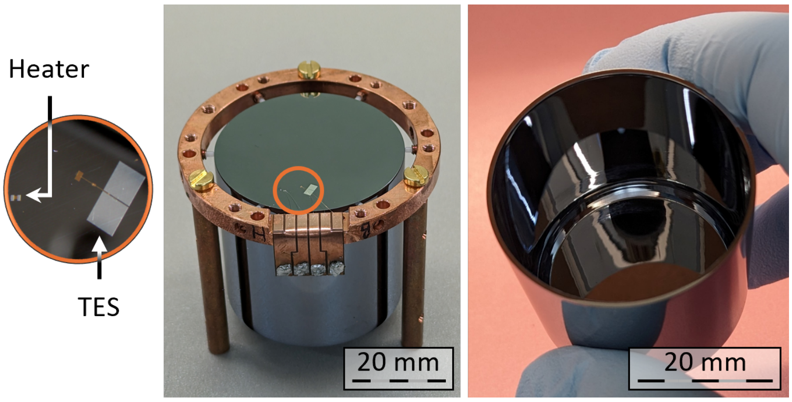

Figure 4.42: Photos of a Si-beaker, as will be used as LD in COSINUS modules. The middle image shows the beaker from the outside, mounted within a Cu-ring. The orange circle marks the TES and heater film used for operation and readout. The right image shows the inside of the beaker.

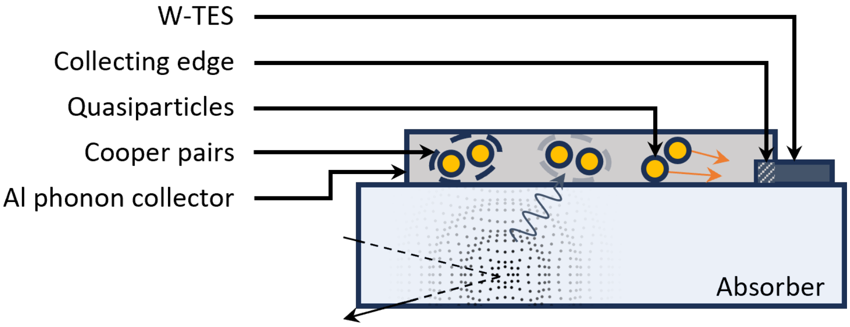

Figure 4.43: Working principle of Al-phonon collectors. Phonons can enter the SC and break Cooper pairs into quasi-particles. The quasi-particles then diffuse to the TES. Also published in [192].

The achieved energy resolutions of the measurements are summarized in table 4.14.

Phonon collector size [mm^2]	Energy resolution [eV]	Comment
$2 \times (1.0 \times 1.0)$	19.3	two TES deposited
$2 \times (1.0 \times 1.0)$	10.2	removed unused TES
$2 \times (1.0 \times 0.5)$	20.2	
$2 \times (1.5 \times 2.3)$	20.8	new TES deposited
$2 \times (1.5 \times 1.9)$	23	11 eV reached underground
(1.5×1.4) & (1.5×1.3)	15	

Table 4.14: Achieved energy resolutions for different phonon collector sizes.

Overall, the energy resolution improved with less phonon collector area, indicating that the optimal dimensions have not yet been found. More precise conclusions will be drawn when comparing SEV and NPS and will be part of a future work.

4.10 A Recipe for the COSINUS-1π remoTES-module

From everything learned so far about NaI and the remoTES, the ideal COSINUS detector would look as shown in figure 4.44

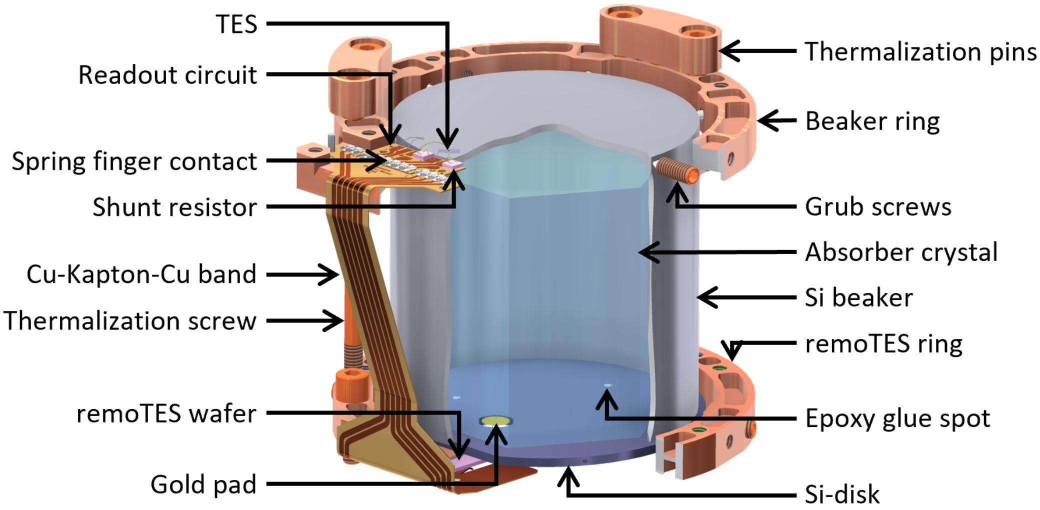

Figure 4.44: Complete COSINUS remoTES module. The absorber crystal (here a 90 g hexagonal crystal) is glued to a Si-disk. It is equipped with a Au-pad that can be connected to the remoTES wafer through a hole in the Si-disk. A Si-beaker instrumented as LD surrounds the absorber.

All in all, the best performing detector would utilize a pure polished NaI-crystal, on which a Au-film is deposited. Deposition by evaporation would be preferred due to the capability of achieving reproducible thin layer thicknesses. Furthermore, the lack of glue is expected to improve phonon collection. The thickness of the Au-pad should be around 1 μm to allow for a damage-free bond. The optimal area of the Au-film is yet to be determined, but a soft minimum is expected due to the trade-off between collection efficiency and parasitic heat capacity.

The TES is deposited on a separate wafer and uses a Au-island as TES-port design. In addition to the TES structure, a heater and bonding pads are deposited on the wafer. Furthermore, the wafer is strongly pressed against the Cu-holding structure to couple it stronger to the heat bath and reduce the sensitivity of the TES to wafer events. A single Au ball bond with the ball on Au-pad side connects the absorber and TES.

Since the wafer is not supposed to be a good detector by itself, there is complete freedom in designing the structures deposited on top. For COSINUS, these structures were optimized to minimize the necessary bond length. A drawing is shown in figure 4.45.

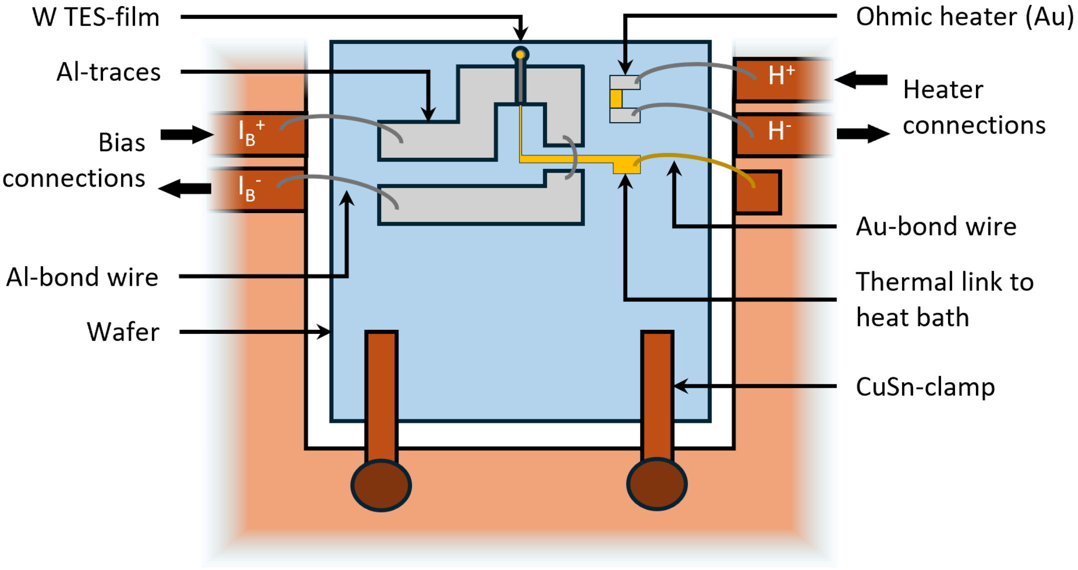

Figure 4.45: COSINUS remoTES-wafer design. The wafer is pressed with two CuSn-clamps on a Cu-holder. Al-bonds are used to bias the TES-film and its heater.

Another innovation of the COSINUS module is the location of the shunt resistor. In the past, shunts with fixed electrical resistance were located separate from the detectors in a dedicated box. Now, it is part of the module and can be adjusted for every TES separately.

In the following, a recipe is presented for the production of the final COSINUS modules of the first batch:

1. **Inspect the absorber crystal:** the crystal should be completely transparent and well polished. No cracks should be visible. When handling the crystal, one should always make sure to only touch it with soft and cleaned tools in a dry (<100 ppm) atmosphere.

2. **Deposit the Au-film:** this can be done by either gluing or evaporation.
   - For **gluing**, one has to mix the glue (EpoTek 301-2) and wait for ≈ 6 h before applying it to NaI. If the waiting time is too short, the crystal might be damaged by the glue catalyst. If the waiting time is too long, the glue might be too viscous and not stick well enough. The whole mixed volume should look evenly clean and transparent.

The Au-foil can be cut beforehand with a scalpel or a laser cutting machine to get the desired area. However, a better film quality, although with a less defined area, is achieved by applying a glue spot to the foil, putting the crystal on it, and waiting for the glue to harden. Then, the surplus Au can be removed with tweezers.

- For **evaporating** Au on NaI an evaporation machine inside a glove box is required. To promote the adhesion of Au on the crystal, a Ti-layer of thickness $\sim$10 nm is deposited first. Afterward, a Au-layer of around 1 μm thickness is evaporated on top of the Ti layer. It is recommended to deposit a similar film simultaneously on a test sample for a non-destructive thickness measurement.

3. **Mount the Si parts:** the Si-beaker and a round Si-disk will surround the crystal and act as 4π-veto for possible α-particle background. They are held by six polyoxymethylene (POM)-tipped grub screws within Cu-rings. The tips should be pressing against the foreseen notches on the Si parts.

4. **Bond the LD:** after the Si beaker is mounted in the Cu-ring the TES can be bonded. The shunt resistance for the LD should be chosen at this step.

5. **Mount and bond the TES-wafer:** on the Cu-ring with the Si-disk, a free slot for the remoTES wafer is located. The wafer can be inserted and pressed with two CuSn clamps. Afterward, the TES is ready to be bonded. The Au-bond of the Au-link will be bonded in a later step.

6. **Glue the crystal to the Si-disk:** in the next step, the glue (Epo-Tek 301-2) is mixed and after the initial curing time (≈ 6 hours) applied to the Si disk. For a (21x21x21) mm^3 crystal, four glue spots are recommended. To avoid damaging the crystal while cooling (due to shear forces), glue spots with smaller diameters are preferred. A gluing machine can be used to support this. The NaI absorber is lowered on the glue spots and left drying for 48 h. The Au-pad should align with the hole in the Si disk.

7. **Connect the Au-link:** after curing the glue, pillars can be mounted to the ring such that it is possible to turn it without touching the crystal. Then the Au-wire between Au-pad and Au-port can be ball-bonded.

8. **Mount LD over absorber:** as soon as all bonded connections are done, both Cu-rings can be screwed together with long screws. The combination of Si-beaker and Si-disk leads to a nearly 4π-coverage of the NaI-crystal and serves two main functions. First, the instrumented beaker serves as LD and measures the scintillation light of the NaI-crystal. Second, the complete 4π-coverage of the absorber by beaker and disk allows for shielding and vetoing of events related to α-decays close to the absorber.

   There are two possible configurations of the 4π-veto: beaker and disk can either be pressed against each other, or a small gap can be left between both parts. In the first option, events within the disk can be read out via the TES on the beaker, which enables a complete active veto and could increase the scintillation collection efficiency.[23] However, for events in the beaker, the disk then acts as an additional loss channel. In the second option, the disk is not actively read out, and the scintillation light absorbed in this part is lost. Instead, the energy resolution of the beaker is maximized, as there is no signal loss through the disk.[24]

9. **Add thermalizations:** the screws should be fixed with additional thermalization pins to ensure good contact between the parts. If desired, further thermalization links can be added to the rings.

With that, the module is ready to be mounted in a detector box. Note that no internal calibration source is foreseen for the final COSINUS detectors.

---

[23] The limited transmission between disk and beaker leads to a reduced amplitude for measured events within the disk.

[24] for the glued connection between NaI absorber and Si disk, this is no issue, as the acoustic mismatch inhibits phonon propagation from NaI to Si. This was also shown to be a disadvantage of the baseline design.

Chapter 5

Vibration Studies

5.1 Vibration Basics

5.1.1 Definitions and Tools

Vibrations are oscillatory movements in a mechanical system. They are characterized by a frequency and an amplitude and are typically described as either displacement or one of its time derivatives (i.e. velocity or acceleration). In general, a mechanical system is exposed to a complete spectrum of vibrations with different amplitudes and frequencies.

Power Spectral Densities

The most common description of vibrations within a system is the Power Spectral Density (PSD) S_{xx}. It can be defined as the Fourier-transformed autocorrelation $R_{xx}(t)$ of a signal $x(t)$.

$$S_{xx}(f) = \int_{\infty}^{\infty} R_{xx}(t)e^{-2\pi i f t}dt \quad \text{with} \quad R_{xx}(t) = \int_{\infty}^{\infty} x(\tau)x^*(\tau + t)d\tau \tag{5.1}$$

A PSD is proportional to the signal power per frequency and is given in units $\frac{[x]^2}{Hz}$, with $[x]$ being the unit of the initial signal. For a more intuitive understanding, a commonly used quantity is the square root of the PSD.

Real measured data is discrete, and the definition from equation 5.1 can not be applied directly. Instead, an algorithm for Discrete Fourier Transform (DFT), e.g. the Fast Fourier Transform (FFT)-algorithm, is used.

$$S_{xx}(f) = \frac{2 \cdot |X(f) \cdot X^*(f)|}{f_s \cdot W} \quad \text{with} \quad X(f) = FFT(x(t)) \tag{5.2}$$

The resulting PSD was scaled with the sampling frequency f_s and a window function correction factor W. Due to the finite measurement window in real signals, frequency peaks in the spectrum are usually subject to spectral leakage. Depending on the requirements, one can reduce leakage by applying a window on the initial signal. However, to recover the correct energy (or power) of the peak, the correction factor is needed. In this thesis, rectangular windows (no change of the initial signal) are used, as they are best suited for broadband measurements and require no knowledge of the initial signal. For a rectangular window, the number of samples in the initial signal is used as the window function correction factor. The factor 2 in equation 5.2 stems from the symmetry of PSDs for real signals. Negative frequencies are not considered, and instead, the PSD is multiplied by a factor 2.

Acceleration, velocity, and displacement can be converted into each other by integration or derivation in time domain.[1] In frequency domain, this simplifies to multiplying or dividing the angular frequency ($\omega = 2\pi f$) from the amplitude (squared for the PSD amplitude).

$$PSD_{\text{acceleration}} = \omega^{-2} \cdot PSD_{\text{velocity}} = \omega^{-4} \cdot PSD_{\text{displacement}} \tag{5.3}$$

Figure 5.1 shows a measured vibration signal and the corresponding PSD for acceleration, velocity, and displacement, measured with an accelerometer. A FFT-algorithm was used to calculate the PSD. The maximum resolved frequency is half of the sampling frequency f_s with a bin width of $\frac{f_s}{N}$. N is the number of data samples in the signal.

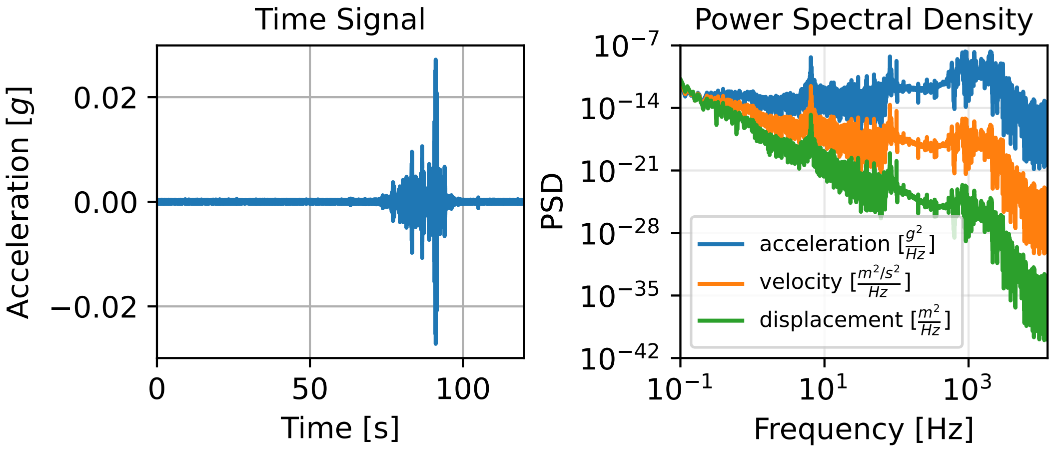

Figure 5.1: Vibration signal (acceleration) measured in time domain (left) and its PSD (right) in frequency domain.

Real PSDs, measured by an accelerometer, typically show a characteristic shape. Very low frequencies are dominated by 1/f-noise, which flattens into a white noise floor dominated by Johnson noise. The exact magnitude of the noise contributions depends on the readout electronics. At higher frequencies, a peak related to a detector-internal resonance appears, after which the accelerometer loses sensitivity. Vibrations are then visible as excess over the noise floor. In many cases, very sharp peaks are indications of either a strong resonance in the system under investigation or an electronic interference in the DAQ.

---

[1] When calculating the displacement from acceleration, the result can indicate an unphysical drift of the sensor. This drift stems from integrated low-frequency noise.

Mechanical Systems

In most cases, when doing a vibration analysis, the device under test can be approximated as Linear Time Invariant (LTI) system. This means that the output signal of the system will always be linear to the input signal. Examples of non-linear systems would be an amplitude-dependent response to an input signal (e.g. granular vibration damping with sand [193]) or an introduction of new frequencies into the system that were not part of the input signal (e.g. 50 Hz from the electrical grid).

A LTI-system is characterized by an impulse response function $h(t)$, and its Laplace transform, the complex transfer function $H(\omega)$[2]. The output of the system $x_{out}(t)$ is calculated by the convolution of the system input $x_{in}(t)$ with $h(t)$.

$$x_{in}(t) * h(t) = \int_{-\infty}^{\infty} x_{in}(\tau)h(t-\tau)d\tau = x_{out}(t) \tag{5.4}$$

In frequency domain, this changes to a simple product of the input signal and transfer function.

$$X_{in}(\omega) \cdot H(\omega) = X_{out}(\omega) \tag{5.5}$$

A measured PSD is influenced by all systems that lie between the vibration generator and the vibration sensor. This includes the mechanical system and any electronic systems, such as amplifiers in the readout chain. One example, later used to characterize the COSINUS decoupling system, is shown in figure 5.2.

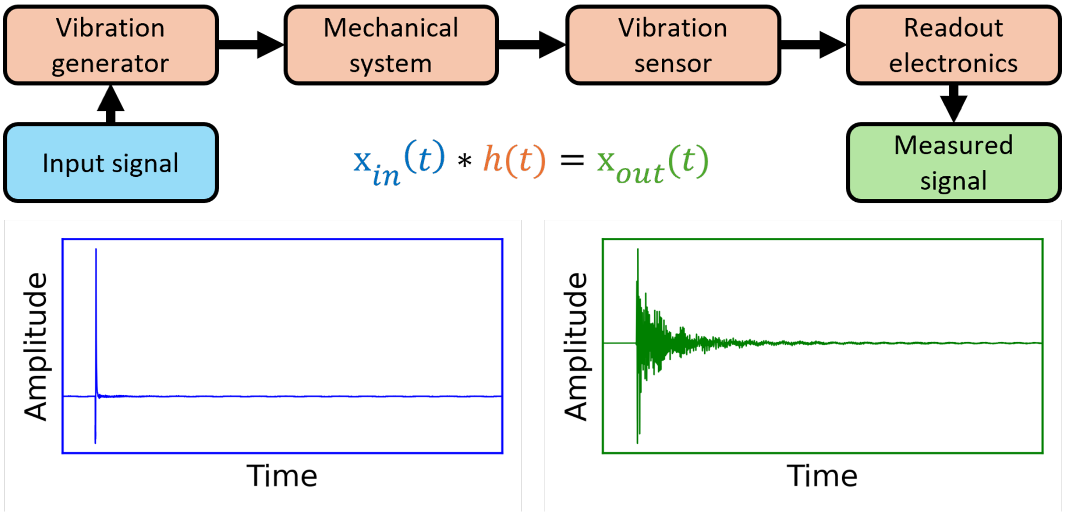

Figure 5.2: Example for a LTI system. A measured signal (right plot) will consist of the signal injected into the system (left plot), convoluted with the system's impulse response function.

By exciting the system with a defined input, such as a wide-band frequency sweep

---

[2] Also called frequency response function, if the Laplace transform is a Fourier transform.

("Chirp signal") or a delta-like impulse, it is possible to measure the transfer function. It results from the division of output and input signals in frequency domain.

$$H(\omega) = \frac{X_{out}(\omega)}{X_{in}(\omega)} \tag{5.6}$$

The transmissibility $T(\omega)$ is a quantity derived from the transfer function by discarding any phase shift information.

$$T(\omega) = |\frac{X_{out}(\omega)}{X_{in}(\omega)}| \tag{5.7}$$

In a noise-less system, the transmissibility is equal to the square root of the ratio of the measured signal PSD and system input PSD. This method was applied in section 5.4.2 to characterize a passive vibration decoupling system.

Spectrograms

Vibration conditions at the same measurement position can change anytime due to environmental changes (e.g. rush hour traffic). The system itself could change as well (e.g. shift of resonances due to changes in mechanical properties while cooling). By computing spectrograms, these shifts can be monitored over time and help to identify possible noise sources. A spectrogram is a three-dimensional plot with time, frequency, and PSD on its axes, with the latter one typically represented in a color scale. It is produced by splitting a data stream into many windows and computing the PSD for each window. One example is shown in figure 5.3.

The system resonances and persistent noise sources are seen as constant horizontal lines in the spectrogram. A shifting or vanishing line indicates a systematic change in the measurement conditions. Vertical lines indicate short bursts of noise, e.g. the steps of a person approaching the vibration sensor.

5.1.2 Vibrational Backgrounds in Cryogenic Calorimeters

Cryogenic calorimeters measure temperature changes induced by energy depositions from particle interactions. One major source of baseline noise in these detectors are vibration-induced microphonics. They can originate from external sources, e.g. trucks passing by the laboratory, but also from internal sources. A major source of vibrational noise in wet refrigerators is the 1K-pot. By pumping on the 1K-pot volume, noise at frequencies on the order of 100 Hz is generated [194]. In modern dry refrigerators, the main source of vibrations is the PT, in particular the rotary valve, which turns with a frequency of 1.4 Hz [140].

Vibrations can influence a detector's output through various channels. Current noise can be induced in cables due to the triboelectric and piezoelectric effects [195, 196]. Furthermore, parasitic currents can be induced by the movement of cables in external magnetic fields.

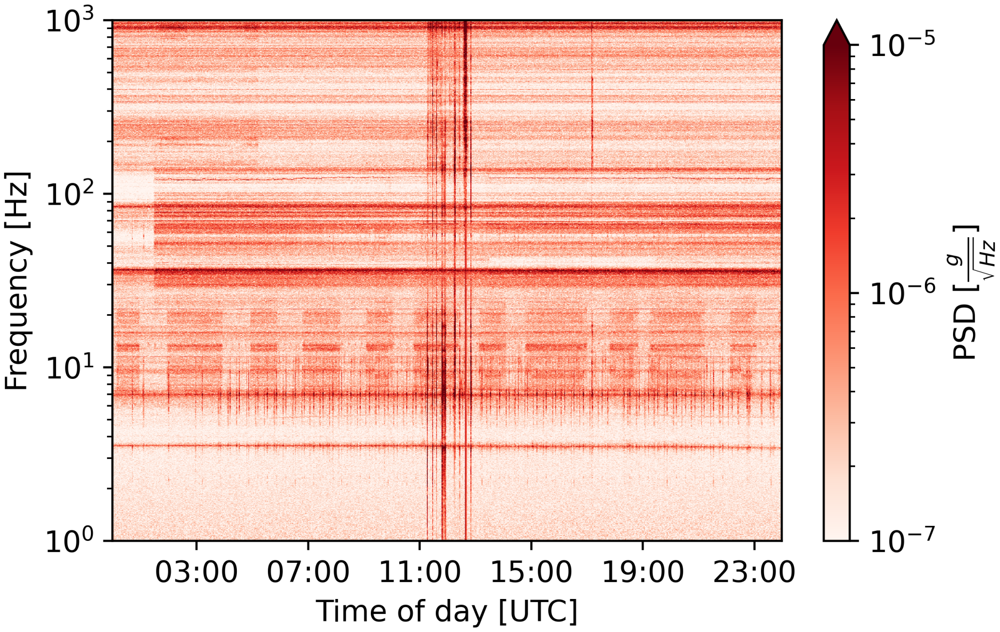

Figure 5.3: Typical spectrogram measured in the COSINUS laboratory in Garching with an accelerometer coupled to the ground floor. Horizontal lines and structures are produced persistent signal or noise sources. Vertical lines indicate vibration bursts picked up by the sensor. In this example, a regular switching machine is picked up in the (7-20) Hz range. Between 11:00-13:00 (UTC), people working in the laboratory close to the sensor were measured.

In the detectors themselves, temperature fluctuations can be generated by internal or external friction. The frictional heating is particularly dependent on the mass of the absorber. The principles of internal and external friction are shown in fig 5.4.

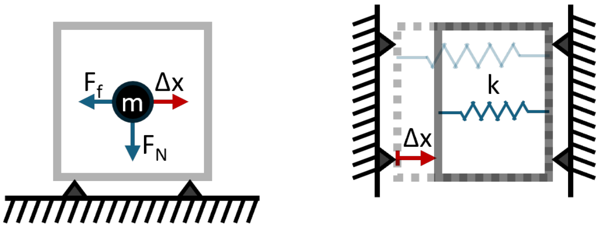

Figure 5.4: Processes inducing external (left) and internal (right) friction in cryogenic detectors.

In external friction, the dissipated energy consists of the product of the frictional force F_f and displacement Δx. The frictional force is proportional to the normal force F_N, in most cases, the gravitational force, which is proportional to the mass m:

$$\Delta E_f = F_f \cdot \Delta x \propto F_N \propto m \tag{5.8}$$

In internal friction, the deformation of the absorber volume is considered. Various processes can lead to a conversion of mechanical energy into heat. When a body is deformed due to inhomogeneous stress (e.g. due to vibrations), a temperature gradient is created between warmer compressed and colder stretched regions. This gradient leads to an irreversible heat flow and, thus, to an increase in entropy, internal energy, and temperature. Other sources of heating can be lattice defects of the crystal structure or internal eddy currents due to magnetic field changes induced by magnetoelastic coupling. [197]

In general, internal friction is characterized by a relative energy loss per cycle $\frac{\Delta E}{E_\kappa}$. The absolute energy loss ΔE (which is converted to heat) is therefore proportional to the energy in each compression cycle E_κ:

$$\Delta E \propto E_\kappa = \int F_k dx = \int k \Delta x dx = \frac{1}{2} k \Delta x^2. \tag{5.9}$$

Thereby, the element can be approximated as a spring system with the compression Δx and stiffness k. The stiffness itself depends on the elasticity module E, the cross-sectional area ($A \propto L^2$) and length of the element L

$$k = E \frac{A}{L} \propto L \propto m^{1/3}. \tag{5.10}$$

The length is related to the mass by $L^3 \propto m$, leading to an overall mass dependence of at least $m^{1/3}$.

Because of these mass dependences, the decoupling from vibrations is more relevant for heavier detectors. This was demonstrated in a dry dilution refrigerator manufactured by Bluefors [157] and owned by the NUCLEUS group at TUM [198]. In a collaborative measurement between COSINUS and NUCLEUS, a NaI-remoTES module with an absorber mass of 3.6 g was tested in parallel with a TES-instrumented NUCLEUS module with an absorber mass below 1 g. An excerpt of the raw data stream of the NaI-remoTES is shown in figure 5.5.

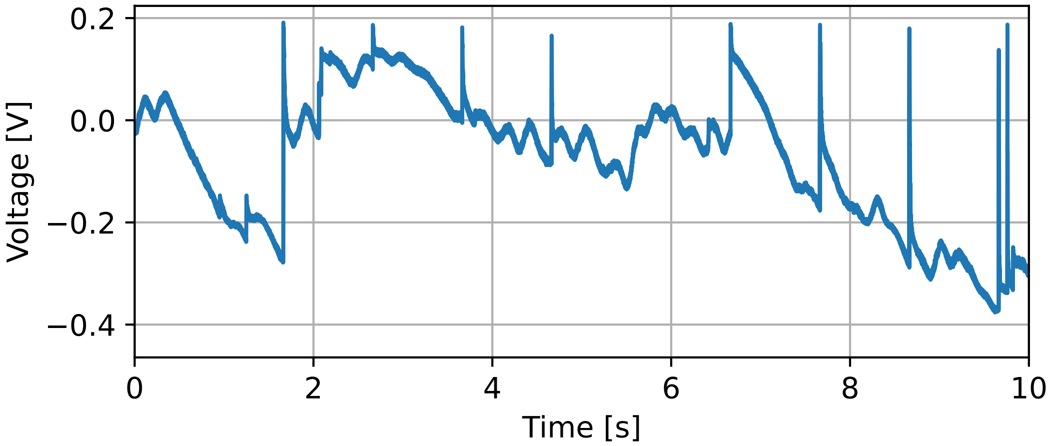

Figure 5.5: Data stream excerpt of a 3.6 g detector subjected to PT-induced noise. Thermal fluctuations from vibrations are on the same order of magnitude (μK) as particle pulses in amplitude as well as frequency and therefore limit the detector performance.

While the NUCLEUS detector could be operated with stable conditions during the run, the COSINUS detector suffered from an extremely noisy baseline with fluctuations on the order of 0.4 V, as is visible in figure 5.5. As soon as the PT was switched off, the baseline stabilized, and the detector could be operated as usual[3].

The typical time scale of a COSINUS detector signal is on the order of 1 s, with more than 99.7 % of its signal contribution being below 100 Hz. Any noise in the same frequency range will reduce the detector's resolution.

5.1.3 Measuring a Vibration PSD

For every measure of vibrations (i.e. displacement, velocity, and acceleration), different classes of instruments exist. In this work, accelerometers and geophones were used.

Accelerometers

Accelerometers measure the acceleration and are the most common vibration sensors in use for industrial applications (e.g. monitoring of machines). Most devices used in this work are accelerometers: their sensor principle is based on the piezoelectric effect and is shown in figure 5.6.

---

[3] The refrigerator can run unobstructed without the pre-cooling provided by the PT for about 5 min.

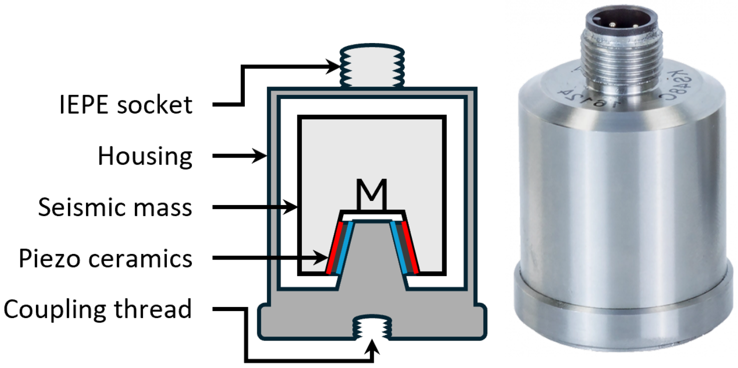

Figure 5.6: Schematic of an accelerometer. Most of the sensors used in this work measure the shear of a piezo crystal due to a moving seismic mass. The components are depicted in the drawing on the left. The photo on the right shows an accelerometer of type KS48C manufactured by MMF [199]. Photo and drawing adapted from [200, 201].

A seismic mass is fixed to one side of a piezoelectric disk, while the other side of the disk is fixed to the sensor housing. If the sensor vibrates, the inert seismic mass applies pressure on the piezoelectric disk, creating a voltage between both disk sides. A piezo-based accelerometer can only measure vibrations in one direction. Commercial systems are usually equipped with integrated electronics to condition the signal.[4] Therefore, it is not possible to use these sensors at very low temperatures.

The sensitivities of the accelerometers in use follow a typical frequency characteristic shown in figure 5.7. In a wide band around the calibration frequency f_0, a flat response with a fixed conversion between voltage and acceleration is expected. Towards higher frequencies, a resonance appears at the frequency f_r. It stems from the mechanical couplings within the device and marks the upper limit of the bandwidth before the device loses sensitivity for even higher frequencies. For very low frequencies, the bandwidth is limited by a lower cutoff f_l, which is defined by the electronics' preamplifier characteristics.

In this work, accelerometers of type KS48 by MMF [199] and PCB393b by PCB [202] were used. They can be read out with custom-made analog amplifier circuit boards with ×1 or ×11 amplification.

Geophones

Geophones measure the velocity and are mostly used in seismic measurements. Their working principle is based on electro-mechanical transducers consisting of a (permanent) magnet and a coil. A schematic is shown in figure 5.8.

Typically, the coil is loosely connected via springs to the sensor housing and acts as seismic mass. The magnet, instead, is rigidly connected to the sensor housing. If the

---

[4] A commonly used format is the technical standard IEPE.

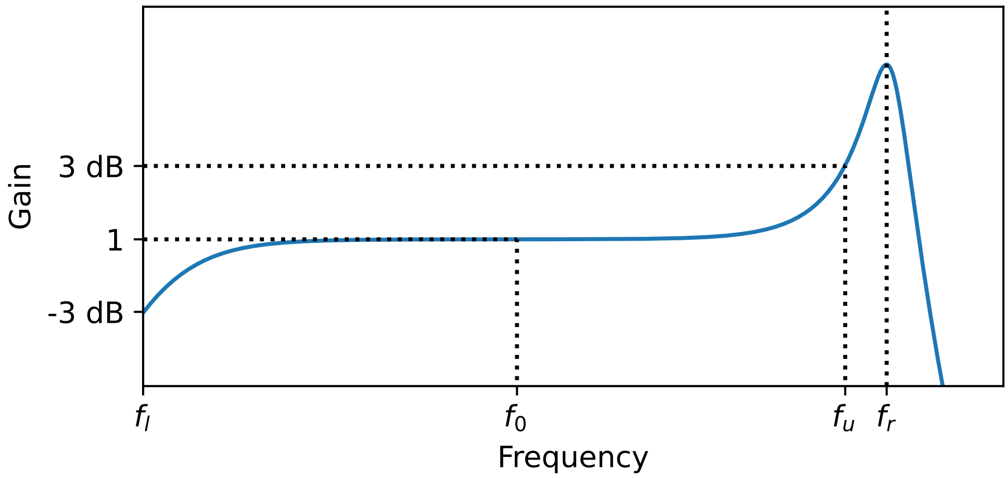

Figure 5.7: Typical response for an accelerometer. For low frequencies $< f_l$, the bandwidth is limited by the readout electronics. At ±3 dB gain, the measured signal power is doubled or halfed. For high frequencies, the response is limited by the intrinsic resonance frequency f_r of the device.

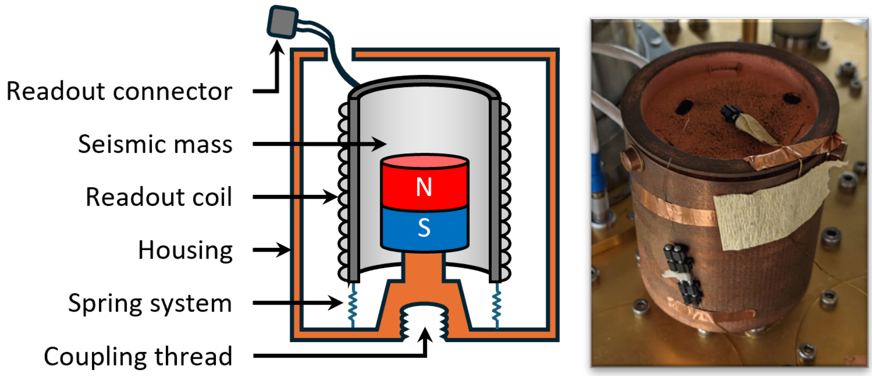

Figure 5.8: On the left: Schematic of a geophone. A magnet is rigidly fixed to the housing, while the coil is fixed to a seismic mass suspended on a spring system. On the right: photo of a geophone adapted to work at mK temperatures.

system vibrates, the coil moves relative to the magnet's magnetic field, and a measurable current is induced. Since geophones measure velocity instead of acceleration, much higher sensitivities are achieved for vibrations at low frequencies than with an accelerometer.[5] On the other hand, the characteristic response curve also has a different shape, as is shown in figure 5.9.

---

[5] As seen in figure 5.1, a vibration signal for velocity is suppressed at higher frequencies compared to an acceleration signal.

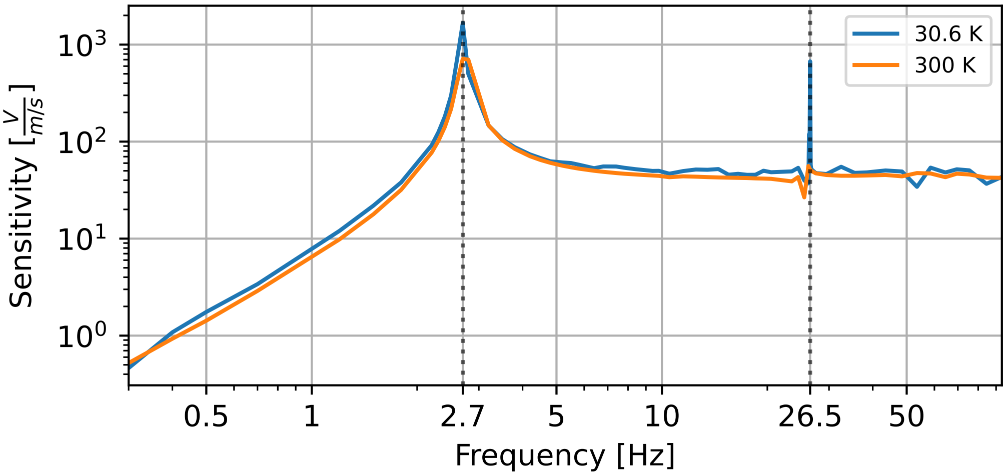

Figure 5.9: Response curve of the geophone used in this work at RT and low temperature (30 K) [203]. The feature at 26.5 Hz could be traced back to an artifact from the DAQ used for acquisition during calibration.

For frequencies higher than the resonance of its mechanical system, a geophone has a flat response to vibrations. Below the resonance, the sensitivity drops drastically. The shown response curve describes the non-commercial geophone used in this work to monitor vibrations within a dilution refrigerator. It utilizes a permanent magnet and a 30 g readout coil made from Nb-Ti wire simultaneously acting as seismic mass and features a resonance frequency of around 2.7 Hz.

This device is among the first vibration sensors worldwide to be shown to operate at sub-Kelvin temperatures. However, around 10 K, a change in this geophone's response could be measured. Figure 5.10 shows a spectrogram acquired during a cooldown of the COSINUS R&D-refrigerator, at the time still located in Munich. For this cooldown, the geophone was mounted on the 4 K-plate. The same behavior was also observed on other temperature stages around the same temperature.

The spectrogram shows a very prominent line that can be attributed to the geophone resonance around 2.7 Hz. When the temperature reaches around 10 K, the line shifts to a higher frequency of around 17 Hz. Thus, the geophone loses sensitivity in the low-frequency region, while for higher frequency, the response stays approximately the same. Figure 5.11 shows an average of the first and last 100 spectra of the spectrogram.

The spectrum confirms a shift of the resonance peak from 2.7 Hz to 16.7 Hz. Frequencies higher than 30 Hz behave approximately the same in both spectra; however, a recalibration is recommended for confirmation.

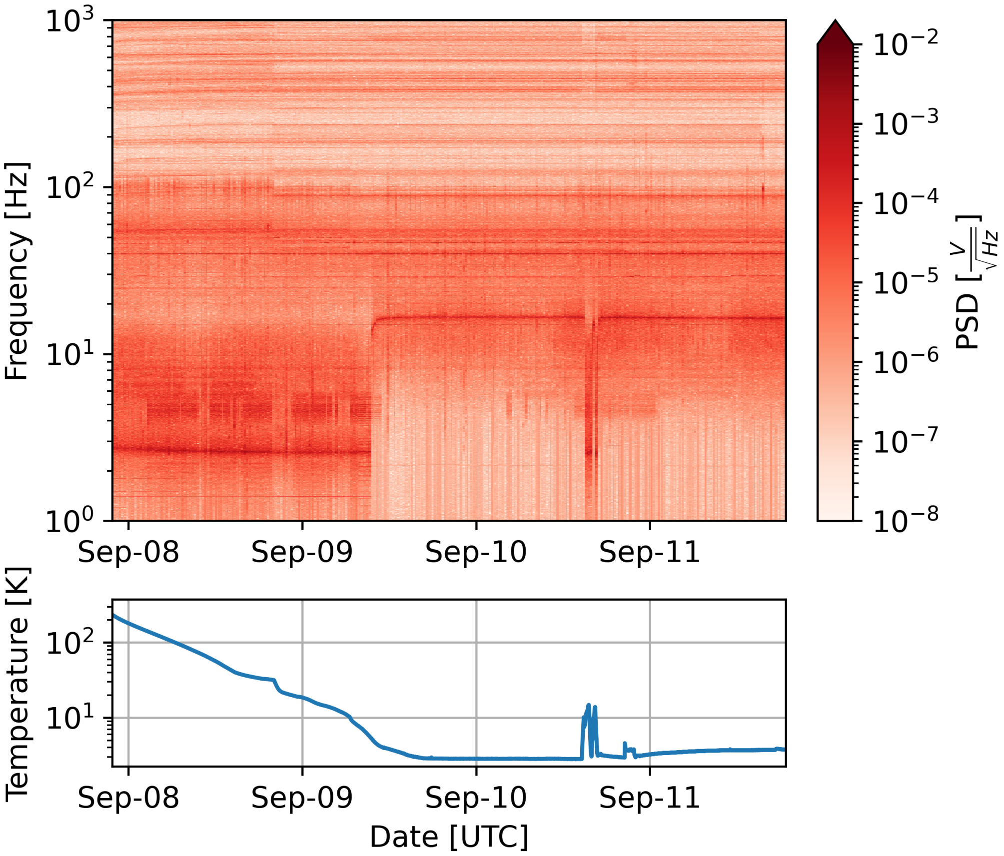

Figure 5.10: Geophone spectrogram for a cooldown from RT to 4 K. The geophone is mounted on the 4 K-plate. The bottom plot shows the measured temperature on the 4 K-plate. On the 10th of September, 2023, an error of the cooldown protocol lead to a warming of the refrigerator. Whenever the temperature decreased below ∼ 10 K, the main frequency seen in the spectrogram shifted from 2.7 Hz to 16.7 Hz.

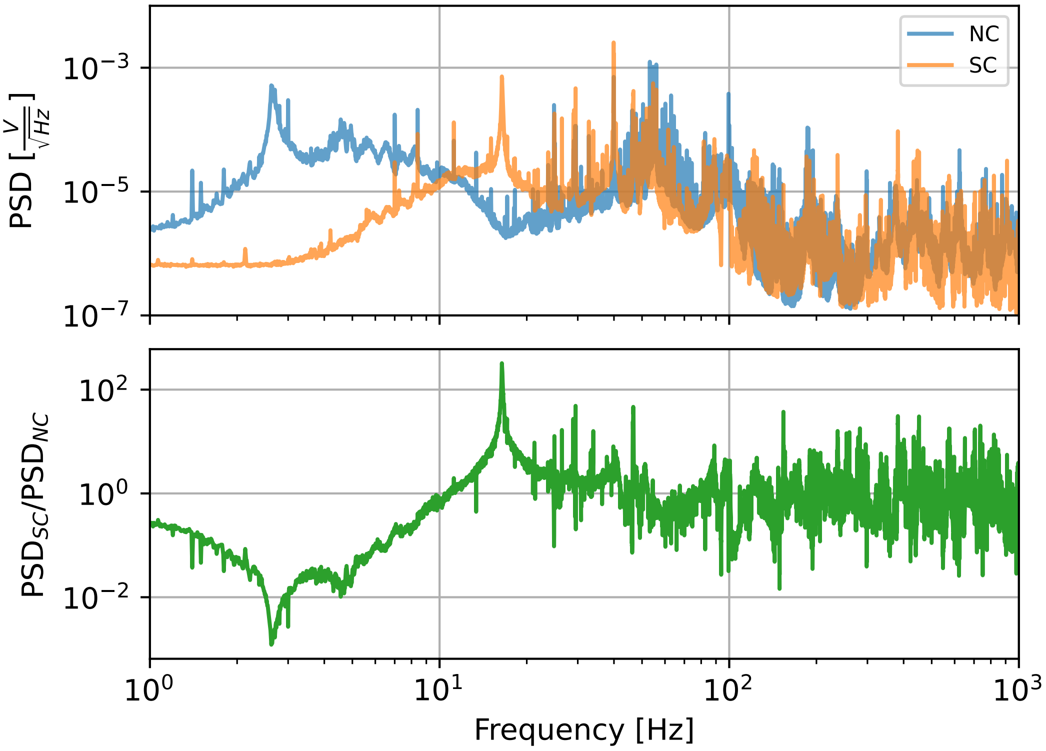

Figure 5.11: Averaged geophone spectrum plotted from the first 100 single spectra (NC) and last 100 single spectra (SC) of the data shown in figure 5.10. The bottom plot shows the ratio of both averaged spectra.

To characterize the response of the geophone in its different states, a constant current source ($100\,\mu$A) was introduced. A single-pole double-throw switch allowed the change of the geophone output between an "excitation mode", in which the current was applied to the geophone, and a "readout mode", in which the geophone was read out with the DAQ. In excitation mode, the coil creates a magnetic field that interacts with the field of the permanent magnet, leading to a displacement of the coil. As soon as the system is switched to readout mode, the generated magnetic field of the coil vanishes, and the step response of the mechanical system can be measured.[6] The resonance frequency and decay rate can be extracted by fitting a damped sine curve to the data. One example is shown in figure 5.12.

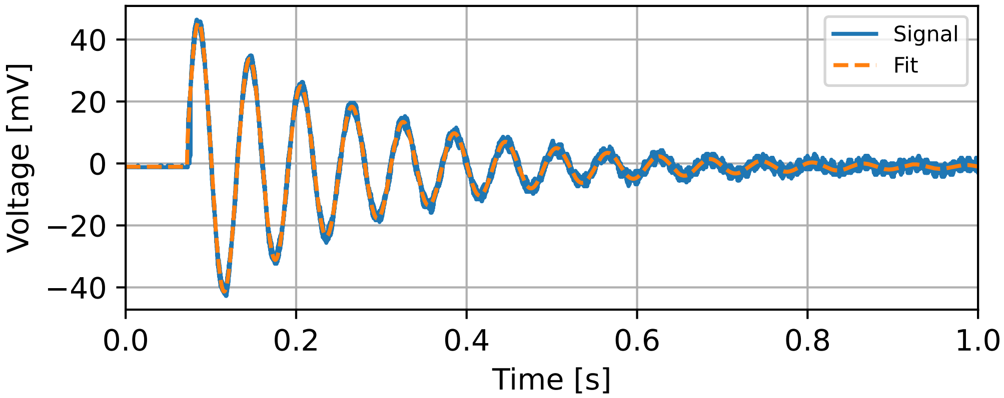

Figure 5.12: Geophone response to a $100\,\mu$A current step sent to the readout line. The signal (blue) was fitted with a damped sine curve (orange).

At RT, a resonance frequency of $(2.7325 \pm 0.0026)\,$Hz was measured, while at base temperature (at 4 K), a frequency of $(16.67 \pm 0.05)\,$Hz was found. The decay rate of the oscillation increased from $(2.59 \pm 0.03)\,\mathrm{s}^{-1}$ to $(4.83 \pm 0.24)\,\mathrm{s}^{-1}$.

A hypothesis that could explain this observation is based on the flux pinning effect that was described in chapter 4.2. The Nb-Ti coil of the geophone, a type-II SC, becomes superconducting when it reaches its critical temperature around 10 K. If the field strength of the magnetic field exceeds the lower critical field strength of the SC, it can penetrate the coil via flux tubes or vortices. The vortices can freely move through the bulk material but are pinned to impurities such that a minimum flux pinning force is needed to move the vortex from its location. The complete ensemble of pinned vortices can accumulate to a macroscopic restoring force that depends on the displacement. For small displacements, this force can be approximated by an additional spring, which changes the dynamics of the system. In the past, this principle was proposed for a contactless vibration isolation system and for docking systems in space applications [204, 205].

---

[6] Due to the sudden change of current through the coil, a high voltage is generated. However, the timescale of that voltage spike is much smaller than the expected signal.

A way to test this hypothesis could be done by modifying the technical details of the geophone. If the change in resonance is a purely mechanical effect, the frequency will only depend on the spring constant and seismic mass. If, instead, a change in magnetic field or SC material at the coil leads to a different behavior, it will be an indication of a new effect introduced by the superconductivity.

Measurement Setup

When setting up a vibration measurement, several aspects are recommended to be considered for a meaningful result:

- The vibration sensors in use for this work effectively measure vibrations only on one axis.[7] For the accelerometers, it is possible to orient the sensor in any desired way. Due to technical limitations, the geophone can only be operated when mounted vertically.
- When coupling a vibration sensor to a structure, special attention has to be given to the interface. The contact should be done along a smooth area to ensure good signal transmission and avoid the introduction of new resonances from the interface itself. Nevertheless, almost every type of coupling will introduce a resonance frequency on the order of 10 kHz. Above this resonance frequency, the transmission of vibrations is reduced, and the sensor loses sensitivity. [206]
- The precise position of the vibration sensor should be chosen depending on the vibration modes of interest. Resonances and antiresonances are position-dependent. In general, it is advisable to place the sensor on a structural nodal point for a characterization of the complete structure.
- The expected signal strength of background measurements in this work is on the order of 0.1 V. These voltages should be resolved by the DAQ with a sufficient bit rate to avoid digitization losses.
- The highest background in this work is airborne acoustic noise that couples directly to the sensor housing or the structure under test. When setting up a measurement, strong acoustic activity should be avoided, and actions to dampen airborne noise should be taken. The most effective measure to minimize this background is to operate the sensor in a vacuum, as is done with the geophone during a cooldown.

5.2 Vibration Backgrounds in COSINUS

5.2.1 LNGS

In June 2021, the ground vibrations within LNGS in hall B were measured using an accelerometer of type PCB393b05 connected to a NI-DAQ USB-6211 from National

---

[7] In complex mechanical systems, it can happen that vibrations from other directions are picked up as well.

Instruments [207]. The sensor was coupled via a magnet to a steel plate that had been screwed into the ground at the position where the COSINUS facility is set up today. Figure 5.13 shows the average PSD measured on the 7th of June, 2021.

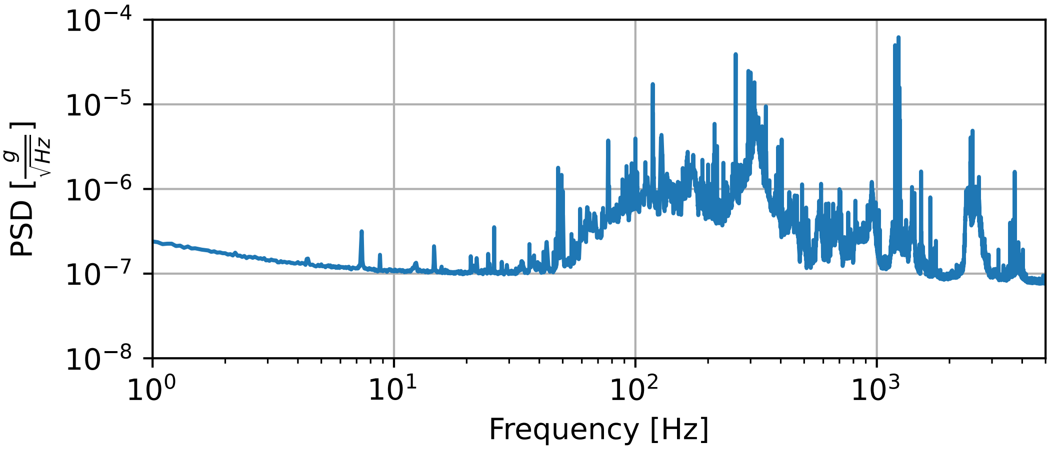

Figure 5.13: Vibrational background measured in 2021 on the floor of hall B in LNGS. Most of the measured vibration power lies between 20 Hz and 1 kHz.

The dataset consists of 800 ten-second windows, sampled with a rate of 10 kS/s. For frequencies below 20 Hz noise dominates the measurement. Between 20 Hz and 1 kHz a wide bump on top of the noise is visible. An airborne acoustic origin within hall B of LNGS can not be excluded. The spectrogram indicated no time-dependent changes of the vibrational background.

5.2.2 R&D-Refrigerator

For detector operation, the vibrational background within the refrigerator is of greatest interest. In the R&D-refrigerator, in ten cooldowns, the geophone was mounted on four different stages, in the order (1) 4 K-plate, (2) Still plate, (3) particle shield, and (4) 60 K-plate. For all positions, a time window during the cooling phase was chosen where the spectrogram did not indicate major background changes and, due to the geophone transition at lower temperatures, where the temperature was above 10 K. A comparison of all average spectra of the chosen windows is shown in figure 5.14.

While the PSD is on the same order of magnitude for all positions, a suppression for high frequencies on the particle shield can be noticed. This is expected to be caused by the particle shield's high inert mass (190 kg).

Another difference is the appearance of a 1.4 Hz peak and its harmonic excitations over the complete spectrum for the measurement on the 60 K-plate and the particle shield. These measurements were taken after moving the refrigerator from Munich to Garching and imply a change of coupling to the PT.

A zoom-in of the low-frequency region is shown in figure 5.15. The low-frequency background reduced in the same order as the measurements were taken, indicating that

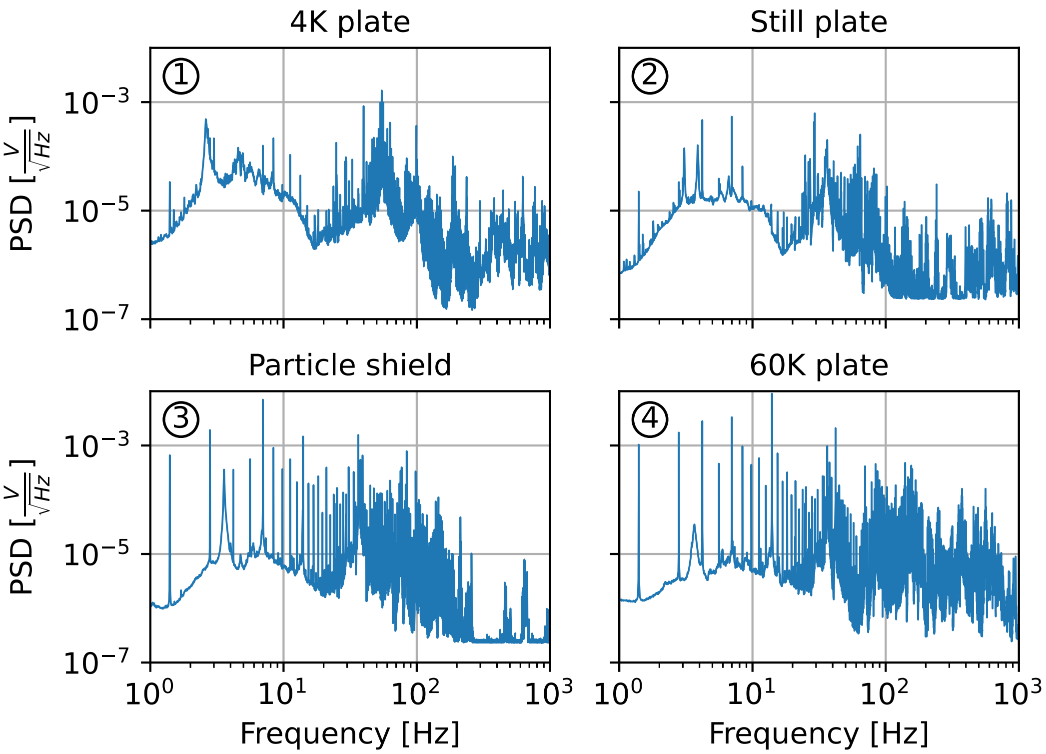

Figure 5.14: Measured PSD during cooldown for the (1) 4 K-plate (2023-09-08), (2) Still plate (2023-11-27), (3) particle shield (2024-04-16), and (4) 60 K-plate (2024-06-08). The first two measurements were taken when the refrigerator was located in Munich. Before the measurements (3) and (4), the refrigerator was moved to Garching. After moving the refrigerator, new strong contributions of 1.4 Hz and its harmonic excitations are visible (as spikes) in the spectrum.

improvements within the laboratory, as described in a later section, 5.3.1, proved to be successful for vibration damping. In general, since the refrigerator is operated in the new MPP building in Garching, the spectrograms seem to have fewer features, and the noise conditions appear more constant over the day.

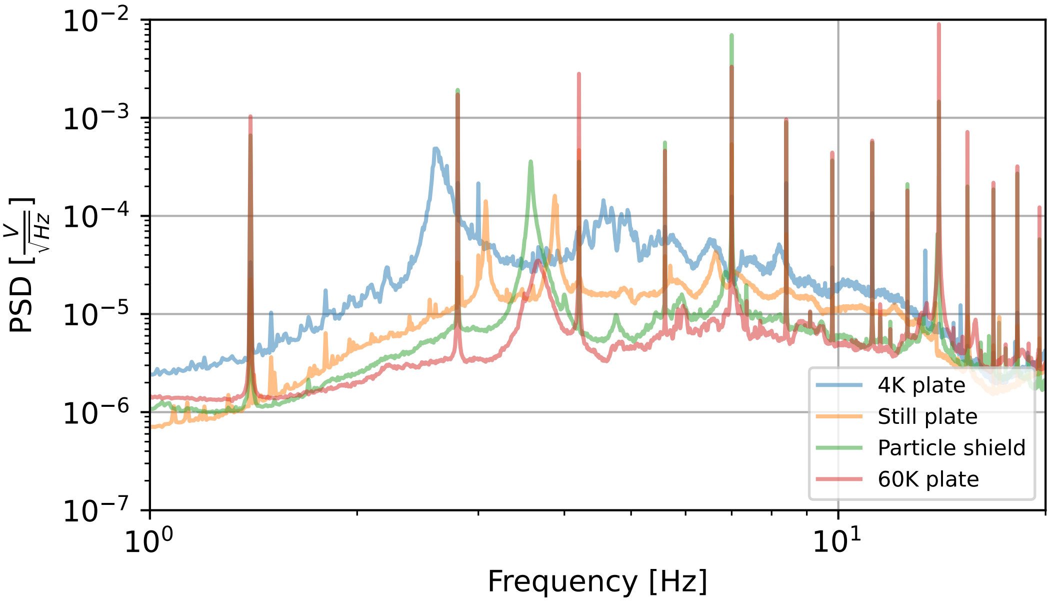

Figure 5.15: Low frequency vibration PSD for different temperature stages. Each dataset was taken on different dates at different locations: (1) 4 K-plate: Munich, 2023-09-08, (2) Still plate: Munich, 2023-11-27, (3) particle shield: Garching, (2024-04-16) and (4) 60 K-plate: Garching, (2024-06-08)). The achieved noise level does not correlate with the position of the geophone within the refrigerator but instead with the date of data taking. The lowest noise was measured on the 60 K-plate, which was measured last.

Nevertheless, the datasets taken in Garching show a new set of features that can be attributed to general traffic, particularly to the Munich subway line “U6”. The spectrogram for one typical day in August is shown in figure 5.16.

In between $(2 - 20)$ Hz, the noise level increases during the day compared to night times. Generally, these phases of higher noise range from roughly 6:00 to 20:00 (local time) and are much less pronounced on weekend days and public holidays. Additionally, the spectrograms show a frequently occurring increased power in the $(5 - 10)$ Hz range. The time schedule of this feature fits remarkably well with the estimated arrival and departure time of the U6 (within some tolerance for delays and cancellations). Figure 5.17 shows the integrated geophone signal between $(5-10)$ Hz and the vertical magnetic field at the refrigerator, measured with a fluxgate magnetometer.

It is shown that the geophone features often coincide with magnetic field changes on the order of $0.2\,\mu$T, and a scheduled U6-arrival or departure.

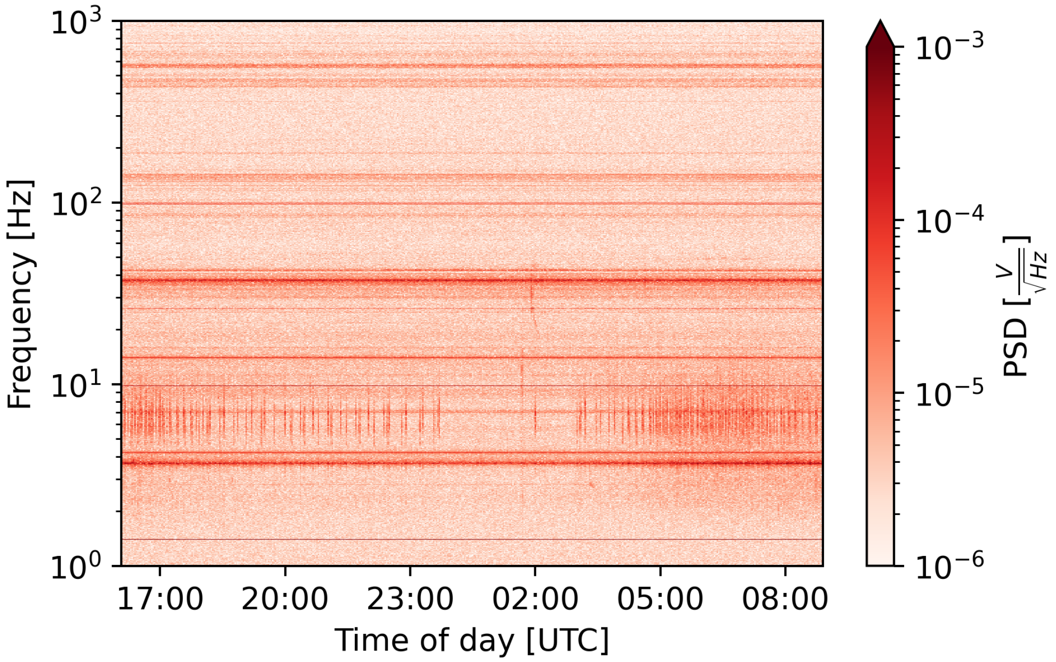

Figure 5.16: Spectrogram measured on the 60 K-plate in the R&D refrigerator in Garching during the night from 20th to 21st of August 2024. The measured vibrations are constant throughout the day except for features in the (5-10) Hz region. The timing fits the arrival and departure schedule of a nearby subway.

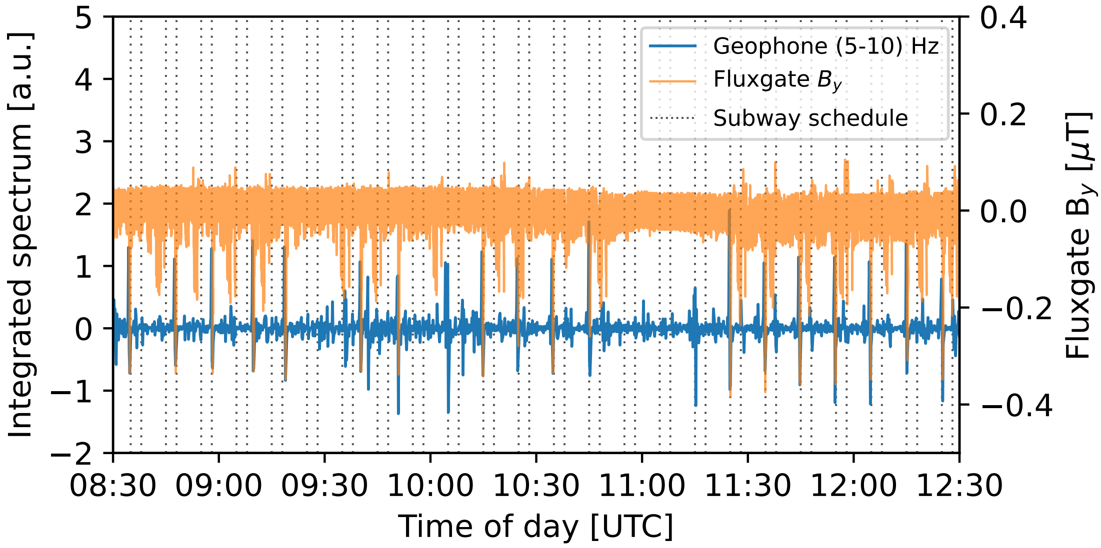

Figure 5.17: Geophone and fluxgate measurements of the vertical magnetic field B_y close to the refrigerator during a working day. The vertical dotted lines mark scheduled arrivals and departures of a nearby subway.

5.2.3 COSINUS-Refrigerator

In October 2024, the commissioning cooldown of the COSINUS-refrigerator at LNGS started. For this cooldown, the geophone was moved to the new refrigerator and mounted to the 4 K-plate below the extension. During the cooldown, the DAQ lost connection to the device due to a faulty cable. However, during the first few days, good data could be collected. A comparison of the average PSD of the R&D-refrigerator in Munich and the COSINUS refrigerator at LNGS is shown in figure 5.18.

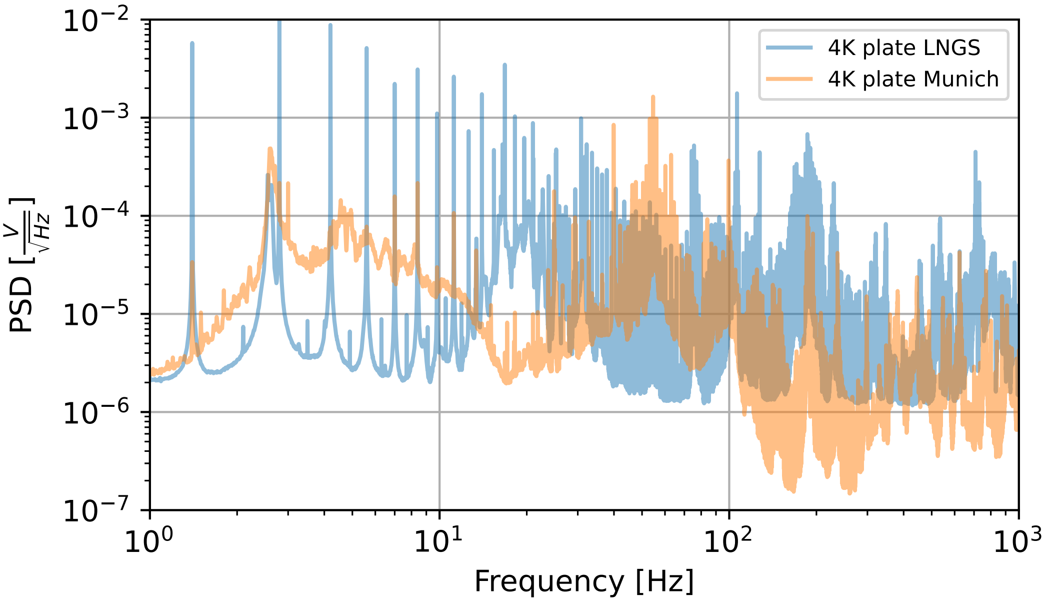

Figure 5.18: Comparison of the vibrational background on the 4 K-plate for both COSINUS refrigerators. The data was taken during the initial cooldown before reaching 10 K. Aside from the strong contributions at 1.4 Hz and its harmonics, the COSINUS-refrigerator is quieter at low frequencies (< 10 Hz), but sees more vibrations at higher frequencies instead.

The vibrational operation conditions within LNGS were constant over the day and, compared to Garching, more quiet for frequencies below 10 Hz. Furthermore, the dataset contains substantial contributions at 1.4 Hz and its harmonic excitations throughout the complete frequency spectrum. This behavior is similar to the one observed in the R&D-refrigerator in Garching after moving it from Munich (as seen in figure 5.15).

5.3 Vibration Mitigation Strategy

The COSINUS strategy for vibration mitigation follows two main principles:

1. **Damping of known noise sources:** Many machines, such as pumps and compressors, are known to be vibrationally active. By rigidly attaching them to a high inert mass, such as a concrete block, the generated displacement can be reduced. Another very effective way of damping is granular damping by sand, which converts the kinetic energy into heat by friction [208].
2. **Decoupling of sensitive parts:** Within the facility, sensitive parts are carefully separated from known noise sources to minimize any transmission. A loose connection with low transmissibility (e.g. a flexible bellow or a cloth) is used where an airtight connection between structures is required.

Both facilities, the R&D-facility in Garching, as well as the COSINUS-facility at LNGS, were designed with these principles in mind. On the refrigerator level, the “UQT”, a unique system among other dilution refrigerators, is used. Finally, on the detector level, a spring-based passive decoupling system leads to a broadband reduction of vibrational noise.

5.3.1 Facility

Garching

The refrigerator in the Garching facility is solidly screwed into the laboratory floor to ensure a solid base without any floating behavior. The (currently known) most active noise sources are the rotary valve of the PT and the Still turbo-molecular pump for the mixing circuit. The measures to dampen and decouple these sources are depicted in figure 5.19.

The rotary valve is bolted to a steel pillar, which itself is bolted to the laboratory ceiling. Between rotary valve and pillar, as well as between pillar and ceiling, rubber-like butyl mats are interleaved to minimize the transmissibility to the refrigerator through the ceiling, walls, and floor.[8] All tubes connecting to the rotary valve, as well as the buffer volumes and valve itself, were wrapped in thermal insulation tubes, which mainly reduced the airborne acoustic noise.

The turbo-molecular pump was bolted to a concrete block to add mass to the system. A chimney-like Al frame was constructed around the Still pumping tube above the pump and filled with sand for granular damping.

---

[8] Immediatly after adding the mat, a new record for the base temperature of the refrigerator could be reached, showing the effectiveness of the measure.

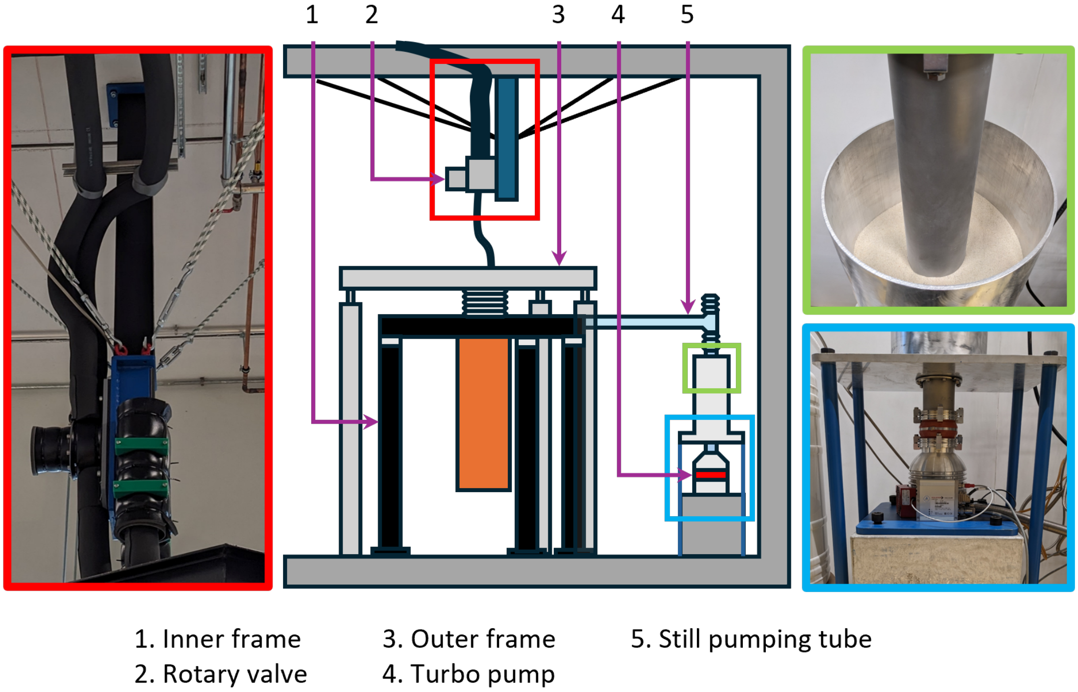

Figure 5.19: Sketch of the R&D-facility in Garching and vibration damping measures taken to reduce the vibrations induced by the infrastructure of the dry dilution refrigerator.

LNGS

The complete structure of the COSINUS facility at LNGS consists of two nested frames with no contact to each other:[9] an inner frame designed for low vibrational noise, and an outer frame that houses any other equipment necessary to operate the refrigerator. The rotary valve is mounted on a pivotable structure, which is connected to the outer frame, while the refrigerator is connected to the inner frame.

Both the pivotable structure and the pillars of the inner frame are filled with sand for further granular damping. The mixing circuit turbo-molecular pump is mounted on the outer frame in a separate box also filled with sand. Similar to the R&D-facility, the tubes connecting the rotary valve with the compressor are covered in thermal insulation tubes. The damping measures are shown in figure 5.20.

In October 2023, the vibrational background on both frames was measured and previously published in [126]. Accelerometers of type PCB393b05 and KS48C by MMF were used for the inner and outer frames, respectively. The measurements were taken within the operational clean room, but without a refrigerator and with an empty water tank.

---

[9] Technically, a loose contact is provided via a flexible sailing cloth connecting both frames to allow for over-pressure in the clean room. However, the transmissibility is assumed to be negligible.

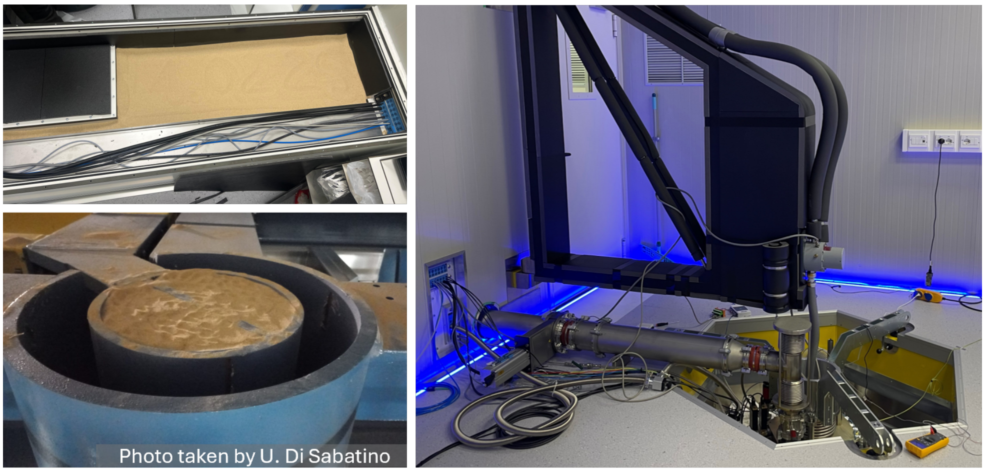

Figure 5.20: Vibration damping measures taken in the COSINUS facility at LNGS. The left photos show the sand used for granular damping within the inner pillar of the building (bottom left) and in a box around the Still pumping tube (top left). The latter is additionally revetted in acoustic insulation. The right photo shows the refrigerator installed in the drywell inside the clean room. The black structure is the pivotable structure that holds the rotary valve of the PT. It is filled with sand and revetted in acoustic insulation as well.

Figure 5.21 shows the exact measurement positions of the sensors. The average PSD for vertical and horizontal vibrations are shown in figure 5.22.

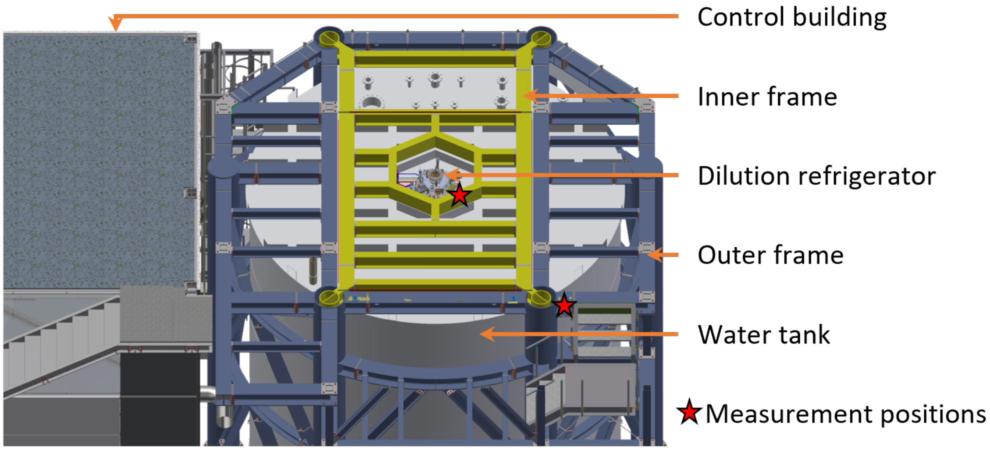

Figure 5.21: Double frame structure of the COSINUS facility. The red stars mark the measurement position for a vibrational background measurement. Reprinted from [126].

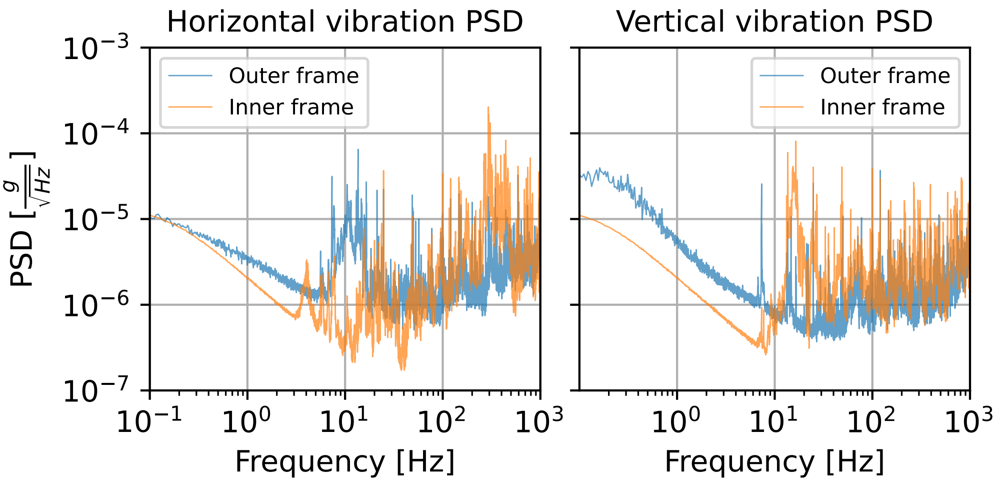

Figure 5.22: Vibrational background measured on both frames in vertical and horizontal direction within the clean room. The inner frame was measured to be more silent below 10 Hz. At higher frequencies, for vertical vibrations, a larger background was measured on the inner frame. Reprinted from [126].

For both directions and frames, the vibrational noise level was measured to be on the same order of magnitude. A clear difference in the vibrational noise is seen for frequencies smaller than 10 Hz, where the PSD of the inner frame is up to a factor 4 reduced, compared to the outer frame. This reduction is more prominent for vertical vibrations than for horizontal vibrations. At higher frequencies, for vertical vibrations, a larger background was measured on the inner frame; however, an airborne acoustic origin can not be excluded. With the operational refrigerator, the difference between both frames is expected to increase due to the added noise sources on the outer frame.

5.3.2 Ultra-Quiet Technology

Both dry dilution refrigerators were manufactured by CryoConcept and designed with the UQT. It is a system that vibrationally and electrically decouples the PT head from the instrumented space within the refrigerator. In [140], the effectiveness of the decoupling was proven, showing a reduction of PT-induced vibrations up to two orders of magnitudes. A demonstration within the COSINUS-refrigerator at LNGS is shown in section 5.6.1.

The PT-head is connected to an outer steel frame, while the remaining parts of the refrigerator are mounted to an inner steel frame. There is no physical contact between both frames except for a flexible bellow that allows for vacuum tightness. Teflon (PTFE) pieces ensure electrical isolation of the inner frame. To provide the required pre-cooling, the PT and the corresponding stages on the instrumented part are equipped with nested radiators with no direct contact with each other. Exchange gas transfers heat from the PT to the DU. The UQT-principle is shown in figure 5.23.

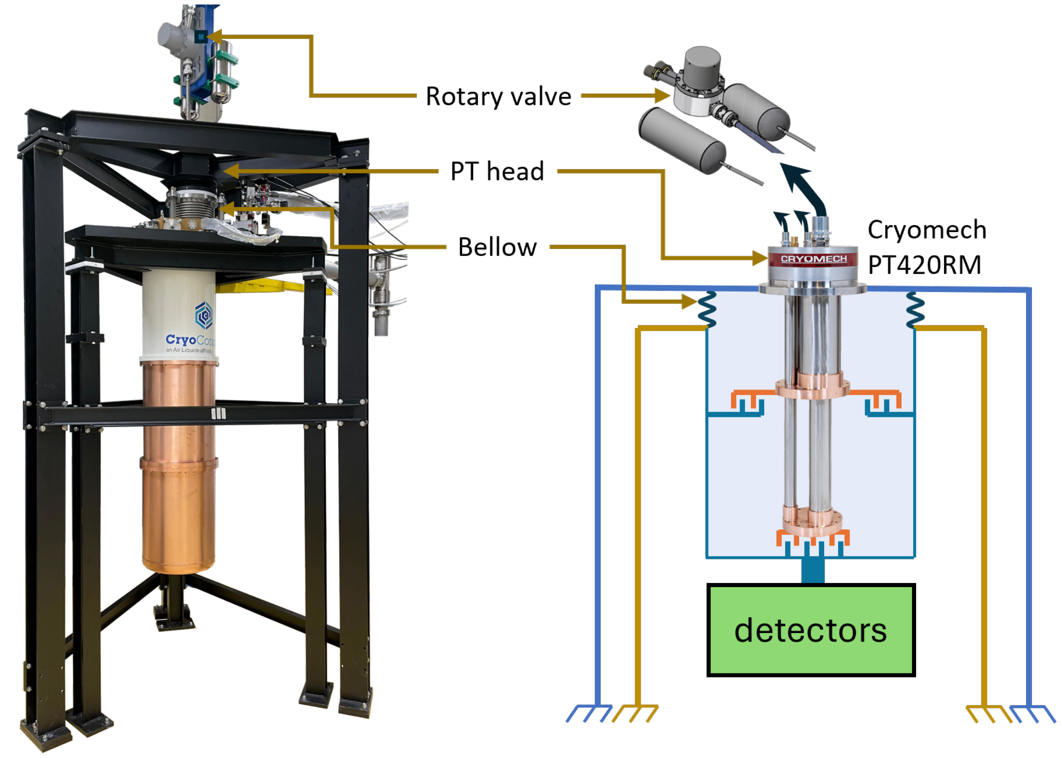

Figure 5.23: UQT-principle in the R&D-refrigerator. The PT-head is connected to the outer frame and the rotary valve on the ceiling, while detectors are connected to the inner frame. Both frames are only in contact via a flexible bellow.

The R&D-refrigerator in Garching is part of a standard production line of CryoConcept with a straightforward implementation of the UQT. At LNGS, the COSINUS-refrigerator is located within the drywell in the water tank, which requires a custom-made implementation of the UQT. A drawing thereof is shown in figure 5.24.

The yellow frame of the facility corresponds to the outer frame of the UQT, onto which the PT-head is fixed, while the water tank plus drywell correspond to the inner frame.[10] To increase the mass of the refrigerator, it is screwed into the topmost ring of the particle shield inside the drywell. The bottom of the OVC is pressed against the bottom of the particle shield. Since the refrigerator will be regularly moved in and out of the drywell, the UQT has to be readjusted for every cooldown using three screws on top of the refrigerator. A camera system was installed to ease the alignment of the setup.

---

[10] The water in the tank will add a big mass to the system, which is subject to internal damping. Therefore, a comparatively low vibrational background is expected.

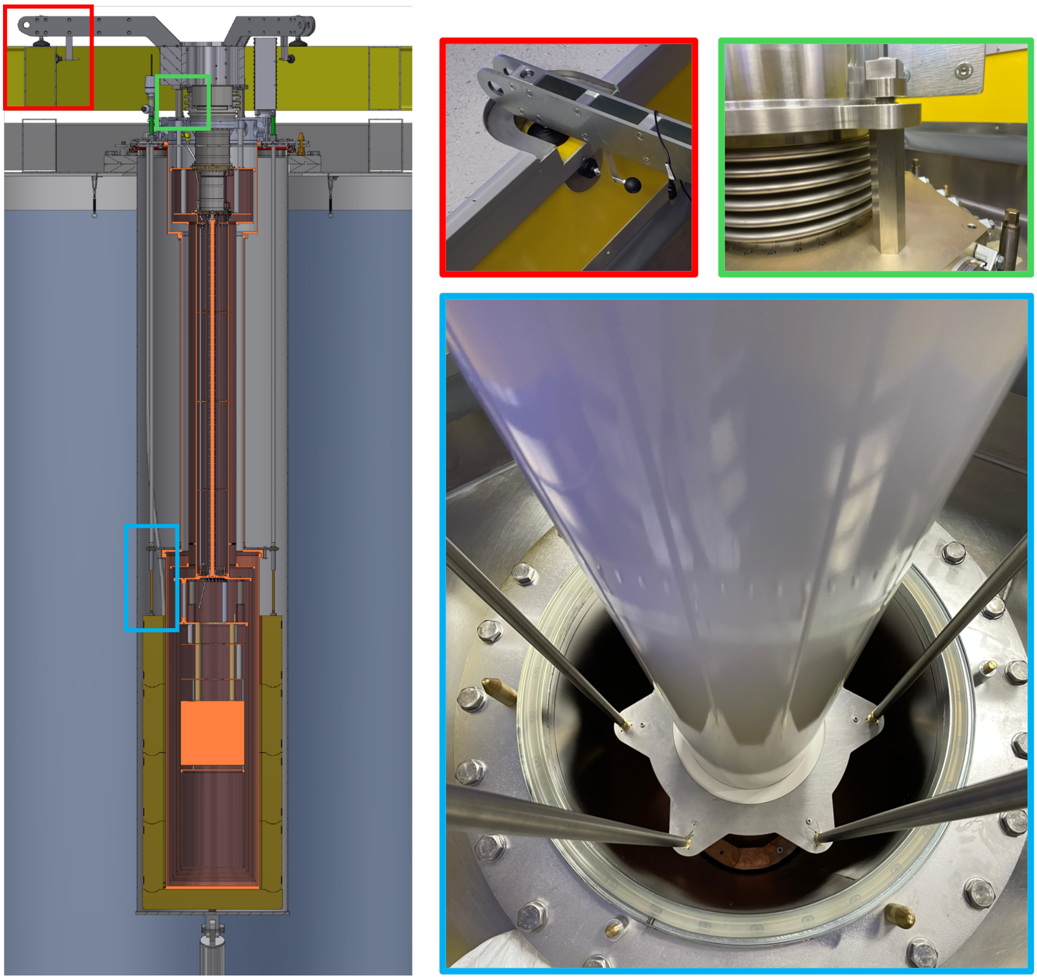

Figure 5.24: Implementation of the UQT for the refrigerator located at LNGS. The PT is fixed to the yellow frame, while the instrumented part of the refrigerator is screwed to the outer particle shield within the drywell (blue box), which rests on a tripod on the water tank floor. In contrast to the R&D-refrigerator in Garching, in this refrigerator, the OVC is not hanging but pressed against the bottom plate of the inner Cu shield. The UQT can be set up via screws on three sides (red box). The green box shows the flexible bellow required for the UQT.

5.3.3 Spring-Based Decoupling System

In the COSINUS R&D-refrigerator, without any additional decoupling, no detector could reach its ideal operation conditions. Only when the PT was switched off were the detectors cooled enough to make temperature stabilization and operation feasible. This points towards vibrations as the source of the instabilities.

Therefore, an additional level of decoupling is added to the MC stage within the refrigerator. It is a single-stage spring-based passive decoupling system that utilizes the frequency response of a damped harmonic oscillator with base excitation [209]. The oscillator is characterized by the resonance frequency ω_0 and quality factor Q:

$$H(\omega) = \frac{1 + \frac{i}{Q}(\frac{\omega}{\omega_0})}{1 + \frac{i}{Q}(\frac{\omega}{\omega_0}) - (\frac{\omega}{\omega_0})^2}. \tag{5.11}$$

Figure 5.25 shows the transmissivity of the system for different Q.

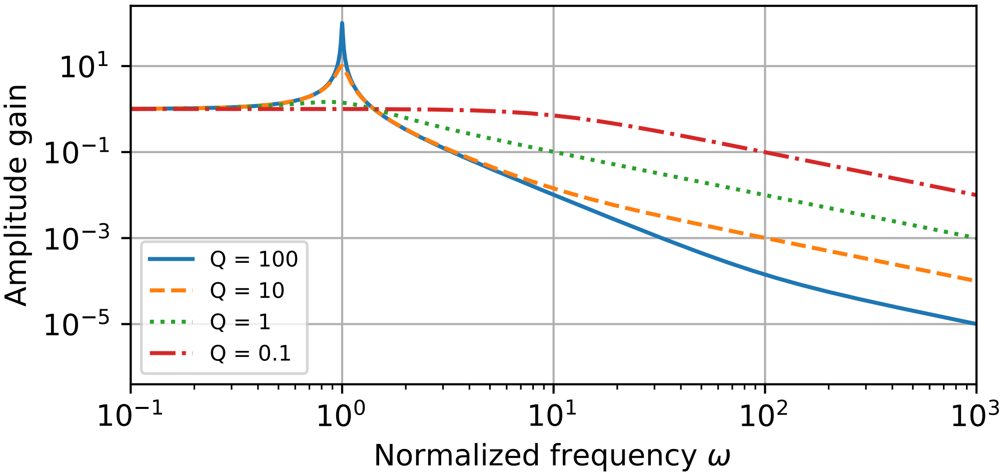

Figure 5.25: Transfer function of a harmonic oscillator for different quality factors Q. Larger quality factors correspond to less damping. A system with a quality factor < 0.5 is overdamped and does not oscillate.

The oscillations of an undamped oscillator are amplified at its natural frequency. For higher frequencies, the response is reduced by ω^{-2}. In an effective decoupling system, the resonance frequency $\omega_0 = \sqrt{\frac{k}{m}}$ should be chosen as low as possible. This is achieved in a spring system by choosing a low spring constant k and high inertial mass m, while an effective pendulum system would feature a long length.

When introducing a damping term proportional to the velocity, the resonance peak reduces, but the frequency response for higher frequencies reduces to an ω^{-1}-behavior. A good decoupling system achieves a good balance between its decoupling capabilities and damping, suppressing the resonance and dissipating the kinetic energy in a controlled channel.

5.4 Internal Passive Vibration Decoupling System

The design and first tests of the COSINUS decoupling system were previously published in [126].

5.4.1 Design

The COSINUS decoupling system consists of the detector box, which is hung on three "decoupling strings" that are fixed and thermalized on the internal particle shield.[11] Each single string is routed through a cutout of the particle shield and consists of a spring, a damping module, and Kevlar wire. They can provide a decoupling in vertical direction (due to the springs) and horizontal direction (like a pendulum). A separate Cu-link between the detector box and MC plate provides the thermalization and introduces damping to the system. Figure 5.26 shows a conceptual drawing of the system.

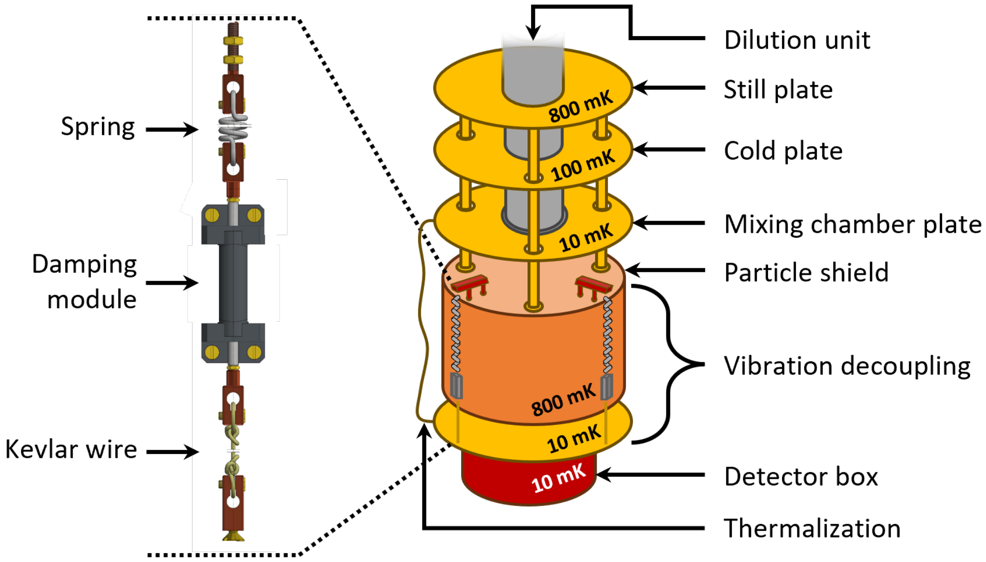

Figure 5.26: Decoupling concept for COSINUS. The detectors will hang from three decoupling strings (on the left) anchored at the particle shield. Reprinted from [126].

The different components fulfill different roles in the system:

- The spring delivers the damping capabilities of the decoupling string in vertical direction. Springs made from CuSn are preferred for their good thermal conductivity. All springs considered and tested are listed in appendix C.
- A damping module can be added to the string if the detector cabling and thermalization do not provide sufficient damping. Eddy current dampers [210, 211] and frictional dampers that dissipate energy to the particle shield were under consideration. However, current operations in the COSINUS R&D-refrigerator indicate that no further damping is needed.
- The Kevlar wire is required to thermally isolate the detector box (T ~ 10 mK)

---

[11] The high inert mass of 190 kg makes the particle shield an ideal starting point for the decoupling system.

from the particle shield (T ∼ 800 mK). Furthermore, it acts as an extension to reach the required pendulum length for horizontal decoupling.

The lowest excitation frequency that is expected in the refrigerator is 1.4 Hz, the PT operation frequency given by the rotary valve. The decoupling system in this work was designed for resonance frequencies around 1 Hz, to ensure that the main PT frequency is in the decoupled range. However, most of the vibration power measured in the refrigerators lies at frequencies higher than 20 Hz. A decoupling with a resonance frequency of 2 Hz proved effective enough for detector operation. In general, systems with higher frequencies are easier to produce due to limited space and material constraints.

5.4.2 Refrigerator Mockup System

A mockup system of the refrigerator was produced and built at MPP to test the first decoupling prototypes. It simulates the lower refrigerator part from the Still plate downwards using steel instead of Cu for the particle shield and Al for the Cold and MC plates. Instead of a detector box, lead bricks and brass weights with a combined mass of 15 kg were used. A photograph of the mockup is shown in figure 5.27

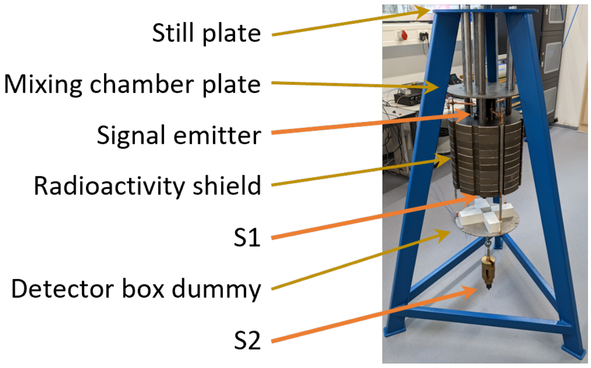

Figure 5.27: Mockup system of the refrigerator used to characterize prototype decoupling systems. Reprinted from [126].

In a first test campaign, three springs made from spring steel 1.4310 with a 25 N pretension were mounted. They reached a length of 213 mm under a load of 50 N per spring. A non-functional damping module dummy with a length of 90 mm and braided Kevlar wire with a length of 155 mm extended the length per decoupling string to 550 mm (including Cu-connection pieces).

On top of the particle shield, a shaker of type 4810 by Brüel and Kjær [212] was mounted as a signal emitter. It can be driven by an arbitrary signal generator connected to a preamplifier with a dynamic range of 10 Hz to 30 kHz. Sensor and shaker were controlled, timed, and read out with a NI-USB 6211 DAQ by National Instruments. On the bottom of the detector box dummy (S1 in figure 5.28), and below the particle shield (S2 in figure 5.28), an accelerometer of type PCB393b05 by PCB was mounted to measure vertical vibrations.

To excite the system, the shaker was set up to emit logarithmic swept sine signals from 0.1 Hz to 5 kHz over 100 s, while the response was measured at both measurement positions, S1 and S2. Additionally, the background without any shaker emission was measured. Figure 5.28 shows all spectra and their ratio.

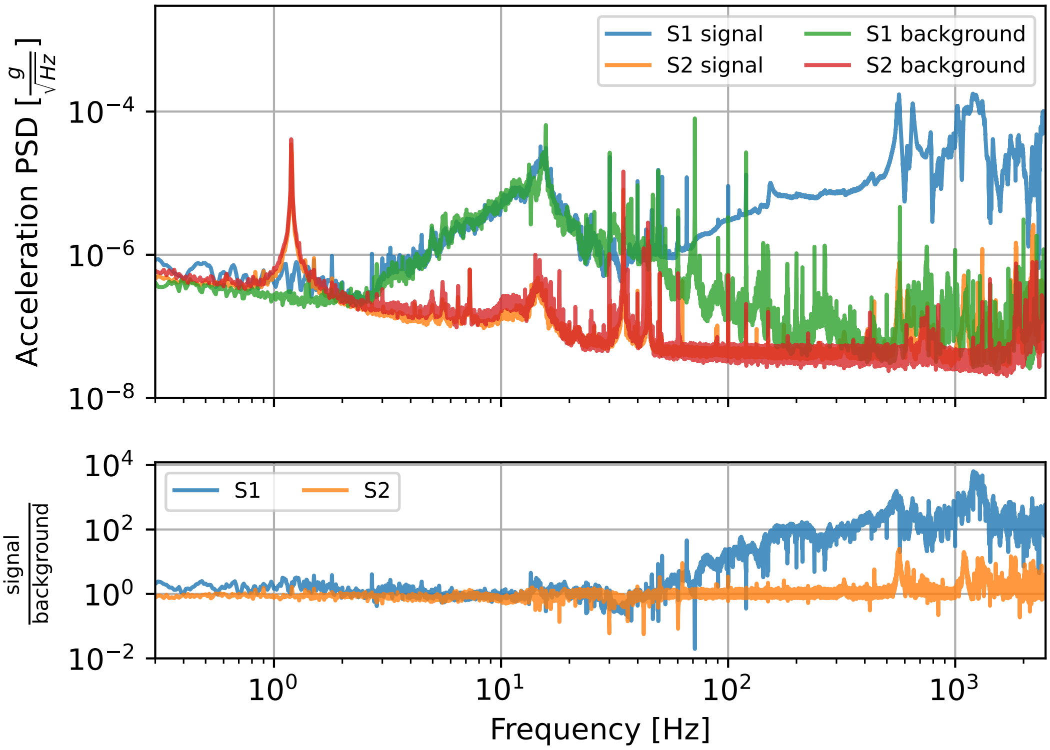

Figure 5.28: Measurement results on the mockup system for swept sine signals sent by a shaker. The top plot shows measured signals and vibration backgrounds on the measurement positions S1 (at the particle shield) and S2 (on the bottom of the decoupled part). For frequencies higher than 50 Hz, the shaker excitations are seen at position S1 only. Reprinted from [126].

The spectrum measured at the detector level shows a sharp peak at 1.2 Hz, corresponding to the springs' resonance frequency. For frequencies higher than 50 Hz, the shaker excitations become visible in the PSD measured on the particle shield. However, for the detector box accelerometer, no significant difference between signal and background is seen, successfully proving the decoupling capabilities at these frequencies.

In a follow-up measurement, the shaker was exchanged with an impulse hammer of type IH-05 by Sigmatest [213]. With this instrument, it is possible to induce stronger broadband excitations into the system. The user applies the hammer on a defined spot on the structure. With an in-built piezo disk, the impact force and duration can be measured and used to discard faulty data. Since with the hammer, a variance in impact strength is introduced, the resulting PSDs can not be averaged directly. Nevertheless, the transmissivity between both measuring positions can be calculated for each hit and then averaged. The PSDs for one example hit, and the resulting averaged transmissivity are shown in figure 5.29.

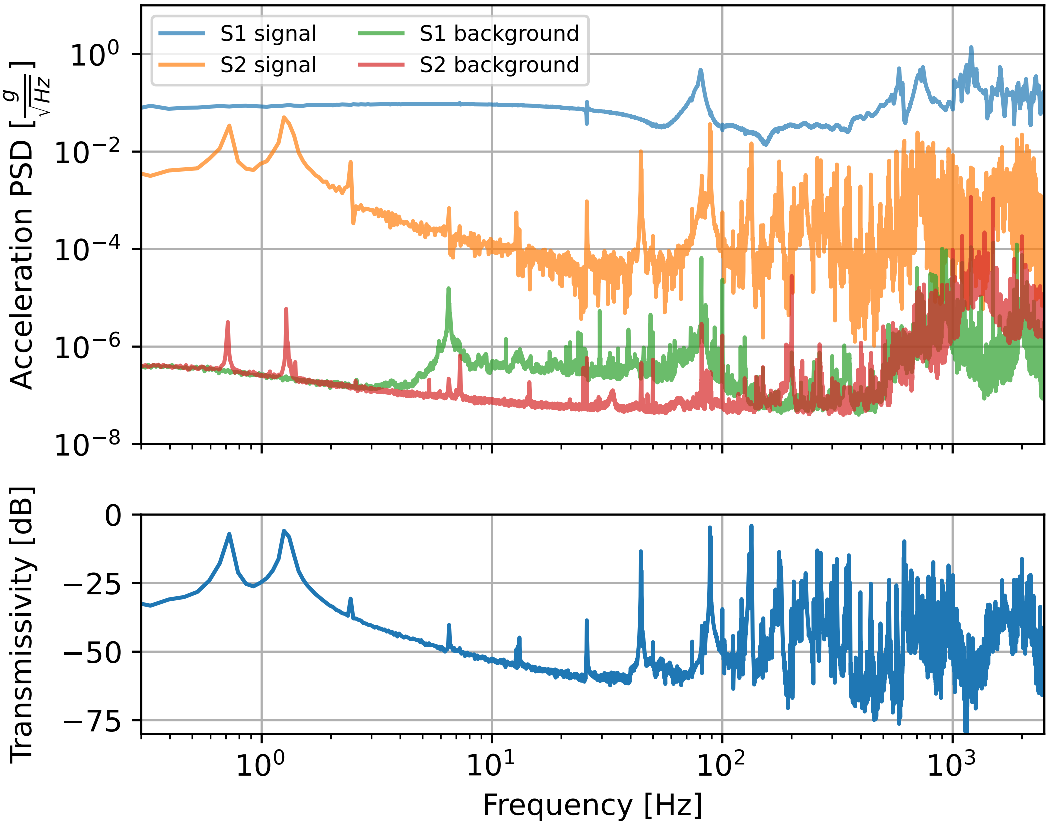

Figure 5.29: Impact test results. The top plot shows an example signal on both measurement positions (S1 signal, S2 signal) and the background on both positions (S1 bkg, S2 bkg). The bottom plot shows the averaged transmissivity calculated from the signals of both positions with five hits.

With the impulse hammer, it is possible to excite the structure with a flat frequency spectrum, as seen from the S1 signal. The excitation is then transformed by the decoupling system, and frequencies higher than the resonance are suppressed. This result proves the principle of the decoupling system. For frequencies higher than 100 Hz the response becomes chaotic due to airborne acoustic background and resonances within the excitation structure.

A new feature in the detector-level data, which was previously not present for the shaker-test data, is a second resonance peak around 0.7 Hz. This peak corresponds to the pendulum frequency of the decoupling system. For the hammer test, the sensor was mounted on the detector plate dummy itself instead of being mounted on the brass weight below (as shown in figure 5.27). The brass weights were instead loaded on top of the plate, changing the dynamics of the system to a system that is closer to the final decoupling system.

5.5 Decoupling System Validation

5.5.1 R&D-refrigerator

After the successful proof of principle on the mockup system, the decoupling prototype was mounted to the R&D-refrigerator. The implementation is shown in figure 5.30.

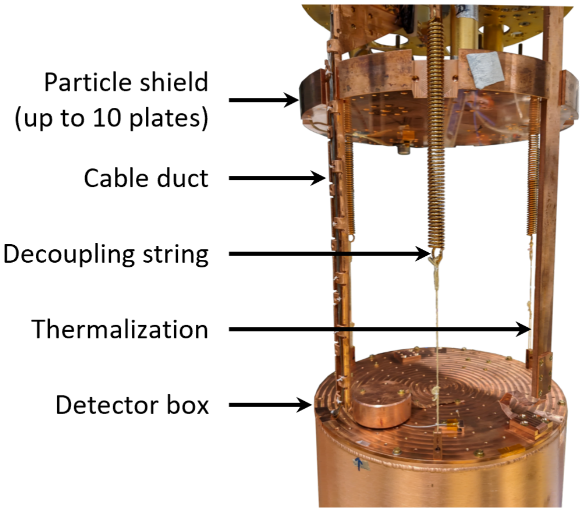

Figure 5.30: Prototype implementation of the decoupling system to the R&D-refrigerator. The system was successfully tested with the complete particle shield mounted (10 plates) and with only 10% mounted (1 plate as depicted).

Three decoupling strings are mounted with CuSn-springs that were designed to keep a detector box mass of 15 kg with a resonance frequency of 2 Hz. They are thermalized by clamping one end between two Cu-pieces, which are screwed into the particle shield. Braided Kevlar wires connect the detector box to the springs. A cable duct made from Cu and a solid Cu-piece for thermalization are routed in parallel to the decoupling strings. The last centimeter distance to the detector box is bridged with soft connections made from thin Cu-foil with high conductance (0.1 mm thickness, 30 mm width, 90 mm length).

With this decoupling system prototype, without further modification, it is possible to operate COSINUS detectors without being subject to strong microphonics. This is demonstrated in figure 5.31 with a 30 g detector, the heaviest so far operated in this refrigerator.

For the future decoupling system in the COSINUS refrigerator, it was concluded that a vertical resonance frequency of 2 Hz is sufficient and that no further means to decouple

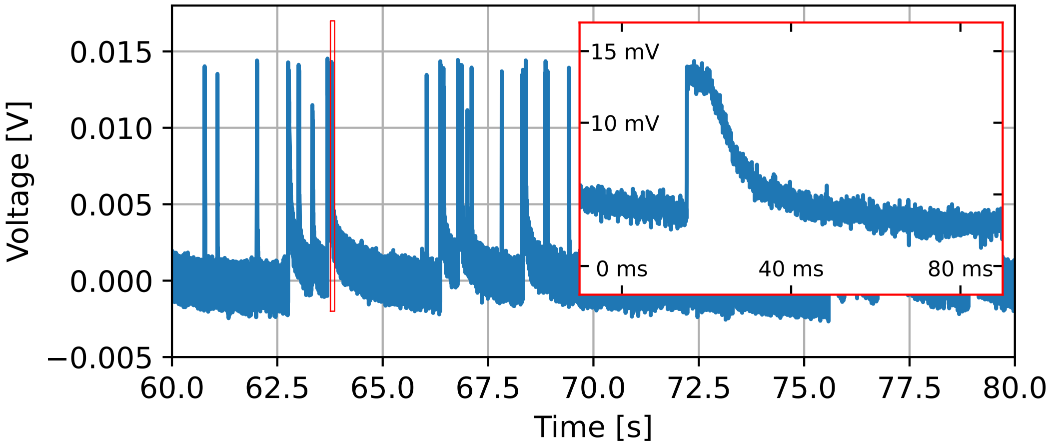

Figure 5.31: Data stream of a 30 g NaI-detector measured above-ground. The inset shows a zoom to a single pulse. This detector is not dominated by microphonics.

the PT main frequency are required. Furthermore, the damping provided by the thermal link and cables is sufficient for detector operation. Therefore, no damping module will be needed.

5.5.2 COSINUS-refrigerator

Shortly before submission of this thesis, the decoupling system was validated in the COSINUS-refrigerator located at LNGS. The system was mounted with the lowest achievable damping, i.e. the detector box was hung on the springs without any detector cabling and very soft thermalization strips. For this measurement, two newly built geophones were mounted on the MC-plate ($f_r \approx 2.3\,\mathrm{Hz}$) and on the detector box ($f_r \approx 1.4\,\mathrm{Hz}$). In contrast to the previous measurement, described in section 5.2.3, the water tank of the COSINUS-facility was now filled with water. This is expected to affect the measured vibration spectra, as the OVC of the refrigerator is in direct contact with the inner shielding inside the drywell and thus in contact with the water tank.

The data shown here was taken in February 2025 and was stable over most of the data taking time. For the first time, the performance of the decoupling system can be characterized at low temperatures. The corresponding plot is shown in figure 5.32.

Both geophones have similar sensitivities (on the order of 10 V/(m/s)), but exact calibration curves have not yet been taken into account. However, the general shape of both spectra allows us to draw first conclusions:

- For the geophone located on the MC (blue), the device resonance frequency can be seen as a peak at 2.3 Hz. The detector plate geophone (orange) exhibits a peak at 1.38 Hz, which is, however, almost indistinguishable from the PT-frequency at 1.4 Hz. A flat geophone response is only ensured well above the resonance frequencies.

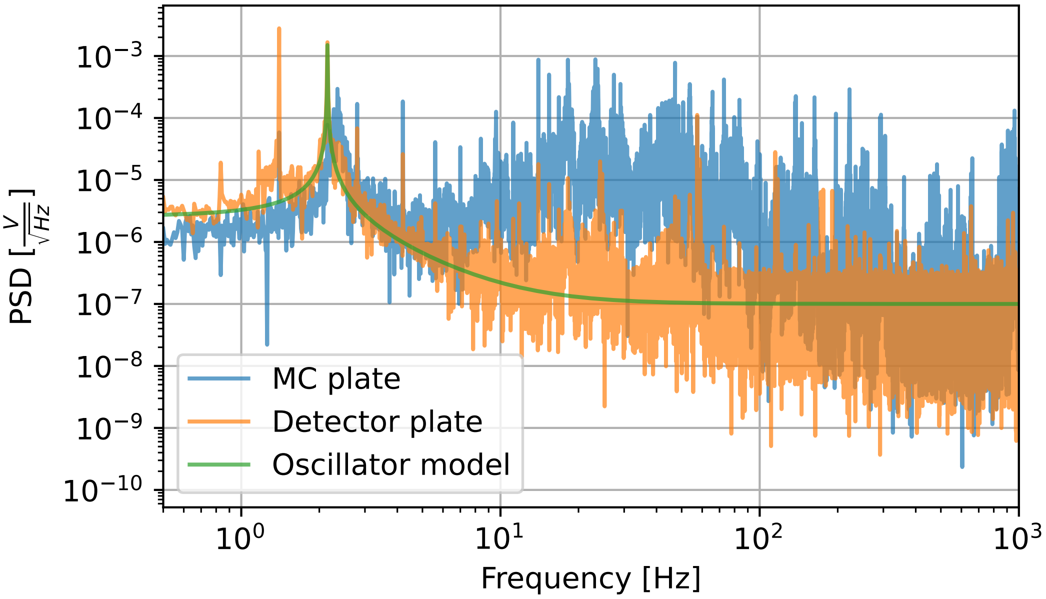

Figure 5.32: Vibration PSD for a 2 min window during data taking. The blue and orange curves show the spectra measured on the MC plate and detector plate, respectively. The green curve is a scaled response curve of an ideal harmonic oscillator with a flat noise contribution of $10^{-7}\,\mathrm{V}/\sqrt{\mathrm{Hz}}$. It has a resonance at 2.15 Hz and a quality factor of 600.

- The spectrum on the MC plate is dominated by higher frequency contributions ($f \gtrsim 10\,\mathrm{Hz}$). Similar observations were made in the earlier measurement on the 4 K-plate (see figure 5.18).
- The decoupling system achieves a decoupling of vibrations at higher frequencies than its resonance frequency. As designed, the spring system behaves like a harmonic oscillator with a resonance frequency of 2.15 Hz and a quality factor of ∼600. This corresponds to the minimal damping case, as there is no detector cabling, which would introduce additional damping.
- Both detectors measure 1.4 Hz and its harmonic excitations. The lines are reduced on the decoupled geophone on the detector box. This implies that they are indeed actual vibrations and not electronic interferences from the PT-rotary valve and that the decoupling system successfully suppresses higher excitations.

In this measurement campaign, the UQT was also validated. During the measurement, the UQT-system was “switched off” by putting both frames within the refrigerator in contact with each other.[12] The results are shown for the geophone on the MC-plate in figure 5.33.

---

[12] This can be achieved by tilting the inner frame with respect to the outer frame.

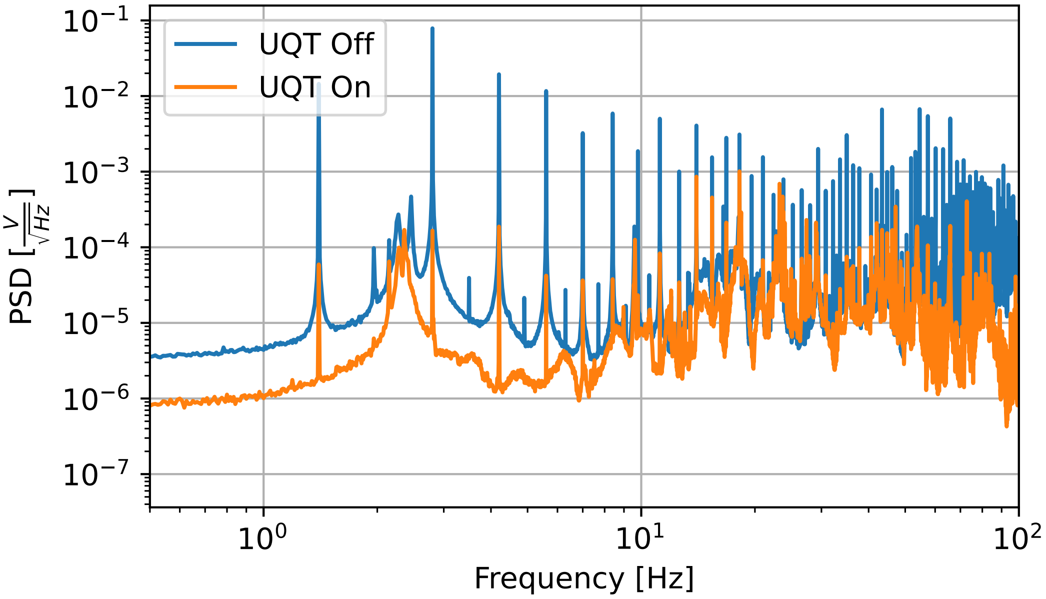

Figure 5.33: Averaged vibration PSD measured on the MC with (orange) and without (blue) UQT. The UQT reduces PT-induced vibrations (1.4 Hz and its harmonic excitations) up to a factor ∼300.

By switching off the UQT, PT vibrations at 1.4 Hz and its harmonic excitations increased up to a factor ∼300.[13] Thus, the working principle of the UQT is proven. A detailed analysis of the complete data is subject of a future publication.

5.6 Future Developments

5.6.1 Final Decoupling Design

The design for the final decoupling system is shown in figure 5.34.

The spring is pressed between two Cu-plates and thermalized on the particle shield. A special holder allows for the fine adjustment of the spring bearing height to balance and level the detector box. On the bottom side, a braided Kevlar wire connects the spring with the detector box. The connection between spring and Kevlar is done with a simple bowline knot. One addition will be a fall stop that is added to the particle shield. If the wire tears, the detector box will not fall into the thermal shield but will be caught by the particle shield.

5.6.2 Future Directions

With the decoupling system developed in this work, it became possible to operate heavy cryogenic detectors with good energy resolution in a dry dilution refrigerator. However,

---

[13] This, again, indicates that the sharp peaks are real vibrations and not electronic interferences.

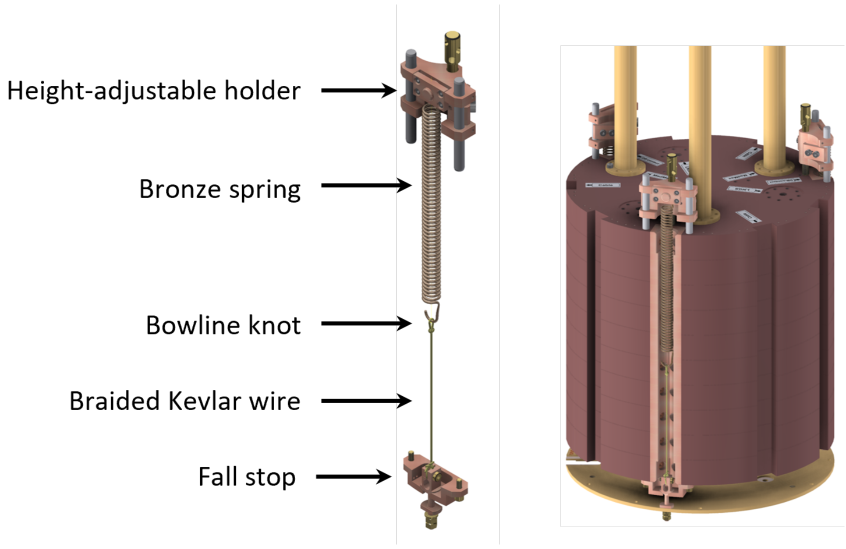

Figure 5.34: CAD of the decoupling system as it will be implemented.

it is yet to be explored if vibration-induced noise still makes up a sizable part of the detector noise. The geophone allows to monitor vibrations within the refrigerator during a cooldown. Future analysis procedures could try correlating measured vibrations with detector data to get an in-depth understanding of the background and possibly improve the performance.

On the hardware side, the decoupling system will be upgraded along the refrigerator to meet new requirements. For this, new spring materials and designs can be explored to allow for lower resonance frequencies. Furthermore, the damping module concept can be explored further for a defined damping rate independent of cabling and thermalization.

An extension that is already under development is a thermal switch for the decoupling. At RT, the detectors would rest in the fall protection, allowing for a safe horizontal movement of the refrigerator from the mounting area to its operating position inside the drywell. When the system cools down, the spring material becomes more rigid, and the spring constant increases. As a result, the length of the complete decoupling string reduces (around 5 mm for the CuSn-springs in use), and the detector box lifts up.

Another extension currently in development is a displacement sensor that can operate at sub-Kelvin temperatures. The benefit of such a sensor would be its excellent sensitivity to vibrations at low frequencies. Furthermore, the geophones are only sensitive to vertical vibrations (z-direction). Depending on its technical details, the new sensor could also measure horizontal vibrations (x- and y-direction).

Chapter 6

Summary and Outlook

This work was carried out alongside the construction and commissioning of the new COSINUS facility in preparation for the first physics run. A flexible cabling concept was created for two new dry dilution refrigerators, and the parts are ready to be installed and tested. At the same time, a new internal spring-based passive vibration decoupling system was designed, characterized, and successfully implemented in a R&D-refrigerator at MPP in Garching and in the COSINUS refrigerator at LNGS.

On the detector side, the novel remoTES-design was introduced to COSINUS and implemented for Si-, TeO_2- and NaI-detectors. For the first time, event-by-event particle discrimination could be demonstrated with a cryogenic NaI-detector, and a record baseline energy resolution of 410 eV for the PD was achieved. Dedicated parameter studies showed ways to improve remoTES-detectors further.

This thesis was structured into six chapters. Chapter 1 gave a short introduction to the scope of this work and the structure of this thesis. Chapter 2 summarized evidence, properties, and detection methods for DM and gave an overview of current direct detection experiments. Furthermore, the DAMA/LIBRA experiment and the current NaI DM-search landscape was introduced.

In chapter 3, COSINUS was described in detail. It was presented how the dual channel readout can lead to competitive DM results despite small exposures compared to other NaI-based experiments. The principle was demonstrated in an underground measurement of a COSINUS prototype module, also published in [4]. Afterward, the newly built high-end, low-background cryogenic facility was described. The second part of the chapter gave an in-depth description of the COSINUS dry dilution refrigerators and the cabling, which will be implemented soon.

Detectors equipped with TES are the main topic of chapter 4. In the beginning, a summary of the relevant basics and an overview of the old COSINUS detector design were given. It was explained why this design was not suited for COSINUS, and the novel remoTES was introduced and adapted to NaI. In various measurements, the design parameters were studied and optimized. A simulation and new ideas to guide the future remoTES development were presented. Some of the results are published in [175, 176, 4]. The chapter concludes with a recipe for a COSINUS run-1 module, which condensed all the knowledge and experience gathered during detector preparation.

Chapter 5 finally treated the expected vibrational background in COSINUS. It was shown why vibrations need to be decoupled with the new dry dilution refrigerators. The decoupling strategy was presented and validated, with the results being previously published in [126]. New follow-up measurements confirmed the effectiveness of the invented decoupling system. 30 g detectors could be operated with no excessive vibrational noise.

The next step for COSINUS is to finish commissioning the facility at LNGS. In 2025, the cabling and decoupling system, both developed within this project, will be implemented. In parallel, the first eight detector modules for the first COSINUS physics run will be manufactured using the recipe from chapter 4.

Besides enabling cryogenic NaI-detectors, the remoTES-design proved promising for future particle physics applications. Separating the TES from the absorber allows for greater production standards and reproducibility and greatly extends the range of possible absorbers. Furthermore, it is easier to control systematic variances for future in-depth detector studies. For the DM direct detection community, this device could provide a promising opportunity to study the LEE and help to clear the biggest roadblock that is currently plaguing low mass DM searches.

Appendix A

COSINUS Dry Dilution Refrigerator

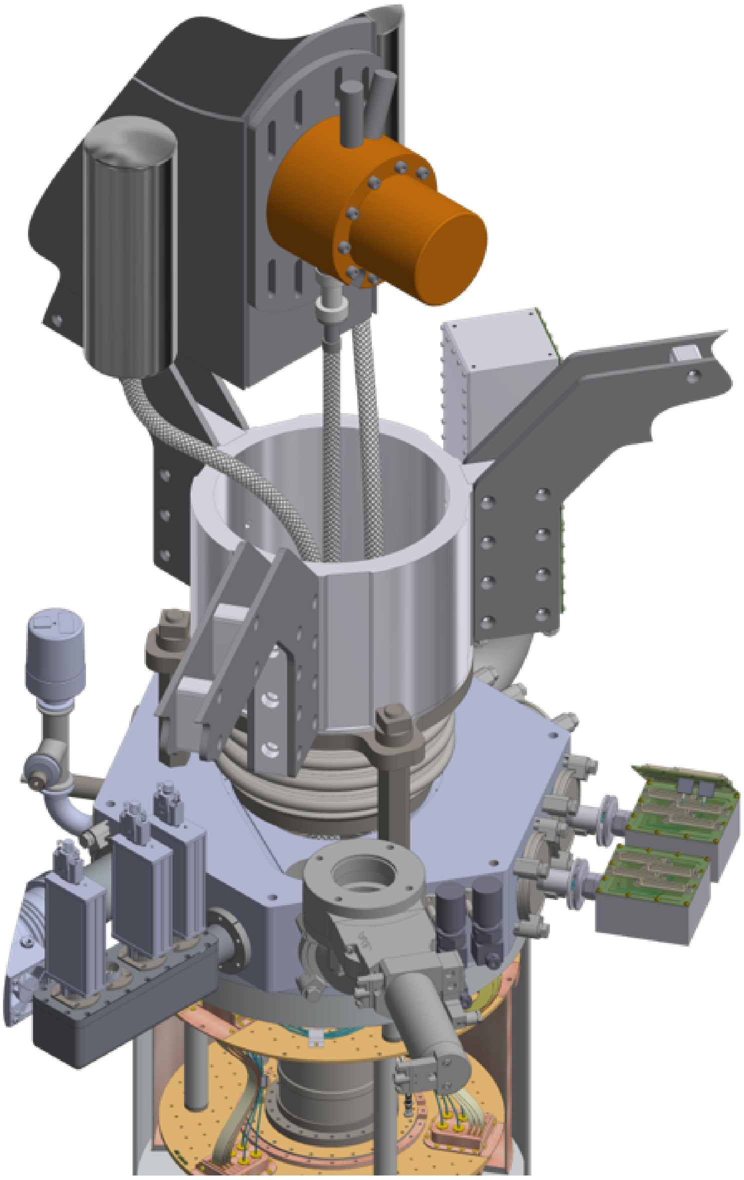

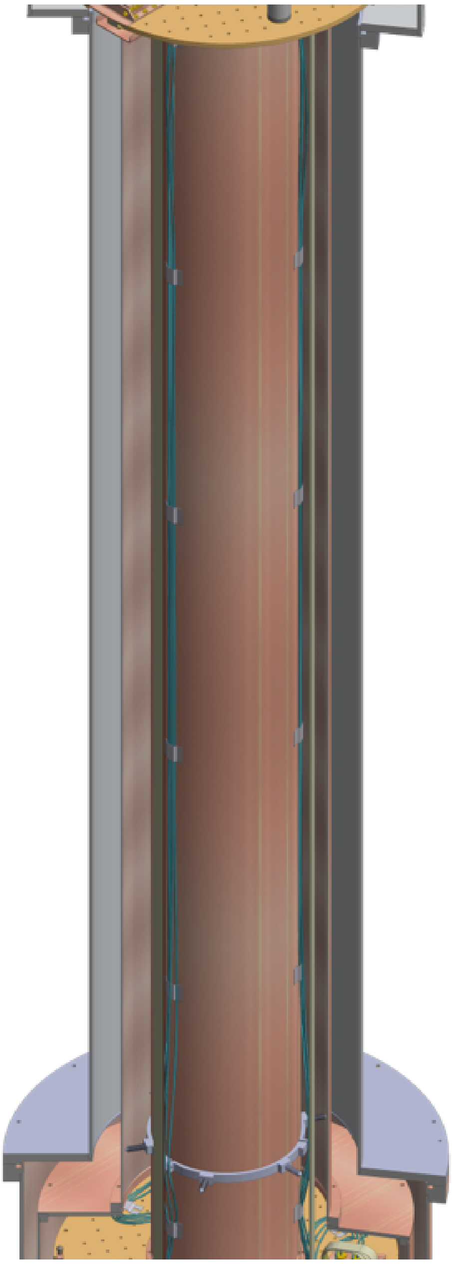

Appendix B

Analysis Procedure

The analysis procedure for TES-based detectors that was applied in this thesis mostly follows the standard procedures developed for the CRESST experiment. This chapter will describe the analysis of hardware-triggered data using the SEV-fit method. In contrast to the OF method mentioned in the main part of the thesis, it is resistant to pile-up, as well as changes in the noise conditions, and therefore more suitable for analyzing above-ground data. More detailed information about the procedures can be found in [214], [215] and [216].

For R&D-measurements, the most important results describing the performance of a detector are its pulse shapes and achieved energy resolution. The examples shown in this chapter are from a dataset of an above-ground TeO_2-remoTES detector that was described in chapter 4. All analyses were carried out using the ROOT-based collaboration-internal software package CAT, or the publicly available Python software package CAIT [217].

Triggering

In general, two different kinds of data sets are available: hardware-triggered data and untriggered stream files. A stream file contains all voltage readings of the DAQ and allows the application of a software trigger, which is optimized for the specific dataset. The hardware-triggered data instead was triggered during data taking with a preliminary threshold and only contains the voltage readings of a fixed record window around the triggering time. Triggered datasets consist of three different event types: particle pulses, test pulses, and empty baselines. Figure B.1 shows an example for every event type.

A particle pulse is an event in which the triggering conditions of the trigger algorithm were fulfilled and, therefore, with high probability, contains a real event from a particle recoil.[1] A test pulse is an artificial event with a fixed input amplitude that is regularly sent to a heater to test the detector response. Usually, multiple sets with different input powers are sent to probe the detector's complete dynamic range. An empty baseline is an event-less window taken randomly (or for hardware-triggered data in fixed intervals) during the measurement. It is used to monitor the noise conditions during the measurement and to optimize the energy reconstruction methods.

---

[1] An additional criterion is no coincidence with a test pulse or an empty baseline.

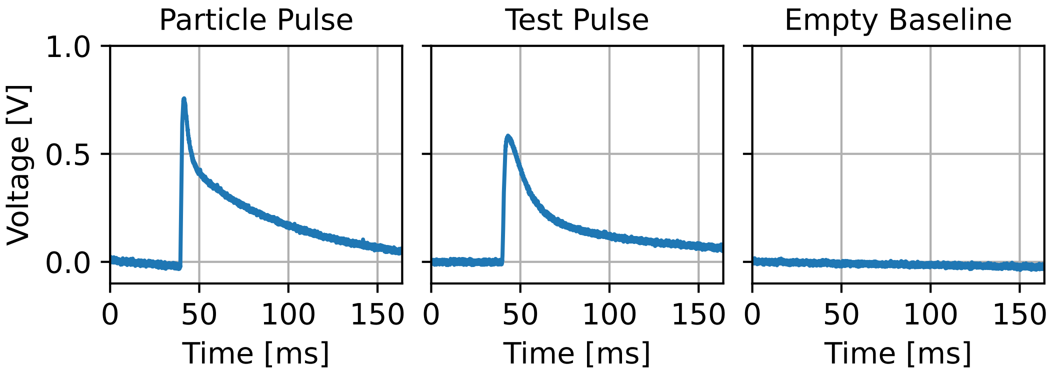

Figure B.1: Event types within a dataset. On the left side, a typical particle pulse; in the middle, a test pulse; and on the right, an event-free empty baseline is shown. The exact timing of every test pulse is known, which allows for the separation of particle pulses and test pulses.

Main Pulse Parameters

For a first characterization and comparison of all measured events, a set of parameters is calculated from each pulse. This set includes the pulse height (reconstructed with a moving average), the onset, the rise time, the decay time, and the difference between the first few and last few samples of a record window. If appropriate, more parameters (e.g. the maximal and minimal derivation of a pulse) can be defined. With the newly calculated parameters, it is possible to define basic quality cuts on the dataset. These cuts aim to remove nonphysical artifacts (e.g. electronics-related artifacts) from the dataset and separate different event classes.

Test Pulse Response

One important cut is the stability cut. Depending on the operating conditions, the operation point of a detector might drift over time, and the detector response changes. A heater pulse response plot can visualize the operation conditions over time. One example is shown in figure B.2.

The measured Test Pulse Amplitudes (TPAs) are shown over time, which, for stable conditions, should result in parallel lines for every input power. A slope of one or more lines indicates a shift of the operating point. For the analysis dataset, a time window with mostly parallel lines should be chosen.

Test pulses also help to measure the dynamic range of the detector. By comparing input power (proportional to the squared input voltage) and measured pulse height, one can find the limit at which pulses leave the linear range of the detector. This is shown in an example in figure B.3.

In general, one would try to correct for the truncation of high-amplitude pulses to increase the detector's dynamic range. However, for this thesis, the low-energy response

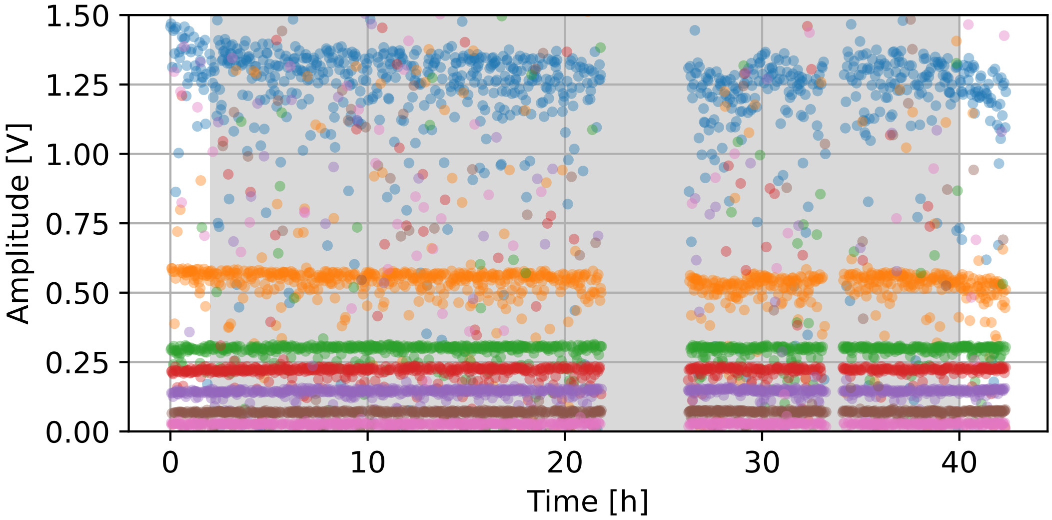

Figure B.2: Heater pulse response plot of a measurement. The plot shows the amplitude of test pulses over time. Different test pulse input powers are drawn in different colors. The event-free zone marks a time window where no data was taken. In stable operation, the amplitudes (in particular for the largest test pulses) will not change, and pulses with similar input power will form a horizontal line. In this example, the gray-shaded region was declared as stable and will be used for analysis

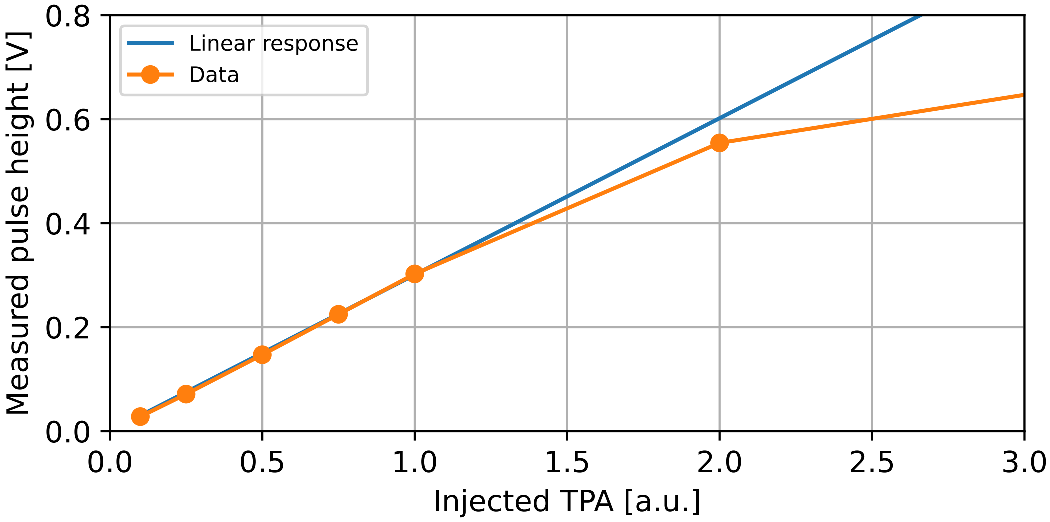

Figure B.3: Test pulse response for injected test pulses with different input power. The linear regime marks the dynamic range of the detector. For higher amplitudes, a different amplitude reconstruction algorithm has to be applied to the data.

is the main subject of interest. Therefore, the analysis of truncated events will not be explained further in this chapter. For more information, the reader is referred to [215].

Standard Event Creation

In cryogenic detectors, the linear range is defined by the energy below which the pulse shape of absorber events is constant. By comparing two parameters related to the pulse shape, it is possible to discriminate particles with different origins, as was also shown in [175].

A SEV is a noise-less template for events of the same type. It can be generated by averaging many of the measured events. To get the best common description of all events, a multi-stage approach is used:

1. A subset of events corresponding to an event class is chosen. This can be done with a box cut on two of the available CMP parameters. After cleaning the subset from artifacts, a first preliminary SEV is created by averaging all events within the subset. An example of the selection is shown in figure B.4.

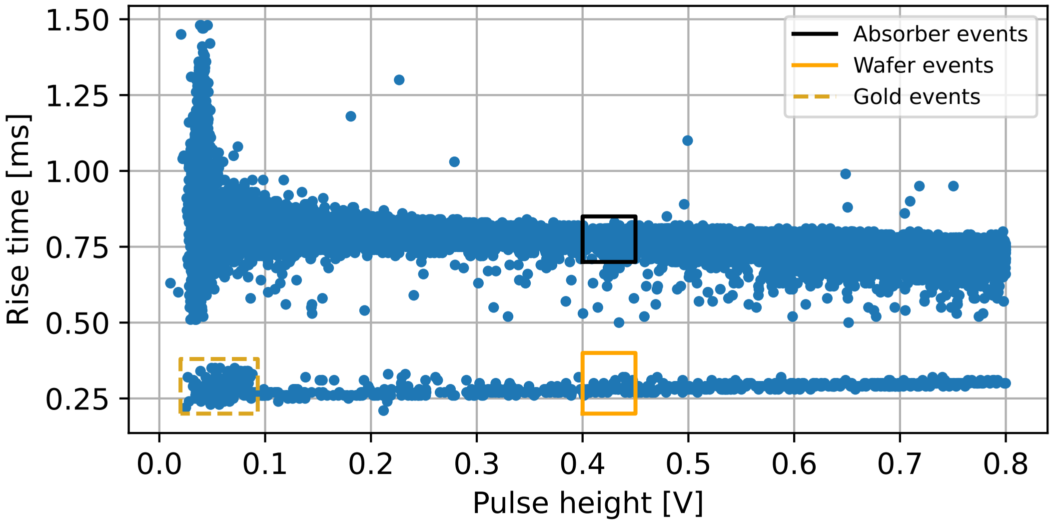

Figure B.4: Event selection for the SEV-creation. The plot shows the rise time of all pulses with respect to their pulse height. This results in the separation of three populations corresponding to gold hits, wafer hits, and absorber hits. The black and orange boxes show the event selection for a preliminary SEV of absorber events and wafer events, respectively.

2. The initial SEV is fitted to every single event by shifting and scaling it to the data. From this, a new parameter for the event quality can be acquired: the Root Mean Square (RMS) of the difference between data and fitted SEV.

3. A new selection of events to refine the SEV is made based on the RMS of the fitted SEV. Thereby, lower RMS numbers correspond to a better fit.

The final SEVs for absorber and wafer events from the example are shown in figure B.5 The SEV contains information about the detector properties (e.g. heat capacities and couplings) and is an important figure to compare between measurements for optimization.

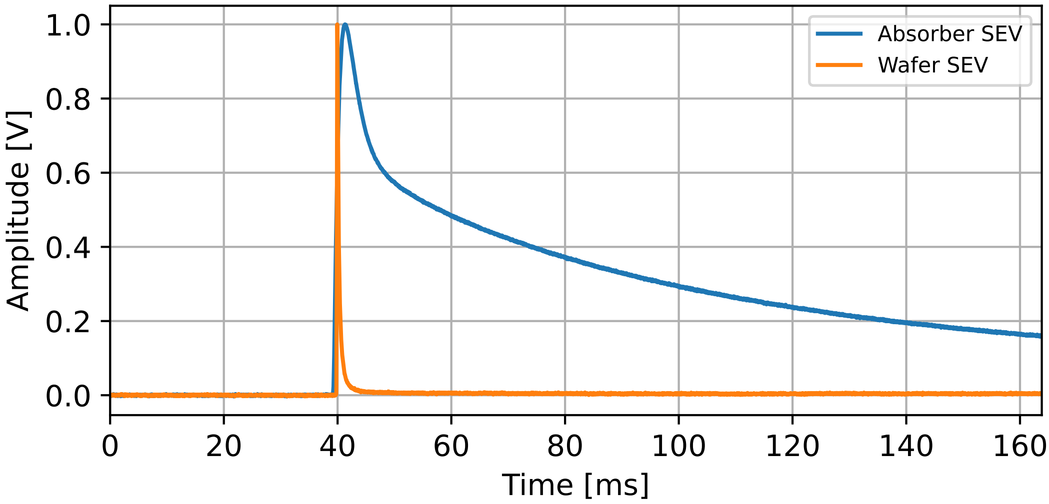

Figure B.5: SEVs for absorber hits (blue) and wafer hits (orange). They encode information about the physical properties of a detector, such as thermal couplings and heat capacities.

Noise

Besides the SEV, the other important figure for the description of a detector is the averaged NPS. It describes the average noise conditions during the measurements and is calculated by averaging the NPS from empty baselines. Figure B.6 shows an averaged NPS. Before averaging, the empty baselines have to be cleaned. Strong cuts are applied to filter out artifacts or stray pulses. Special attention has to be given if the noise conditions change during a measurement. In this case, the analysis procedure has to be carried out separately for the different time intervals. The achieved resolution of the detector could then be time-dependent as well.

Baseline Resolution

The baseline resolution is the energy resolution that the detector achieves for events close to the energy threshold. To calculate it, events are simulated by adding the SEV,

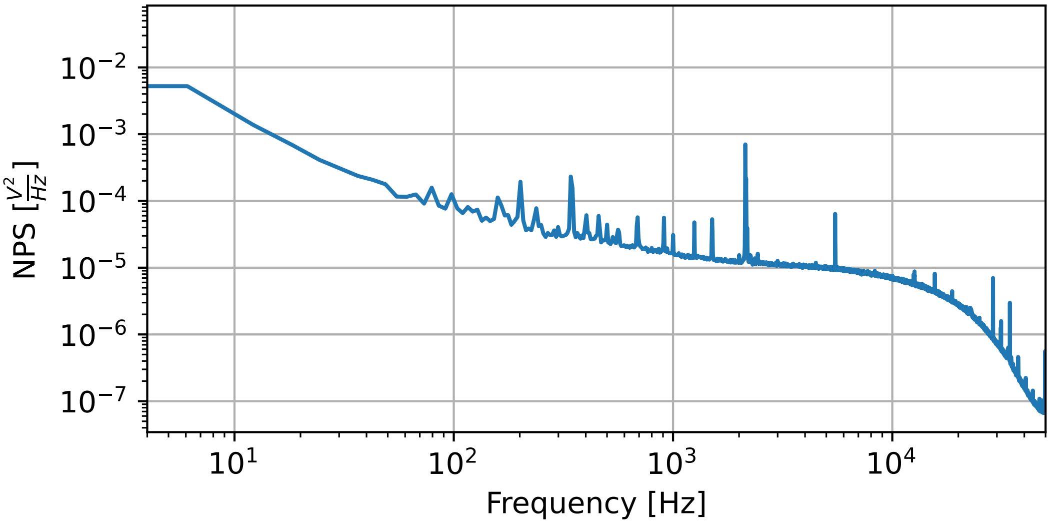

Figure B.6: NPS of a measurement. It typically is dominated by 1/f-noise for low frequencies and merges into a white noise part. For high frequency, there is a cut-off due to a low pass filter in the readout circuit. Various readout noise contributions are visible as peaks.

scaled to a small amplitude, on all cleaned empty baselines. Afterward, the amplitude of the simulated event is reconstructed using an amplitude reconstruction algorithm. An example of a simulated event and its reconstruction is shown in figure B.7

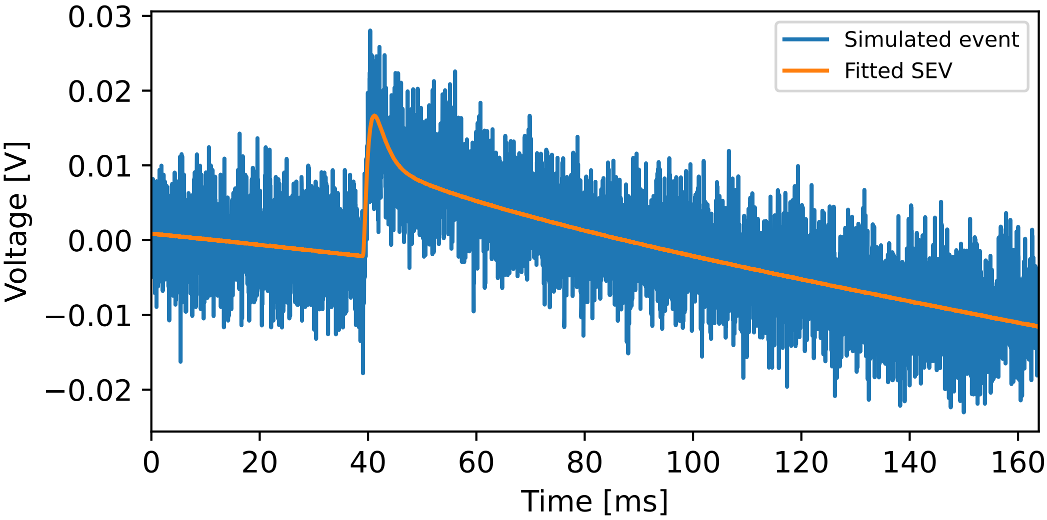

Figure B.7: Simulated event close to threshold. The event (blue) was created by adding a SEV to an empty baseline. Afterward, it was fitted (orange) with a template consisting of the SEV and noise described by a third-order polynomial.

Generally, two types of amplitude reconstruction algorithms are used:

1. The OF is an optimized filter applied to the event, reducing the noise while conserving the amplitude.
2. The SEV fit shifts and scales the SEV to the simulated event. The baseline noise is thereby described by a third-order polynomial function. The example shows an amplitude reconstructed with the SEV fit method.

After reconstructing the amplitudes, they are counted in a histogram and generally should generate a peak around the simulated pulse height. One example is shown in B.8. The width of a Gaussian fitted to the distribution yields the energy resolution for this amplitude in voltage units.

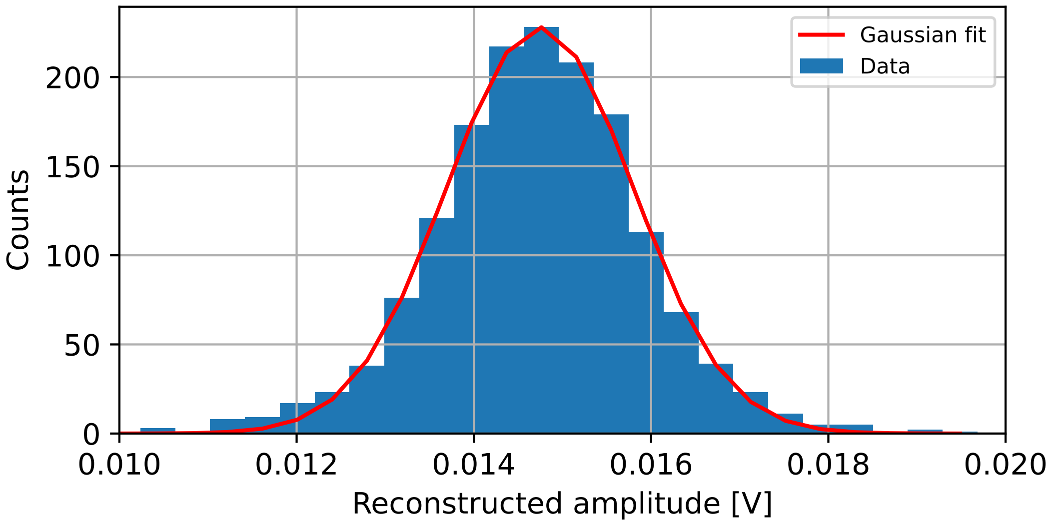

Figure B.8: Histogram of reconstructed amplitudes from simulated events. The width of the Gaussian describes the baseline resolution of the amplitude reconstruction algorithm.

Energy Calibration

Finally, for an energy resolution in physical units, the measured spectrum has to be calibrated with a peak with known energy. The amplitude reconstruction algorithm is applied to all particle pulses to recover a conversion factor between V and eV. In the process, the spectrum is cleaned from poorly reconstructed events. A cleaned spectrum is shown in figure B.9.

Calibration sources with sufficient activity cause features such as peaks in the measured spectrum. In above-ground measurements, in addition to radiogenic peaks (e.g. from calibration sources), a wide distribution from $\sim 80\,\mathrm{keV}$ to $\sim 200\,\mathrm{keV}$ from atmospheric

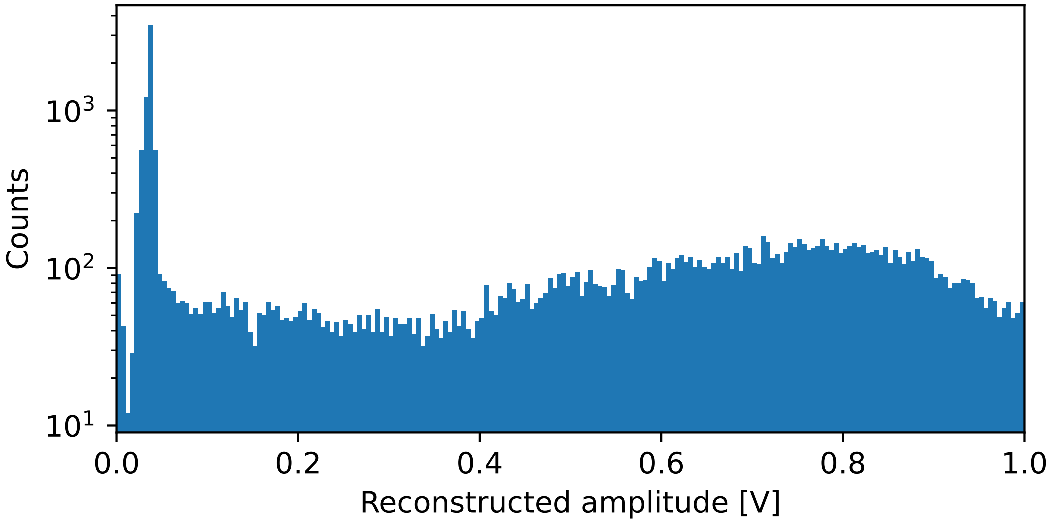

Figure B.9: Cleaned pulse height spectrum of the measured events. The peak at low energies corresponds to events from an ^{55}Fe-source.

muons is expected. A commonly used calibration source is ^{55}Fe, which produces a prominent peak at 5.9 keV.[2] Figure B.10 shows a fitted Gaussian to the ^{55}Fe-peak.

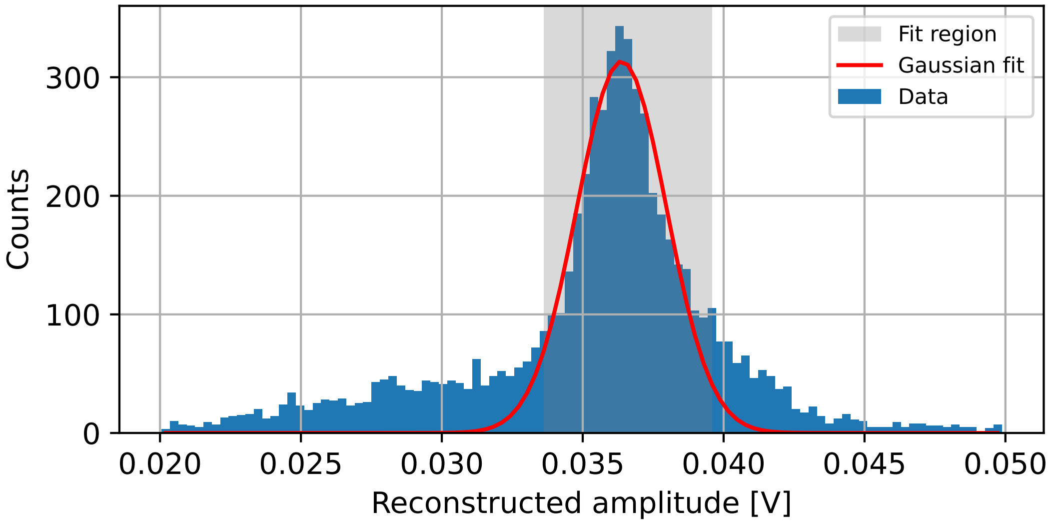

Figure B.10: Energy calibration using the ^{55}Fe-peak. The peak region (gray) was fitted with a Gaussian (red) to get a conversion factor between energy (expected at 5.9 eV) and voltage.

---

[2] The expected ^{55}Fe peak consists of two single peaks: K_α at 5.9 keV and K_β at 6.5 keV, with the latter one having a much smaller amplitude. Good detectors are able to resolve this double structure.

With the fit, a conversion factor between voltage and energy was determined. By multiplying the conversion factor with the baseline resolution in V, the detector's energy resolution can be calculated.

Appendix C

Spring Characterization

The vibration decoupling system developed in this thesis is based on tension springs and was designed to decouple vibrations at 1 Hz and above. In this work, five different spring types were procured and tested. Figure C.1 shows a photo with one spring of each batch.

Figure C.1: Springs investigated in this thesis.

The materials tested were spring steel of type 1.4310, stainless steel with the designation ISO 6931-1-4310301-00-I, and CuSn with a 6% tin portion (CuSn6). The first one is a widespread standard material for springs, but due to its ferromagnetic behavior, it could have a negative effect on the TES operation. Therefore, the stainless steel springs were procured and tested. The CuSn springs were chosen for their large Cu-portion, which can assist in thermalizing the springs in the refrigerator.

Spring Parameters

The springs were designed for a test mass of 15 kg with a resonance frequency of around 1 Hz. They follow Hooke's law, which states that the restoring force F_n of a deformed spring is linear to the length s_n of its deformation

$$F_n = -ks_n. \tag{C.1}$$

The factor k is defined as the spring constant. Dynamically, a mass-spring system is characterized by its resonance frequency f_r, which can be calculated from the mass m and the spring constant k by

$$f_r = \frac{1}{2\pi}\sqrt{\frac{k}{m}}. \tag{C.2}$$

It is possible to manufacture a spring with a pre-tension F_0. The pre-tension is the minimal force needed to elongate a spring and reduces the total length of a loaded spring while conserving the spring constant.

A spring is subject to material-specific limitations and can not be manufactured with any spring constant and pre-tension. For example, CuSn is softer than steel and can not achieve the same spring constant at the same load with similar dimensions. The springs that were procured for this work and their realistic target characteristics (mass load m_T and resonance frequency f_r) are listed in table C.1.

Name	Material	#	m_T [kg]	f_r [Hz]	k $[\frac{\mathrm{N}}{\mathrm{m}}]$	F_0 [N]
Spring steel$_1$	1.4310	4	5.0	1.2	300	0
Spring steel$_2$	1.4310	4	5.0	1.2	300	25
Nonmagnetic steel	ISO 6931-1-4310301-00-I	4	5.0	0.9	160	30
Bronze$_1$	CuSn6	8	2.5	0.9	80	15
Bronze$_2$	CuSn6	10	5.0	2	790	0

Table C.1: Target properties of the procured springs. The springs were designed for different test scenarios adapted to different masses and frequencies.

In the COSINUS decoupling system, a multiple of three springs are used to carry masses up to 30 kg. The allowed diameter is thereby limited by cutouts in the particle radiation shield within the refrigerator, while the length should be limited to around 300 mm.[1]

All springs that were ordered had slight differences in their dimensions due to production tolerances. The dimensions are given in intervals of their extrema in table C.

From the batches under investigation, the springs made from stainless steel and the Bronze$_1$ batch had the largest spread. While it was possible to find sets of three springs

---

[1] The absolute limit for the length is given by the size of the detector boxes. They should not touch the thermal shield on the bottom of the refrigerator.

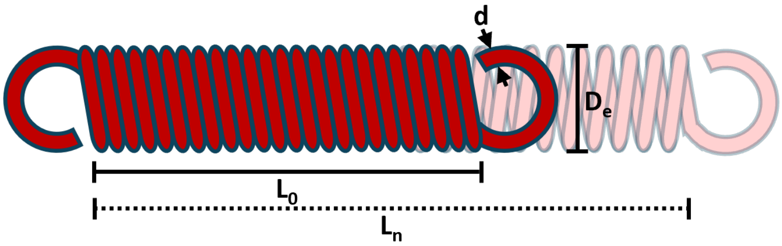

Name	d [mm]	D$_e$ [mm]	L$_0$ [mm]	L$_n$ [mm]
Spring steel$_1$	1.4	14	116	261 – 266
Spring steel$_2$	1.4	14	116	212 – 213
Stainless steel	1.4	14	147 – 148	258 – 287
Bronze$_1$	1.4	14	177 – 178	289 – 317
Bronze$_2$	2.0	14	121 – 122	172 – 177

Table C.2: Drawing of a spring with its characteristic dimensions (wire thickness d, outer spring diameter D$_e$, spring length without load L$_0$, and spring length at design load L$_n$). The table below lists the dimensions of the springs used in this work. The ranges given are set by the shortest and longest spring of each batch.

with similar properties, many of them did not pass simple quality criteria, such as a linear response over a broader load range. One possible reason for these defects is that those materials have very high pre-tension.

Test at Room Temperature

All springs were characterized at room temperature by hanging different masses to the spring and measuring the elongation.[2] The results are plotted in figure C.2.

By applying a linear fit, it is possible to recover the true spring constant as well as the pre-tension of each spring. They are listed in table C.3.

While the target parameters were only met within roughly 10%, the spring constants are relatively close to each other within a batch. The differences in the pre-tension can vary more. However, it only affects the length of a spring and can be leveled out by adjusting the Kevlar wire of the decoupling (see chapter 5).

---

[2] At the time of the measurement, only four springs of the Bronze$_2$ batch were available.

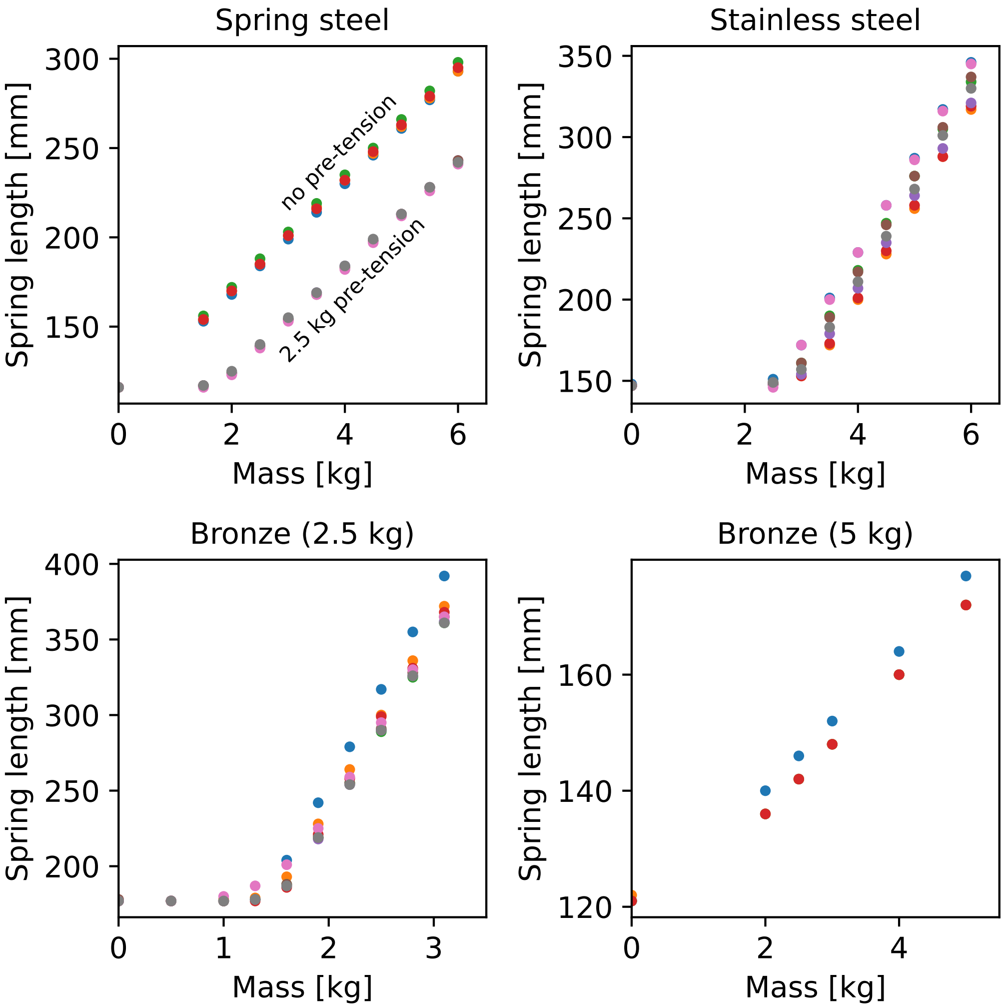

Figure C.2: Measurement of the spring behavior for each spring. The first plot shows both spring steel batches at once. All lengths were measured with an estimated precision of ±1 mm.

Spring	No	k [N/m]	F_0 [N]
Spring steel$_1$	1	316 ± 1	3.19 ± 0.12
	2	318 ± 1	2.48 ± 0.12
	3	312.6 ± 0.7	2.20 ± 0.09
	4	314.5 ± 0.8	2.81 ± 0.09
Spring steel$_2$	1	331.4 ± 0.9	16.94 ± 0.07
	2	331.0 ± 0.9	17.04 ± 0.07
	3	334 ± 1	17.21 ± 0.08
	4	336.0 ± 1.1	16.52 ± 0.08
Nonmagnetic steel	1	169.5 ± 0.7	25.50 ± 0.09
	2	169 ± 2	30.38 ± 0.22
	3	170.6 ± 0.4	27.14 ± 0.05
	4	168.8 ± 1.6	30.19 ± 0.17
	5	172.6 ± 0.7	28.96 ± 0.07
	6	167.6 ± 1.5	27.41 ± 0.17
	7	170.3 ± 0.6	25.34 ± 0.08
	8	169.3 ± 2.5	28.28 ± 0.28
Bronze$_1$	1	78.39 ± 0.17	13.607 ± 0.022
	2	82.26 ± 0.19	14.454 ± 0.023
	3	83.3 ± 0.5	15.18 ± 0.06
	4	80.5 ± 1.1	15.04 ± 0.13
	5	83.5 ± 1.0	15.10 ± 0.11
	6	80.8 ± 0.4	15.40 ± 0.05
	7	84.0 ± 0.4	14.68 ± 0.05
	8	84.1 ± 0.8	15.04 ± 0.09
Bronze$_2$	1	800	4.6
	2	819	8.2
	3	819	7.4
	4	819	7.4

Table C.3: Spring constant and pre-tension for all measured springs. The values were extracted from a linear fit to the data. The uncertainties given correspond to the fit uncertainties. The Bronze$_2$ batch behaved extremely linear (within the measurement uncertainties), leading to vanishing small fit uncertainties.

Test at 77 K

It is expected that the stiffness and, therefore, the spring constant increases while cooling down. To get an estimate of this effect, all springs were submerged in liquid N_2 and cooled to 77 K. Then, the length of the springs under a load of 5 kg (2.5 kg for the Bronze$_1$-batch) was compared between warm and cold. The results are summarized in table C.4.

Spring	Number	$L_{5\,\mathrm{kg}}$ warm [mm]	$L_{5\,\mathrm{kg}}$ cold [mm]	Difference [mm]
Spring steel$_1$	1	263	257	6
	2	267	260	7
	3	263	255	8
	4	263	257	6
Spring steel$_2$	1	214	207	7
	2	213	208	7
	3	214	206	8
	4	213	205	8
Nonmagnetic steel	1	288	279	9
	2	264	254	10
	3	281	268	13
	4	285	267	18
	5	274	258	16
	6	278	262	16
	7	263	247	16
	8	288	274	14
Bronze$_1$	1	294	275	19
	2	292	273	19
	3	301	283	18
	4	302	283	19
	5	294	275	19
	6	321	302	19
	7	297	278	19
	8	303	284	19
Bronze$_2$	1	172	168	4
	2	177	174	3
	3	172	168	4
	4	172	168	4

Table C.4: Spring length under load of 5 kg (2.5 kg for the Bronze$_1$ batch). The lengths were measured at room temperature (warm) and shortly after submerging the spring in liquid N_2 (cold). All lengths were measured with an estimated precision of ±1 mm.

All springs experienced a shortening, with the Bronze$_1$ batch shortening up to 19 mm. While the measured shortening is consistent between springs of a batch, the given numbers only place a lower limit on the actual changes, as the springs warmed up in the short time before and during the measurement.

The shortening effect has to be accounted for when designing a vibration decoupling system for a refrigerator. It is expected that the dynamics of the spring system, and thus the resonance frequency, change as well when cooling down. However, this could not be tested in a laboratory environment outside of the refrigerator.

Abbreviations

ΛCDM	Λ-Cold Dark Matter
^{3}H	Tritium
^{8}B	Boron-8
^{210}Pb	Lead-210
^{222}Rn	Radon-222
^{232}Th	Thorium-232
^{238}U	Uranium-238
^{3}He	Helium-3
^{40}K	Potassium-40
^{4}He	Helium-4
^{55}Fe	Iron-55
^{57}Co	Cobalt-57
Al	Aluminum
Al_2O_3	Sapphire
ALP	Axion-Like Particle
Am	Americium
Ar	Argon
Au	Gold
BCS	Bardeen-Cooper-Schrieffer
Be	Beryllium
CAD	Computer-Aided Design
$CaWO_4$	Calcium Tungstate
CCD	Charged Coupled Device
Cd	Cadmium
$CdWO_4$	Cadmium Tungstate
CEνNS	Coherent Elastic Neutrino-Nucleus Scattering
CERN	European Organization for Nuclear Research
CMB	Cosmic Microwave Background
COSINUS	Cryogenic Observatory for SIgnatures seen in Next-generation Underground Searches
CP	Charge conjugation Parity
CsI	Caesium Iodide
Cu	Copper

CuKaCu	Copper-Kapton-Copper
CuSn	Bronze
DAQ	Data Acquisition system
DC	Direct Current
DFT	Discrete Fourier Transform
DM	Dark Matter
DU	Dilution Unit
FFT	Fast Fourier Transform
FPGA	Field Programmable Gate Array
Ge	Germanium
GHS	Gas Handling System
Hg	Mercury
I	Iodine
Ir	Iridium
IVC	Inner Vacuum Chamber
LD	Light Detector
LEE	Low Energy Excess
LIBRA	Large sodium Iodide Bulk for RAre processes
LNGS	Laboratori Nazionali del Gran Sasso
LTI	Linear Time Invariant
LY	Light Yield
MACHO	Massive Astrophysical Compact Halo Object
MC	Mixing Chamber
MOND	Modified Newtonian Dynamics
MPP	Max-Planck-Institut für Physik
N_2	Nitrogen
Na	Sodium
NaI	Sodium Iodide
Nb	Niobium
NFW	Navarro-Frenk-White
Ni	Nickel
NPS	Noise Power Spectrum
NTD	Neutron Transmutation Doped
OF	Optimal Filter
OVC	Outer Vacuum Chamber

Pb	Lead
PBH	Primordial Black Hole
PCB	Printed Circuit Board
PD	Phonon Detector
PE	Polyethylene
PMT	Photomultiplier Tube
POM	Polyoxymethylene
PSD	Power Spectral Density
PT	Pulse Tube
PTFE	Teflon
QCD	Quantum Chromo Dynamics
QF	Quenching Factor
R&D	Research and Development
RF	Radio Frequency
RMS	Root Mean Square
ROI	Region Of Interest
RT	Room Temperature
RuO_2	Ruthenium Dioxide
SC	Superconductor
SEV	Standard EVent
SFC	Spring Finger Contact
Si	Silicon
SiO_2	Silicon Dioxide
SM	Standard Model
SNR	Signal-to-Noise Ratio
SOS	Silicon-On-Sapphire
SQUID	Superconducting Quantum Interference Device
TeO_2	Tellurium Dioxide
TES	Transition Edge Sensors
Ti	Titanium
Tl	Thallium
TPA	Test Pulse Amplitude
TUM	Technische Universität München
UQT	Ultra-Quiet Technology
W	Tungsten
WIMP	Weakly Interacting Massive Particle

Xe	Xenon

Bibliography

[1] Planck Collaboration, N. Aghanim, et al. Planck 2018 results - VI. Cosmological parameters. *A&A*, 641:A6, 2020. doi:10.1051/0004-6361/201833910.

[2] R. Bernabei et al. First model independent results from DAMA/LIBRA-phase2. *Nucl. Phys. At. Energy*, 19(4):307–325, 2018. doi:10.15407/jnpae2018.04.307.

[3] G. Angloher et al. Water Cherenkov muon veto for the COSINUS experiment: design and simulation optimization. *Eur. Phys. J. C*, 84(5), 2024. doi:10.1140/epjc/s10052-024-12923-2.

[4] G. Angloher et al. Deep-underground dark matter search with a COSINUS detector prototype. *Phys. Rev. D*, 110:043010, 2024. doi:10.1103/PhysRevD.110.043010.

[5] E. Hubble. A Relation between Distance and Radial Velocity among Extra-Galactic Nebulae. *Proc. Natl. Acad. Sci.*, 15(3):168–173, 1929. doi:10.1073/pnas.15.3.168.

[6] G. Lemaître. Republication of: A homogeneous universe of constant mass and increasing radius accounting for the radial velocity of extra-galactic nebulae. *Gen Relativ Gravit*, 45:1635–1646, 2013. doi:10.1007/s10714-013-1548-3.

[7] S. Navas et al. Review of Particle Physics. *Phys. Rev. D*, 110:030001, 2024. doi:10.1103/PhysRevD.110.030001.

[8] E. Di Valentino et al. In the realm of the Hubble tension—a review of solutions. *Class. Quantum Grav.*, 38(15):153001, 2021. doi:10.1088/1361-6382/ac086d.

[9] V. C. Rubin and Jr. Ford, W. K. Rotation of the Andromeda Nebula from a Spectroscopic Survey of Emission Regions. *Astrophys. J.*, 159:379, 1970. doi:10.1086/150317.

[10] G. Bertone and D. Hooper. History of dark matter. *Rev. Mod. Phys.*, 90:045002, 2018. doi:10.1103/RevModPhys.90.045002.

[11] Wikimedia Commons. File:Rotation curve of spiral galaxy Messier 33 (Triangulum).png — Wikimedia Commons, the free media repository, 2025. URL `https://commons.wikimedia.org/w/index.php?title=File:Rotation_curve_of_spiral_galaxy_Messier_33_(Triangulum).png&oldid=996791990`. [Online; accessed 25-February-2025].

[12] F. Zwicky. Die Rotverschiebung von extragalaktischen Nebeln. *Helv. Phys. Acta*, 6:110–127, 1933. doi:10.1007/s10714-008-0707-4.

[13] R. Massey, T. Kitching, and J. Richard. The dark matter of gravitational lensing. *Rep. Prog. Phys.*, 73(8):086901, 2010. doi:10.1088/0034-4885/73/8/086901.

[14] M. Kilbinger. Cosmology with cosmic shear observations: a review. *Rep. Prog. Phys.*, 78(8):086901, 2015. doi:10.1088/0034-4885/78/8/086901.

[15] R. Massey et al. Dark matter maps reveal cosmic scaffolding. *Nature*, 445:286, 2007. doi:10.1038/nature05497.

[16] Euclid Collaboration, Y. Mellier, et al. Euclid. I. Overview of the Euclid mission. *arXiv e-prints*, art. arXiv:2405.13491, 2024. doi:10.48550/arXiv.2405.13491.

[17] R. Barrena et al. The dynamical status of the cluster of galaxies 1E0657-56*. *A&A*, 386(3):816–828, 2002. doi:10.1051/0004-6361:20020244.

[18] D. Clowe et al. A Direct Empirical Proof of the Existence of Dark Matter. *Astrophys. J.*, 648(2):L109–L113, 2006. doi:10.1086/508162.

[19] Wikimedia Commons. File:1e0657 scale.jpg — Wikimedia Commons, the free media repository, 2024. URL `https://commons.wikimedia.org/w/index.php?title=File:1e0657_scale.jpg&oldid=910816411`. [Online; accessed 25-February-2025].

[20] N. W. Boggess et al. The COBE mission - Its design and performance two years after launch. *Astrophys. J.*, 397:420–429, 1992. doi:10.1086/171797.

[21] C. L. Bennett et al. NINE-YEAR WILKINSON MICROWAVE ANISOTROPY PROBE (WMAP) OBSERVATIONS: FINAL MAPS AND RESULTS. *Astrophys. J. Suppl. Ser.*, 208(2):20, 2013. doi:10.1088/0067-0049/208/2/20.

[22] Planck Collaboration, N. Aghanim, et al. Planck 2018 results - I. Overview and the cosmological legacy of Planck. *A&A*, 641:A1, 2020. doi:10.1051/0004-6361/201833880.

[23] V. Springel et al. Simulations of the formation, evolution and clustering of galaxies and quasars. *Nature*, 435(7042):629–636, 2005. doi:10.1038/nature03597.

[24] T. Zimmermann et al. Dwarf galaxies imply dark matter is heavier than 2.2×10^{-21} eV, 2024. URL `https://arxiv.org/abs/2405.20374`.

[25] A. Del Popolo and M. Le Delliou. Review of Solutions to the Cusp-Core Problem of the ΛCDM Model. *Galaxies*, 9(4), 2021. doi:10.3390/galaxies9040123.

[26] J. R. Primack. Whatever Happened to Hot Dark Matter?, 2001. URL `https://arxiv.org/abs/astro-ph/0112336`.

[27] J. Billard et al. Direct detection of dark matter—APPEC committee report. *Rep. Prog. Phys.*, 85(5):056201, 2022. doi:10.1088/1361-6633/ac5754.

[28] M. Aker et al. Direct neutrino-mass measurement based on 259 days of KATRIN data, 2024. URL `https://arxiv.org/abs/2406.13516`.

[29] G. Arcadi et al. The waning of the WIMP? A review of models, searches, and constraints. *Eur. Phys. J. C*, 78(3), 2018. doi:10.1140/epjc/s10052-018-5662-y.

[30] J. L. Feng. The WIMP paradigm: Theme and variations. *SciPost Phys. Lect. Notes*, page 71, 2023. doi:10.21468/SciPostPhysLectNotes.71.

[31] K. M. Zurek. Dark Matter Candidates of a Very Low Mass. *Annu. Rev. Nucl. Part. Sci.*, 74(1):287–319, 2024. doi:10.1146/annurev-nucl-101918-023542.

[32] R. D. Peccei and H. R. Quinn. CP Conservation in the Presence of Pseudoparticles. *Phys. Rev. Lett.*, 38:1440–1443, 1977. doi:10.1103/PhysRevLett.38.1440.

[33] I. G. Irastorza. An introduction to axions and their detection. *SciPost Phys. Lect. Notes*, page 45, 2022. doi:10.21468/SciPostPhysLectNotes.45.

[34] R. Bähre et al. Any light particle search II — Technical Design Report. *J. Instrum.*, 8(09):T09001, 2013. doi:10.1088/1748-0221/8/09/T09001.

[35] E. Armengaud et al. Physics potential of the International Axion Observatory (IAXO). *J. Cosmol. Astropart. Phys.*, 2019(06):047–047, 2019. doi:10.1088/1475-7516/2019/06/047.

[36] A. Á. Melcón et al. Axion searches with microwave filters: the RADES project. *J. Cosmol. Astropart. Phys.*, 2018(05):040, 2018. doi:10.1088/1475-7516/2018/05/040.

[37] A. Boyarsky et al. Sterile neutrino Dark Matter. *Prog. Part. Nucl. Phys.*, 104: 1–45, 2019. doi:https://doi.org/10.1016/j.ppnp.2018.07.004.

[38] S. Mertens et al. A novel detector system for KATRIN to search for keV-scale sterile neutrinos. *J. Phys. G: Nucl. Part. Phys.*, 46(6):065203, 2019. doi:10.1088/1361-6471/ab12fe.

[39] T. Blaineau et al. New limits from microlensing on Galactic black holes in the mass range $10\mathrm{M}_\odot < M < 1000\mathrm{M}_\odot$. *A&A*, 664:A106, 2022. doi:10.1051/0004-6361/202243430.

[40] N. Christensen. Stochastic gravitational wave backgrounds. *Rep. Prog. Phys.*, 82 (1):016903, 2018. doi:10.1088/1361-6633/aae6b5.

[41] N. Bartolo et al. Primordial Black Hole Dark Matter: LISA Serendipity. *Phys. Rev. Lett.*, 122:211301, 2019. doi:10.1103/PhysRevLett.122.211301.

[42] M. Milgrom. A Modification of the Newtonian dynamics as a possible alternative to the hidden mass hypothesis. *Astrophys. J.*, 270:365–370, 1983. doi:10.1086/161130.

[43] D. Carney, S. Ghosh, G. Krnjaic, and J. M. Taylor. Proposal for gravitational direct detection of dark matter. *Phys. Rev. D*, 102(7), 2020. doi:10.1103/physrevd.102.072003.

[44] F. Donato, N. Fornengo, and S. Scopel. Effects of galactic dark halo rotation on WIMP direct detection. *Astropart. Phys.*, 9(3):247–260, 1998. doi:https://doi.org/10.1016/S0927-6505(98)00025-5.

[45] J. I. Read. The local dark matter density. *J. Phys. G: Nucl. Part. Phys.*, 41(6): 063101, 2014. doi:10.1088/0954-3899/41/6/063101.

[46] J. F. Navarro, C. S. Frenk, and S. D. M. White. The Structure of Cold Dark Matter Halos. *Astrophys. J.*, 462:563, 1996. doi:10.1086/177173.

[47] Y. Sofue. Rotation Curve of the Milky Way and the Dark Matter Density. *Galaxies*, 8(2), 2020. doi:10.3390/galaxies8020037.

[48] M. C. Smith et al. The RAVE survey: constraining the local Galactic escape speed. *Mon. Not. R. Astron. Soc.*, 379(2):755–772, 2007. doi:10.1111/j.1365-2966.2007.11964.x.

[49] J. D. Lewin and P. F. Smith. Review of mathematics, numerical factors, and corrections for dark matter experiments based on elastic nuclear recoil. *Astropart. Phys.*, 6(1):87–112, 1996. doi:https://doi.org/10.1016/S0927-6505(96)00047-3.

[50] K. Freese, M. Lisanti, and C. Savage. Colloquium: Annual modulation of dark matter. *Rev. Mod. Phys.*, 85(4):1561–1581, 2013. doi:10.1103/revmodphys.85.1561.

[51] R. Bernabei et al. No role for muons in the DAMA annual modulation results. *Eur. Phys. J. C*, 72(7), 2012. doi:10.1140/epjc/s10052-012-2064-4.

[52] S. E. Vahsen, C. A.J. O'Hare, and D. Loomba. Directional Recoil Detection. *Annu. Rev. Nucl. Part. Sci.*, 71(1):189–224, 2021. doi:10.1146/annurev-nucl-020821-035016.

[53] A. Kurylov and M. Kamionkowski. Generalized analysis of weakly interacting massive particle searches. *Phys. Rev. D*, 69:063503, 2004. doi:10.1103/PhysRevD.69.063503.

[54] A. H. Abdelhameed et al. Description of CRESST-III Data, 2020. URL `https://arxiv.org/abs/1905.07335`.

[55] G. Angloher et al. First observation of single photons in a CRESST detector and new dark matter exclusion limits. *Phys. Rev. D*, 110:083038, Oct 2024. doi:10.1103/PhysRevD.110.083038.

[56] E. Aprile et al. Search for Coherent Elastic Scattering of Solar ^{8}B Neutrinos in the XENON1T Dark Matter Experiment. *Phys. Rev. Lett.*, 126:091301, 2021. doi:10.1103/PhysRevLett.126.091301.

[57] P. Agnes et al. Search for low-mass dark matter WIMPs with 12 ton-day exposure of DarkSide-50. *Phys. Rev. D*, 107:063001, 2023. doi:10.1103/PhysRevD.107.063001.

[58] J. Aalbers et al. First Dark Matter Search Results from the LUX-ZEPLIN (LZ) Experiment. *Phys. Rev. Lett.*, 131(4), 2023. doi:10.1103/physrevlett.131.041002.

[59] Z. Bo et al. Dark Matter Search Results from 1.54 Tonne · Year Exposure of PandaX-4T. *Phys. Rev. Lett.*, 134:011805, 2025. doi:10.1103/PhysRevLett.134.011805.

[60] C. Savage, G. Gelmini, P. Gondolo, and K. Freese. Compatibility of DAMA/LIBRA dark matter detection with other searches. *J. Cosmol. Astropart. Phys.*, 2009(04):010, 2009. doi:10.1088/1475-7516/2009/04/010.

[61] C. A. J. O'Hare. New Definition of the Neutrino Floor for Direct Dark Matter Searches. *Phys. Rev. Lett.*, 127:251802, 2021. doi:10.1103/PhysRevLett.127.251802.

[62] E. Aprile et al. Excess electronic recoil events in XENON1T. *Phys. Rev. D*, 102: 072004, 2020. doi:10.1103/PhysRevD.102.072004.

[63] E. Aprile et al. Search for New Physics in Electronic Recoil Data from XENONnT. *Phys. Rev. Lett.*, 129:161805, 2022. doi:10.1103/PhysRevLett.129.161805.

[64] XENON Collaboration, E. Aprile, et al. The XENONnT Dark Matter Experiment, 2024. URL `https://arxiv.org/abs/2402.10446`.

[65] S. Li et al. Search for Light Dark Matter with Ionization Signals in the PandaX-4T Experiment. *Phys. Rev. Lett.*, 130:261001, 2023. doi:10.1103/PhysRevLett.130.261001.

[66] XENONnT collaboration. First measurement of a nuclear recoil signal from solar neutrinos with XENONnT, 2024. URL `https://xenonexperiment.org/first-measurement-of-a-nuclear-recoil-signal-from-solar-neutrinos-with-xenonnt/`. [Online; accessed 25-February-2025].

[67] A.B. McDonald. Dark matter detection with liquid argon. *Nucl. Phys. B*, 1003: 116436, 2024. doi:https://doi.org/10.1016/j.nuclphysb.2024.116436. Special Issue of Nobel Symposium 182 on Dark Matter.

[68] XLZD Collaboration, J. Aalbers, et al. The XLZD Design Book: Towards the Next-Generation Liquid Xenon Observatory for Dark Matter and Neutrino Physics, 2024. URL `https://arxiv.org/abs/2410.17137`.

[69] R. Agnese et al. Results from the Super Cryogenic Dark Matter Search Experiment at Soudan. *Phys. Rev. Lett.*, 120:061802, 2018. doi:10.1103/PhysRevLett.120.061802.

[70] A. H. Abdelhameed et al. First results from the CRESST-III low-mass dark matter program. *Phys. Rev. D*, 100:102002, 2019. doi:10.1103/PhysRevD.100.102002.

[71] P. Adari et al. EXCESS workshop: Descriptions of rising low-energy spectra. *SciPost Phys. Proc.*, page 001, 2022. doi:10.21468/SciPostPhysProc.9.001.

[72] R. Anthony-Petersen et al. Demonstration of the HeRALD superfluid helium detector concept. *Phys. Rev. D*, 110(7), 2024. doi:10.1103/physrevd.110.072006.

[73] B. von Krosigk et al. DELight: A Direct search Experiment for Light dark matter with superfluid helium. *SciPost Phys. Proc.*, page 016, 2023. doi:10.21468/SciPostPhysProc.12.016.

[74] J. Tiffenberg et al. Single-Electron and Single-Photon Sensitivity with a Silicon Skipper CCD. *Phys. Rev. Lett.*, 119:131802, 2017. doi:10.1103/PhysRevLett.119.131802.

[75] A. Aguilar-Arevalo et al. Search for low-mass WIMPs in a 0.6 kg day exposure of the DAMIC experiment at SNOLAB. *Phys. Rev. D*, 94:082006, 2016. doi:10.1103/PhysRevD.94.082006.

[76] I. Arnquist et al. First Constraints from DAMIC-M on Sub-GeV Dark-Matter Particles Interacting with Electrons. *Phys. Rev. Lett.*, 130(17), 2023. doi:10.1103/physrevlett.130.171003.

[77] O. Abramoff et al. SENSEI: Direct-Detection Constraints on Sub-GeV Dark Matter from a Shallow Underground Run Using a Prototype Skipper CCD. *Phys. Rev. Lett.*, 122(16), 2019. doi:10.1103/physrevlett.122.161801.

[78] C. Kittel. *Introduction to Solid State Physics*. Wiley, 8 edition, 2004. ISBN 9780471415268.

[79] A. Aguilar-Arevalo et al. Confirmation of the spectral excess in DAMIC at SNOLAB with skipper CCDs. *Phys. Rev. D*, 109:062007, 2024. doi:10.1103/PhysRevD.109.062007.

[80] A. Aguilar-Arevalo et al. The Oscura Experiment, 2022. URL `https://arxiv.org/abs/2202.10518`.

[81] N. Saffold et al. The DarkNESS mission: probing dark matter with a Skipper-CCD satellite observatory. *PoS*, TAUP2023:062, 2024. doi:10.22323/1.441.0062.

[82] C. Amole et al. Dark matter search results from the complete exposure of the PICO-60 C_3F_8 bubble chamber. *Phys. Rev. D*, 100:022001, 2019. doi:10.1103/PhysRevD.100.022001.

[83] L. Balogh et al. The NEWS-G detector at SNOLAB. *J. Instrum.*, 18(02):T02005, 2023. doi:10.1088/1748-0221/18/02/t02005.

[84] E. Baracchini et al. CYGNO: a CYGNUs Collaboration 1 m^3 Module with Optical Readout for Directional Dark Matter Search, 2019. URL `https://arxiv.org/abs/1901.04190`.

[85] DAMA collaboration. Schematic view of the DAMA/LIBRA set-up, 2024. URL `https://dama.web.roma2.infn.it/?page_id=64`. [Online; accessed 27-August-2024].

[86] DAMA collaboration. DAMA/NaI, 2024. URL `https://dama.web.roma2.infn.it/?page_id=281`. [Online; accessed 27-August-2024].

[87] DAMA collaboration. DAMA/LIBRA, 2024. URL `https://dama.web.roma2.infn.it/?page_id=279`. [Online; accessed 27-August-2024].

[88] R. Bernabei et al. New limits on WIMP search with large-mass low-radioactivity NaI(Tl) set-up at Gran Sasso. *Phys. Lett. B*, 389(4):757–766, 1996. doi:https://doi.org/10.1016/S0370-2693(96)80020-7.

[89] R. Bernabei et al. Dark Matter particles in the galactic halo: results and implications from DAMA/NaI. *Int. J. Mod. Phys. D*, 13(10):2127–2159, 2004. doi:10.1142/s0218271804006619.

[90] R. Cerulli. Annual modulation results from DAMA/LIBRA. Talk given at the 15th International Workshop on the Identification of Dark Matter, 2024.

[91] R. Bernabei et al. Dark Matter: DAMA/LIBRA and its perspectives. *SciPost Phys. Proc.*, page 025, 2023. doi:10.21468/SciPostPhysProc.12.025.

[92] F. Kahlhoefer et al. Model-independent comparison of annual modulation and total rate with direct detection experiments. *J. Cosmol. Astropart. Phys.*, 2018 (05):074, 2018. doi:10.1088/1475-7516/2018/05/074.

[93] E. Barbosa de Souza et al. First search for a dark matter annual modulation signal with NaI(Tl) in the Southern Hemisphere by DM-Ice17. *Phys. Rev. D*, 95:032006, 2017. doi:10.1103/PhysRevD.95.032006.

[94] S. C. Kim et al. New Limits on Interactions between Weakly Interacting Massive Particles and Nucleons Obtained with CsI(Tl) Crystal Detectors. *Phys. Rev. Lett.*, 108:181301, 2012. doi:10.1103/PhysRevLett.108.181301.

[95] G. Adhikari et al. Three-year annual modulation search with COSINE-100. *Phys. Rev. D*, 106(5), 2022. doi:10.1103/physrevd.106.052005.

[96] N. Carlin et al. COSINE-100 Full Dataset Challenges the Annual Modulation Signal of DAMA/LIBRA, 2024. URL `https://arxiv.org/abs/2409.13226`.

[97] I. Coarasa et al. ANAIS–112 three years data: a sensitive model independent negative test of the DAMA/LIBRA dark matter signal. *Commun. Phys.*, 7(1):345, 2024. doi:10.1038/s42005-024-01827-y.

[98] J. Amaré et al. Towards a robust model-independent test of the DAMA/LIBRA dark matter signal: ANAIS-112 results with six years of data, 2025. URL `https://arxiv.org/abs/2502.01542`.

[99] J. A. Allué. Dark matter search opportunities with NaI scintillating crystals using SiPMs at cryogenic temperatures. Talk given at the 15th International Workshop on the Identification of Dark Matter, 2024.

[100] B. Suerfu et al. Growth of ultra-high purity NaI(Tl) crystals for dark matter searches. *Phys. Rev. Res.*, 2:013223, 2020. doi:10.1103/PhysRevResearch.2.013223.

[101] R. Bernabei et al. The DAMA/LIBRA apparatus. *Nucl. Instrum. Methods Phys. Res. Sect. A: Accel. Spectrometers Detect. Assoc. Equip.*, 592(3):297–315, 2008. doi:https://doi.org/10.1016/j.nima.2008.04.082.

[102] F. Calaprice et al. Performance of the SABRE detector module in a purely passive shielding. *Eur. Phys. J. C*, 82(12), 2022. doi:10.1140/epjc/s10052-022-11108-z.

[103] E. Barberio et al. Simulation and background characterisation of the SABRE South experiment: SABRE South Collaboration. *Eur. Phys. J. C*, 83(9), 2023. doi:10.1140/epjc/s10052-023-11817-z.

[104] K. Fushimi et al. PICOLON dark matter search project. *J. Phys.: Conf. Ser.*, 2156(1):012045, 2021. doi:10.1088/1742-6596/2156/1/012045.

[105] D. D'Angelo et al. The ASTAROTH project. *AIP Conf. Proc.*, 2908(1):100007, 2023. doi:10.1063/5.0161723.

[106] J. Amaré et al. Annual modulation results from three-year exposure of ANAIS-112. *Phys. Rev. D*, 103:102005, 2021. doi:10.1103/PhysRevD.103.102005.

[107] F. Calaprice et al. High sensitivity characterization of an ultrahigh purity NaI(Tl) crystal scintillator with the SABRE proof-of-principle detector. *Phys. Rev. D*, 104: L021302, 2021. doi:10.1103/PhysRevD.104.L021302.

[108] G. Adhikari et al. Strong constraints from COSINE-100 on the DAMA dark matter results using the same sodium iodide target. *Sci. adv.*, 7(46), 2021. doi:10.1126/sciadv.abk2699.

[109] Triangle Universities Nuclear Laboratory, 2025. URL `https://tunl.duke.edu/`.

[110] S. H. Lee et al. Measurements of low-energy nuclear recoil quenching factors for Na and I recoils in the NaI(Tl) scintillator. *Phys. Rev. C*, 110:014614, 2024. doi:10.1103/PhysRevC.110.014614.

[111] D. Cintas et al. Measurement of the sodium and iodine scintillation quenching factors across multiple NaI(Tl) detectors to identify systematics. *Phys. Rev. C*, 110:014613, 2024. doi:10.1103/PhysRevC.110.014613.

[112] L.J. Bignell et al. Quenching factor measurements of sodium nuclear recoils in NaI:Tl determined by spectrum fitting. *J. Instrum.*, 16(07):P07034, 2021. doi:10.1088/1748-0221/16/07/P07034.

[113] J. Xu et al. Scintillation efficiency measurement of Na recoils in NaI(Tl) below the DAMA/LIBRA energy threshold. *Phys. Rev. C*, 92:015807, 2015. doi:10.1103/PhysRevC.92.015807.

[114] T. Stiegler, C. Sofka, R. C. Webb, and J. T. White. A study of the NaI(Tl) detector response to low energy nuclear recoils and a measurement of the quenching factor in NaI(Tl), 2017. URL `https://arxiv.org/abs/1706.07494`.

[115] M. J. Zurowski. Hidden dependencies in model independent tests of DAMA. *SciPost Phys. Proc.*, page 027, 2023. doi:10.21468/SciPostPhysProc.12.027.

[116] Commissione Scientifica Nazionale V. Proposed experiments for the year 2016, 2015. URL `https://web.infn.it/csn5/index.php/en/experiments/name-spokeman-referee/54-esperimento-2016`.

[117] Laboratori Nazionali del Gran Sasso. Toward the discovery of the hidden side of our Universe, 2021. URL `https://www.lngs.infn.it/en/news/cosinus-universe-2`. [Online; accessed 10-November-2024].

[118] CERN Grey Book Secretariat. The CERN Experimental Programme - Grey Book database, 2021. URL `https://greybook.cern.ch/experiment/detail?id=RE41`.

[119] T. Miyata. Exciton Structure of NaI and NaBr. *J. Phys. Soc. Jpn.*, 27(1):266–266, 1969. doi:10.1143/JPSJ.27.266.

[120] P. A. Rodnyi, P. Dorenbos, and C. W. E. van Eijk. Energy Loss in Inorganic Scintillators. *Phys. Status Solidi (B)*, 187(1):15–29, 1995. doi:https://doi.org/10.1002/pssb.2221870102.

[121] G. Angloher et al. The COSINUS project: perspectives of a NaI scintillating calorimeter for dark matter search. *Eur. Phys. J. C*, 76(8), 2016. doi:10.1140/epjc/s10052-016-4278-3.

[122] V.I. Tretyak. Semi-empirical calculation of quenching factors for ions in scintillators. *Astropart. Phys.*, 33(1):40–53, 2010. doi:https://doi.org/10.1016/j.astropartphys.2009.11.002.

[123] L. Einfalt. *Light quenching in scintillator-based cryogenic detectors for dark matter searches.* PhD thesis, Technische Universität Wien, 2024.

[124] V. Zema et al. Dark matter-electron scattering search using cryogenic light detectors. *Phys. Rev. D*, 110:123012, 2024. doi:10.1103/PhysRevD.110.123012.

[125] C. Ananna et al. Detectors and Shieldings: Past and Future at LUNA. *Universe*, 10(5), 2024. doi:10.3390/universe10050228.

[126] M. Kellermann et al. A Vibration Decoupling System for TES Operation in the COSINUS Dry Dilution Refrigerator. *J. Low Temp. Phys.*, 217:418–425, 2024. doi:10.1007/s10909-024-03206-x.

[127] M. Ambrosio et al. Vertical muon intensity measured with MACRO at the Gran Sasso laboratory. *Phys. Rev. D*, 52:3793–3802, 1995. doi:10.1103/PhysRevD.52.3793.

[128] W. Woodley, A. Fedynitch, and M. Piro. Cosmic ray muons in laboratories deep underground. *Phys. Rev. D*, 110:063006, 2024. doi:10.1103/PhysRevD.110.063006.

[129] G. Angloher et al. Simulation-based design study for the passive shielding of the COSINUS dark matter experiment. *Eur. Phys. J. C*, 82(3), 2022. doi:10.1140/epjc/s10052-022-10184-5.

[130] Aurubis AG, 2024. URL `https://www.aurubis.com/en/`.

[131] V.A. Kudryavtsev, N.J.C. Spooner, and J.E. McMillan. Simulations of muon-induced neutron flux at large depths underground. *Nucl. Instrum. Methods Phys. Res. Sect. A: Accel. Spectrometers Detect. Assoc. Equip.*, 505(3):688–698, 2003. doi:https://doi.org/10.1016/S0168-9002(03)00983-5.

[132] Shijiazhuang Dajia New materials Technology Co.,Ltd, 2025. URL `https://www.ddplasticfilm.com/`.

[133] 3M, 2025. URL `https://www.3m.com/`.

[134] J. E. Sadleir et al. Proximity effects and nonequilibrium superconductivity in transition-edge sensors. *Phys. Rev. B*, 84(18), 2011. doi:10.1103/physrevb.84.184502.

[135] J. Rothe. *Low-Threshold Cryogenic Detectors for Low-Mass Dark Matter Search and Coherent Neutrino Scattering.* PhD thesis, Technische Universität München, 2021.

[136] Bartington, 2024. URL `https://www.bartington.com/products/mag-13/`.

[137] A Raccanelli, L.A Reichertz, and E Kreysa. Eliminating the vibrational noise in continuously filled 1 K pots. *Cryogenics*, 41(10):763–766, 2001. doi:https://doi.org/10.1016/S0011-2275(01)00157-6.

[138] A. Nordrum. The era of cheap helium is over—and that's already causing problems, 2024. URL `https://www.technologyreview.com/2024/02/25/1088930/global-helium-market-semiconductors/`. [Online; accessed 24-November-2024].

[139] Bluefors Oy. Pt420 cryocooler with remote motor option, 2021. URL `https://bluefors.com/products/pulse-tube-cryocoolers/pt420-pulse-tube-cryocooler/`.

[140] E. Olivieri et al. Vibrations on pulse tube based Dry Dilution Refrigerators for low noise measurements. *Nucl. Instrum. Methods Phys. Res. Sect. A: Accel. Spectrometers Detect. Assoc. Equip.*, 858:73–79, 2017. doi:10.1016/j.nima.2017.03.045.

[141] C. Enss and S. Hunklinger. *Cooling Techniques*, pages 449–504. Springer Berlin Heidelberg, Berlin, Heidelberg, 2005. ISBN 978-3-540-26619-8. doi:10.1007/3-540-26619-4_11.

[142] CryoConcept, 2024. URL `https://cryoconcept.com/`.

[143] Pfeiffer Vacuum GmbH, 2021. URL `https://www.pfeiffer-vacuum.com`.

[144] GVL Cryoengineering, 2025. URL `http://www.gvl-cryoengineering.de/`.

[145] Tekdata Interconnections Limited, 2025. URL `https://www.alpha3manufacturing.com/`.

[146] STAR Cryoelectronics, 2024. URL `https://starcryo.com/`.

[147] Mouser Electronics, Inc. 2306334-3, n. d. URL `https://eu.mouser.com/images/tycoelectronics/lrg/2306334-3_SPL.jpg`.

[148] TE Connectivity Corporation, 2025. URL `https://www.te.com/`.

[149] L. Gottardi and K. Nagayashi. A Review of X-ray Microcalorimeters Based on Superconducting Transition Edge Sensors for Astrophysics and Particle Physics. *Appl. Sci.*, 11(9), 2021. doi:10.3390/app11093793.

[150] A. Jain et al. Commentary: The Materials Project: A materials genome approach to accelerating materials innovation. *APL Mater.*, 1(1):011002, 2013. doi:10.1063/1.4812323.

[151] The Materials Project. Materials Data on NaI by Materials Project, 2020. doi:10.17188/1199379.

[152] B. Campbell-Deem et al. Dark matter direct detection from the single phonon to the nuclear recoil regime. *Phys. Rev. D*, 106:036019, 2022. doi:10.1103/PhysRevD.106.036019.

[153] J. Åström et al. Fracture processes observed with a cryogenic detector. *Phys. Lett. A*, 356(4):262–266, 2006. doi:https://doi.org/10.1016/j.physleta.2006.03.059.

[154] J. V. Yakhmi. Introduction to superconductivity, superconducting materials and their usefulness. In *Superconducting Materials and Their Applications*, 2053-2563, pages 1–1 to 1–24. IOP Publishing, 2021. ISBN 978-0-7503-2256-0.

doi:10.1088/978-0-7503-2256-0ch1. URL https://dx.doi.org/10.1088/978-0-7503-2256-0ch1.

[155] A. Abdelhameed. *Aspects of TES Novel Reproducibility for Cryogenic Detectors Dedicated to Dark Matter Search.* PhD thesis, Technische Universität München, 2022.

[156] S. Henry et al. The 66-channel SQUID readout for CRESST II. *J. Instrum.*, 2 (11):P11003, 2007. doi:10.1088/1748-0221/2/11/P11003.

[157] Bluefors Oy, 2024. URL https://bluefors.com/.

[158] J. Rothe. Achieving low thresholds: Cryogenic detectors for low-mass dark matter searches. Master's thesis, Ludwig-Maximilians-Universität München, 2016.

[159] W.M. Haynes. *CRC Handbook of Chemistry and Physics.* CRC Handbook of Chemistry and Physics. CRC Press, 2014. ISBN 9781482208689.

[160] E. Creutz (eds.). *Nuclear Instrumentation II / Instrumentelle Hilfsmittel der Kernphysik II.* Encyclopedia of Physics / Handbuch der Physik 8 / 45. Springer-Verlag Berlin Heidelberg, 1 edition, 1958. ISBN 978-3-642-45905-4,978-3-642-45903-0.

[161] LLC MatWeb. MatWeb material property data: sodium iodide, NaI, 2024. URL https://www.matweb.com/search/datasheet.aspx?matguid=95a611c896f94733bb666901bf06056d. [Online; accessed 06-November-2024].

[162] F. Pröbst et al. Model for cryogenic particle detectors with superconducting phase transition thermometers. *J. Low Temp. Phys.*, 100(1):69–104, 1995. doi:10.1007/BF00753837.

[163] F. Wagner. *Towards next-generation cryogenic dark matter searches with superconducting thermometers.* PhD thesis, Technische Universität Wien, 2023.

[164] M. Kiefer et al. Glued CaWO4 detectors for the CRESST-II experiment. *Opt. Mater.*, 31(10):1410–1414, 2009. doi:https://doi.org/10.1016/j.optmat.2008.09.019.

[165] G. Angloher et al. Results on low mass WIMPs using an upgraded CRESST-II detector. *Eur. Phys. J. C*, 74(12), 2014. doi:10.1140/epjc/s10052-014-3184-9.

[166] G. Angloher et al. A CsI low-temperature detector for dark matter search. *Astropart. Phys.*, 84:70–77, 2016. doi:https://doi.org/10.1016/j.astropartphys.2016.08.005.

[167] G. Angloher et al. Results from the first cryogenic NaI detector for the COSINUS project. *J. Instrum.*, 12(11):P11007–P11007, 2017. doi:10.1088/1748-0221/12/11/p11007.

[168] F. Reindl et al. Results of the first NaI scintillating calorimeter prototypes by COSINUS. *J. Phys.: Conf. Ser.*, 1342(1):012099, 2020. doi:10.1088/1742-6596/1342/1/012099.

[169] V. Zema. *Unveiling the Nature of Dark Matter with Direct Detection Experiments.* PhD thesis, Chalmers University of Technology, 2020.

[170] M. Stahlberg. personal communication, 2025.

[171] M. Pyle, E. Figueroa-Feliciano, and B. Sadoulet. Optimized Designs for Very Low Temperature Massive Calorimeters, 2015. URL `https://arxiv.org/abs/1503.01200`.

[172] W.T. Kim et al. Optimization of cryogenic calorimetric detection with lithium molybdate crystals for AMoRE-II experiments. *J. Instrum.*, 17(07):P07034, 2022. doi:10.1088/1748-0221/17/07/P07034.

[173] C. Augier et al. Results from a prototype TES detector for the Ricochet experiment. *Nucl. Instrum. Methods Phys. Res. Sect. A: Accel. Spectrometers Detect. Assoc. Equip.*, 1057:168765, 2023. doi:https://doi.org/10.1016/j.nima.2023.168765.

[174] Applied Physics Systems, 2024. URL `https://appliedphysics.com/`.

[175] G. Angloher et al. First measurements of remoTES cryogenic calorimeters: Easy-to-fabricate particle detectors for a wide choice of target materials. *Nucl. Instrum. Methods Phys. Res. Sect. A: Accel. Spectrometers Detect. Assoc. Equip.*, 1045: 167532, 2023. doi:https://doi.org/10.1016/j.nima.2022.167532.

[176] G. Angloher et al. Particle discrimination in a NaI crystal using the COSINUS remote TES design. *Phys. Rev. D*, 109:082003, 2024. doi:10.1103/PhysRevD.109.082003.

[177] V. Zema et al. Description and Performance of the COSINUS remoTES Design. *J. Low Temp. Phys.*, 2024. doi:10.1007/s10909-024-03201-2.

[178] K. Shera. Studies on the remoTES-based cryogenic calorimeters for the COSINUS experiment. Master's thesis, Technische Universität München, 2023.

[179] I. Alkhatib et al. Light Dark Matter Search with a High-Resolution Athermal Phonon Detector Operated above Ground. *Phys. Rev. Lett.*, 127:061801, 2021. doi:10.1103/PhysRevLett.127.061801.

[180] G. Angloher et al. Results on sub-GeV dark matter from a 10 eV threshold CRESST-III silicon detector. *Phys. Rev. D*, 107:122003, 2023. doi:10.1103/PhysRevD.107.122003.

[181] Micro to Nano BV, 2025. URL `https://www.microtonano.com/`.

[182] Epoxy technology, 2024. URL `https://www.epotek.com/`.

[183] G. Angloher et al. A likelihood framework for cryogenic scintillating calorimeters used in the CRESST dark matter search. *The European Physical Journal C*, 84 (9), 2024. doi:10.1140/epjc/s10052-024-13141-6.

[184] Gößl + Pfaff GmbH, 2024. URL `https://www.goessl-pfaff.de/`.

[185] E. T. Swartz and R. O. Pohl. Thermal boundary resistance. *Rev. Mod. Phys.*, 61: 605–668, 1989. doi:10.1103/RevModPhys.61.605.

[186] P. Reddy, K. Castelino, and A. Majumdar. Diffuse mismatch model of thermal boundary conductance using exact phonon dispersion. *Appl. Phys. Lett.*, 87(21): 211908, 2005. doi:10.1063/1.2133890.

[187] G. Angloher et al. DoubleTES detectors to investigate the CRESST low energy background: results from above-ground prototypes. *Eur. Phys. J. C*, 84(10), 2024. doi:10.1140/epjc/s10052-024-13282-8.

[188] R. Strauss et al. The ν-cleus experiment: a gram-scale fiducial-volume cryogenic detector for the first detection of coherent neutrino–nucleus scattering. *Eur. Phys. J. C*, 77(8), 2017. doi:10.1140/epjc/s10052-017-5068-2.

[189] C. R. Harris et al. Array programming with NumPy. *Nature*, 585(7825):357–362, 2020. doi:10.1038/s41586-020-2649-2.

[190] R. N. Claytor and B. J. Marshall. Specific Heat and Elastic Constants of Sodium Iodide at Low Temperatures. *Phys. Rev.*, 120:332–334, 1960. doi:10.1103/PhysRev.120.332.

[191] A. Cruciani et al. BULLKID: Monolithic array of particle absorbers sensed by kinetic inductance detectors. *Appl. Phys. Lett.*, 121(21):213504, 2022. doi:10.1063/5.0128723.

[192] M. Kaznacheeva and K. Schäffner. Scintillating low-temperature calorimeters for direct dark matter search. *J. Adv. Instrum. Sci.*, 2024(1), 2024. doi:10.31526/jais.2024.514.

[193] F. Terzioglu, J. A. Rongong, and C. E. Lord. Motional phase maps for estimating the effectiveness of granular dampers. *Mech. Syst. Signal Process.*, 188:110038, 2023. doi:https://doi.org/10.1016/j.ymssp.2022.110038.

[194] S. Pirro et al. Vibrational and thermal noise reduction for cryogenic detectors. *Nucl. Instrum. Methods Phys. Res. Sect. A: Accel. Spectrometers Detect. Assoc. Equip.*, 444(1):331–335, 2000. doi:https://doi.org/10.1016/S0168-9002(99)01376-5.

[195] R. Kalra et al. Vibration-induced electrical noise in a cryogen-free dilution refrigerator: Characterization, mitigation, and impact on qubit coherence. *Rev. Sci. Instrum.*, 87(7):073905, 2016. doi:10.1063/1.4959153.

[196] E. Mykkänen et al. Reducing current noise in cryogenic experiments by vacuum-insulated cables. *Rev. Sci. Instrum.*, 87(10):105111, 2016. doi:10.1063/1.4963904.

[197] C. Zener. Internal friction in solids. *Proc. Phys. Soc.*, 52(1):152, 1940. doi:10.1088/0959-5309/52/1/322.

[198] NUCLEUS, 2024,. URL `https://nucleus-experiment.org`.

[199] Metra Mess- und Frequenztechnik in Radebeul e.K., 2024. URL `https://mmf.de/`.

[200] Metra Mess- und Frequenztechnik in Radebeul e.K. ks48c-c2bfd880.webp, 2024. URL `https://mmf.de/wp-content/themes/yootheme/cache/c2/ks48c-c2bfd880.webp`. [Online; accessed 27-December-2024].

[201] Metra Mess- und Frequenztechnik in Radebeul e.K. scher_schnitt.png, 2024. URL `https://mmf.de/wp-content/uploads/2023/08/scher_schnitt.png`. [Online; accessed 27-December-2024].

[202] PCB Piezotronics, 2024. URL `https://www.pcb.com/`.

[203] S. Pirro. personal communication, 2023.

[204] L. Jones and M. A. Peck. Stability and control of a flux-pinned docking interface for spacecraft. *AIAA Guid. Navig. Control Conf.*, 2010. doi:10.2514/6.2010-8298.

[205] T. Shibata and S. Sakai. A Contactless Micro-Vibration Isolator Using the Flux Pinning Effect for Space Telescopes. *J. Spacecr. Rockets*, 59(2):651–659, 2022. doi:10.2514/1.A35045.

[206] Metra Mess- und Frequenztechnik in Radebeul e.K. Accelerometer Mounting, 2024. URL `https://mmf.de/en/accelerometer-mounting/`. [Online; accessed 27-December-2024].

[207] NATIONAL INSTRUMENTS CORP., 2024. URL `https://www.ni.com/`.

[208] F. Duvigneau, S. Koch, E. Woschke, and U. Gabbert. An effective vibration reduction concept for automotive applications based on granular-filled cavities. *J. Vib. Control*, 24(1):73–82, 2018. doi:10.1177/1077546316632932.

[209] T. Irvine. *An Introduction to Shock and Vibration Response Spectra, rev E.* 08 2023.

[210] J. Wang, X. Bian, Q. Li, and J. Wu. A magnetic damper for low temperature. *AIP Adv.*, 10(10):105107, 2020. doi:10.1063/5.0018572.

[211] A. Ahmine et al. Test of ^{116}CdWO$_4$ and Li$_2$MoO$_4$ scintillating bolometers in the CROSS underground facility with upgraded detector suspension. *J. Instrum.*, 18 (12):P12004, 2023. doi:10.1088/1748-0221/18/12/P12004.

[212] Brüel & Kjær, 2023. URL `https://www.bksv.com/`.

[213] Sigmatest Messtechnik, 2024. URL `https://www.sigmatest.net/index.html`.

[214] F. Reindl. *Exploring Light Dark Matter With CRESST-II Low-Threshold Detectors*. PhD thesis, Technische Universität München, 2016.

[215] M. Stahlberg. *Probing Low-Mass DarkMatter with CRESST-III - Data Analysis and First Results*. PhD thesis, Technische Universität Wien, 2021.

[216] M. Gapp. Implementation of automated analysis modules for large arrays of cryogenic detectors. Master's thesis, Technische Universität München, 2024.

[217] F. Wagner et al. CAIT - analysis toolkit for cryogenic particle detectors in python. *Comput. Softw. Big Sci.*, 6(1):19, 2022. doi:10.1007/s41781-022-00092-4.

Acknowledgements

This thesis marks the end of an important chapter of my life. I am grateful to the many people who supported me on this journey and made my time in Munich unforgettable. These last pages are dedicated to thanking them:

First and foremost, I thank Prof. Dr. Stefan Schönert for allowing me to pursue my PhD and for your supervision. Many thanks to Prof. Dr. Allen Caldwell, who agreed to be my second referee.

This work would not have been possible without Dr. Karoline Schäffner, who patiently supervised me and led our group with inspiring enthusiasm. You introduced me to this exciting field of cryogenic detectors and taught me many things in physics and in life. Thank you for allowing me to be part of this group as its first Ph.D. student.

I am deeply grateful to Dr. Michele Mancuso and the whole CRESST group of MPP. Without your assistance, expertise, and equipment, producing or measuring any of our particle detectors would not have been possible.

I also want to extend my gratitude to Dr. Johannes Rothe and the NUCLEUS group of TUM for the insightful discussions and for sharing your equipment with us.

Thanks to Christoph Schwertner, who built a great data acquisition system and who helped devise the detector cabling with great expertise.

Many thanks to Dr. Stefano Pirro for sharing your vibration sensors and expertise in vibrational analysis with me.

Thanks should also go to Dr. Torsten Frank for your help in devising the vibration decoupling system and for your valuable comments and ideas that helped improve my work.

I thank Dr. Franz Pröbst and Dr. Godehard Angloher for our insightful discussions over the years. I always enjoyed listening to your experiences.

To Dr. Martin Stahlberg: thank you for always taking the time to answer my questions and requests and for patiently teaching me about data analysis and computing.

To Dr. Vanessa Zema: I enjoyed our conversations about physics and beyond. Your enthusiasm is contagious, and you inspired me to stay true to the fundamentals.

Special thanks also to Dr. Maximilian Hughes for always being available whenever I needed technical assistance or had a question about nuclear physics.

Many thanks to Mukund Bharadwaj. You have been a great office mate, and I enjoyed our time studying together. Your perspective on things helped me whenever I needed to sort my thoughts. I wish you all the best for your own thesis!

In the last few years, our group has kept growing. I thank the next generation of Ph.D. students Kumrie, Clemens, and Maxi, as well as our Bachelor-, Master- and working students Henrik, Pablo, Kilian, Sarah, Elisa, and Lutz for bringing new life and momentum to the group.

Besides our group at MPP, I want to thank all former and current members of the COSINUS collaboration. Working with you towards a common goal is very enjoyable, and I liked all our discussions in and outside our meetings.

A special thanks to our analysis team, which always provided quick and good feedback whenever we tested a new detector.

I want to thank everyone again who proofread parts of my thesis: Mukund, Maxi, Martin, Mariano, Clemens, Vanessa, Kumrie, and Karo.

Als Experiment im Aufbau konnten wir uns stets auf die technischen Abteilungen vom MPP verlassen. Ich bedanke mich für die Geduld und Professionalität, mit der ihr uns stets unterstützt habt. Ich möchte mich dabei besonders bei unserem “A-Team” bedanken. Unsere gemeinsamen Aufenthalte in Italien habe ich sehr genossen.

Mein besonderer Dank gilt auch Karlheinz Ackermann und Robert Stadler. Ihr habt aus kleinen und großen Ideen Realität werden lassen, auch wenn sie noch so unmöglich schienen. Insbesondere für die vielen Ideen, Entwürfe und Zeichnungen zur Verkabelung und Vibrationsentkopplung will ich mich ausdrücklich bedanken.

Ich bedanke mich außerdem bei den Verwaltungsabteilungen des MPPs für die Unterstützung bei Dienstreisen, Beschaffungen und anderen administrativen Angelegenheiten.

Zuletzt möchte ich bei meiner Familie bedanken. Danke, dass ihr mich stets unterstützt habt. Über jeden Besuch von euch und bei euch habe ich mich sehr gefreut und ich weiß, dass ich auch weiterhin auf euch zählen kann. Danke!